# ⁸⁹Zr-immuno-PET:

## Towards a clinical tool to guide antibody-based therapy in cancer

Yvonne Jauw

# $^{89}$Zr-immuno-PET:

## Towards a clinical tool to guide antibody-based therapy in cancer

Yvonne Jauw

**2019**

VRIJE UNIVERSITEIT

# [89]Zr-immuno-PET:

## Towards a clinical tool to guide antibody-based therapy in cancer

ACADEMISCH PROEFSCHRIFT

ter verkrijging van de graad Doctor aan
de Vrije Universiteit Amsterdam,
op gezag van de rector magnificus
prof.dr. V. Subramaniam,
in het openbaar te verdedigen
ten overstaan van de promotiecommissie
van de Faculteit der Geneeskunde
op donderdag 19 september 2019 om 15.45 uur
in de aula van de universiteit,
De Boelelaan 1105

door

Yvonne Wen Sian Jauw

geboren te Utrecht

# CONTENTS

# CHAPTER 1

**General introduction**

# ANTIBODY-BASED TREATMENT IN CANCER

The scientific concept of a "magic bullet" to specifically eradicate disease, without harming the body, was developed by Paul Ehrlich (1854-1915) (*1*). Treatment of cancer with chemotherapy or radiotherapy does not meet these expectations as significant toxicity is caused by destruction of normal healthy cells.

In 1975, George Kohler and Cesar Milstein discovered a way to produce large numbers of identical, monoclonal antibodies (mAbs) directed against specific target antigens (*2*). This hybridoma technique allowed the development of rituximab, a chimeric mouse/human monoclonal antibody with binding specificity to the target antigen CD20. This target antigen is a transmembrane protein expressed on the surface of normal and malignant B cells. It was considered a suitable target antigen as absence of CD20 expression in B-cell non Hodgkin lymphoma at initial diagnosis is extremely rare (1-2%) (*3*). Although normal B cells are targeted as well, overall toxicity (e.g. increased infection risk) is limited and treatment with rituximab is usually well tolerated. Depletion of CD20-positive B-cells generally does not cause permanent side effects as mature plasma cells and B-cell progenitor cells do not express CD20.

In 1980, proof-of-principle of efficacy was demonstrated as the first patient receiving an anti-CD20 antibody showed a decrease in circulating tumor cells (*4*). Rituximab was the first therapeutic mAb in oncology and was initially approved in 1997 for the treatment of follicular lymphoma (*5*). Subsequently, rituximab was implemented in the treatment for all B-cell malignancies. The clinical impact has been found to be significant. For example, the 2-year overall survival of previously untreated elderly patients with diffuse large B cell lymphoma was 70% vs 57% for rituximab combined with chemotherapy versus chemotherapy alone (*6*).

*"All that glitters is not gold"*
Despite the initial response, patients often relapse (*7*). It remains unclear which patients will benefit from further treatment with rituximab. Various mechanisms of rituximab resistance have been proposed (*8*).

One mechanism is insufficient cell death after rituximab binds to CD20 (downstream effects). To increase cell death, novel, fully humanized, anti-CD20 mAbs have been developed: ofatumumab for increased complement-dependent cytotoxicity and obinutuzumab for increased antibody-dependent cellular cytotoxicity. Other approaches for increased efficacy include radio-immunotherapy

(tositumomab and ibritumomab-tiuxetan), antibody-drug conjugates (for example rituximab conjugated to doxorubicin) and bispecific mAbs (antiCD20xantiCD3 mAb).

When using the same target, in this case CD20, it is important to know whether the target antigen is still present and whether there is target engagement. Reduced CD20 expression has been associated with an inferior survival indeed (*9*). However, at relapsed/refractory disease, a biopsy is not always performed. Even when a biopsy is available, there are several limitations. Reduced CD20 expression cannot be reliably quantified by immunohistochemistry (IHC) (*9*). In addition, a single biopsy may not be representative due to sampling error and target expression may be heterogeneous. Therefore, even when CD20 expression is considered absent by IHC, it is still a matter of debate whether subsequent treatment with rituximab should be withheld.

This emphasizes the need for a reliable biomarker to predict which patients will benefit from rituximab treatment. Moreover, this would lead to improved cost effectiveness of the treatment, as rituximab is an expensive drug (*10*). For patients who are not likely to respond, different treatment approaches (e.g. aimed at different target antigens or other modalities) should be considered. In 2018, 33 mAbs have been approved by the FDA for the treatment of cancer (*11*). Ideally, mAbs provide selective treatment by targeting the tumor, without affecting normal tissues. For mAb-based treatments, the choice of a target antigen which is 'available' and tumor-selective is essential to increase chances of success (maximal efficacy, minimal toxicity). Assessment of target engagement in normal tissues should provide information which target is suitable for development of antibody-drug conjugates and help to improve safety. Preclinical studies provide limited information, as target expression in normal tissues may be different between animals and humans. Traditionally, in drug development, safety and dose finding is assessed in a first-in-human phase I dose escalation trial, followed by evaluation of preliminary efficacy in a phase II trial. If the results are promising late-stage trials in larger patient cohorts are performed, before the new drug is ready for regulatory review. Currently, many mAbs are under development for the treatment of cancer (phase 1 [200 mAbs], phase 2 [110 mAbs], late stage trials [33 mAbs]) (*11*). This process requires a considerable amount of time, effort, financial resources and large numbers of patients to participate in clinical trials. In general, the time from drug discovery to regulatory approval is estimated at 15 years, of which approximately 7 years in phase I to III trials (*12*).

1

Patient and drug selection becomes increasingly important in nowadays societal discussions about affordability of so-called "expensive targeted drugs" (*13*). Therefore, it is important to answer the following questions:

- Which patient (or subgroup of patients) will benefit from the drug?
- Which drug has high potential (safety and efficacy) for further development?

For antibody-based therapy, target engagement in the tumor is considered a requirement for efficacy, while target engagement in normal tissues considered unfavorable (e.g. for development of antibody-drug conjugates).

A reliable biomarker of target engagement could increase efficacy and reduce unnecessary toxicity and costs. In addition, detection of subgroups of patients benefitting from treatment would omit the need for large randomized clinical trials with heterogeneous patient populations. Intelligent trial design including a biomarker could shorten the time from early clinical development to approval of antibody-based therapy.

## Antibody imaging with immuno-PET

Antibody imaging can provide a potential biomarker to predict toxicity and efficacy. Advantages of an imaging biomarker are that it is non-invasive and provides whole body information about normal tissues and tumors. Positron emission tomography (PET) can be used as an imaging modality to obtain functional information on a mAb, after its labeling with a positron emitting radionuclide. A radiolabeled mAb is administered intravenously and subsequently PET-CT scans are acquired to visualize and quantify the distribution over the body. This technique is referred to as antibody-PET or more common as immuno-PET.

Intact mAbs require a relative long period of time (days) to reach the target and accumulate. Therefore, zirconium-89 with a half-life of 78.4 hours is a suitable long-lived positron emitter for immuno-PET (*14*). Radiolabeling methods were developed and reagents made worldwide available to allow production of stable $^{89}$Zr-labeled mAbs according to Good Manufacturing Practice (GMP) for clinical use (*15, 16*).

In daily clinical practice, $^{18}$F-fluoro-2-deoxy-glucose (FDG) is the most widely used radiotracer for PET. Increased uptake of $^{18}$F-FDG corresponds with increased glucose metabolism (*17*). As high glucose uptake is a hallmark of

malignant cells, ^{18}F-FDG-PET is used for staging and response evaluation for different types of cancer (*18, 19*). But uptake of ^{18}F-FDG does not provide information on target engagement of mAbs. For this purpose, we aim to develop [89]Zr-immuno-PET as a clinical tool to guide antibody-based therapy in cancer.

*"It is usually a bad idea to develop a new measurement instrument"*
Feasibility (including safety), technical validation, biological/clinical validation and cost effectiveness are required for successful implementation of a novel imaging biomarker in clinical cancer research and in daily clinical practice. Only when no existing measurement instrument is suitable for the specific need, and the purpose is of utmost importance, development of a new measurement instrument can be justified. We consider [89]Zr-immuno-PET as a clinical tool to guide antibody-based therapy to meet these criteria, as we described in the previous paragraphs.

Contrary to biospecimen-derived biomarkers (measured from blood or tissue samples), where technical validation usually occurs before biological/clinical validation, these steps are performed in parallel for imaging biomarkers (*20*).

The following aspects have to be considered to develop [89]Zr-immuno-PET as a clinical tool to guide antibody-based therapy in cancer:

1. Feasibility
    o Are [89]Zr-labeled mAbs safe to administer?
    o What is the radiation exposure due to [89]Zr-immuno-PET?
    o Can [89]Zr-immuno-PET visualize tumor uptake?
    o Can tumor uptake and bloodpool activity be quantified with [89]Zr-immuno-PET?
    o Are the ideas and findings of using [89]Zr-immuno-PET relevant and sustainable?
2. Validation
    • Technical validation
      What is the measurement variability of [89]Zr-immuno-PET?
        o What is the measurement variability due to noise (e.g. counting statistics)?
        o What is the interobserver reproducibility of tumor quantification?
    • Biological/clinical validation
      Is [89]Zr-immuno-PET able to measure the underlying biology?

o Can [89]Zr-immuno-PET be used to assess tumor targeting and is uptake correlated to target expression in biopsies?

o Can [89]Zr-immuno-PET be used to assess target-mediated specific uptake in normal tissues (defined as dose-dependent uptake)?

o Can [89]Zr-immuno-PET be used to assess non-specific uptake in normal tissues (defined as reversible, (e.g. blood volume) or irreversible (due to [89]Zr-residualization after mAb degradation)?

## Outline of this thesis

The aim of this thesis was to develop [89]Zr-immuno-PET as a clinical tool to guide antibody-based treatment in cancer. This thesis consists of two parts.

Part I describes the feasibility of the first clinical [89]Zr-immuno-PET study ever. The step from preclinical research to clinical translation of [89]Zr-immuno-PET was performed by the first-in-human study with [89]Zr-labeled chimeric monoclonal antibody (cmAb) U36. Twenty patients with head and neck cancer, scheduled for surgery, received [89]Zr-cmAb U36. Chapter 2 evaluates safety, biodistribution, dosimetry and PET quantification of immuno-PET with [89]Zr-cmAb U36. Chapter 3 reports on the diagnostic imaging performance of [89]Zr-immuno-PET for the detection of primary head and neck tumors and lymph node metastases for the same cohort of patients.

In **Chapter 4**, a review is provided of the first 15 clinical trials with [89]Zr-immuno-PET in oncology. Lessons learned and technical aspects of study design are discussed.

**Part II** focuses on validation of [89]Zr-immuno-PET. **Chapter 5** describes the measurement of variability due to noise. In **Chapter 6**, interobserver reproducibility of tumor uptake measures of [89]Zr-immuno-PET was investigated. **Chapter 7**, deals on the performance of [89]Zr-rituximab-PET as an imaging biomarker to assess CD20 targeting in patients with relapsed/refractory diffuse large B cell lymphoma. **Chapter 8** describes the use of immuno-PET in a phase I dose escalation study for detection of specific, target-mediated uptake in normal tissues, using the antiCD44 antibody RG7356 as an example. In **Chapter 9**, non-specific uptake in normal tissues for therapeutic mAbs (antiCD20, antiEGFR, antiPSMA and antiHER2) was determined as a critical step towards quantification of target engagement. In **Chapter 10**, the results presented in this thesis are summarized and future perspectives are discussed.

# REFERENCES

1. The Collected Papers of Paul Ehrlich. Elsevier; 1960.

2. Köhler G, Milstein C. Continuous cultures of fused cells secreting antibody of predefined specificity. *Nature*. 1975;256:495-497.

3. Katchi T, Liu D. Diagnosis and treatment of CD20 negative B cell lymphomas. *Biomarker Research*. 2017;5:5.

4. Nadler LM, Stashenko P, Hardy R, et al. Serotherapy of a patient with a monoclonal antibody directed against a human lymphoma-associated antigen. *Cancer Res*. 1980;40:3147-3154.

5. Pierpont TM, Limper CB, Richards KL. Past, Present, and Future of Rituximab-The World's First Oncology Monoclonal Antibody Therapy. *Front Oncol*. 2018;8:163.

6. Coiffier B, Lepage E, Brière J, et al. CHOP Chemotherapy plus Rituximab Compared with CHOP Alone in Elderly Patients with Diffuse Large-B-Cell Lymphoma. *New England Journal of Medicine*. 2002;346:235-242.

7. Gisselbrecht C, Glass B, Mounier N, et al. Salvage regimens with autologous transplantation for relapsed large B-cell lymphoma in the rituximab era. *J Clin Oncol*. 2010;28:4184-4190.

8. Rezvani AR, Maloney DG. Rituximab resistance. *Best Pract Res Clin Haematol*. 2011;24:203-216.

9. Johnson NA, Boyle M, Bashashati A, et al. Diffuse large B-cell lymphoma: reduced CD20 expression is associated with an inferior survival. *Blood*. 2009;113:3773-3780.

10. The Top 15 Best-Selling Drugs of 2017 [Internet]. GEN - Genetic Engineering and Biotechnology News. 2018 [cited 2019 Feb 19]. Available from: https://www.genengnews.com/a-lists/the-top-15-best-selling-drugs-of-2017/

11. Kaplon H, Reichert JM. Antibodies to watch in 2019. *mAbs*. 2019;11:219-238.

12. Matthews H, Hanison J, Nirmalan N. "Omics"-Informed Drug and Biomarker Discovery: Opportunities, Challenges and Future Perspectives. *Proteomes*. 2016;4:28.

13. National Academies of Sciences, Engineering, and Medicine, Health and Medicine Division, Board on Health Care Services, Committee on Ensuring Patient Access to Affordable Drug Therapies. Making Medicines Affordable: A National Imperative. (Nass SJ, Madhavan G, Augustine NR, eds.). Washington (DC): National Academies Press (US); 2017.

14. Van Dongen GA, Huisman MC, Boellaard R, et al. 89Zr-immuno-PET for imaging of long circulating drugs and disease targets: why, how and when to be applied? *Q J Nucl Med Mol Imaging*. 2015;59:18-38.

15. Verel I, Visser GWM, Boellaard R, et al. 89Zr Immuno-PET: Comprehensive Procedures for the Production of 89Zr-Labeled Monoclonal Antibodies. *J Nucl Med*. 2003;44:1271-1281.

16. Vosjan MJWD, Perk LR, Visser GWM, et al. Conjugation and radiolabeling of monoclonal antibodies with zirconium-89 for PET imaging using the bifunctional chelate p-isothiocyanatobenzyl-desferrioxamine. *Nature Protocols*. 2010;5:739-743.

17. Graham M, Peterson L, Hayward R. Comparison of simplified quantitative analyses of FDG uptake. *Nuclear Medicine and Biology*. 2000;27:647-655.

18. Cheson BD, Fisher RI, Barrington SF, et al. Recommendations for initial evaluation, staging, and response assessment of Hodgkin and non-Hodgkin lymphoma: the Lugano classification. *J Clin Oncol*. 2014;32:3059-3068.

19. Wahl RL, Jacene H, Kasamon Y,et al. From RECIST to PERCIST: Evolving Considerations for PET response criteria in solid tumors. *J Nucl Med*. 2009;50 Suppl 1:122S-50S.

20. O'Connor JPB, Aboagye EO, Adams JE, et al. Imaging biomarker roadmap for cancer studies. *Nat Rev Clin Oncol*. 2017;14:169-186.

# PART I

**Feasibility of $^{89}$Zr-immuno-PET**
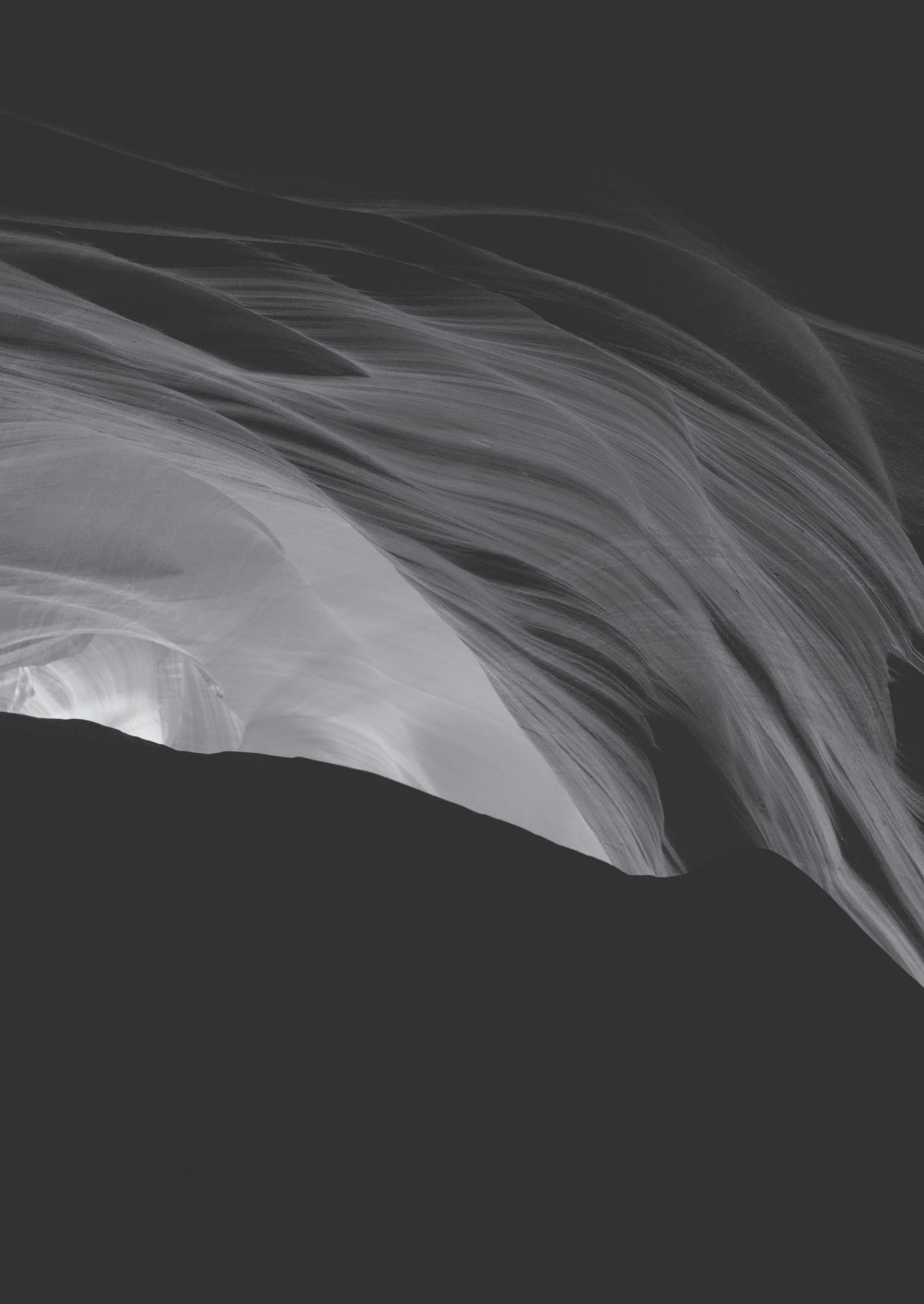
# Radiation dosimetry of $^{89}$Zr-labeled chimeric monoclonal antibody U36 as used for immuno-PET in head and neck cancer patients

Pontus K.E. Börjesson
Yvonne W.S. Jauw
Remco de Bree
Jan C. Roos
Jonas A. Castelijns
C. René Leemans
Guus A.M.S. van Dongen
Ronald Boellaard

# ABSTRACT

Immuno-PET is an appealing concept in tumor detection and planning of antibody-based therapy. For this purpose, the long-lived positron emitter zirconium-89 (t½ = 78.4 h) became recently available. The aim of the present first-in-man $^{89}$Zr-immuno-PET study was to assess safety, biodistribution, radiation dose, and quantification of $^{89}$Zr-labeled-chimeric monoclonal antibody (cmAb) U36 in patients with head and neck squamous cell carcinoma (HNSCC). In addition, performance of immuno-PET for detecting lymph node metastases was evaluated, as described previously (1).

**Methods:** Twenty HNSCC patients, scheduled to undergo surgical tumor resection, received 75 MBq $^{89}$Zr-cmAb U36 (10 mg). Immuno-PET scans were acquired at 1, 24, 72, and/or 144 h p.i. Biodistribution of the radioimmunoconjugate was evaluated by *ex vivo* radioactivity measurement in blood and in biopsies from the surgical specimen obtained 168 h after injection. Uptake levels and residence times in blood, tumors, and organs of interest were derived from quantitative immuno-PET studies and absorbed doses were calculated using OLINDA/EXM 1.0. Red marrow dose was calculated using the residence time for blood.

**Results:** $^{89}$Zr-cmAb U36 was well tolerated by all subjects. PET quantification of blood pool activity in the left ventricle of the heart showed a good agreement with sampled blood activity (mean deviation, 0.2 ± 16.9 %), except for heavy weight patients (> 100 kg). A good agreement was also found for assessment of mAb uptake in primary tumors (mean deviation, -8.4 ± 34.5 %). The mean absorbed red marrow dose was 0.07 ± 0.02 and 0.09 ± 0.01 mSv/MBq in males and females, respectively. The normal organ with the highest absorbed dose was the liver (mean dose of 1.25 ± 0.27 in males and 1.35 ± 0.21 mSv/MBq in females), thereafter followed by kidneys, thyroid, lungs, and spleen. The mean effective dose was 0.53 ± 0.03 mSv/MBq in males and 0.66 ± 0.03 mSv/MBq in females. Measured excretion via the urinary tract was < 3% during the first 72h.

**Conclusion:** $^{89}$Zr-immuno-PET can be safely used to quantitatively assess biodistribution, uptake, organ residence times, and radiation dose. This justifies its further clinical exploitation in tumor detection and planning of mAb-based therapy.

# INTRODUCTION

Monoclonal antibodies (mAbs) have been approved for use as diagnostics and therapeutics in a broad range of medical indications, but especially in oncology (*1*). Immuno-PET, the tracking and quantification of mAbs with PET *in vivo*, is an exciting novel option to improve diagnostic imaging and to guide mAb-based therapy (*2-6*).

To enable PET imaging of mAbs , an appropriate positron emitter, with a half-life ($t_{1/2}$) that is compatible with the time needed to achieve optimal tumor-to-nontumor ratios (typically 2-4 days for intact mAbs), has to be securely coupled to the targeting molecule. [124]I ($t_{1/2}$ 100.3 h) and [89]Zr ($t_{1/2}$ 78.4 h) are particularly suitable in combination with intact mAbs, because their long half-lives allow imaging at late time points for obtaining maximum information. While the non-residualizing positron emitter [124]I is particular suitable for immuno-PET when used in combination with non-internalizing intact mAbs, the residualizing positron emitter [89]Zr may be optimal in combination with internalizing intact mAbs, since [89]Zr stays in the targeted cell ("residualization") after intracellular catabolism of the radioimmunoconjugate (*7*). [89]Zr can also be used as a PET surrogate label for prediction of the biodistribution and dosimetry of ^{177}Lu-mAb and ^{90}Y-mAb conjugates as used in radioimmunotherapy trials, although deviations have to be anticipated due to subtle differences in the metal-chelate complexes used (*8,9*).

While first clinical immuno-PET studies with [124]I-labeled mAbs have been performed about 15 years ago, technology for [89]Zr-immuno-PET became available just recently (*10*). For this purpose, we developed the large scale production of pure [89]Zr and a strategy for labeling mAbs with [89]Zr via a multi-step synthesis using a succinylated-derivative of desferrioxamine B (Df) as bifunctional chelate (*10*). Labeling technology is universal and, therefore, can be used for each individual mAb or other type of protein. In the mean time, several preclinical immuno-PET studies have been performed with [89]Zr-labeled mAbs as prelude to clinical trials, for example with chimeric (mouse/human) mAb (cmAb) U36 (anti-CD44v6) (*10*), DN30 (anti-cMet) (*11*), G250 (anti-carbonic anhydrase IX)(*12*), ibritumomab tiuxetan and rituximab (anti-CD20)(*9*), bevacizumab (anti-VEGF) (*13*), cetuximab (anti-epidermal growth factor receptor)(*8,14*), and trastuzumab (anti-human epidermal growth factor receptor-2)(*15*).

In a first-in-man [89]Zr-immuno-PET clinical trial, we recently determined the diagnostic value of immuno-PET with anti-CD44v6 [89]Zr-cmAb U36 in patients

with head and neck squamous cell carcinoma (HNSCC), who were at high risk of having neck lymph node metastases. Twenty HNSCC patients underwent [89]Zr-cmAb U36 immuno-PET prior to surgery. Immuno-PET detected all primary tumors (n = 17) as well as lymph node metastases in 18 of 25 positive neck levels. It was concluded that for the detection of HNSCC lymph node metastases (and probably distant metastases), immuno-PET with [89]Zr-cmAb U36 performs at least as good as CT or MRI.

No radiation dose estimates have been previously described for [89]Zr-cmAb U36 or other [89]Zr-labeled mAbs. Therefore, the aim of the present study was to assess safety, biodistribution, radiation dose, and the potential for quantification of immuno-PET with [89]Zr-cmAb U36 in HNSCC patients using data of aforementioned clinical trial.

## MATERIALS AND METHODS

### Patient Study

Twenty patients (8 females and 12 males) with histologically proven HNSCC (Table 1), at high risk of having neck lymph node metastasis and, therefore, planned to undergo neck dissection with or without resection of the primary tumor, participated in this study. Other eligibility criteria have been decribed previously (2). Patients received cmAb U36 IgG radiolabeled with [89]Zr (74.9 ± 0.6 MBq). The total administered cmAb U36 dosage was 10 mg for all patients. In previous studies, it had been demonstrated that biodistribution is not mAb dose dependent within the range 2 - 52 mg (16,17). Surgery was performed 6-8 days after administration of radiolabeled cmAb U36.

### Safety

Prior and up to 6 wk after administration of radiolabeled cmAb U36, routine laboratory analyses were performed, including hemoglobin, hematocrit, mean corpuscular volume, red blood cell count, white blood cell count (including automated differential), platelet count, sodium, potassium, calcium, chloride, creatinine, urea, uric acid, alanine aminotransferase, aspartate aminotransferase, alkaline phosphatase, gamma glutamyl transferase, albumin, glucose, bilirubin, thyroid stimulating hormone, and urine sediment. Vital signs including pulse rate, blood pressure, temperature, and respiratory rate were recorded before and up to

3 h post-injection (p.i.). On the basis of previous studies with anti-CD44v6 mAbs, cmAb U36 included, no adverse effects had to be expected (*17*). Dose rates (μSv/h) were measured at 1, 24, and 72 h p.i. at a distance of 100 cm with a γ-radiation dose rate counter (Berthold LB 1230 EG&G, Wildbad, Germany). In addition, human anti-cmAb U36 and anti-Df-cmAb U36 antibody responses were assessed (*2*).

**Table 1.** Patient and tumor characteristics

| Patient | Sex | Age | Weight (kg) | Primary tumor | cTNM | pTNM |
|---|---|---|---|---|---|---|
| 1 | F | 57 | 68 | Oral cavity, tongue, right | T2N0M0 | T2N1M0 |
| 2 | M | 57 | 82 | Oropharynx, base of tongue, right | TXN2aM0 | T1N2bM0 |
| 3 | F | 72 | 71 | Oropharynx, tonsil, right | T2N2bM0 | T2N2bM0 |
| 4 | F | 53 | 81 | Oropharynx, tonsil, right | T3N0M0 | T3N2bM0 |
| 5 | M | 63 | 78 | Oropharynx, tonsil, right | T4N0M0 | T4N2bM0 |
| 6 | F | 58 | 62 | Oral cavity, floor of mouth, left | T4N0M0 | T4N2bM0 |
| 7 | M | 54 | 67 | Oral cavity, tongue, right | T3N0M0 | T3N2bM0 |
| 8 | M | 55 | 72 | Oropharynx, tonsil, left | T4N2aM0 | T4N2bM0 |
| 9 | F | 54 | 82 | Hypopharynx, piriform sinus, left | T4N2bM0 | T4N2bM0 |
| 10 | F | 65 | 67 | Oral cavity, base of tongue, right | T2N0M0 | T2N0M0 |
| 11 | M | 53 | 90 | Larynx, glottic | T4N0M0 | T4N0M0 |
| 12 | M | 59 | 75 | Larynx, supraglottic | T4N0M0 | T4N0M0 |
| 13 | F | 49 | 49 | Residual disease of T2N0 tonsil carcinoma, left | NA | NA |
| 14 | M | 58 | 100 | Oropharynx, base of tongue, right | T2N2bM0 | T2N2bM0 |
| 15 | M | 48 | 115 | Oropharynx, tonsil, right | T3N0M0 | T3N1M0 |
| 16 | F | 63 | 67 | Oropharynx, tonsil, left | T3N2bM0 | T3N2cM0 |
| 17 | M | 53 | 104 | Oropharynx, tonsil, right | T2N3M0 | T2N3M0 |
| 19 | M | 71 | 87 | Oropharynx, soft palate, right | T3N2cM0 | T2N2cM0 |
| 20 | M | 60 | 58 | Larynx, supraglottic, recurrence | NA | NA |

Abbreviations: NA, not applicable

## Monoclonal antibody U36

Selection and production of mouse mAb (mmAb) U36 and its chimeric IgG1 derivative cmAb U36 have been described previously (*17*). mAb U36 binds to the v6 region of CD44 (CD44v6). Expression of CD44v6 was found to be abundant and homogenous in 96% of all primary HNSCC and HNSCC lymph node metastases (*18*). In normal tissues, expression has been found in epithelial tissues such as skin, breast and prostate myoepithelium, and bronchial epithelium (*19*). CD44v6 has been suggested to be involved in tumor formation, tumor cell invasion, metastasis formation, and cancer cell stemness (*20,21*).

## Synthesis of [89]Zr-cmAb U36

The synthesis and purification of [89]Zr, its coupling to cmAb U36 via the chelate Df (Desferal®, Novartis Pharma AG, Basel, Switzerland), as well as the procedures and results of quality tests, have been described previously (2). [89]Zr emits positrons with a main energy of 897 keV and an abundance of 22.7%. In addition, non-prompt 909 keV photons are emitted at an abundance of 99.9%.

## Pharmacokinetics

Serial blood samples were taken from a peripheral vein of the arm opposite the infusion site for determination of activity at the following time points: 5, 10, and 30 min, and 1, 2, 4, 16, 21, 72, and 168 h after completion of infusion. Urine was collected in intervals 0-24, 24-48, and 48-72 h p.i. to determine renal excretion of [89]Zr. Aliquots of blood, plasma, and urine samples were measured for [89]Zr activity in an isotope well-counter (1470 Wizard, Wallac, Turku, Finland), compared to an aliquot retained from the conjugate preparation, and corrected for decay. Blood activity was expressed as the percentage of the injected dose per kg (%ID/kg).

## PET acquisition

PET scans were obtained at 1 h (all patients, except no 4 and 16), 24 h (patients 1-6), 72 h (all patients) and/or 144 h (all patients, except no 1, 2, and 13) after intravenous injection of [89]Zr-cmAb U36, using a dedicated full ring PET scanner (ECAT EXACT HR+, CTI/Siemens, Knoxville, TN, USA) as described before (2). Prior to this study, the PET scanner was calibrated using a standard cylindrical calibration phantom filled with a 5 kBq/cm$^3$ [89]Zr solution. This calibration was performed to verify the quantitative accuracy of the scanner in the presence of 909 keV gamma photons emitted by [89]Zr and the impact of emission spillover into the transmission scans. This procedure indicated that activity concentrations measured with the HR+ were accurate within 5%. During image reconstruction all scans were normalized and corrected for randoms, scatter, attenuation, and decay. Reconstructions were performed using an attenuation and normalization weighted ordered subset expectation maximization (OSEM) algorithm (ECAT software version 7.2, CTI/Siemens) with 2 iterations and 16 subsets followed by post-smoothing of the reconstructed image using a 5-mm FWHM Gaussian filter. Due to the low amount of radioactivity administered to the patients (for radiation exposure reasons), images with attenuation correction showed high noise levels. Therefore, OSEM reconstructions without attenuation (and thus scatter) correction were performed as well and used for visual interpretation only.

## Validation of quantitative [89]Zr-immuno-PET imaging

OSEM reconstructions with attenuation correction of the immuno-PET scans were used to investigate the accuracy of quantification [89]Zr-cmAb U36 PET *in vivo*. To this end, three 1.5 cm diameter 'regions of interest' (ROIs) were defined within the left ventricle of the heart in three subsequent image planes using an axial view of the PET images. The average activity concentration within these ROIs, representing PET assessed bloodpool activity concentration, were directly compared with the activity concentration measured in manual blood samples ("sampled blood activity") using a calibrated well counter in order to validate the quantitative accuracy of [89]Zr-PET *in vivo*.

In addition, the uptake of the radioimmunoconjugate in tumors (%ID/cm$^3$) as assessed from scans acquired at 144 h p.i., was compared with the uptake (%ID/g) derived from tumor biopsies collected at 168 h p.i. %ID/cm$^3$ as derived from the PET scans was converted to %ID/g using a soft tissue density factor of 1.04 g/cm$^3$.

## VOI definition

The uptake in different organs was determined by manually defined ROIs using the Clinical Application Programming Package (CAPP, provided with the ECAT software). [89]Zr uptake was determined in the following organs: lung, liver, spleen, kidney, heart, and if visible, thyroid. In addition, a semi-automatic 'volume of interest' (VOI) was defined over the tumor using in-home developed software tools (*22*).

*Details of ROI/VOI definition*: As most organs could be visually best identified on the 1 h p.i. emission scans, most organ 3D VOIs were defined manually using this early uptake scan. However, VOIs for the thyroid and tumor were defined on the last scan, because their delineation was optimal at this last time point. Finally, lung regions were defined on reconstructed transmission scans, using the semi-automatic isocontour tool within the CAPP software. All 3D VOIs were defined using a coronal view of the PET images.

A 3D VOI was generated from multiple 2D ROIs by grouping these ROIs into the VOI. The ROIs on the first and last slices were not used for the VOIs, since these were prone to partial volume effects (spill-in and spill-out) and/or sampling errors. The VOIs defined on the 1 h p.i. scan were saved and imported to the other time frames, where the organs were not as clearly visible. To allow for projection of VOIs onto scans obtained at other time intervals, patients were scanned in the

same (patient and bed) position during subsequent studies, by using rigid head immobilization devices (e.g. radiotherapy mask) and belts around the patient. To ensure correct positioning of the VOIs, the elevation of the bed was registered for all scans and in case of differences in patient or bed position, scans were aligned using in home-developed software program. Furthermore, in case of remaining dislocation of VOIs, all VOIs were relocated in one step to keep the internal relations intact. For relocation, the alignment of lungs VOIs and the contour of the head and neck were verified using reconstructed transmission scans (for each subsequent study) as well. However, if still necessary, VOIs were ungrouped and individual VOIs were relocated to improve the position. After this VOI positioning procedure all VOIs were saved and projected onto the emission scans. The mean uptake in Bq/cm³ was then derived using these final VOIs.

The tumor was defined on 144 h p.i. scan using a tool, which semi-automatically defined a 3D 50% (to max) isocontour around the tumor, and next the mean uptake in Bq/cm³ was calculated. The mean tumor uptake was determined for the latest acquired PET study only, as correct repositioning of the tumor VOI onto earlier scans could not be reliably visually verified due to lack of signal from the tumor.

All VOIs set on organs and tumors, were evaluated by 2 experienced nuclear physicians.

**Internal radiation dosimetry**

The internal radiation dosimetry for the adult human was evaluated through the normalized cumulated activities for each patient provided as input to the OLINDA/EXM 1.0 code (*23*).

Residence times were calculated for liver, kidneys, lungs, spleen, and the remainder of the body, entering the percentage of the injected dose at each time point for each patient in OLINDA/EXM 1.0 and fitting these data using a mono-exponential function. The residence times for the thyroid were calculated using trapezoidal integration. The remaining area under the curve from the end of data collection until infinity was determined by considering physical decay only. The residence time of the remainder of the body was defined as: 113 - sum of residence times of source organs. A total residence time for the entire body of 113 h is obtained in case of no biological clearance. Red marrow dose was estimated using sampled blood clearance data (*24,25*). The red marrow concentration was assumed to be 30% of the blood activity concentration (conversion factor = 0.3). In addition, the dose from the remainder of the body onto red marrow was considered as well.

# RESULTS

Unless otherwise specified, all [89]Zr activities are decay corrected to time of injection. For 1 patient (patient 18) imaged, not enough data were available for adequate dosimetric analysis. Regarding the evaluation of [89]Zr-immuno-PET imaging to quantify tumor uptake, 4 patients (patients 1, 2, 13, and 18) were excluded from analysis because the lack of a scan at 144 h p.i. Another patient (patient 6) was excluded because of delayed surgery 2 wk p.i.

### Safety

[89]Zr-cmAbU36 was found to be safe and well tolerated in all subjects. Neither adverse reactions nor significant changes in earlier mentioned blood and urine parameters were observed, that could be related to the study drug. The mean radiation dose rates measured 1, 24, and 72 h p.i. at a distance of 100 cm were 7.0 ± 0.3, 5.7 ± 0.3 and 3.8 ± 0.2 μSv/h, respectively. Patient 9 and 10 developed a human anti-chimeric antibody (HACA) response, and elevated titers were found at 1 and 6 wk p.i., irrespective whether cmAb U36 IgG or [89]Zr-*N*-sucDf-cmAb U36 was used in the ELISA. These data indicate that the response was directed to the protein part of the conjugate and not to the *N*-sucDf chelate attached to the cmAb.

### Biodistribution

Images of a representative male patient between 1 and 144 h after injection of [89]Zr-cmAbU36 are presented in Figure 1. Whole body images obtained directly after administration of [89]Zr-cmAb U36 showed mainly blood-pool activity with delineation of the heart, lungs, liver, kidneys, spleen and nose. Uptake of radioactivity for most organs decreased over time, while increased uptake was only seen at tumor sites and in the thyroid of some of the patients (patients 1, 6, 7, 10, and 11).

The estimated uptake of [89]Zr-cmAbU36 in single organs, is presented in Table 2. The visual quality of the immuno-PET images varied between different patients. Figure 2 illustrates the difference in visual quality between an average weight patient (58 kg) and an obese patient (104 kg).
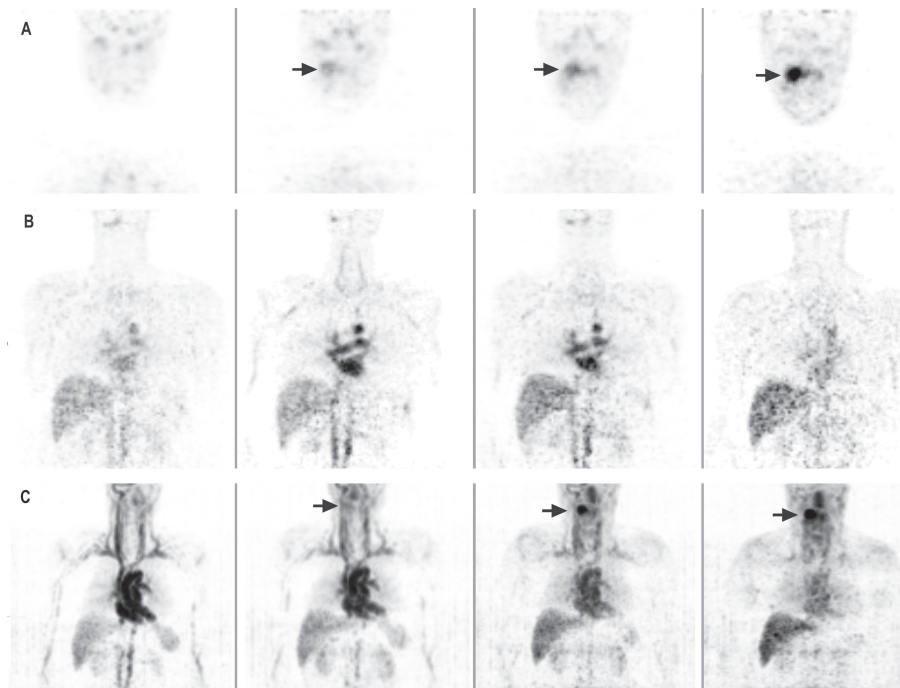
**Figure 1.** Representative coronal images of male patient with an oropharyngeal tumor, left to right arranged from 1, 24, 72, and 144 h p.i. A: shows the increased uptake in time of $^{89}$Zr-cmAb U36 in tumor. B: shows circulating $^{89}$Zr-cmAb U36 in the heart and uptake in organs. C: maximum intensity projections of the same patient as shown in A and B. Note that grayscale settings were set for each image independently for clarity reasons.

**Table 2.** Uptake of $^{89}$Zr-cmAbU36 in single organs

| Organ | t = 0 h | t = 24 h | t = 72 h | t = 144 h |
|---|---|---|---|---|
| **Males (mean %ID ± SD)** | | | | |
| Kidneys | 1.21 ± 0.23 | 1.36 ± 0.14 | 0.70 ± 0.16 | 0.26 ± 0.09 |
| Liver | 12.23 ± 2.12 | 11.98 ± 0.78 | 6.18 ± 1.44 | 2.83 ± 0.79 |
| Lungs | 4.51 ± 3.58 | 5.86 ± 1.30 | 1.84 ± 1.20 | 0.69 ± 0.47 |
| Spleen | 0.99 ± 0.27 | 0.75 ± 0.12 | 0.29 ± 0.10 | 0.10 ± 0.04 |
| Thyroid | 0.08 ± 0.02 | 0.11 | 0.07 ± 0.04 | 0.05 ± 0.02 |
| **Females (mean %ID ± SD)** | | | | |
| Kidneys | 1.78 ± 0.34 | 1.69 ± 0.44 | 0.95 ± 0.27 | 0.37 ± 0.07 |
| Liver | 11.50 ± 2.45 | 7.98 ± 1.02 | 4.94 ± 0.95 | 2.36 ± 0.52 |
| Lungs | 5.91 ± 1.94 | 3.86 ± 1.52 | 2.52 ± 0.75 | 1.16 ± 0.29 |
| Spleen | 1.02 ± 0.36 | 0.72 ± 0.09 | 0.27 ± 0.12 | 0.10 ± 0.05 |
| Thyroid | 0.06 ± 0.03 | 0.06 ± 0.04 | 0.10 ± 0.03 | 0.05 ± 0.03 |
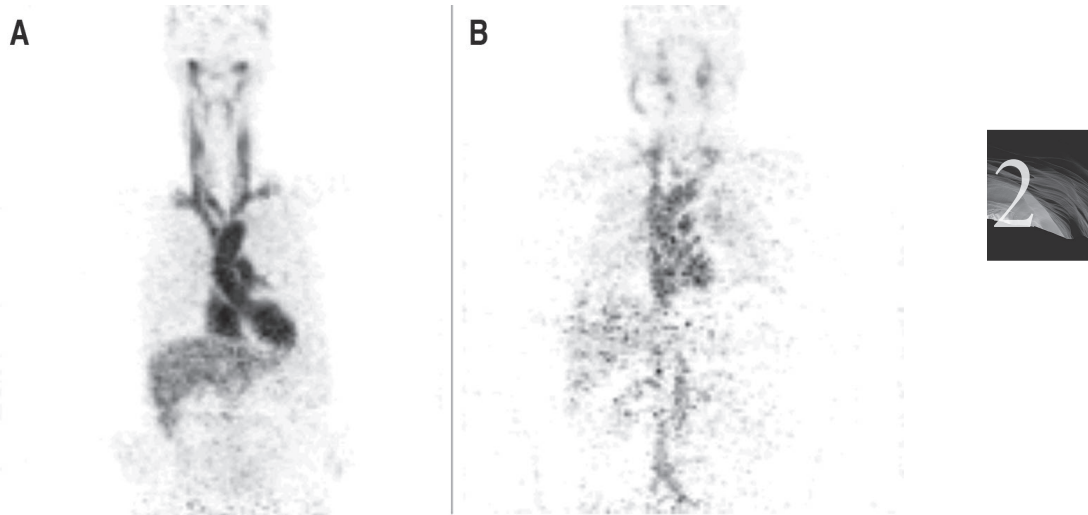
**Figure 2.** Illustration of the difference in visual quality of coronal PET images obtained 1 h after injection of [89]Zr-cmAb U36 between A: an average weight patient (58 kg) and B: an obese patient (104 kg).

## PET derived bloodpool activity vs sampled blood

Variation in visual image quality also affects the quantitative analysis of the [89]Zr-cmAbU36 immuno-PET images in a proportion of patients, as shown in Figure 3. This plot depicts the percentage under- and overestimation of the blood activity as assessed by immuno-PET. To this end, immuno-PET derived activity in the left ventricle of the heart was compared to activity in sampled blood. Patients with a weight lower than 100 kg showed in general a good agreement with manually sampled data (mean deviation 0.2 ± 16.9%). Patients above 100 kg showed an underestimation of activity by immuno-PET, especially for later time images.

Figure 4 shows blood kinetics, either assessed by immuno-PET or by blood sampling, for the whole group of evaluable patients (n=19). For the group of patients as a whole, no statistically significant ($P = 0.503$) differences were observed between the two methods used for assessment of activity. In addition, the small variances suggest a consistency of the pharmacokinetics in these patients, also for patients who developed a HACA response. Therefore, we decided to use data of all these patients for radiation dose estimations.
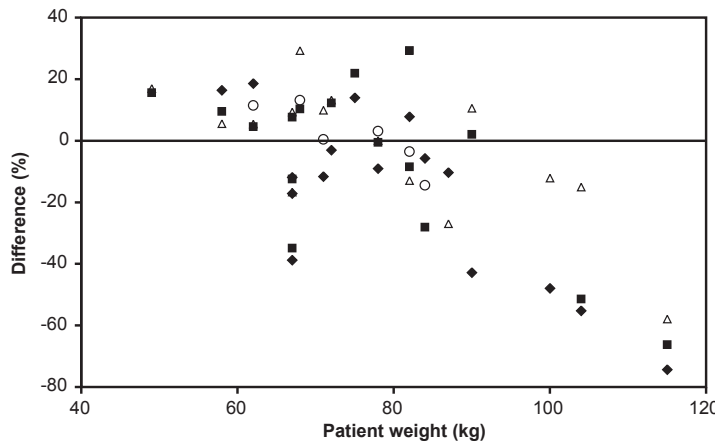
Figure 3. Difference between PET assessed blood pool activity and sampled blood activity of $^{89}$Zr-cmAb U36 as function of patient weight. Difference in activity was assessed at 1 h (Δ), 24 h (○), 72 h (■), and 144 h (♦) after injection.
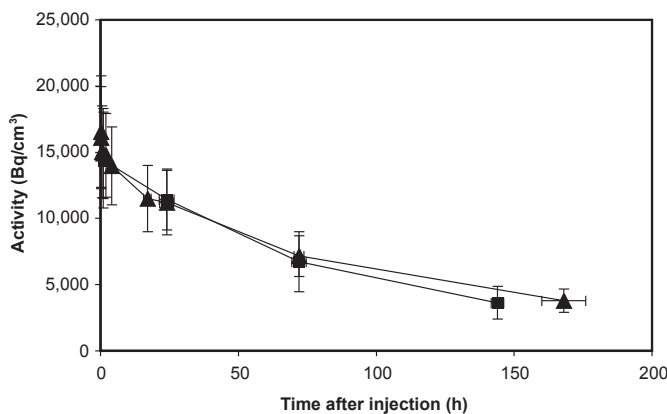


**Figure 4.** Mean $^{89}$Zr-cmAb U36 activity in blood (Bq/cm$^3$) of the study population: PET assessed bloodpool activity within the left ventricle of the heart (■), and sampled bloodpool activity (▲).

## Quantification of mAb uptake in tumors

Antibody uptake was assessed on 144 h p.i. scans for all primary tumors, and compared with uptake data from biopsies obtained 168 h p.i. Comparison of %ID/g derived from biopsy data and PET data, respectively, showed a good agreement with slightly lower values for PET (mean deviation -8.4 ± 34.5%). The mean tumor uptake at 168 h p.i. as assessed by biopsies appeared to be 0.019 ± 0.010 %ID/g (range 0.006 - 0.038 %ID/g).

## Red marrow doses

The doses absorbed in the red marrow were estimated in 19 patients, as presented in Table 3. The mean red marrow dose was 0.07 ± 0.02 mSv/MBq in males and 0.09 ± 0.01 mSv/MBq in women.

**Table 3.** Absorbed doses in red marrow

| Patient no. | Red marrow dose* (mSv/MBq) |
| --- | --- |
| Males | |
| 2 | 0.07 |
| 5 | 0.07 |
| 7 | 0.06 |
| 8 | 0.06 |
| 11 | 0.08 |
| 12 | 0.07 |
| 14 | 0.09 |
| 15 | 0.11 |
| 17 | 0.09 |
| 19 | 0.07 |
| 20 | 0.05 |
| Mean ± SD | 0.07 ± 0.02 |
| Females | |
| 1 | 0.09 |
| 3 | 0.10 |
| 4 | 0.11 |
| 6 | 0.09 |
| 9 | 0.11 |
| 10 | 0.09 |
| 13 | 0.07 |
| 16 | 0.09 |
| Mean ± SD | 0.09 ± 0.01 |

* Conversion factor = 0.3

## Absorbed doses in source organs and whole body

Residence times of the source organs were entered into the OLINDA/EXM 1.0 program. The results of the OLINDA/EXM 1.0 analysis are listed in Table 4. The effective dose for each patient was calculated using the available organ dosimetry data of the source organs. Excretion of [89]Zr via the urinary pathway was 2.59 ± 1.89 %ID during the first 72 h after injection. As there is also very little activity seen in the intestines, most loss of radioactivity is due to physical decay. The mean effective dose for the whole body was 0.53 ± 0.03 mSv/MBq in males and 0.66 ± 0.03 mSv/MBq in females. As an alternative, the effective dose was also calculated by considering the body to be a homogenous mass, i.e. ignoring organ doses and

assuming a residence time of 113 h for the entire patient. This simplified procedure showed only a minor decrease of the estimated effective dose: 0.44 ±0.002 mSv/MBq in males and 0.54 ± 0.002 mSv/MBq in females. Difference in estimated effective dose between males and females, with versus without ignoring the biodistribution, suggests that this difference might be explained by use of different models (male versus female) within OLINDA/EXM 1.0.

The normal organs with the highest absorbed dose were the liver (mean dose in males 1.25 ± 0.27 mSv/MBq; in females 1.35 ± 0.21 mSv/MBq) and kidneys (mean dose in males 0.82 ± 0.15 mSv/MBq; in females 1.18 ± 0.26 mSv/MBq).

**Table 4.** Absorbed organ doses

| Patient no. | Kidneys | Liver | Lungs | Spleen | Thyroid | Total body | Organ dosimetry |
|---|---|---|---|---|---|---|---|
| | | | Organ dose (mSv/MBq) | | | | Effective dose (mSv/MBq) |
| **Males** | | | | | | | |
| 2 | 1.01 | 1.60 | 0.93 | 0.74 | 1.28 | 0.45 | 0.60 |
| 5 | 0.85 | 1.47 | 0.83 | 0.66 | NV | 0.45 | 0.54 |
| 7 | 0.86 | 1.20 | 0.68 | 0.74 | 0.70 | 0.44 | 0.53 |
| 8 | 0.84 | 1.17 | 1.01 | 0.71 | NV | 0.44 | 0.55 |
| 11 | 0.96 | 1.48 | 0.54 | 0.81 | 1.40 | 0.45 | 0.56 |
| 12 | 1.01 | 1.55 | 0.53 | 0.82 | NV | 0.45 | 0.52 |
| 14 | 0.73 | 1.01 | 0.44 | 0.58 | 0.86 | 0.44 | 0.52 |
| 15 | 0.69 | 1.23 | 0.50 | 0.57 | 0.70 | 0.44 | 0.52 |
| 17 | 0.58 | 0.69 | 0.42 | 0.47 | 0.72 | 0.44 | 0.49 |
| 19 | 0.80 | 1.14 | 0.54 | 0.59 | 0.85 | 0.44 | 0.52 |
| 20 | 0.64 | 1.23 | 0.49 | 0.70 | 0.81 | 0.44 | 0.52 |
| Mean ± SD | 0.82 ± 0.15 | 1.25 ± 0.27 | 0.63 ± 0.20 | 0.67 ± 0.11 | 0.91 ± 0.27 | 0.44 ± 0.0022 | 0.53 ± 0.03 |
| **Females** | | | | | | | |
| 1 | 1.26 | 1.31 | 0.63 | 0.89 | 1.12 | 0.54 | 0.64 |
| 3 | 1.12 | 1.19 | 0.84 | 0.86 | NV | 0.54 | 0.65 |
| 4 | 0.87 | 1.15 | 0.96 | 0.62 | NV | 0.54 | 0.63 |
| 6 | 1.32 | 1.56 | 1.01 | 0.87 | 0.93 | 0.55 | 0.67 |
| 9 | 0.99 | 1.65 | 1.11 | 0.86 | NV | 0.55 | 0.66 |
| 10 | 1.04 | 1.09 | 1.05 | 0.84 | 1.44 | 0.54 | 0.69 |
| 13 | 1.71 | 1.52 | 1.12 | 0.64 | 1.11 | 0.55 | 0.71 |
| 16 | 1.15 | 1.33 | 0.83 | 0.55 | 0.98 | 0.54 | 0.65 |
| Mean ± SD | 1.18 ± 0.26 | 1.35 ± 0.21 | 0.94 ± 0.17 | 0.77 ± 0.14 | 1.12 ± 0.20 | 0.54 ± 0.0024 | 0.66 ± 0.03 |

Abbreviations: NV, not visible

# DISCUSSION

The purpose of this study was to assess the safety, and to evaluate the biodistribution, the radiation dose, and the potential for quantification of immuno-PET with [89]Zr-labeled-chimeric mAb (cmAb) U36 in HNSCC patients. In this study, the tracer was found to be safe and well tolerated. No adverse events occurred. A HACA response was only seen in two patients, while none of the antibody responses was directed to the chelate. In all normal organs, the uptake of radioactivity decreased in time. Only in the tumor and in a few patients in the thyroid, uptake increased in time, suggesting specific uptake of [89]Zr-cmAb U36. Such variable and sometimes high thyroid uptake was previously observed in head and neck cancer patients who had been injected with ^{99m}Tc-cmAb U36 (*16*). This might indicate that in some individuals CD44v6 is expressed in the thyroid.

Furthermore, the advantage of the more detailed images obtained with [89]Zr-immuno-PET is the possibility of non-invasive quantification. In the majority of the images the visual quality was acceptable for defining ROI's, but there was a variation between images of different patients and in some images the delineation of organs and tumor was suboptimal. Nevertheless, quantification results seem plausible. The [89]Zr calibration procedure indicated that the quantitative accuracy of the scanner was not compromised by the presence of 909 keV gamma photons emitted from [89]Zr and due to emission spillover into the transmission scans. In fact, the procedure was repeated for activity concentrations of about 17 kBq/cc (111 MBq in a phantom of 6283 ml) showing that quantitative accuracy was not affected at higher count rates as well. Although the 909 keV photons could have resulted in increased dead time and randoms fraction, the [89]Zr activity in the field of view is much lower than usually applied for e.g. FDG studies (up to 370 MBq FDG for patients and about 70 MBq FDG in a 6 L phantom for calibrations). Moreover, the 511 keV photon flux from [89]Zr is much lower than that seen in FDG studies due to lower positron emission abundance compared with [18]F. Another effect that could hamper quantification might be emission spillover into the transmission scan. However, emission spillover into the transmission scan is minimized in two ways. First, transmission scans are based on coincidence counting of the 511 keV photons emitted by the [68]Ge transmission rod sources, thereby reducing the detection of non-coincident emitted photons (although these still result in increased randoms fraction). Second, during transmission scanning a "rod windowing" technique is applied (*26*). Rod windowing discards all detected

coincidences that do not intersect the rod source (within a certain distance) and, as such, it reduces the influence of scatter, randoms, and emission spillover. To further validate quantitative accuracy, a comparison was made between blood pool activity seen in the PET scanner versus those in manual samples.

Quantification of blood pool activity in the left ventricle of the heart showed good agreement with the sampled blood activity, except for a few heavy weight patients (> 100 kg). This suggests that immuno-PET with [89]Zr-cmAb U36 can be used to quantify the radiation dose of the whole body and normal organs of interest. However, as earlier shown with FDG-PET, excessive body weight has negative effects on both quantitative and qualitative scan analysis (*27-30*). For [89]Zr studies these effects may be even more pronounced due to the low positron emission abundance resulting in lower noise equivalent count rates (NECR) than seen with FDG studies. The low NECR could potentially hamper the accuracy and precision of the scatter correction, but further studies are required to fully understand the negative bias seen with heavier patients. Yet the association between patient weight and bias suggests that this effect is indeed related to scatter correction issues. Despite this fact, a good agreement between PET and sample derived blood pool activities was seen for most other scans and subjects (Figure 3). Note that in future studies, with the use of modern PET/CT-scanners in combination with time-of-flight reconstruction and optimized scan protocols, it is probable that these problems will be of less magnitude, but this would require further validation as well.

Also in the assessment of tumor uptake, a good agreement was found between PET derived data and data obtained from biopsies, despite there was one day difference in assessment time (144 h p.i. versus 168 h p.i.). This good agreement is quite remarkable since both methods are prone to errors. For example, for uptake assessment in tumor biopsies it is difficult to take a representative part of the tumor. For PET assessment, partial volume effects will cause an underestimation of the tumor dose. This problem with partial volume effects is a known limitation of PET and correction methods are currently being developed to deal with this. At this point we can at least identify patients with low and high tumor uptake, respectively, and, therefore, it is possible to select the patients who may and may not benefit from therapy.

Although [89]Zr-immuno-PET can become an important tool in the detection and treatment of cancer, there are some limitations to overcome. Drawing of the organ VOI´s requires anatomical knowledge, training, and is time consuming.

However, with modern PET/CT scanners, [89]Zr-immuno-PET data can be collected along with a structural CT image in one scanning session. The aligned CT data can then be used for a more accurate and automated VOI definition.

The mean radiation dose for patients in this study was about 40 mSv, which is high and will limit repeated application of [89]Zr-immuno-PET. However, the introduction of the new generation PET/CT scanners will also make that better quality immuno-PET images can be obtained with the use of less [89]Zr radioactivity dose. This can be concluded from preliminary PET/CT studies in which 37 MBq [89]Zr-trastuzumab was used for HER2 immuno-PET imaging in breast cancer patients (*15*). Using [89]Zr-cmAb U36 in combination with these scanners would mean an effective dose of about 20 mSv for a whole body scan. Theoretically, shorter lived residualizing positron emitters like [64]Cu (t½ = 12.7 h) and [86]Y (t½ = 14.7 h) might give less dose exposure, although, clinical experience with these positron emitters is very limited. In a study of Cutler et al., immuno-PET with 370 MBq ^{64}Cu-labeled intact mAb 1A3 was evaluated for detection of colorectal cancer with a Siemens/CTI ECAT EXACT PET scanner as was also used in the present study (*31,32*). The average whole body dose for these patients was 11.1 mSv. However, due to the short half-life of ^{64}Cu, most of the patients had to be imaged within 24 h p.i. to obtain good quality images. As shown in Figure 1A, for cmAb U36 delineation of tumors is much better at later time points (72 and 144 h), and therefore, the use of ^{64}Cu might be a less suitable alternative. For immuno-PET evaluation of antibody fragments, however, ^{64}Cu as well as [86]Y might be suitable candidates.

## CONCLUSION

In the present study we evaluated the use of immuno-PET with [89]Zr-labeled-cmAb U36 in HNSCC patients regarding safety, biodistribution, radiation dose, and the potential for quantification. [89]Zr-cmAb U36 was found to be safe and well tolerated in all subjects. Uptake of radioactivity in heart, lungs, liver, kidneys, and spleen was decreasing over time, while increased uptake was only seen at tumor sites and in the thyroid of some of the patients. Quantitative analysis, comparing PET derived bloodpool activity and sampled blood activity, showed good agreement except for the patients with a body weight above 100 kg. Also a good agreement was found for assessment of antibody uptake in tumors. The mean effective dose

for the whole body was 0.53 ± 0.03 mSv/MBq in males and 0.66 ± 0.03 mSv/MBq in females.

## ACKNOWLEDGMENTS

# REFERENCES

1. Oldham RK, Dillman RO. Monoclonal antibodies in cancer therapy: 25 years of progress. *J Clin Oncol*. 2008;26:1774-1777.

2. Börjesson PKE, Jauw YWS, Boellaard R, et al. Performance of immuno-positron emission tomography with zirconium-89-labeled chimeric monoclonal antibody U36 in the detection of lymph node metastases in head and neck cancer patients. *Clin Cancer Res*. 2006;12:2133-2140.

3. Verel I, Visser GWM, Dongen GA van. The Promise of Immuno-PET in Radioimmunotherapy. *J Nucl Med*. 2005;46:164S-171S.

4. Dongen GAMS van, Visser GWM, Hooge MNL, Vries EG de, Perk LR. Immuno-PET: A Navigator in Monoclonal Antibody Development and Applications. *The Oncologist*. 2007;12:1379-1389.

5. Wu AM. Antibodies and Antimatter: The Resurgence of Immuno-PET. *J Nucl Med*. 2009;50:2-5.

6. Nayak TK, Brechbiel MW. Radioimmunoimaging with longer-lived positron-emitting radionuclides: potentials and challenges. *Bioconjug Chem*. 2009;20:825-841.

7. Verel I, Visser GWM, Boerman OC, et al. Long-lived positron emitters zirconium-89 and iodine-124 for scouting of therapeutic radioimmunoconjugates with PET. *Cancer Biother Radiopharm*. 2003;18:655-661.

8. Perk LR, Visser GWM, Vosjan MJWD, et al. 89Zr as a PET Surrogate Radioisotope for Scouting Biodistribution of the Therapeutic Radiometals 90Y and 177Lu in Tumor-Bearing Nude Mice After Coupling to the Internalizing Antibody Cetuximab. *J Nucl Med*. 2005;46:1898-1906.

9. Perk LR, Visser OJ, Stigter-van Walsum M, et al. Preparation and evaluation of (89)Zr-Zevalin for monitoring of (90)Y-Zevalin biodistribution with positron emission tomography. *Eur J Nucl Med Mol Imaging*. 2006;33:1337-1345.

10. Verel I, Visser GWM, Boellaard R, Walsum MS, Snow GB, Dongen GAMS van. 89Zr Immuno-PET: Comprehensive Procedures for the Production of 89Zr-Labeled Monoclonal Antibodies. *J Nucl Med*. 2003;44:1271-1281.

11. Perk LR, Stigter-van Walsum M, Visser GWM, et al. Quantitative PET imaging of Met-expressing human cancer xenografts with 89Zr-labelled monoclonal antibody DN30. *Eur J Nucl Med Mol Imaging*. 2008;35:1857-1867.

12. Brouwers A, Verel I, Van Eerd J, et al. PET radioimmunoscintigraphy of renal cell cancer using 89Zr-labeled cG250 monoclonal antibody in nude rats. *Cancer Biother Radiopharm*. 2004;19:155-163.

13. Nagengast WB, de Vries EG, Hospers GA, et al. In vivo VEGF imaging with radiolabeled bevacizumab in a human ovarian tumor xenograft. *J Nucl Med*. 2007;48:1313-1319.

14. Aerts HJWL, Dubois L, Perk L, et al. Disparity between in vivo EGFR expression and 89Zr-labeled cetuximab uptake assessed with PET. *J Nucl Med*. 2009;50:123-131.

15. Dijkers ECF, Kosterink JGW, Rademaker AP, et al. Development and characterization of clinical-grade 89Zr-trastuzumab for HER2/neu immunoPET imaging. *J Nucl Med*. 2009;50:974-981.

16. Bree R de, Roos JC, Quak JJ, Hollander W den, Snow GB, Dongen GA van. Radioimmunoscintigraphy and biodistribution of technetium-99m-labeled monoclonal antibody U36 in patients with head and neck cancer. *Clin Cancer Res*. 1995;1:591-598.

17. Colnot DR, Quak JJ, Roos JC, et al. Phase I Therapy Study of 186Re-Labeled Chimeric Monoclonal Antibody U36 in Patients with Squamous Cell Carcinoma of the Head and Neck. *J Nucl Med*. 2000;41:1999-2010.

18. De Bree R, Roos JC, Quak JJ, Den Hollander W, Snow GB, Van Dongen GA. Clinical screening of monoclonal antibodies 323/A3, cSF-25 and K928 for suitability of targetting tumours in the upper aerodigestive and respiratory tract. *Nucl Med Commun*. 1994;15:613-627.

19. Heider KH, Mulder JW, Ostermann E, et al. Splice variants of the cell surface glycoprotein CD44 associated with metastatic tumour cells are expressed in normal tissues of humans and cynomolgus monkeys. *Eur J Cancer*. 1995;31A:2385-2391.

20. Prince ME, Sivanandan R, Kaczorowski A, et al. Identification of a subpopulation of cells with cancer stem cell properties in head and neck squamous cell carcinoma. *Proc Natl Acad Sci USA*. 2007;104:973-978.

21. Mack B, Gires O. CD44s and CD44v6 expression in head and neck epithelia. *PLoS ONE*. 2008;3:e3360.

22. Boellaard R, Hoekstra O, Lammertsma A. Software tools for standardized analysis of FDG whole body studies in multi-center trials. *J Nucl Med*. 2008;49:159P-159P.

23. Stabin MG, Sparks RB, Crowe E. OLINDA/EXM: the second-generation personal computer software for internal dose assessment in nuclear medicine. *J Nucl Med*. 2005;46:1023-1027.

24. Sgouros G. Bone marrow dosimetry for radioimmunotherapy: theoretical considerations. *J Nucl Med*. 1993;34:689-694.

25. Plaizier MA, Roos JC, Teule GJ, et al. Comparison of non-invasive approaches to red marrow dosimetry for radiolabelled monoclonal antibodies. *Eur J Nucl Med*. 1994;21:216-222.

26. Jones WF, Digby WM, Luk WK, Casey ME, Byars LG. Optimizing rod window width in positron emission tomography. *IEEE Trans Med Imaging*. 1995;14:266-270.

27. Tatsumi M, Clark PA, Nakamoto Y, Wahl RL. Impact of body habitus on quantitative and qualitative image quality in whole-body FDG-PET. *Eur J Nucl Med Mol Imaging*. 2003;30:40-45.

28. Botkin CD, Osman MM. Prevalence, challenges, and solutions for (18)F-FDG PET studies of obese patients: a technologist's perspective. *J Nucl Med Technol*. 2007;35:80-83.

29. Halpern BS, Dahlbom M, Quon A, et al. Impact of patient weight and emission scan duration on PET/CT image quality and lesion detectability. *J Nucl Med*. 2004;45:797-801.

30. Halpern BS, Dahlbom M, Auerbach MA, et al. Optimizing imaging protocols for overweight and obese patients: a lutetium orthosilicate PET/CT study. *J Nucl Med*. 2005;46:603-607.

31. Philpott GW, Schwarz SW, Anderson CJ, et al. RadioimmunoPET: detection of colorectal carcinoma with positron-emitting copper-64-labeled monoclonal antibody. *J Nucl Med*. 1995;36:1818-1824.

32. Cutler PD, Schwarz SW, Anderson CJ, et al. Dosimetry of copper-64-labeled monoclonal antibody 1A3 as determined by PET imaging of the torso. *J Nucl Med*. 1995;36:2363-2371.
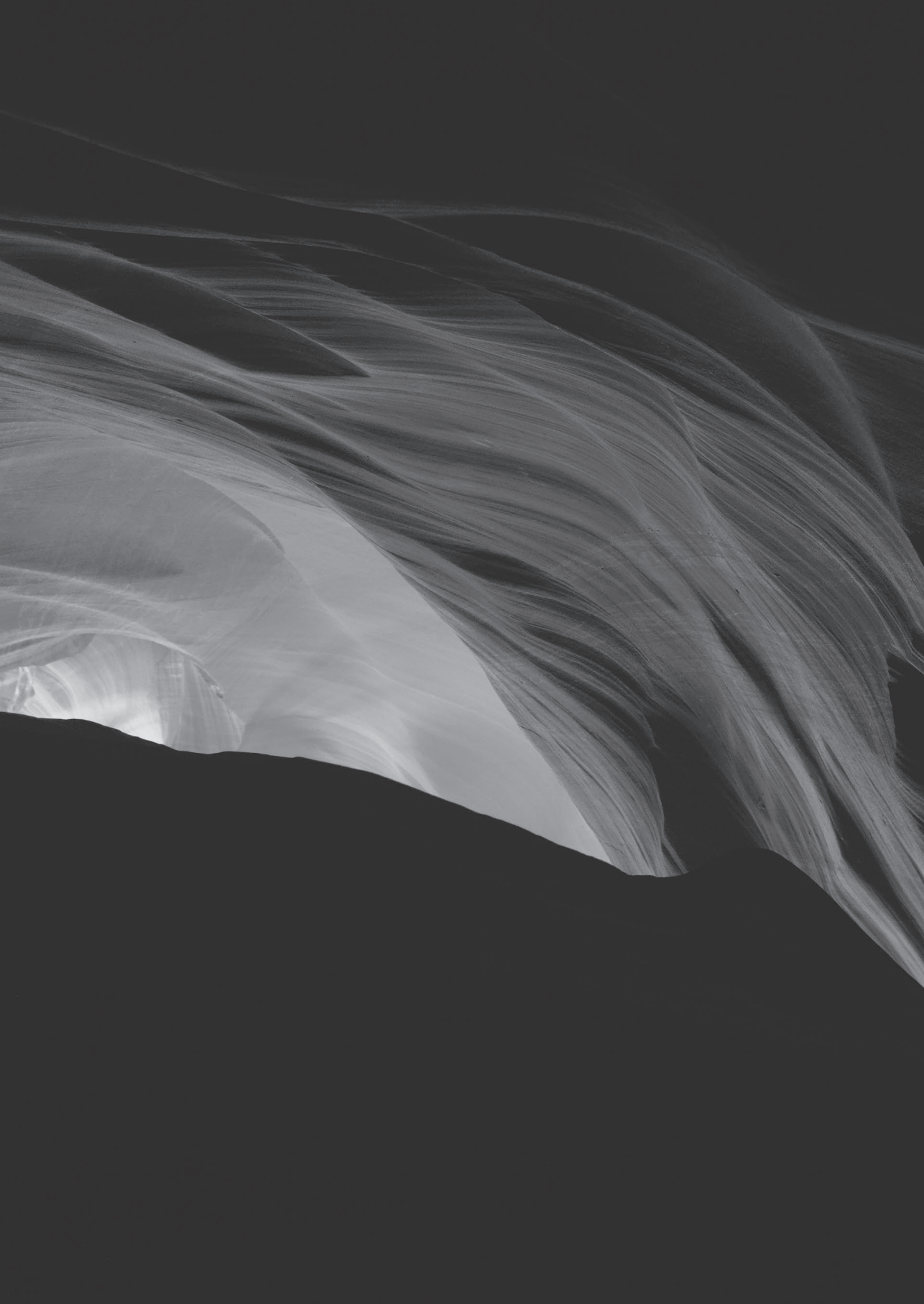
# Performance of immuno-positron emission tomography with zirconium-89-labeled chimeric monoclonal antibody U36 in the detection of lymph node metastases in head and neck cancer patients

Pontus K.E. Börjesson
Yvonne W.S. Jauw
Ronald Boellaard
Remco de Bree
Emile F.I. Comans
Jan C. Roos
Jonas A. Castelijns
Maria J.W.D. Vosjan
J. Alain Kummer
René Leemans
Adriaan A. Lammertsma
Guus A.M.S. van Dongen

# ABSTRACT

**Purpose:** Immuno-positron emission tomography (PET), the combination of (PET) with monoclonal antibodies (MAb), is an attractive option to improve tumor detection and to guide MAb-based therapy. The long-lived positron emitter zirconium-89 ([89]Zr) has ideal physical characteristics for immuno-PET with intact MAbs, but has never been used in a clinical setting. In the present feasibility study, we aimed to evaluate the diagnostic imaging performance of immuno-PET with [89]Zr-labeled-chimeric MAb (cMAb) U36 in patients with squamous cell carcinoma of the head and neck (HNSCC), who were at high risk of having neck lymph node metastases.

**Experimental design:** Twenty HNSCC patients, scheduled to undergo neck dissection with or without resection of the primary tumor, received 75 MBq [89]Zr coupled to the anti-CD44v6 cMAb U36 (10 mg). All patients were examined by computed tomography (CT) and/or magnetic resonance imaging (MRI) and immuno-PET prior to surgery. Six patients also underwent PET with ^{18}F-fluoro-2-deoxy-D-glucose (FDG-PET). Immuno-PET scans were acquired up to 144 hours after injection. Diagnostic findings were recorded per neck side (left or right) as well as per lymph node level (6 levels per side), and compared with histopathological outcome. For this purpose the CT/MRI scores were combined and the best of both scores was used for analysis.

**Results:** Immuno-PET detected all primary tumors (n = 17) as well as lymph node metastases in 18 of 25 positive levels (sensitivity 72%) and in 11 of 15 positive sides (sensitivity 73%). Interpretation of immuno-PET was correct in 112 of 121 operated levels (accuracy 93%) and in 19 of 25 operated sides (accuracy 76%). For CT/MRI sensitivities of 60% and 73% and accuracies of 90% and 80% were found per level and side, respectively. In the six patients with seven tumor involved neck levels and sides, immuno-PET and ^{18}F-fluoro-2-deoxy-D-glucose PET gave comparable diagnostic results.

**Conclusion:** In this study, immuno-PET with [89]Zr-cMAb U36 performed at least as good as CT/MRI for detection of HNSCC lymph node metastases.

## INTRODUCTION

Radiolabeled monoclonal antibodies (MAb) have shown considerable potential for diagnosis and treatment of cancer (*1,2*). In clinical radioimmunoscintigraphy and radioimmunotherapy studies performed at our institute, the potential of the CD44v6-specific murine MAb (mMAb) U36 for these purposes has been shown. Radioimmunoscintigraphy with technetium-99m (^{99m}Tc)-labeled mMAb U36 IgG was found to be as reliable as the radiological imaging techniques computed tomography (CT) and magnetic resonance imaging (MRI) for the detection of lymph node metastases in patients with head and neck squamous cell carcinoma (HNSCC), but the detection of tumor deposits smaller than 1 cm appeared to be a problem despite the proven accumulation of the MAb in these tumors (*3*). Subsequently, chimeric MAb (cMAb) U36 was tested in clinical phase I dose escalation radioimmunotherapy trials (*4,5*). Promising antitumor effects were observed with [186]Re-cMAb U36 in HNSCC patients with end-stage disease.

Introduction of immuno-PET, the combination of PET with MAbs, is an attractive option to improve tumor detection because it combines the high sensitivity and resolution of a PET camera with the specificity of a MAb (*6-8*). The latter might be an advantage in comparison with the currently used PET tracers such as fluorine-18 labeled fluoro-2-deoxy-D-glucose ([18]FDG), which shows increased uptake not only in tumors but also in normal tissues with high metabolic activity. Apart from its diagnostic capabilities, PET also has potential for quantification of molecular interactions, which is particularly attractive when immuno-PET is used as prelude to antibody-based therapy. First, patients can be selected who have the best chance to benefit from MAb treatment (*6-8*). Next, in an individualized therapeutic approach, immuno-PET enables the confirmation of tumor targeting and the quantification of MAb accumulation in tumor and normal tissues. For this purpose, we started the coupling of positron emitters to MAbs and a preclinical evaluation of these radiolabeled MAbs in immuno-PET.

For being suitable for immuno-PET, a positron emitter has to fulfill several requirements. Its physical half-life has to be compatible with the time needed for a MAb to achieve optimal tumor-to-nontumor ratios. For intact MAbs, presently the most frequently used format for targeting solid tumors, this time is generally 2 to 4 days.

Two positron emitters with a proper half-life for immuno-PET with intact MAbs are zirconium-89 ([89]Zr, half-life 78.4 hours) and iodine-124 ([124]I, half-life

100.3 hours). Of these isotopes, [89]Zr can be obtained with high yield, high radionuclide purity, and low production costs (*9*). Moreover, [89]Zr has ideal characteristics for optimal image quality and accurate quantification. Stable coupling of [89]Zr to MAbs was accomplished using the succinylated chelate desferrioxamine B (desferal) (*9*). The suitability of such conjugates, [89]Zr-labeled cMAb U36 included, for detection of millimeter-sized tumors was shown in HNSCC xenograft-bearing nude mice (*10*). In addition, the potential of PET for quantification of [89]Zr-labeled MAbs was shown in these studies (*10*).

Based on aforementioned encouraging preclinical results, we hypothesized that PET with [89]Zr-labeled MAb U36 might be better suited for detection of lymph node metastases in HNSCC patients than previously tested single-photon emission computerized tomography (SPECT) approaches with MAb U36. To the best of our knowledge, the long-lived positron emitter [89]Zr has never been tested in a clinical setting before. In the present study, PET with [89]Zr-labeled MAb U36 was evaluated for its safety and preliminary diagnostic accuracy in patients with proven HNSCC and clinically at high risk of having lymph node metastases.

## MATERIALS AND METHODS

### Patient Study

Twenty patients, who were at high risk of having neck lymph node metastasis from a proven HNSCC and who were planned to undergo neck dissection with or without resection of the primary tumor, participated in this study. Decision about the need for neck dissection, and the type of neck dissection, was based on primary tumor site and tumor stage as found by conventional clinical and diagnostic examinations. Immuno-PET did not influence this decision. Confirmation of CD44v6 expression by biopsy was not required, as > 96% of tumors show CD44v6 expression by at least 50% of the cells (*11*). The primary tumor and the status of neck lymph nodes were classified according to the tumor-node-metastasis system of the International Union Against Cancer (*12*). Patient and tumor characteristics are given in Table 1.

Prior and up to 6 weeks after administration of radiolabeled cMAb U36, routine laboratory analyses were done, including complete blood cell counts, serum electrolytes, urine sediment, liver enzymes, and renal and thyroid functions. Vital signs were recorded before and up to 3 hours after injection.

Patients received cMAb U36 IgG radiolabeled with [89]Zr (74.9 ± 0.6 MBq). The first 14 patients simultaneously received 55 MBq [186]Re-labeled cMAb U36 IgG for comparison of pharmacokinetics and biodistribution. This comparison is beyond the scope of the present manuscript and will be reported elsewhere. The total administered cMAb U36 dosage was 10 mg for all patients. Seventeen of 20 patients had surgery of their primary tumor, whereas all patients had unilateral (n = 16) or bilateral (n = 4) neck dissections done 6 to 8 days after administration of radiolabeled cMAb U36. All patients underwent radical neck dissection (patient 2, 14 and 16) or modified radical neck dissection comprising levels I through V, except for patient 11, 12, and 18. Patient 11 and 18 underwent selective bilateral neck dissection (levels II–IV + VI for patient 11, and II – IV for patient 18), whereas patient 12 underwent selective neck dissection (II-IV) on the left side and modified radical neck dissection (level I-VI) on the right side. The study was reviewed and approved by the Medical Ethics Committee of the VU University Medical Center. All patients gave written informed consent after receiving a thorough explanation of the study.

Table 1. Patient and Tumor Characteristics

| Patient | Sex | Age | Primary tumor | cTNM | pTNM |
|---|---|---|---|---|---|
| 1 | F | 57 | Oral cavity, tongue, right | T2N0M0 | T2N1M0 |
| 2 | M | 57 | Unknown primary, base of tongue right side suspected | TXN2aM0 | TisN2bM0 |
| 3 | F | 72 | Oropharynx, tonsil, right | T2N2bM0 | T2N2bM0 |
| 4 | F | 53 | Oropharynx, tonsil, right | T3N0M0 | T3N2bM0 |
| 5 | M | 63 | Oropharynx, tonsil, right | T4N0M0 | T4N2bM0 |
| 6 | F | 58 | Oral cavity, alveolar process and floor of mouth, left | T4N0M0 | T4N2bM0 |
| 7 | M | 54 | Oral cavity, tongue/floor of mouth, right | T3N0M0 | T3N2bM0 |
| 8 | M | 55 | Oropharynx, tonsil, left | T4N2aM0 | T4N2bM0 |
| 9 | F | 54 | Hypopharynx, piriform sinus, left | T4N2bM0 | T4N2bM0 |
| 10 | F | 65 | Oral cavity, base of tongue, right | T2N0M0 | T2N0M0 |
| 11 | M | 53 | Larynx, glottic | T4N0M0 | T4N0M0 |
| 12 | M | 59 | Larynx, supraglottic | T4N0M0 | T4N0M0 |
| 13 | F | 49 | Residual disease after T2N0 tonsil carcinoma, left | NA | NA |
| 14 | M | 58 | Oropharynx, base of tongue, right | T2N2bM0 | T2N2bM0 |
| 15 | M | 48 | Oropharynx, tonsil, right | T3N0M0 | T3N1M0 |
| 16 | F | 63 | Oropharynx, tonsil, left | T3N2bM0 | T3N2b/cM0 |
| 17 | M | 53 | Oropharynx, tonsil, right | T2N3M0 | T2N3M0 |
| 18 | M | 58 | Larynx, supraglottic, recurrence | NA | NA |
| 19 | M | 71 | Oropharynx, soft palate, right | T3N2cM0 | T2N2cM0 |
| 20 | M | 60 | Larynx, supraglottic, recurrence | NA | NA |

Abbreviations: NA, not applicable

## Monoclonal antibody U36

Selection and production of MAb U36 and its chimeric (mouse/human) IgG1 derivative (cMAb U36) have been described previously (*4*). MAb U36 binds to the v6 region of CD44 (CD44v6). Homogeneous expression of CD44v6 has been observed in squamous cell carcinoma of the head and neck, lung, skin, esophagus, and cervix, whereas heterogeneous expression was found in adenocarcinomas of the breast, lung, colon, pancreas, and stomach. In normal tissues, expression has been found in epithelial tissues such as skin, breast, and prostate myoepithelium, and bronchial epithelium (*13*).

## Production of [89]Zr-cMAb U36

The production and purification of [89]Zr and its coupling to cMAb U36 have been described previously (*9*). [89]Zr was produced by a (p,n) reaction on natural yttrium ([89]Y).

Labeling of cMAb U36 was achieved starting from the chelate desferrioxamine B (Df; desferal, Novartis, Basel, Switzerland). All procedures were done under aseptic conditions in a shielded laminar flow hood. In short, Df was succinylated (*N*-sucDf), temporarily filled with stable iron [Fe(III)], and coupled to the lysine residues of cMAb U36 by means of a tetrafluorophenol-*N*-sucDf ester. After removal of Fe(III) by transchelation to EDTA, the premodified cMAb U36 was purified on a PD10 column. Subsequently, *N*-sucDf-cMAb U36 (5 mg) was labeled with [89]Zr (185 MBq). Finally, [89]Zr-*N*-sucDf-cMAb U36 was purified on a PD10 column [eluent: 0.9 % NaCl/gentisic 5 mg/mL (pH 5.0)]. [89]Zr-*N*-sucDf-cMAb U36 will be abbreviated to [89]Zr-cMAb U36 in the rest of this article. The mean labeling efficiency was 87.4 ± 11.0%. Finally, cold cMAb U36 and for 14 of the 20 patients [186]Re-MAG3-cMAb U36 were added and the conjugates were filter sterilized (total amount of cMAb U36 to be administered was 10 mg). These procedures resulted in a sterile final product with endotoxin levels < 5 EU/mL. The molar ratio *N*-sucDf to cMAb U36 was always <2. The radiochemical purity was always >94.9 % (mean, 96.0 ± 1.2%). After each preparation of [89]Zr-cMAb U36, the immunoreactivity was determined by measuring binding to a serial dilution of UM-SCC-11B cells as described previously (*10*). The immunoreactive fraction of the [89]Zr-cMAb U36 preparations ranged from 74.8% to 91.0% (mean, 85.1 ± 4.5%) at the highest cell concentration. In addition, the data were graphically analyzed in a modified Lineweaver-Burk plot and the immunoreactivity was determined by extrapolating to conditions representing infinite antigen excess. By doing so, the immunoreactive fraction ranged from 89.4% to 100 % (mean, 98.7 ± 3.1%).

## Imaging studies

All patients were examined by palpation, CT and/or MRI, and [89]Zr-cMAb U36 PET (immuno-PET), whereas six patients were also examined by FDG-PET. The latter procedure was indicated for the detection of unknown primary tumors and/or for screening of distant metastases.

Preoperative palpation was performed in all patients by the same experienced head and neck surgeon. CT, MRI, FDG-PET, and immuno-PET were performed in 17, 15, 6, and 20 patients, respectively. In all patients diagnostic examinations and surgery were done within a 3-week period. CT scans were obtained with a third-generation Siemens Somaton Volume Zoom (Siemens AG, Erlangen, Germany). After contrast administration, axial scans with a slice thickness of 3 mm and increment of 3 mm were obtained. MRI examinations were done on a 1.5 T imaging system (Vision-system, Siemens AG, Erlangen, Germany) using a dedicated neck coil. Axial T2-weighed spin-echo, short-term inversion recovery, and pre- and post-gadolinium-diethylenetriaminepentaacetic acid (Magnevist, Schering AG, Germany) T1-weighed spin-echo MRI examinations were made. Slice thickness varied, depending on the MRI pulse sequence used, from 4 to 7 mm, with an interslice gap of 10%. Criteria for the optimal assessment of cervical lymph node metastases by CT or MRI, as defined by our Institute, were used (*14*). At CT and MRI, lymph nodes were considered malignant if nodes with necrosis were depicted, or if the minimal diameter in the axial plane of the node was ≥11 mm for nodes located in level II (subdigastric) and >10 mm for nodes in other levels. In routine diagnostic work-up, patients with enlarged lymph nodes of 4–11 mm (n = 14) went for additional diagnosis by ultrasound-guided fine-needle aspiration cytology.

PET scans were performed using a dedicated full-ring PET scanner (ECAT EXACT HR+, CTI/Siemens, Knoxville, TN). In case of immuno-PET scanning, whole body scans were made consisting of approximately seven bed positions covering the patient from base of the skull to the pelvis. At each bed position, a 3-minute transmission scan, acquired using three germanium-68 rod sources, and a 7-minute emission scan in three-dimensional mode were acquired. Whole body scans were performed starting within 1 hour and at 24, 72, and/or 144 hours after i.v. injection of [89]Zr-cMAb U36. All scans were normalized and corrected for randoms, scatter, attenuation, and decay. Reconstructions were performed using an attenuation and normalization weighted ordered subset expectation maximization (OSEM) algorithm (ECAT software version 7.2, CTI/Siemens) with

two iterations and 16 subsets followed by postsmoothing of the reconstructed image using a 5-mm FWHM Gaussian filter. Because images with attenuation correction showed high noise levels due to the low amount of radioactivity administered to the patients (for radiation exposure reasons), OSEM reconstructions without attenuation correction were done as well. Reconstructions without attenuation correction provided images with a quality similar to that of the diagnostic FDG scans (next paragraph). Interpretation of the scans was therefore performed using these non-attenuation-corrected images and was based on asymmetry and retention of activity, especially on late images.

In case of FDG-PET scanning, all patients fasted overnight before the PET study. Whole body scans were made using approximately seven bed positions from the base of the skull to the pelvis. At each bed position, a 7-minutes emission scan in two-dimensional mode was made. Scanning started ~ 60 minutes after i.v. injection of 370 MBq $^{18}$FDG (Cyclotron BV, Amsterdam, the Netherlands). All scans were corrected as described above for the $^{89}$Zr scans; however, no attenuation correction was done. The PET images were evaluated visually using standard ECAT (CTI/Siemens) software: foci with increased uptake versus background were considered abnormal, taking physiological biodistribution of FDG into account.

CT and MRI were scored by one experienced radiologist (J.A. Castelijns), FDG-PET by one experienced nuclear physician (E.F.I. Comans), whereas immuno-PET examinations were scored by consensus of two experienced nuclear physicians (E.F.I. Comans and J.C. Roos). CT/MRI and nuclear imaging examinations were performed in an independent and blinded way, without knowledge of the pathologic outcome. Observers were not informed about the sites of tumor involvement. All patients had neck dissections performed 6 to 8 days after the administration of the radio-immunoconjugate. After fixation, all palpable and visible lymph nodes were dissected from the surgical specimen and cut into 2- to 4-mm-thick slices for microscopic examinations. The different slices of one lymph node were examined by a pathologist and the percentage tumor involvement was estimated. The outcome of the histopathologic examination of the neck dissection specimen was used as the gold standard.

For topographical examination, the findings were recorded per side as well as per lymph node level according to the classification of the American Academy of Otorhinolaryngology and Head and Neck Surgery (15). Patients underwent either CT or MRI or both. For evaluation of overall anatomic imaging results, the

data on CT and MRI were combined, and if patients had undergone both diagnostic modalities only the best performing modality was used for analysis.

### Human anti-cMAb U36 and anti-N-sucDf-cMAb U36 responses

To evaluate the immunogenicity of cMAb U36 and [89]Zr-*N*-sucDf-cMAb U36, a human-anti-cMAb U36 (anti-isotypic) and a human anti-[89]Zr-*N*-sucDf-cMAb U36 assay were done. Human antibody response was tested in patient sera before administration of [89]Zr-*N*-sucDf-cMAb U36 and at 1 and 6 weeks after administration. The concentrations of human anti-cMAb U36 and anti-[89]Zr-*N*-sucDf-cMAb U36 antibodies were measured, essentially as described previously (*4*). In short, microtiter plates (Costar Europe LtD, Badhoevedorp, the Netherlands) were coated with cMAb U36 IgG or with [89]Zr-*N*-sucDf-cMAb U36 (after decay), 2 µg/well, in PBS (pH 7.2), and incubated overnight at room temperature. After blocking with assay buffer [PBS with 1% FCS (BioWhittaker, Verviers, Belgium) and 0.02% Tween 20 (Sigma, Zwijndrecht, the Netherlands)] and extensive washing with wash buffer (PBS with 0.05% Tween 20), 100 µL of standard dilutions of rabbit anti-human IgG (DAKO, Glostrup, Denmark) and diluted patient serum (1:10 in assay buffer) were pipetted into the wells and incubated for 1 hour at room temperature. Human antichimeric antibody-positive sera from previous clinical trials with cMAb U36 served as reference samples. The rabbit anti-human IgG was used to construct a calibration curve. After extentive washing with wash buffer and PBS, 100 µL biotinylated cMAb U36 or biotinylated [89]Zr-*N*-sucDf-cMAb U36 were added (± 1 µg/well), and the plate was incubated for 1 hour at room temperature. All subsequent steps, including incubation with horseradish peroxidase-conjugated streptavidin (CLB, Amsterdam, the Netherlands) and tetramethylbenzidine substrate, as well as absorption measurement at 450 nm, were exactly the same as previously described (*4*). Also, criteria for considering a sample positive were the same (*4*).

## STATISTICS

In this feasibility study, descriptive statistics were used with assessment of sensitivity, specificity and accuracy for [89]Zr-immuno-PET as well as for the routine diagnostic modalities palpation, CT/MRI, and FDG-PET. This was considered most appropriate because (a) in routine diagnostic work up CT/MRI might have

additional diagnostic value by identification of patients with enlarged lymph nodes (4-11 mm) eligible for ultrasound-guided fine-needle aspiration cytology, (b) clinical $^{89}$Zr-immuno-PET was used for the first time ever, and therefore it was not known beforehand whether all parameters were optimal for tumor detection, e.g., injected $^{89}$Zr dose and image acquisition, reconstruction, and evaluation. In addition, procedures for $^{89}$Zr quantification are under development, and were not available for the present evaluation.

## RESULTS

Neither adverse reactions nor significant changes in blood and urine values were observed, which could be related to the injection of the antibody. Patient 9 and 10 developed a human antichimeric antibody response, and elevated titers were found at 1 and 6 weeks post injection, whether or not cMAb U36 IgG or $^{89}$Zr-*N*-sucDf-cMAb U36 was used in the ELISA. These data indicate that the response was directed to the protein part of the conjugate and not to the *N*-succinyldesferrioxamine B chelate attached to the cMAb. None of the samples showed exclusive positivity in the $^{89}$Zr-*N*-sucDf-cMAb U36 ELISA, indicating that immunogenicity of the chelate is low.

Whole body images obtained directly after administration of $^{89}$Zr-cMAb U36 showed mainly blood-pool activity with delineation of nose, heart, lungs, liver, spleen, and kidneys. Uptake of radioactivity in these organs decreased over time, whereas increased uptake was seen only at tumor sites. No selective accumulation at nontumor sites was observed. Representative whole body scans are shown in Figure 1.  In the 20 patients studied, all 17 tumors at the primary site were visualized by immuno-PET, including one unknown primary tumor (patient 2). From the 20 patients, lymph nodes present in 25 neck dissections in 121 levels were examined histopathologically for tumor involvement. HNSCC metastases were found in 25 levels in 15 sides. There was no evidence for presence of distant metastases. Representative immuno-PET images of patients with primary tumor and lymph node involvement (patients 16 and 19) are shown in Figures 2 and 3.
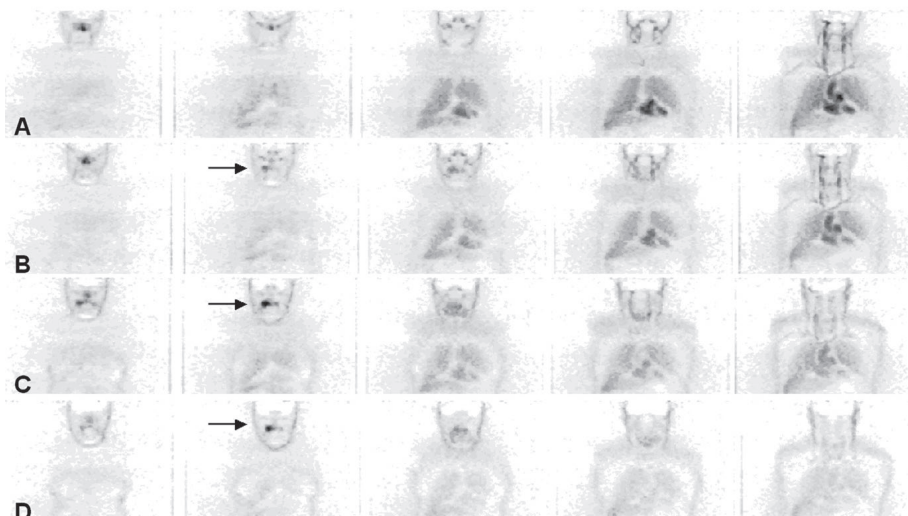
**Figure 1.** Immuno-PET images with ⁸⁹Zr-cMAb U36 of head and neck cancer patient 5, with a tumor of the right tonsil and a lymph node metastasis at the right side of the neck. Images were obtained within 1 h (A), at 24 h (B), at 72 h (C), and at 144 h (D) postinjection. Slices from anterior (left) to posterior (right). Early images show mainly blood-pool activity with visualization of nose, heart, lungs, and liver. At later images the primary tumor is clearly visualized (arrow). The lymph node metastasis was missed by immuno-PET.
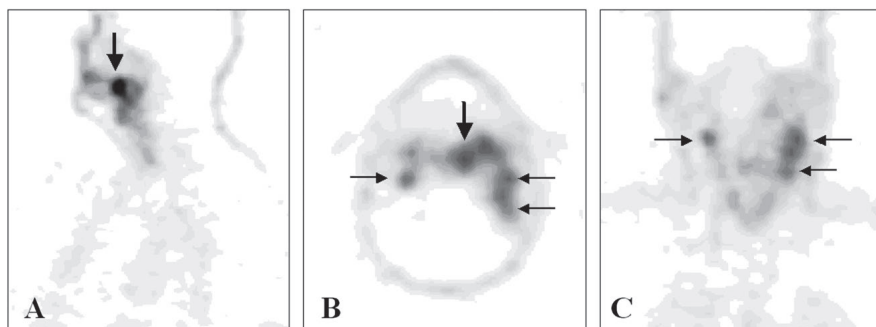


**Figure 2.** Immuno-PET images with ⁸⁹Zr-cMAb U36 of head and neck cancer patient 16, with a tumor in the left tonsil (large arrow) and lymph node metastases (small arrows) at the left (level II and III) and right (level II) side of the neck. Images were obtained 72 h postinjection. A, sagittal image; B, axial image, and C, coronal image.
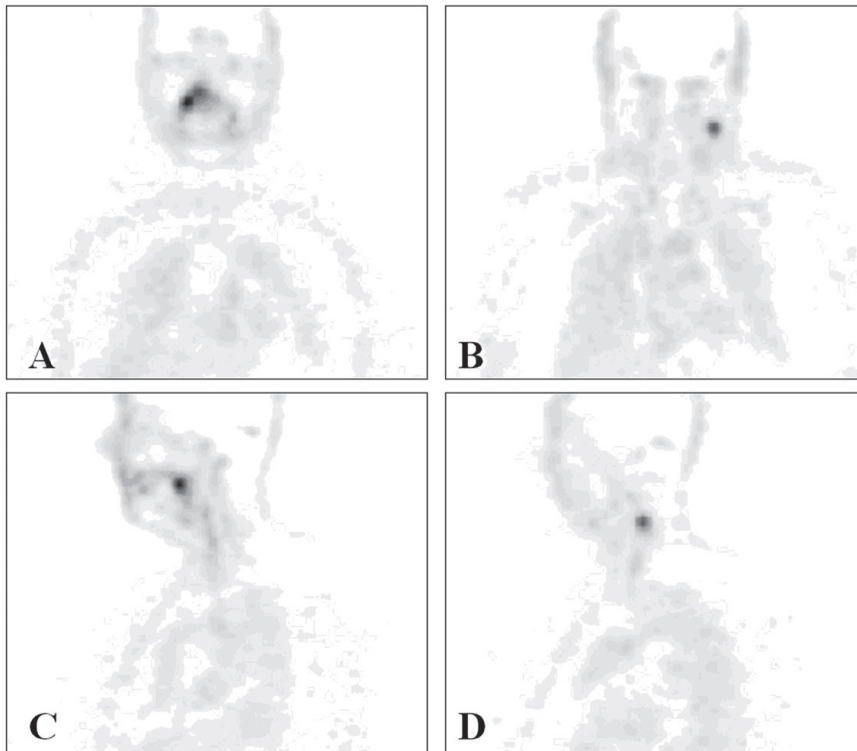
**Figure 3:** Immuno-PET images with $^{89}$Zr-cMAb U36 of head and neck cancer patient 19, with a tumor on the right side of the soft palate and a lymph node metastasis at the left side of the neck (level III). Images were obtained 72 h postinjection. A, coronal image of primary tumor; B, coronal image of lymph node metastasis in the neck; C, sagittal image of primary tumor; D, sagittal image of lymph node metastasis in the neck.

Preoperative findings obtained with immuno-PET, palpation, CT/MRI, and for a subgroup of patients with FDG-PET were compared with the histopathologic findings. Sensitivity, specificity, and accuracy of the different diagnostic modalities for detection of lymph node metastases per level and per side in the whole group of patients, are shown in Tables 2 and 3. Respective sensitivities of immuno-PET, palpation and CT/MRI were 72%, 44% and 60% when evaluated per neck level, and 73%, 53%, and 73% when evaluated per neck side. Accuracy of immuno-PET, palpation, and CT/MRI for the whole group of patients was per level 93%, 88%, and 90%, and per side 76%, 72%, and 80%, respectively.

Table 2. Correlation of Preoperative Findings with Histopathologic Findings per Level

| 121 operated levels 25 tumors involved | Sensitivity | Specificity | ACCURACY |
|---|---|---|---|
| Palpation | 11/25 = 44% | 96/96 = 100% | 107/121 = 88% |
| CT/MRI | 15/25 = 60% | 94/96 = 98% | 109/121 = 90% |
| [89]Zr-immuno-PET | 18/25 = 72% | 94/96 = 98% | 112/121 = 93% |

Table 3. Correlation of Preoperative Findings with Histopathologic Findings per Side

| 25 operated sides 15 tumors involved | Sensitivity | Specificity | ACCURACY |
|---|---|---|---|
| Palpation | 8/15 = 53% | 10/10 = 100% | 18/25 = 72% |
| CT/MRI | 11/15 = 73% | 9/10 = 90% | 20/25 = 80% |
| [89]Zr-immuno-PET | 11/15 = 73% | 8/10 = 80% | 19/25 = 76% |

Six patients also underwent FDG-PET. For these patients, the sensitivity of immuno-PET and FDG-PET for detection of tumor-involved lymph node levels was 85% and 62%, respectively (Table 4).

False-positive findings were obtained with immuno-PET (two levels), CT (two levels), and MRI (one level). No false-positive cases were observed with palpation and FDG-PET.

The paraffin slides of the seven tumor-involved lymph node levels that had been missed with immuno-PET were reexamined by histopathologic examination (Table 5). The tumor-involved lymph nodes found in these levels were relatively small, and contained just a small proportion of tumor tissue. No necrosis was observed in these tumors. Six of seven tumor-involved lymph node levels that had been missed by immuno-PET, were also missed by CT and/or MRI. The smallest tumor involved lymph node detected by immuno-PET was 5 x 5 mm, with 75% tumor involvement.

Table 4. Correlation of Preoperative Findings with Histopathologic Findings per Level in six Patients who Received FDG-PET

| 40 operated levels 13 tumors involved | Sensitivity | Specificity | ACCURACY |
|---|---|---|---|
| Palpation | 7/13 = 54% | 27/27 = 100% | 34/40 = 85% |
| CT/MRI | 10/13 = 77% | 27/27 = 100% | 37/40 = 93% |
| FDG-PET | 8/13 = 62% | 27/27 = 100% | 35/40 = 88% |
| [89]Zr-immuno-PET | 11/13 = 85% | 27/27 = 100% | 38/40 = 95% |

Table 5. Tumor involvement of tumor containing levels missed by immuno-PET

| Patient no., level | Size (mm) | %Tumor | REMARKS |
|---|---|---|---|
| 1, level II | 7 x 11 | 25 | Missed by MRI/detected by CT |
| 3, level III | 9 x 15 | 50 - 75 | Missed by CT/MRI |
| 5, level III | 4 x 4 | 10 | Missed by CT/MRI |
|  | 8 x 15 | 10 |  |
| 6, level II | 5 x 7 | 5 | Missed by CT/MRI |
|  | 6 x 8 | 50 - 75 |  |
|  | 5 x 9 | 5 |  |
| 7, level I | 5 x 7 | 5 | Missed by CT (no MRI) |
| 14, level IV | 8 x 12 | 10 - 25 | Missed by CT/MRI |
| 15, level II | 5 x 5 | 25 - 50 | Detected by CT/MRI |

# DISCUSSION

Immuno-PET combines the high resolution of PET with the high specificity and selectivity of MAbs. This makes immuno-PET an attractive modality for tumor detection. In addition, immuno-PET can also be used in a therapeutic setting with MAbs for confirmation of tumor targeting and for quantitative dose calculations. The possibility for combined use of MAbs in tumor detection, therapy planning, and therapy, makes the position of immuno-PET fundamentally different from FDG-PET.

In the current study, the long-lived positron emitter $^{89}$Zr was evaluated for the first time ever in a clinical immuno-PET trial. $^{89}$Zr was coupled to cMAb U36 via the bifunctional chelate $N$-succinyldesferrioxamine B. Modification procedures were standardized to arrive at a chelate/MAb molar ratio <2. No impairment of the immunoreactivity of cMAb U36 was observed upon radiolabeling. Administration of $^{89}$Zr-cMAb U36 (75 MBq, 10 mg) to HNSCC patients seemed to be safe. Just 2 of 20 patients showed an antibody response directed against cMAb U36, while in a previous RIT study this was 5 of 12 after administration of 50 mg radiolabeled cMAb U36. No evidence was found for antibody reactions against the chelate.

Immuno-PET with $^{89}$Zr-cMAb U36 seemed to be a promising method for imaging of primary head and neck tumors as well as metastases in the neck. All primary tumors were visualized, whereas 18 of 25 tumor-containing neck levels were also identified. In this feasibility study, the sensitivity of immuno-PET for detection of lymph node metastases was at least as good as of CT/MRI: 72% versus 60%. In a previous SPECT study with $^{99m}$Tc-labeled mMAb U36 in a comparable

group of patients, a sensitivity of 50% was found for nuclear imaging, the same as for CT and MRI. Because the number of patients in both studies was small, it is not justified to compare the performance of [89]Zr-immuno-PET and ^{99m}Tc-SPECT just on the basis of sensitivity percentages. Nevertheless, it became clear from the present study that [89]Zr-immuno-PET performs better with respect to tumor delineation. One reason for this is the better spatial resolution of PET. [89]Zr-immuno-PET showed detailed delineation of organs like heart as well as of tumors and blood vessels (Figure 1). This had not been the case with ^{99m}Tc-SPECT (3). Another reason for better delineation is the longer half- life of [89]Zr than of [99m]Tc (78.4 versus 6.0 hours), which allowed imaging at later time points, when tumor-to-nontumor radioactivity uptake ratios are higher (Figure 1). Indeed, in the present study delineation of primary tumors and lymph node metastases was better at later time points (72 and 144 hours) than at earlier time points (data not shown). Image quality might be further improved by elongation of the scanning time for the two bed positions covering the head and neck region.

Although good resolution is an advantage, it is fair to say that immuno-PET is hampered by the lack of anatomic structures. For example, because of the slow clearance of the conjugate from the blood, it might be difficult to distinguish a targeted lymph node metastasis from a cross-section through a blood vessel. In the present study, no explanation was found for the two false-positive observations with [89]Zr-immuno-PET. An improvement in image interpretation might be obtained by fusion of immuno-PET images with CT or MRI images. This approach enables the combination of (tumor) biological and anatomic information. We explored this approach for a few patients, including patient 16 with extensive bilateral lymph node involvement (Figure 2). Figure 4 shows the fused PET-CT image of the same patient 16, and the fusion makes clear that increased uptake of [89]Zr-cMAb U36 indeed is confined to the enlarged lymph nodes in the neck. To get a proper match between the immuno-PET and CT images, the head of this patient had to be fixed in the same way during both imaging procedures by using a thermoplastic radiotherapy mask. Problems related to matching will be solved when PET imaging and anatomical CT or MRI imaging are performed simultaneously by use of hybrid scanners. The use of combined PET/CT scanners is rapidly expanding and first efforts in developing MRI-compatible PET scanners have been reported (16). The availability of anatomic data will not only provide landmarks for PET image interpretation, but can also be used for more accurate quantification of MAb distribution (e.g., partial volume correction).
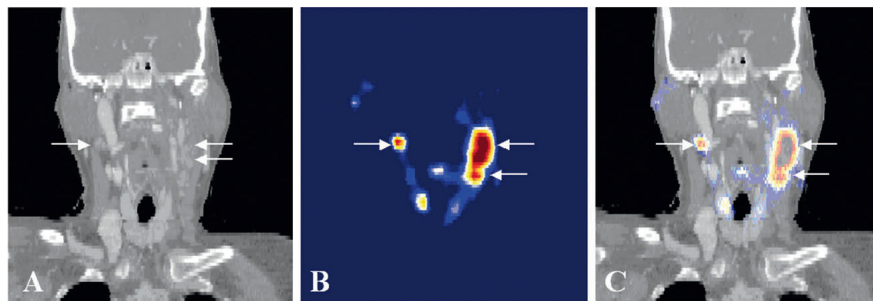
Figure 4. Fusion (C) of CT (A) and coronal immuno-PET (B) images of head and neck cancer patient 16 (same as in Figure 2), with a tumor in the left tonsil and lymph node metastases at the left (level II and III) and right (level II) side of the neck. Images were obtained 72 h postinjection. In these slices, only lymph node metastases are visible.

Following this feasibility study, the exact position of immuno-PET using [89]Zr-cMAb U36 within the current armamentarium for diagnosis of head and neck cancer still has to be established. One has to realize that apart from noninvasive imaging methods for the neck, invasive diagnostic procedures are also available, e.g., ultrasound-guided fine-needle aspiration cytology. In ultrasound-guided fine-needle aspiration cytology, selection of lymph nodes to be aspired is based on known patterns of lymphatic spread and/or lymph node size and morphology as assessed with ultrasound, sometimes after obtaining evidence by CT or MRI scan. Although ultrasound-guided fine-needle aspiration cytology enables detection of lymph node metastases at a single cell level it has also some unfavorable aspects, however: (a) its accuracy is strongly dependent on the skills of the ultrasonographer and the cytopathologist, (b) it is an invasive method, and (c) it gives only information of a selected part of the neck and not on the primary tumor or distant metastases.

At the current stage of development, immuno-PET with [89]Zr-cMAb U36 is not able to detect micrometastases in the neck, an observation that has also been previously reported for FDG-PET (*17,18*). False-negative observations in the present study were mostly due to the presence of small metastatic lymph nodes with minimal tumor involvement (Table 5), whether or not such small tumors are efficiently targeted by MAb U36, as previously shown in a biodistribution study with mMAb U36 (*19*).

From a diagnostic point of view, immuno-PET with [89]Zr-cMAb U36 might also have perspectives for the detection of distant metastases. Approximately 25% of advanced-stage (stage III and IV) head and neck cancer patients develop distant

metastases. Because surgical management is reserved for patients with locoregional disease, the presence of distant metastases is critical and may significantly influence treatment. Recent studies have shown that there is a role for FDG-PET in the detection of occult distant metastases (*20*). It can be anticipated, however, that the use of immuno-PET with [89]Zr-labeled MAbs might add another dimension to the detection of distant metastases, especially when the same MAb is used for systemic therapy. Within such a strategy, immuno-PET might play a dual role: tumor detection as well as treatment planning.

MAbs are gaining momentum for the use in tumor-selective systemic therapy, also for treatment of head and neck cancer. Presently, 17 MAbs (all intact IgGs) have been approved by the Food and Drug Administration for therapy, most of them for systemic treatment of cancer. Of the approved MAbs, cetuximab (directed against the epidermal growth factor receptor) and bevacizumab (directed against the vascular endothelial growth factor) are also used in strategies for treatment of head and neck cancer. In addition, several other MAbs are under evaluation for therapy of head and neck cancer, such as the radiolabeled MAbs U36 (*4,5*) and L19. The latter MAb is directed against the ED-B domain of fibronectin, and capable of selective targeting of tumor neovasculature (*21-23*). Data presented in this initial clinical feasibility study justify further exploration of [89]Zr-immuno-PET as an imaging tool for the selection of high-potential candidate MAbs for therapy as well as of patients most likely to benefit from (expensive) MAb treatment.

## ACKNOWLEDGMENTS

# REFERENCES

1. Zuckier LS, DeNardo GL. Trials and tribulations: Oncological antibody imaging comes to the fore. *Seminars in Nuclear Medicine*. 1997;27:10-29.

2. Goldenberg DM. Advancing role of radiolabeled antibodies in the therapy of cancer. *Cancer Immunol Immunother*. 2003;52:281-296.

3. Bree R de, Roos JC, Quak JJ, Hollander W den, Snow GB, Dongen GA van. Radioimmunoscintigraphy and biodistribution of technetium-99m-labeled monoclonal antibody U36 in patients with head and neck cancer. *Clin Cancer Res*. 1995;1:591-598.

4. Colnot DR, Quak JJ, Roos JC, et al. Phase I Therapy Study of 186Re-Labeled Chimeric Monoclonal Antibody U36 in Patients with Squamous Cell Carcinoma of the Head and Neck. *J Nucl Med*. 2000;41:1999-2010.

5. Colnot DR, Ossenkoppele GJ, Roos JC, et al. Reinfusion of Unprocessed, Granulocyte Colony-stimulating Factor-stimulated Whole Blood Allows Dose Escalation of 186Relabeled Chimeric Monoclonal Antibody U36 Radioimmunotherapy in a Phase I Dose Escalation Study. *Clin Cancer Res*. 2002;8:3401-3406.

6. Eary JF. PET Imaging for Planning Cancer Therapy. *J Nucl Med*. 2001;42:770-771.

7. Lee FT, Scott AM. Immuno-PET for Tumor Targeting. *J Nucl Med*. 2003;44:1282-1283.

8. Verel I, Visser GWM, Dongen GA van. The Promise of Immuno-PET in Radioimmunotherapy. *J Nucl Med*. 2005;46:164S-171S.

9. Verel I, Visser GWM, Boellaard R, Walsum MS, Snow GB, Dongen GAMS van. 89Zr Immuno-PET: Comprehensive Procedures for the Production of 89Zr-Labeled Monoclonal Antibodies. *J Nucl Med*. 2003;44:1271-1281.

10. Verel I, Visser GWM, Boellaard R, et al. Quantitative 89Zr Immuno-PET for In Vivo Scouting of 90Y-Labeled Monoclonal Antibodies in Xenograft-Bearing Nude Mice. *J Nucl Med*. 2003;44:1663-1670.

11. De Bree R, Roos JC, Quak JJ, Den Hollander W, Snow GB, Van Dongen GA. Clinical screening of monoclonal antibodies 323/A3, cSF-25 and K928 for suitability of targetting tumours in the upper aerodigestive and respiratory tract. *Nucl Med Commun*. 1994;15:613-627.

12. Sobin LH, Wittekind Ch, editors. TNM classification of malignant tumors 6th edition. *UICC, International Union Against Cancer*. New York: Wiley-Liss;2002.

13. Heider K-H, Mulder J-WR, Ostermann E, et al. Splice variants of the cell surface glycoprotein CD44 associated with metastatic tumour cells are expressed in normal tissues of humans and cynomolgus monkeys. *European Journal of Cancer*. 1995;31:2385-2391.

14. van den Brekel MW, Stel HV, Castelijns JA, et al. Cervical lymph node metastasis: assessment of radiologic criteria. *Radiology*. 1990;177:379-384.

15. Robbins KT, Clayman G, Levine PA, et al. Neck Dissection Classification Update: Revisions Proposed by the American Head and Neck Society and the American Academy of Otolaryngology–Head and Neck Surgery. *Arch Otolaryngol Head Neck Surg*. 2002;128:751-758.

16. Marsden PK, Strul D, Keevil SF, Williams SCR, Cash D. Simultaneous PET and NMR. *BJR*. 2002;75:S53-S59.

17. Stoeckli SJ, Steinert H, Pfaltz M, Schmid S. Is there a role for positron emission tomography with 18F-fluorodeoxyglucose in the initial staging of nodal negative oral and oropharyngeal squamous cell carcinoma. *Head Neck*. 2002;24:345-349.

18. Brouwer J, de Bree R, Comans EFI, Castelijns JA, Hoekstra OS, Leemans CR. Positron emission tomography using [18F]fluorodeoxyglucose (FDG-PET) in the clinically negative neck: is it likely to be superior? *Eur Arch Otorhinolaryngol*. 2004;261:479-483.

19. de Bree R, Roos JC, Plaizier MA, et al. Selection of monoclonal antibody E48 IgG or U36 IgG for adjuvant radioimmunotherapy in head and neck cancer patients. *Br J Cancer*. 1997;75:1049-1060.

20. Regelink G, Brouwer J, de Bree R, et al. Detection of unknown primary tumours and distant metastases in patients with cervical metastases: value of FDG-PET versus conventional modalities. *European Journal of Nuclear Medicine and Molecular Imaging*. 2002;29:1024-1030.

21. Birchler MT, Milisavlijevic D, Pfaltz M, et al. Expression of the extra domain B of fibronectin, a marker of angiogenesis, in head and neck tumors. *Laryngoscope* 2003;113:1231-1237.

22. Neri D, Bicknell R. Tumour vascular targeting. *Nat Rev Cancer* 2005;5:436-446.

23. Santimaria M, Moscatelli G, Viale GL Giovannoni L, Neri G, Viti F, et al. Immunoscintigraphic detection of the ED-B domain of fibronectin, a marker of angiogenesis, in patients with cancer. *Clin Cancer Res* 2003;9:571-579.
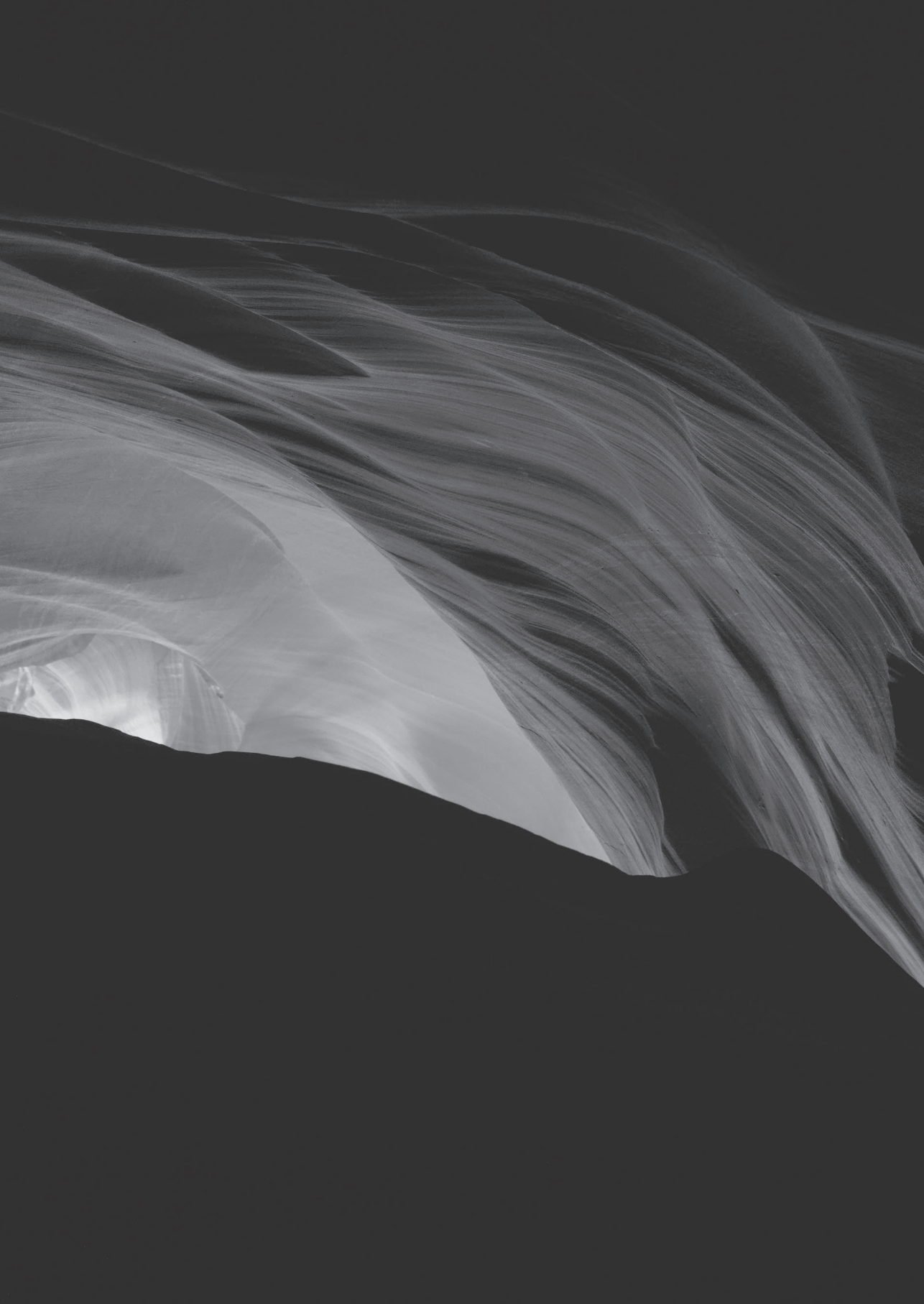
# Immuno-positron emission tomography with zirconium-89-labeled monoclonal antibodies in oncology:

# What can we learn from initial clinical trials?

Yvonne W.S. Jauw

C. Willemien Menke - van der Houven van Oordt

Otto S. Hoekstra

N. Harry Hendrikse

Daniëlle J. Vugts

Josée M. Zijlstra

Marc C. Huisman

Guus A.M.S. van Dongen

# ABSTRACT

Selection of the right drug for the right patient is a promising approach to increase clinical benefit of targeted therapy with monoclonal antibodies (mAbs). Assessment of in vivo biodistribution and tumor targeting of mAbs to predict toxicity and efficacy is expected to guide individualized treatment and drug development.

Molecular imaging with positron emission tomography (PET) using zirconium-89 ([89]Zr)-labeled monoclonal antibodies also known as [89]Zr-immuno-PET, visualizes and quantifies uptake of radiolabeled mAbs. This technique provides a potential imaging biomarker to assess target expression, as well as tumor targeting of mAbs.

In this review we summarize results from initial clinical trials with [89]Zr-immuno-PET in oncology and discuss technical aspects of trial design.

In clinical trials with [89]Zr-immuno-PET two requirements should be met for each [89]Zr-labeled mAb to realize its full potential. One requirement is that the biodistribution of the [89]Zr-labeled mAb (imaging dose) reflects the biodistribution of the drug during treatment (therapeutic dose). Another requirement is that tumor uptake of [89]Zr-mAb on PET is primarily driven by specific, antigen-mediated, tumor targeting.

Initial trials have contributed towards the development of [89]Zr-immuno-PET as an imaging biomarker by showing association between uptake of [89]Zr-labeled mAbs on PET and target expression levels in biopsies. However, no definitive proof has been reported that [89]Zr-immuno-PET reflects specific, antigen-mediated binding. [89]Zr-immuno-PET was shown to predict toxicity of RIT, but thus far results indicating that toxicity of mAbs or mAb-drug conjugate treatment can be predicted are lacking. So far, one study has shown that molecular imaging combined with early response assessment is able to predict response to treatment with the antibody-drug conjugate trastuzumab-emtansine, in patients with human epithelial growth factor-2 (HER2)-positive breast cancer. Future studies would benefit from a standardized criterion to define positive tumor uptake, possibly supported by quantitative analysis, and validated by linking imaging data with corresponding clinical outcome.

Taken together, these results encourage further studies to develop [89]Zr-immuno-PET as a predictive imaging biomarker to guide individualized treatment, as well as for potential application in drug development.

# INTRODUCTION

In recent years, monoclonal antibodies (mAbs) have become widely used for treatment of cancer. Immunotherapy with mAbs aims for specific targeting and therefore less toxicity compared to chemotherapy. Some mAbs have resulted in a significant improvement of survival, for example the anti-CD20 antibody rituximab for B cell lymphoma (1). However, not all patients benefit from mAb treatment. Monotherapy with the anti-epidermal growth factor receptor (EGFR) antibody cetuximab results in clinical benefit for half of the patients with advanced colorectal cancer (without relevant gene mutations; RAS wild type) (2).

Next generation mAbs are aiming for increased potency, for example antibody-drug conjugates (ADC's), mAbs capable of inhibiting immune checkpoints and multi-specific mAbs recognizing at least two different targets (3-5). The number of novel targeted treatment options increases, however drug development requires time, efforts and significant resources. In addition, investigational drugs are evaluated in large patient cohorts before successful introduction in routine clinical care.

Improving response rates by quickly selecting the right drug for the right patient is paramount to reducing unnecessary toxicity and costs. In order to obtain clinical benefit from mAb treatment, the target antigen should be expressed in the tumor and the drug is required to reach and bind to the target (tumor targeting). Absence of target expression on normal tissue is important to limit toxicity of treatment.

Molecular imaging with [89]Zr-labeled mAbs, also known as [89]Zr-immuno-PET, provides a potential imaging biomarker to evaluate tumor targeting of mAbs. This technique is non-invasive and provides whole body information on both target expression and tumor targeting, as opposed to immunohistochemistry on a single biopsy, which only provides information on target expression. Prediction of efficacy and toxicity of mAb treatment by molecular imaging may be used to select individual patients for a treatment, or to select promising candidate drugs in drug development.

[89]Zr-immuno-PET allows visualization and quantification of biodistribution and tumor uptake (6). [89]Zr is considered a suitable radioisotope for this purpose, due to its relatively long half-life ($t_{1/2}$ = 78.4 hours), which corresponds with the time a mAb needs to reach the target. The use of [89]Zr as a radiolabel and the coupling of [89]Zr to mAbs, under Good Manufacturing Practice conditions, have

been described previously (*7-9*). Harmonization of quantitative [89]Zr-immuno-PET imaging has also been reported, allowing for broad scale application, e.g. in a multi-center setting (*10*).

Before starting clinical [89]Zr-immuno-PET trials, the following conditions are essential to allow appropriate interpretation of data. Prerequisites are that the radioimmunoconjugate of interest is stable and has the same binding and biodistribution characteristics as the unlabeled parental mAb. Imaging procedures should be standardized and validated in order to provide reliable quantification. Assuming these requirements are fulfilled, biodistribution and tumor uptake of a [89]Zr-mAb, defined on PET, can be used as an imaging biomarker for tumor targeting of the "cold" therapeutic antibody.

Until now, at least 15 clinical [89]Zr-immuno-PET trials have been reported, see Table 1, providing first information on the clinical performance of [89]Zr-immuno-PET. Therefore, evaluation of the potential and current limitations of this novel imaging technique seems timely to enable optimal design of future trials. This review summarizes the results from initial clinical [89]Zr-immuno-PET in oncology, and technical aspects of trial design are discussed.

Table 1. Summary of clinical studies on [89]Zr-immuno-PET in oncology

| Author | Year | Target | mAb | Tumor type | N |
|---|---|---|---|---|---|
| Börjesson | 2006 2009 | CD44v6 | cmAb U36 | Head and neck cancer | 20 |
| Dijkers | 2010 | HER2 | trastuzumab | Breast cancer | 14 |
| Rizvi | 2012 | CD20 | ibritumomab-tiuxetan | B-cell lymphoma | 7 |
| Gaykema | 2013 | VEGF-A | bevacizumab | Breast cancer | 23 |
| van Zanten | 2013 | VEG-F | bevacizumab | Glioma | 3 |
| van Asselt | 2014 | VEGF-A | bevacizumab | Neuroendocrine tumors | 14 |
| Bahce | 2014 | VEGF-A | bevacizumab | Non-small cell lung cancer | 7 |
| Pandit-Taskar | 2014 2015 | PSMA | Hu-J591 | Prostate cancer | 50 |
| Den Hollander | 2015 | TGF-β | fresolimumab | Glioma | 12 |
| Gaykema | 2015 | HER2 VEGF-A | trastuzumab bevacizumab | Breast cancer | 10 6 |
| Gebhart | 2015 | HER2 | trastuzumab | Breast cancer | 56 |
| Lamberts | 2015 | MSLN | MMOT0530A | Pancreatic cancer Ovarian cancer | 11 4 |
| Menke-van der Houwen van Oordt | 2015 | EGFR | cetuximab | Colorectal cancer | 10 |
| Muylle | 2015 | CD20 | rituximab | B-cell lymphoma | 5 |
| Oosting | 2015 | VEGF-A | bevacizumab | Renal cell carcinoma | 22 |

## [89]Zr-labeled anti-CD44v6 mAb in head and neck cancer

[89]Zr-immuno-PET is considered to be an attractive imaging technique for whole body tumor detection, due to the combined sensitivity of PET and the specificity of the mAb. Assessment of biodistribution of the mAb to confirm specificity of the mAb is particularly of interest to qualify the suitability of the mAb for therapy.

Börjesson et al. reported on the first clinical [89]Zr-immuno-PET study ever (11). In this study, twenty pre-operative patients with head and neck squamous cell carcinoma (HNSCC) were included. Immuno-PET with [89]Zr-labeled chimeric mAb U36 (cmAb U36) was investigated in order to improve tumor detection of HNSCC, especially in lymph nodes, and to assess the targeting potential of the mAb for therapy. cmAb U36 targets the v6 region of CD44 (cluster of differentiation; CD44v6). Homogeneous expression of CD44v6 has been observed in several malignancies, including HNSCC, lung, skin, esophagus, and cervix carcinoma. Expression of CD44v6 has also been reported in normal epithelial tissues, such as skin, breast, and prostate myoepithelium, and bronchial epithelium.

Administration of 74 megabecquerel (MBq) [89]Zr-mAb U36 (10 mg) appeared to be safe, as no adverse reactions were observed. A human anti-chimeric antibody response was reported in 2 patients, which was not directed to the chelate, but to the protein part of the conjugate. [89]Zr-immuno-PET scans were visually scored. All primary tumors were detected and [89]Zr-immuno-PET performed equally to computed tomography (CT)/magnetic resonance imaging (MRI) for detection of lymph node metastasis. Although biopsies were obtained in this study to confirm tumor localization, immunohistochemistry for CD44v6 was not performed, as in literature > 96% of HNSCC show CD44v6 expression by at least 50% of the cells. This study shows that immuno-PET with [89]Zr-cmAb U36 can be used as an imaging modality for tumor detection. However, traditional imaging techniques as ^{18}F-fluoro-deoxy-glucose(FDG)-PET and sentinel node procedures for assessment of lymph node status remain standard of care for tumor detection in HNSCC patients, as the added value of immuno-PET with [89]Zr-cmAb U36 has not been demonstrated.

In a separate publication, biodistribution, radiation dose and quantification of [89]Zr-labeled cmAb U36 were reported for the same patient cohort (12). [89]Zr-cmAb U36 in blood pool, lungs, liver, kidneys and spleen decreased over time. Increasing uptake of [89]Zr-cmAb U36 over time was seen only at tumor sites and in the thyroid of some patients (suggesting expression of CD44v6 in thyroid of these patients). Although expression of CD44v6 in normal epithelial tissue has been described, no

obvious targeting of [89]Zr-mAb U36 was observed in the skin. However, Tijink et al. reported a fatal adverse event due to skin toxicity after treatment with the ADC bivatuzumab mertansine, a humanized anti-CD44v6 mAb conjugated to a potent maytansine derivate (*13*). This toxicity profile, most probably due to expression of CD44v6 in the skin, was not predicted based on assessment of biodistribution of [89]Zr-cmAbU36 as reported by Börjesson et al. (*12*). Among others, this may due to detection limitations of PET, inter-individual differences in target expression, or differences in biodistribution between the mAb and the ADC.

A technical aspect of this first [89]Zr-immuno-PET study to be considered is the rationale for the total protein dose of cmAb U36 administered. This protein dose of 10 mg was chosen as previous studies observed that biodistribution was not mAb-dose dependent within the range of 2-52 mg (*14-16*).

Finally, good agreement was reported for image-derived quantification of blood pool radioactivity as well as tumor uptake of [89]Zr-cmAb U36 compared to *ex vivo* radioactivity measurements in, respectively, venous blood samples and biopsies from surgical tumor resection. This is an important achievement in performance, showing accurate quantification of [89]Zr-mAb with PET.

## [89]Zr-labeled trastuzumab in breast cancer

Treatment with trastuzumab, which targets the human epidermal growth factor receptor 2 (HER2), has improved the prognosis for patients with HER2-positive breast cancer (*17*) and gastric cancer (*18*). HER2 is involved in cell survival, proliferation, cell maturation, metastasis, angiogenesis and has anti-apoptotic effects. It is also expressed in other malignancies, including ovarian and endometrial carcinoma, and in normal epithelial cells and hematopoietic cells (*19*). It is known that the extracellular domain of HER2 can enter the circulation after shedding from the surface of tumor cells (*20*).

Currently assessment of HER2 status is performed with immunohistochemistry (IHC) or fluorescent in situ hybridization on tumor biopsies. Some studies have shown up to 15% intra-individual heterogeneity in HER2 status between primary tumors and metastases (*21*) leading to the recommendation to repeat biopsies to assess HER2 status during the course of the disease. As some tumor lesions are inaccessible for biopsies and it is impossible to biopsy every tumor lesion to assess heterogeneity, there is a need for a non-invasive technique to assess whole body HER2 status for diagnosis, staging and to guide individualized treatment.

*[89]Zr-trastuzumab-PET for whole body assessment of HER2 target status*
Dijkers et al. reported a feasibility study to determine optimal dosage and time of administration of [89]Zr-trastuzumab (37 MBq) to enable PET visualization and quantification of tumor lesions in 14 patients with HER2-positive metastatic breast cancer" (*22*).

Trastuzumab naïve patients who received a total dose of 10 mg trastuzumab (n=2), showed relatively high liver uptake and pronounced intestinal excretion, with low blood pool activity, indicating rapid clearance. This rapid clearance was most probably due to complex formation of trastuzumab with extracellular HER2 domains shed in the plasma. For optimal imaging, trastuzumab naïve patients required a total dose of 50 mg trastuzumab (n=5). This resulted in less liver uptake, lower intestinal excretion and increased blood pool activity, as illustrated by Figure 1(A) and (B). This dose was considered the optimal dose, as good tumor-to-non-tumor ratio and favorable biodistribution were observed, although higher doses were not evaluated due to expected target saturation. Patients already on trastuzumab treatment received a dose of 10 mg trastuzumab. As these patients (n=7) showed minimal intestinal excretion and slow blood clearance, this was considered an adequate dose, see Figure 1(C). This study illustrates a dose-dependent relationship between imaging dose and biodistribution of [89]Zr-trastuzumab.

Best timing for evaluation of tumor uptake of [89]Zr-trastuzumab was 4-5 days post injection (p.i.) while scans performed at day 6 or 7 p.i. yielded decreased image quality because of insufficient counting statistics. Image quality with [89]Zr-trastuzumab-PET was superior to previous [111]Indium-labeled-trastuzumab single photon emission computed tomography.
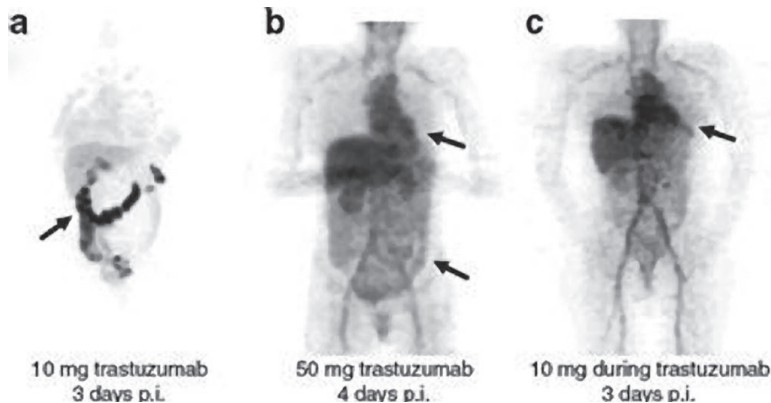
Figure 1. Dose-dependent biodistribution and clearance of [89]Zr-trastuzumab. Radioactivity in the blood pool and intestinal excretion are indicated by arrows.

(**A**) Trastuzumab-naïve patient, imaging dose = 10 mg
(**B**) Trastuzumab-naïve patient, imaging dose = 50 mg
(**C**) Patient on trastuzumab treatment, imaging dose = 10 mg
Reprinted with permission from "Dijkers, E.C., Oude Munnink, T.H., Kosterink, J.G., Brouwers, A.H., Jager, P.L., de Jong, J.R., et al. (2010). Biodistribution of [89]Zr-trastuzumab and PET imaging of HER2-positive lesions in patients with metastatic breast cancer. *Clin. Pharmacol. Ther*. 87, 586-592. doi: 10.1038/clpt.2010.12"

[89]Zr-trastuzumab-PET allowed detection of most of the known lesions and some that had remained unnoticed with conventional imaging. In 6 of the 12 patients not all known lesions were detected. Liver lesions were missed in 3 out of 7 patients, possibly due to the high background activity in normal liver tissue, which is involved in mAb catabolism. Interestingly, while poor penetration of trastuzumab in the brain was expected, in 3 patients brain lesions could be visualized. This might be due to disruption of blood-brain barrier in brain metastasis. A limitation of this study was the lack of biopsies for confirmation of the HER2 status of immuno-PET negative lesions.

Tumor lesions showing no uptake of [89]Zr-trastuzumab may be due to suboptimal imaging conditions, as illustrated by a case report of a trastuzumab naïve breast cancer patient (12). 37 MBq trastuzumab (50 mg) was administered and a PET scan was obtained 2 days p.i.. Low blood pool levels and massive uptake of [89]Zr-trastuzumab in liver metastases (48% of the injected dose) were observed, as well as intestinal uptake, suggesting intestinal excretion. Known bone metastases were hardly visible and no uptake in the brain lesion was observed. This might be the result of an extensive tumor load and/or soluble HER2, which reduces uptake in other tumor lesions, due to an insufficient amount of trastuzumab. After

administration of 220 mg unlabeled trastuzumab, immediately followed by 10 mg [89]Zr-trastuzumab, liver uptake was lowered (33% of the injected dose) and an increase in uptake in the other tumor lesions, such as bone metastases, was observed. Based on a theoretical calculation the authors conclude that a dose of 280 mg trastuzumab could only saturate 47% of all HER2 present in the liver metastases of this patient, indicating a higher dose of trastuzumab is required to saturate lesions in case of extensive HER2-positive tumor load. Based on this important observation that pharmacokinetics and organ distribution can be influenced by the extent of tumor load, dosing of trastuzumab for metastatic breast cancer should be reconsidered. An individualized dosing schedule of trastuzumab based on tumor load, guided by [89]Zr-trastuzumab-PET, instead of patient weight, might improve efficacy of treatment.

*[89]Zr-trastuzumab to assess response by alteration of antigen expression*
Gaykema et al. evaluated [89]Zr-trastuzumab-PET to determine alteration of HER2 expression after anti-angiogenic treatment with the novel heat shock protein 90 (HSP90) inhibitor NVP-AUY922 in 10 patients with HER2-positive breast cancer (*24*). HSP90 inhibition can deplete client proteins like HER2. This study was performed with 37 MBq [89]Zr-trastuzumab (50 mg), while NVP-AUY922 was administered i.v. in a weekly schedule of 70 mg/m$^2$. Change in tumor uptake of [89]Zr-trastuzumab at baseline versus 3 weeks on treatment was correlated to change in size on CT after 8 weeks treatment. This feasibility study suggests that [89]Zr-immuno-PET can be used to monitor alteration of antigen expression and supports further evaluation of [89]Zr-trastuzumab-PET in providing insight in treatment response of novel anti-cancer agents like the HSP90 inhibitor NVP-AUY922 in larger studies.

*[89]Zr-trastuzumab-PET as predictive imaging biomarker for ADC treatment*
Recently, the ADC trastuzumab-emtansine (T-DM1) was approved for treatment of patients with progression of HER2-positive breast cancer, previously treated with trastuzumab-based therapy. The ZEPHIR study investigated the use of [89]Zr-trastuzumab-PET, combined with early response assessment with FDG-PET, as a predictive imaging biomarker for treatment with T-DM1 (*25*). In this study intra- and interpatient heterogeneity in HER2 mapping of metastatic disease was also explored, see Figure 2. The study was performed by administration of 37 MBq [89]Zr-trastuzumab (50 mg). [89]Zr-trastuzumab-PET scans were acquired 4 days p.i.

and visually scored. After 1 cycle of T-DM1 an early metabolic response was evaluated by FDG-PET. Clinical outcome after treatment with 3 cycles of T-DM1 was evaluated by CT.
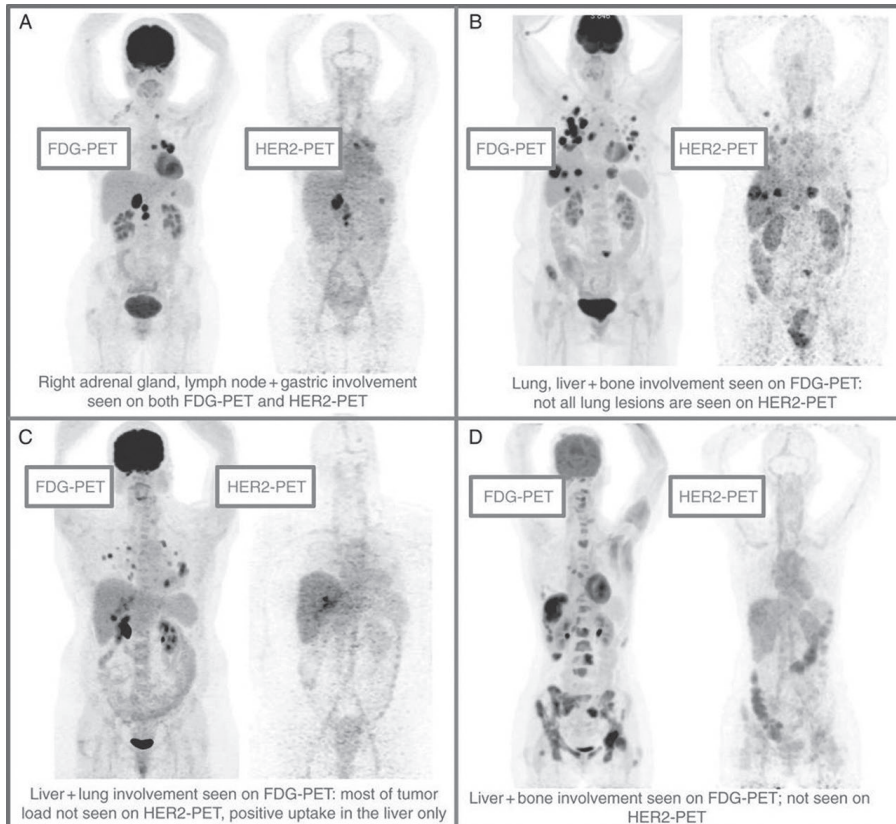


Figure 2. Patterns of HER2-PET/CT confronted with FDG-PET/CT, maximum intensity projection. Lesion uptake was considered pertinent when visually higher than blood pool.

(**A**) entire tumor load showed pertinent tracer uptake
(**B**) dominant part of tumor load showed tracer uptake
(**C**) minor part of tumor load showed tracer uptake
(**D**) entire tumor load lacked tracer uptake

Reprinted with permission from "Gebhart, G., Lamberts, L.E., Wimana, Z., Garcia, C., Emonts, P., Ameye, L., et al. (2015). Molecular imaging as a tool to investigate heterogeneity of advanced HER2-positive breast cancer and to predict patient outcome under trastuzumab emtansine (T-DM1): the ZEPHIR trial. Epub ahead of print. *Ann Oncol*. doi: 10.1093/annonc/mdv577"

For 55 evaluable patients with HER2-positive metastatic breast cancer, assessment of [89]Zr-trastuzumab uptake resulted in a positive predictive value of 72% and a negative predictive value of 88% for prediction of clinical outcome. For early metabolic response assessment with FDG-PET the positive predictive value was 96% and the negative predictive value was 83%. Intrapatient heterogeneity in tumor uptake was observed in 46% of patients, as illustrated by Figure 3. When combining [89]Zr-trastuzumab-PET with early FDG-PET response after 1 cycle of T-DM1, a negative predictive value of 100% was obtained for all concordant patients (with both a negative [89]Zr-trastuzumab-PET, as well as absence of response on early FDG-PET). This strategy of combining HER2-PET with early FDG-PET response monitoring was able to separate patients with a median time to treatment failure of 2.8 month from patients with a median time to treatment failure of 15 months.

It is not known why 2/16 patients with a negative [89]Zr-trastuzumab-PET did show response on treatment with T-DM1. Some possibilities are lack of receptor overexpression, receptor masking, or an induced response despite low HER2 expression due to the extreme potency of T-DM1. Absence of tumor uptake can also be explained by an insufficient tracer dose due to the extent of tumor load or the amount of soluble HER2 in these patients.

These results support that pre-treatment imaging of HER2-targeting is a promising tool to improve the understanding of tumor heterogeneity in metastatic breast cancer and to select patients who are deemed not to benefit from T-DM1. This might avoid toxicity and costs of T-DM1 and improve patient outcome by switching sooner to a more effective therapy (personalized medicine). A plausible explanation for the added value of early FDG-PET is that although target expression of HER2 is a prerequisite for clinical benefit, even with adequate targeting intracellular resistance mechanisms may be responsible for treatment failure. The authors recommend a future randomized trial with cost-effectiveness as secondary endpoint, to test the concept of interrupting T-DM1 treatment after 1 cycle in case of FDG-PET non-responsiveness, which can be expected in 20% of the patients. As such, this trial paved the road towards improved individualization of anti-HER2 therapy.

**$^{89}$Zr-labeled bevacizumab in breast cancer, lung cancer, renal cell carcinoma, neuroendocrine tumors and pontine glioma**
Another target for treatment of breast cancer and many other tumor types is vascular endothelial growth factor A (VEGF-A), which is involved in tumor angiogenesis. Overexpression of VEGF-A has been reported in malignant breast tumors and ductal carcinoma in situ and has been related to aggressiveness of the disease. Bevacizumab is a mAb that targets all splice variants of VEGF-A, both small isoforms which can diffuse freely in the circulation, as well as larger isoforms which are primarily matrix-bound. Despite the fact that VEGF-A is not a membrane target like HER2, it is partly associated with the tumor blood vessels and to some extent with the extracellular matrix of tumor cells, which could enable imaging of tumor lesions.

It can be hypothesized that local VEGF-A concentration reflects whether tumor progression is driven by angiogenesis and if anti-angiogenic treatment is likely to be effective. Therefore, $^{89}$Zr-bevacizumab-PET is of interest for several applications: biological characterization of tumors, prediction of therapeutic outcome, and treatment evaluation of VEGF-A targeting drugs.

*$^{89}$Zr-labeled bevacizumab in breast cancer*
Gaykema et al. performed a study to assess whether VEGF-A can be visualized by $^{89}$Zr-bevacizumab-PET in patients with primary breast cancer who were scheduled for surgery (*26*). In this study 37 MBq $^{89}$Zr-labeled bevacizumab (5 mg) was administered and PET scans were acquired at 4 days p.i.. The same dose was used in a previous study with $^{111}$Indium-labeled bevacizumab, which visualized all known melanoma lesions (*27*). Tumor uptake of $^{89}$Zr-bevacizumab was observed in 25 of 26 tumors in 23 patients with primary breast cancer. The false-negative tumor was a 10 mm VEGF-A-positive invasive ductal carcinoma. Besides assessment of tumor uptake in the primary tumors, uptake of $^{89}$Zr-bevacizumab in lymph node metastasis regions was evaluated. 4 of 10 metastasis-involved lymph node regions were detected in 9 patients. 0 of 4 axillary regions with lymph node metastases were detected by $^{89}$Zr-bevacizumab-PET.

For all available tumors (n=25) VEGF-A expression was quantified by enzyme-linked immunosorbent assay. $^{89}$Zr-bevacizumab uptake in tumors correlated with the VEGF-A tumor levels measured. Microvessel density on immunohistochemistry was not correlated with $^{89}$Zr-bevacizumab uptake. This was the first clinical study showing a significant correlation between antigen

expression and tumor uptake of the mAb. The fact that VEGF-A is not/hardly expressed in normal tissue, while the antigen might be well accessible for mAbs in tumor tissue, might be favorable factors for finding such a correlation. This observation opens avenues for the use of [89]Zr-bevacizumab-PET for response monitoring in therapeutic strategies aiming to downregulate VEGF-A.

The effect of the HSP90 inhibitor NVP-AUY922 on alteration of VEGF-A status was evaluated in the same study discussed earlier for [89]Zr-trastuzumab in breast cancer (*24*). However, [89]Zr-bevacizumab-PET was not able to predict treatment outcome measured by CT in patients with estrogen-receptor-positive breast cancer (n=6).

### [89]Zr-labeled bevacizumab in lung cancer

Bevacizumab is also used for treatment of non-small cell lung carcinoma and [89]Zr-bevacizumab is a potential predictive imaging biomarker for this patient group. In a pilot study it was evaluated whether tumor uptake of [89]Zr-bevacizumab could be visualized and quantified in 7 patients with lung cancer (*28*). Moreover, in this study the correlation between tumor uptake of [89]Zr-bevacizumab and response to a bevacizumab-based treatment regimen was explored. [89]Zr-bevacizumab PET was performed at day 4 and 7 after injection of 37 MBq [89]Zr-labeled bevacizumab (5 mg), one week prior to start of induction therapy with carboplatin, paclitaxel and bevacizumab (15 mg/kg), followed by bevacizumab maintenance upon non-progression after 4 cycles.

All tumor lesions showed visible [89]Zr-bevacizumab uptake. Tumor-to-blood ratios increased from $1.23 \pm 0.4$ to $2.2 \pm 1.2$ between day 4 and 7 p.i.. Tumor lesions had an approximately four times higher [89]Zr-bevacizumab uptake compared to non-tumor background tissues (muscle, healthy lung and fatty tissue). A positive trend, but no significant correlation, was observed for tumor uptake and progression-free survival and overall survival after combined chemo-immunotherapy.

A limitation of this study design is that no distinction is possible between therapeutic contribution of chemotherapy and immunotherapy, as this is a combined treatment regimen. Therefore, further [89]Zr-bevacizumab-PET studies are required to assess VEGF-target status after combination treatment, as a response predictor for effectiveness of subsequent bevacizumab maintenance therapy.

As all lesions were visualized with a total protein dose of 5 mg [89]Zr-bevacizumab, and no targeting of normal tissues became apparent, there is no indication of an antigen sink for this mAb. A limitation of the current study was that no extra biopsies were obtained to confirm VEGF-A tumor expression as driver for [89]Zr-bevacizumab uptake and therapeutic response. In order to provide more insight in the effect of perfusion, additional imaging of perfusion may be considered in further studies. For such studies, the authors also suggest not to include small tumor lesions in which PET quantification would suffer from partial volume effects.

### [89]Zr-labeled bevacizumab in renal cell carcinoma

Oosting et al. investigated [89]Zr-bevacizumab-PET in patients with metastatic renal cell carcinoma as an imaging modality for treatment evaluation of anti-angiogenic drugs (*29*).

Patients were randomized between treatment with bevacizumab (10 mg/kg intravenously every 14 days) combined with interferon-α (3 million IU, 3 times per week) (n=11) or sunitinib (50 mg orally, daily for 4 weeks followed by 2 weeks off treatment) (n=11), which is a multi-targeted receptor tyrosine kinase inhibitor. At baseline, and 2 and 6 weeks after treatment, PET scans were acquired after administration of 37 MBq [89]Zr-labeled bevacizumab (5 mg).

Tumor lesions were visualized in all patients (in total 125 lesions), including 35 that had not been detected at CT. 19 lesions were outside the field of view of the CT, including 5 brain lesions in 3 patients (two had known brain metastasis). Remarkable interpatient and intrapatient heterogeneity in tumor uptake of [89]Zr-bevacizumab was observed. A strong decrease in tumor uptake of -47.0 % at week 2 was observed for patients on bevacizumab/interferon-α treatment, with an additional change of -9.7 % at week 6. For patients on sunitinib treatment, a mean change in tumor uptake of -14.3 % at week 2 and a rebound of +72.6 % at week 6 was reported (after 2 drug-free weeks).

Change in tumor uptake of [89]Zr-bevacizumab did not correlate with time to progression. Baseline tumor uptake of [89]Zr-bevacizumab corresponded with longer time to progression. Although reduced [89]Zr-bevacizumab tumor uptake after treatment might be caused by saturation due to treatment with unlabeled bevacizumab, other clinical studies have suggested that bevacizumab-induced vascular changes do occur after treatment.

Further studies are required to assess whether baseline tumor uptake of [89]Zr-bevacizumab can be used to predict benefit from anti-angiogenic treatment. Heterogeneity in tumor uptake of [89]Zr-bevacizumab may offer a possibility to differentiate patients groups based on tumor biology and to guide the choice between anti-angiogenic and other treatment strategies.

### [89]Zr-labeled bevacizumab in neuroendocrine tumors

In another feasibility study with [89]Zr-bevacizumab, the effect of everolimus, a mammalian target of rapamycin inhibitor, on tumor uptake was investigated in patients with advanced progressive neuroendocrine tumors (NET) (*30*). As everolimus can reduce VEGF-A production, it was evaluated whether NET lesions can be visualized by [89]Zr-bevacizumab PET and whether tumor uptake of [89]Zr-bevacizumab decreases from baseline to week 2 and 12 during everolimus therapy (10 mg orally once daily). This study was also performed with 37 MBq [89]Zr-labeled bevacizumab (5 mg), with imaging 4 days p.i.. In 4 of 14 patients no tumor lesions could be visualized with [89]Zr-bevacizumab-PET, in the remaining patients only 19% of tumor lesions ≥ 1 cm (63 lesions in total) known by CT were positive at PET, demonstrating variable [89]Zr-bevacizumab tumor uptake in NET patients. [89]Zr-bevacizumab uptake diminished during everolimus treatment with a mean of -7% at 2 weeks and -35% at 12 weeks. Change in tumor uptake correlated with treatment outcome, assessed by CT after 3 months. There was no correlation between baseline tumor uptake and change of tumor size as assessed by CT, indicating that [89]Zr-bevacizumab-PET was not qualified for response prediction before therapy.

Interestingly, in 4 of 14 patients no visual uptake was observed, while no patient had progressive disease after 3 and 6 months of treatment with everolimus. This might indicate that everolimus exerts also other mechanisms of action than just reduction of VEGF-A, or reflect that NETs are slow growing tumors.

### [89]Zr-labeled bevacizumab in pontine glioma

For brain tumors like diffuse intrinsic pontine glioma in children, it is not known whether targeted drugs actually can reach the tumor. Nevertheless, several studies are ongoing to investigate treatment with bevacizumab for this indication. The first report ever on molecular imaging in children, was a feasibility study on the therapeutic potential of bevacizumab and toxic risks, due to VEGF-A expression in normal organs in children with pontine glioma (*31*). 3 patients, aged 6, 7 and 17

years received 0.9 MBq/kg (range 18-37 MBq) $^{89}$Zr–bevacizumab (0.1 mg/kg). Whole body PET scans were obtained at 1, 72 and 144 hours p.i.. Tumor uptake of $^{89}$Zr-bevacizumab was observed in 2 of 3 patients, limited to the T1-MRI contrast-enhanced part of the tumor. These findings suggest that disruption of the blood-brain barrier, as indicated by MRI contrast, is necessary for effective tumor targeting by $^{89}$Zr-bevacizumab. Uptake in normal organs was highest in the liver, followed by the kidneys, lungs and bone marrow. This study illustrates that also in children $^{89}$Zr-immuno-PET is a feasible procedure, and has potential as a response and toxicity predictor for treatment with bevacizumab and other targeted drugs.

### $^{89}$Zr-labeled fresolimumab in high-grade glioma

As indicated before, mAbs might be prevented from reaching tumor lesions in the brain by impermeability of the blood-brain barrier, while tumor targeting is a prerequisite for effective treatment. An appealing target molecule for treatment of high-grade glioma is transforming growth factor β (TGF-β), which functions as a tumor promotor and induces proliferation and metastasis, while suppressing the immune response. TGF-β and its receptors are overexpressed in high-grade glioma and can be targeted with several types of TGF-β inhibitors. Fresolimumab is a mAb capable of neutralizing all mammalian isoforms of TGF-β (i.e. 1, 2 and 3) and has been investigated in phase I trials with patients with melanoma, renal cell carcinoma and in a phase II trial in patients with mesothelioma.

Den Hollander et al. investigated uptake of $^{89}$Zr-fresolimumab in 12 patients with recurrent high-grade glioma and assessed clinical outcome after fresolimumab treatment (*32*). In this study an imaging dose of 37 MBq $^{89}$Zr-fresolimumab (5 mg) was used before start of treatment (5 mg/kg i.v. every 3 weeks) and PET scans were obtained for all patients on day 4 p.i., while 4 patients also received a scan at day 2 p.i..

In all patients uptake of $^{89}$Zr-fresolimumab was observed in brain tumor lesions (n=16), while in 8 patients not all known brain tumor lesions were visualized with $^{89}$Zr-fresolimumab-PET (mostly small lesions, <10 mm on MRI). The three lesions larger than 10 mm that were missed by $^{89}$Zr-fresolimumab-PET were suspected to represent radionecrosis instead of viable tumor tissue (therefore probably lacking TGF-β expression), based on previous irradiation or disappearance on follow-up MRI. Tumor-to-blood ratios increased from day 2 to 4 p.i. in patients who underwent whole body PET scans (n=4), which was considered to be suggestive for tumor-specific TGF-β-driven mAb uptake. All

patients showed progressive disease on fresolimumab treatment, therefore no correlation between tumor uptake of [89]Zr-fresolimumab and clinical response was observed. Because of absence of clinical benefit the study was closed after the first 12 patients.

In conclusion, this study showed that [89]Zr-fresolimumab reaches brain tumor lesions. mAb treatment with TGF-β targeting drugs remains an interesting approach for treatment of high-grade glioma, especially since targeting of brain tumor lesions has been observed by [89]Zr-fresolimumab-PET. It remains unclear to which extent antibody leakage due to disruption of the blood-brain barrier may have caused non-specific uptake of [89]Zr-fresolimumab.

### [89]Zr-labeled cetuximab in colorectal carcinoma

Another target antigen of interest is EGFR, which can be targeted with cetuximab. Binding of cetuximab to EGFR prevents growth factor binding to the receptor, induces receptor internalization, and causes inhibition of the receptor tyrosine kinase activity. In this way cetuximab interferes with cell growth, differentiation and proliferation, apoptosis and cellular invasiveness. Colorectal cancer with RAS wild type can be effectively treated with cetuximab, while it is known that patients with a K-RAS or N-RAS mutation do not respond to anti-EGFR treatment (*33*). Only patients with RAS wild type colorectal cancer are eligible for anti-EGFR treatment. However, even in this selected patient group efficacy of single agent cetuximab remains limited, as clinical benefit is observed in only half of the patients (*34*). Additional growth activating mutations or insufficient tumor targeting may affect clinical efficacy. As EGFR is highly expressed on hepatocytes in normal liver tissue, this might lead to sequestration of anti-EGFR-mAbs shortly after administration and interfere with effective tumor targeting.

Assuming that response to treatment is dependent on uptake of cetuximab in tumor lesions, only patients in whom tumor targeting can be confirmed will be susceptible to treatment. Menke-van der Houwen van Oordt et al. performed a feasibility study in 10 patients with advanced colorectal cancer to investigate biodistribution and tumor uptake of [89]Zr-cetuximab and evaluated [89]Zr-cetuximab as a predictive imaging biomarker (*35*). While blood pool, spleen, kidney and lung activity decreased, uptake in the liver increased during the first 2 days, after which a plateau was reached. Total radioactivity derived from the whole body PET images decreased due to gastro-intestinal excretion, while no excretion via the bladder was observed.

Tumor uptake was visible in 6 of 10 patients, of which 4 had clinical benefit. In a patient with 2 lung lesions, one lesion could be visualized, while the other could not, possibly indicating intra-individual heterogeneity of receptor expression or an effect of tumor size (the lesion not visualized was smaller). Of the remaining 4 out of 10 patients without tumor uptake, 3 had progressive disease and 1 had clinical benefit without visible [89]Zr-cetuximab uptake. Possibly, the amount of cetuximab that reached the latter tumor was insufficient for visual detection, but did induce anti-tumor activity. This example indicates that for appropriate interpretation of tumor uptake-response relationships it is of paramount importance that [89]Zr-cetuximab and unlabeled cetuximab show exactly the same biodistribution.

Altogether these results support further investigations in a larger cohort to assess whether [89]Zr-cetuximab can discriminate between cetuximab responding and non-responding patients. Currently a follow-up study, including dose escalation for patients without visible tumor uptake of [89]Zr-cetuximab and assessment of cetuximab concentrations in tumor biopsies, is ongoing (ClinicalTrials.gov Identifier: NCT02117466). A limitation of [89]Zr-cetuximab-PET reported by the authors is its inability to detect tumor lesions in the liver. In contrast to [89]Zr-trastuzumab, [89]Zr-cetuximab specifically accumulates in normal liver tissue resulting in spillover when quantifying hepatic lesions. Important technical aspects to consider are whether the imaging dose ([89]Zr-labeled cetuximab) and the therapeutic dose (unlabeled cetuximab) show similar biodistribution, and if the degree of similarity can be influenced by the sequence of administration.

In this study patients were treated with a cold therapeutic dose of cetuximab (500 mg/m$^2$), within 2 hours followed by the infusion of 37 MBq [89]Zr-cetuximab (10 mg). It was assumed that within this time frame the therapeutic dose and the imaging dose behave as if injected simultaneously due to slow pharmacokinetics. Sequential administration was chosen to make radiation safety precautions during administration of [89]Zr-cetuximab easier.

Previous studies with ^{111}In-cetuximab (C225) in patients with squamous cell lung carcinoma have indicated a dose-dependent biodistribution, showing liver sequestration of ^{111}In-cetuximab, which decreased with increasing doses of unlabeled cetuximab (up to 300 mg), while tumor uptake increased (*36*). To get better insight in the dose-dependent biodistribution of [89]Zr-cetuximab, Menke-van der Houwen van Oordt et al. administered a scouting dose of 0.1 mg [89]Zr-cetuximab before the dose of unlabeled cetuximab in 3 patients (*35*). Blood

samples 2 and 3 hours post injection of the scouting dose revealed that only <10 % of the injected dose of [89]Zr-cetuximab was left in the blood circulation. When subsequently cold cetuximab (500 mg/m^{2}) was administered, [89]Zr-cetuximab reappeared in the blood, indicating that it can be reversibly extracted, most probably by the liver. On the other hand, the biological half-life of [89]Zr-cetuximab, if administered directly after the unlabeled dose, was comparable with the half-life as reported for unlabeled cetuximab. This indicates that upon such sequential administration [89]Zr-cetuximab indeed reflects the biodistribution of unlabeled cetuximab. Future studies are required to assess to which extent sequential administration of imaging and therapeutic doses influences tumor biodistribution and tumor uptake of [89]Zr-cetuximab.

### [89]Zr-labeled anti-PSMA in prostate cancer

Current clinical challenges in imaging of metastatic prostate cancer include limited sensitivity and specificity to detect early metastases (especially in bone) and active disease and to monitor treatment of metastatic prostate cancer. The humanized mAb huJ591 targets the extracellular domain of prostate-specific membrane antigen (PSMA), a transmembrane glycoprotein expressed by both benign and malignant prostate epithelial cells. Nearly all prostate cancers express PSMA. Upon binding, the huJ591-PSMA complex becomes rapidly internalized. Binding of anti-PSMA mAbs to non-prostate tissue, as the liver, duodenal epithelial (brush border) cells and proximal tubule cells in the kidney, has been observed, as well as binding to tumor-associated neovasculature in other solid malignancies, including clear cell renal carcinoma, colon and breast carcinoma (*37*).

Recently, Pandit-Taskar et al. performed a clinical study with [89]Zr-labeled huJ591 in 50 patients with castrate-resistant metastatic prostate cancer (*38*). Results of the first 10 patients were reported separately, including assessment of optimal imaging time post-injection for lesion detection of [89]Zr-huJ591 PET imaging (*39*). These 10 patients received 4 scans within 8 days after injection. Based on optimal tumor-to-background ratios, the other 40 patients were imaged once at 6-8 days p.i.. This relatively long period post injection required for optimal imaging, may be a practical limitation of [89]Zr-immuno-PET for routine application in diagnosis. Promising alternative ligands for molecular imaging of prostate cancer are smaller molecules as radiolabeled minibodies or urea-based small peptides, although none have been validated in controlled clinical trials for routine clinical use (*40*).

Pandit-Taskar et al. evaluated performance characteristics of [89]Zr-DFO-huJ591 PET/CT for detecting metastases compared to conventional imaging modalities (baseline FDG-PET, ^{99m}Tc-methylenediphosphonate (MDP) bone scans and CT scans) and pathology, to provide evidence for the use of [89]Zr-huJ591 as an imaging biomarker. In a lesion-based analysis [89]Zr-J591 imaging demonstrated superior visualisation of bone lesions relative to conventional imaging, see Figure 3. However, detection of soft tissue lesions was suboptimal. A generalized lower tumor uptake was observed for soft tissue lesions compared to bone lesions. Low uptake was observed in normal bone and considered to be non-specific. Among the possibilities explaining a lower tumor uptake in soft tissue are: lower PSMA expression, absence of tumor in lesions presumed to be disease by CT and FDG-PET scan, or impaired accessibility of PSMA for intact mAbs. For the biopsy-confirmed lesions overall accuracy of [89]Zr-J591 was 95.2% (20/21) for osseous lesions and 60% (15/25) for soft-tissue lesions. No data is provided on [89]Zr-J591 uptake related to PSMA expression in tumor biopsies.

The authors conclude that [89]Zr-huJ591 imaging is able to detect active disease earlier than conventional imaging, making PSMA an attractive target for diagnosis of prostate cancer. Despite the fact that just a small proportion of lesions were biopsied, statistical arguments indicated that [89]Zr-huJ591 imaging detects 50% more bone lesions (occult disease) than bone scan. However, no single imaging modality can serve as gold standard, therefore a known site of disease was defined as any lesions identified by conventional imaging at baseline. Small lesions were most probably missed, while the treatment of patients after imaging was variable, which limits the detection of lesions through follow-up imaging.

In this [89]Zr-immuno-PET study a total mAb dose of 25 mg huJ591 was used, of which 1.7 mg was [89]Zr-labeled (203 MBq). This dose was based on prior studies with ^{111}In-J591 and ^{177}Lu-J591 that showed saturation of PSMA expressed by the normal liver at 25 mg of huJ591 (41). A dose-dependent uptake in the liver with increasing mAb dose was observed, and optimal trade off was reached at a mAb dose of 25 mg. The unlabeled dose of huJ591 was administered intravenously within 5 minutes, immediately followed by injection of [89]Zr-huJ591 within 1 minute.
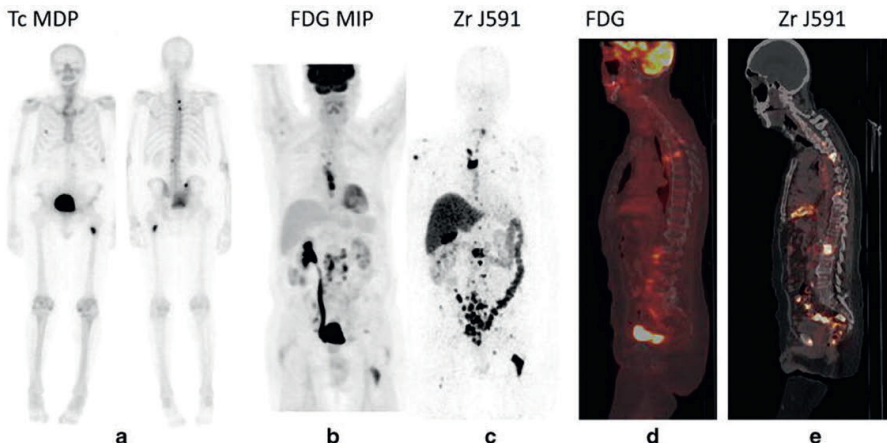
Figure 3. [89]Zr-huJ591-PET and conventional imaging modalities of a patient with rising prostate specific antigen. ^{99m}Tc-MDP bone scan shows only a few lesions. FDG-PET shows nodal disease in the thorax, retroperitoneum, and pelvic region and a few bone lesions in the spine. Overall more bone lesions were seen on [89]Zr-huJ591-PET than on FDG-PET, including multiple lesions in vertebrae, pelvic bones, ribs and humerus. Targeting was also seen to the retroperitoneal and pelvic lymph nodes by [89]Zr-huJ59-PET.

(A) Anterior and posterior ^{99m}Tc-MDP bone scan
(B) FDG-PET maximum intensity projection
(C) [89]Zr-huJ591 PET
(D) FDG-PET sagittal fused image
(E) [89]Zr-hu J591 PET sagittal fused image

Reprinted with permission from "Pandit-Taskar, N., O'Donoghue, J.A., Beylergil, V., Lyashchenko, S., Ruan, S., Solomon, S.B., et al. (2014) [89]Zr-huJ591 immuno-PET imaging in patients with advanced metastatic prostate cancer. *Eur. J. Nucl. Med. Mol. Imaging.* 41, 2093-2105. doi: 10.1007/s00259-014-2830-7"

## [89]Zr-labeled anti-MSLN in pancreatic and ovarian carcinoma

For several tumor types, such as pancreatic and ovarian carcinoma, no important drug targets are available yet for targeted therapy. A promising approach is the exploitation of tumor-specific membrane proteins, even those without a known role in oncogenesis, as targets for delivery of potent drugs by ADCs. In this respect, a potential target molecule, with largely unknown biological function, is membrane-bound surface glycoprotein mesothelin (MSLN). It is minimally expressed by normal mesothelial cells, lining pleural, pericardial and peritoneal surfaces. Besides in mesothelioma, it is also highly overexpressed in 80-100% of pancreatic and ovarian cancers (and some other cancers). In preclinical studies with MSLN-expressing tumor bearing mice, [89]Zr-anti-MSLN antibody MMOT0530A showed progressive and antigen-specific tumor uptake with micro-PET (*42*).

Therefore, Lamberts et al. evaluated [89]Zr-labeled MMOT0530A as a predictive imaging biomarker for treatment (in a phase I setting) with the ADC

DMOT4039A, containing the MSLN-antibody MMOT0530A combined with the cytotoxic agent monomethyl auristatin E (43). For such an approach either the ADC itself can be labeled with [89]Zr or the corresponding "naked" mAb, if available for human use. Labeling of the mAb part of the ADCs with [89]Zr is well possible, but requires advanced analytical tools to prove that labeling is performed inertly. Assuming that both types of conjugates demonstrate similar biodistribution, which is a research question as such, PET imaging of the target will provide insight into drug distribution (tissue exposure, but also expression of the target and internalization of the antibody). Ideally, clinical [89]Zr-immuno-PET studies with the "naked" mAb are performed before resources are put in the development of an ADC.

The aim of this imaging study was to assess biodistribution and tumor uptake, and the relationship between tumor uptake and MSLN expression, as well as response to treatment. Uptake in normal tissues was as expected, and did not indicate specific uptake, except for high hepatic uptake of [89]Zr-MMOT0530A. This might be due to normal hepatic catabolism of the antibody, maybe slightly elevated by complex formation of the mAb with MSLN antigen shed into the circulation, as MSLN is not expressed on normal liver. Nevertheless, the uptake level in liver was similar to that of other antibodies such as trastuzumab and huJ591. Significant clinical toxicity, reported as dose limiting toxicity, were hypophosphatemia and hyperglycaemia and liver function abnormalities occurred in less than 10% of these patients. Tumor uptake of [89]Zr-MMOT0530A was observed in 37 tumor lesions in 11 patients with pancreatic cancer and 4 patients with ovarian cancer, while 6 measurable tumor lesions visible on diagnostic CT in 4 patients were not detected by [89]Zr-immuno-PET. Within patients a mean 2.4 ± 1.1-fold difference in uptake between tumor lesions was observed, indicating interlesional heterogeneity of tumor uptake.

Tumor uptake of [89]Zr-MMOT0530A was correlated with MSLN expression levels determined with IHC scores (6 patients with pancreatic cancer and 4 patients with ovarian cancer). No correlation was found when the two tumor types were analyzed separately. Tumor uptake of [89]Zr-MMOT0530A was not correlated with progression free survival, on both patient and lesion-based analysis.

The imaging dose for this study was considered to be sufficient, since the amount of tracer still present at 7 days p.i. was enough to clearly visualize the circulation. A first cohort of two patients received 37 MBq [89]Zr-anti-MSLN (1 mg) and were imaged at days 2, 4 and 7 p.i.. Patients in the second cohort (n=10)

received a total protein dose of 10 mg mAb, administered as a co-infusion. The biological half-life of [89]Zr-anti-MSLN in cohort 1 was shorter than in cohort 2, most likely due to faster antibody clearance related to small amounts of shed MSLN antigen present in the circulation. Bioavailability of the imaging dose in the second cohort was considered sufficient to evaluate tumor uptake.

This was the first study aiming the use of [89]Zr-immuno-PET as an imaging biomarker for whole body target expression and organs at risk for toxicity, to ultimately guide dosing, confirm delivery, and predict efficacy of the ADC. At this stage of development, however, [89]Zr-immuno-PET was not able yet to add valuable information for individualized treatment decisions.

## [89]Zr-labeled anti-CD20 mAbs in B cell lymphoma

Especially when using mAbs for radioimmunotherapy (RIT), [89]Zr-immuno-PET may be applied to predict toxicity by assessment of biodistribution. This information may enable individualized treatment by optimizing dose schedules to limit unnecessary toxicity for patients.

RIT is used in the treatment of lymphoma, as this type of cancer is highly radiosensitive. More than 90% of B-cell non-Hodgkin lymphoma (NHL) express CD20, making it an attractive target for treatment. The transmembrane phosphoprotein CD20 is also expressed on mature B cells. The biological function of CD20 is still unclear. CD20 is highly expressed on the cell surface and is not rapidly internalized after antibody binding. The anti-CD20 antibody rituximab is widely used in both first-line, as well as subsequent treatment lines for patients with B-cell NHL. Anti-CD20 based RIT with yttrium-90 (^{90}Y)-labeled-ibritumomab tiuxetan is currently approved for treatment of relapsed and refractory NHL (44). Bone marrow toxicity of RIT is dose-limiting, and especially patients with bone marrow infiltration may suffer excessive hematotoxicity.

Rizvi et al. published a clinical study on [89]Zr-immuno-PET to predict toxicity of RIT in NHL patients in order to guide individualized dose optimization (45). The aim of this study was to assess whether pre-therapy scout scans with [89]Zr-ibritumomab tiuxetan can be used to predict biodistribution of ^{90}Y-ibritumomab tiuxetan and the dose limiting organ during therapy. Patients received standard treatment of 250 mg/m$^2$ rituximab 1 week before and on the same day prior to both ^{90}Y-and/or [89]Zr-ibritumomab tiuxetan (70 MBq) administrations. The correlation between predicted pre-therapy and therapy organ absorbed doses as based on [89]Zr-ibritumomab tiuxetan images was high. Biodistribution of [89]Zr-

ibritumomab tiuxetan was not influenced by simultaneous therapy with ^{90}Y-ibritumomab tiuxetan. Pre-therapy scout scans with [89]Zr-ibritumomab tiuxetan can therefore be used to predict biodistribution and dose-limiting organ during therapy. These results indicate that [89]Zr-immuno-PET may guide safe individualized therapy by optimizing the radioimmunotherapy dose of ^{90}Y-ibritumomab tiuxetan.

The standard treatment with a high amount of cold rituximab before anti-CD20 based RIT, also administered to the patients in the study of Rizvi et al., is common practice to enhance the therapeutic index for RIT. It is thought that the usage of excess unlabeled mAb before RIT may reduce toxicity, in particular bone marrow toxicity. Preloading with unlabeled mAb might prevent normal tissue toxicity by providing a more predictable biodistribution of ^{90}Y-labeled mAb, decreasing clearance rates, and prolonging its circulation half-life. This preload is assumed to clear the peripheral blood of circulating CD20-positive B cells and enhance tumor targeting of the ^{90}Y-labeled antibody to tumor cells. However, supportive data for this approach is limited. It is unclear whether the preload may block subsequently administered ^{90}Y-labeled anti-CD20 antibody, which might impair therapeutic effects.

Muylle et al. performed a study with [89]Zr-rituximab-PET to explore the influence of a preload with unlabeled rituximab in five patients with CD20-positive B-cell lymphoma, scheduled for subsequent RIT with ^{90}Y-labeled rituximab (*46*). The aim of the study was to compare the distribution of [89]Zr-rituximab without and with a preload of unlabeled rituximab (within the same patient) to assess the impact on tumor targeting and radiation dose of subsequent radioimmunotherapy with ^{90}Y-labeled rituximab. PET scans were obtained at baseline after administration of 111 MBq [89]Zr-labeled rituximab (10 mg). After 3 weeks, a standard preload of unlabeled rituximab (250 mg/m$^2$) was administered, immediately followed by administration of 10 mg [89]Zr-rituximab, and PET scans were acquired.

For the patients with B cell depletion (n=3) tumor uptake without a preload was consistently higher. In patients with preserved circulating B cells (n=2), 3 lesions showed less or no uptake without a preload, while other lesions showed higher uptake. The authors explain higher tumor uptake upon preload by improved biodistribution and prevention of sequestration of [89]Zr-rituximab in the 'antigen-sink', consisting of CD20-positive B cells in the circulation and in the spleen. Impaired targeting of other tumor sites, however, is explained by partial saturation with unlabeled rituximab.

For patients with preserved circulating CD20-positive B-cells (n = 2) without a preload of unlabeled rituximab, an increase in whole-body radiation dose of 59% and 87% was observed mainly due to increased uptake in the spleen, see Figure 4. The effective dose of [89]Zr-rituximab was 0.50 milliSievert (mSv)/MBq without a preload and 0.41 mSv/MBq with a preload.

These results suggest that administration of the standard preload of unlabeled rituximab impairs tumor targeting of [89]Zr-rituximab in patients with B-cell depletion, due to previous treatment with rituximab. These data suggest that common practice of preloading with unlabeled rituximab before RIT should be re-evaluated and reconsidered.
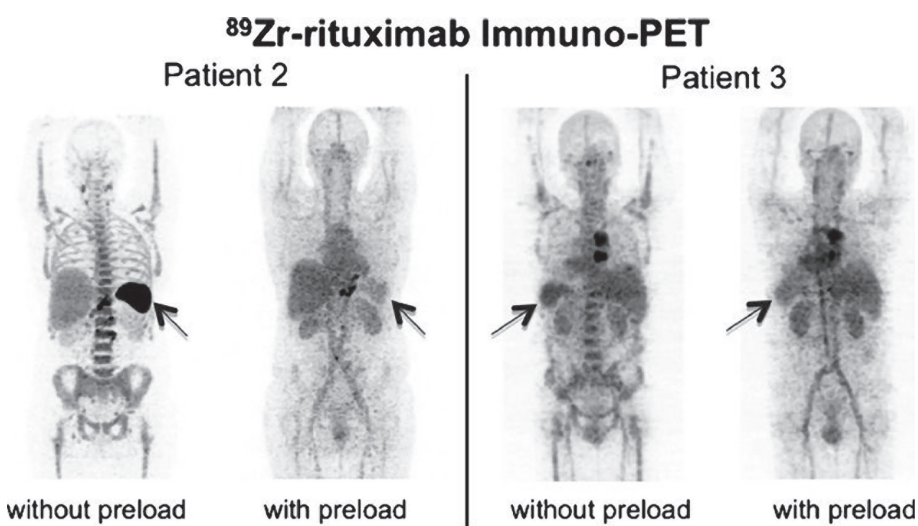


Figure 4. [89]Zr-rituximab-PET images obtained 6 days after injection

(A) Patient 2 without B cell depletion, anterior view
(B) Patient 3 with B cell depletion, posterior view

Reprinted with permission from "Muylle, K., Flamen, P., Vugts, D.J., Guiot, T., Ghanem, G., Meuleman, N., et al. (2015). Tumour targeting and radiation dose of radioimmunotherapy with ^{90}Y-rituximab in CD20+ B-cell lymphoma as predicted by [89]Zr-rituximab immuno-PET: impact of preloading with unlabelled rituximab. *Eur. J. Nucl. Med. Mol. Imaging.* 42, 1304-1314. doi: 10.1007/s00259-015-3025-6"

## CONCLUSIONS AND FUTURE DIRECTIONS

In clinical trials with [89]Zr-immuno-PET, two requirements should be met in order to realize its full potential. One requirement is that the biodistribution of the [89]Zr-mAb (imaging dose) should reflect the biodistribution of the drug during

treatment (therapeutic dose). An important pitfall to eliminate is a "false negative" [89]Zr-immuno-PET due to absence of tumor uptake of the imaging dose, while there is tumor targeting of the therapeutic dose of unlabeled mAb. This situation may occur in case of expression of target antigen on normal tissue, or in case of a large tumor load with antigen expression. This causes an "antigen sink" that absorbs the tracer dose, leaving insufficient [89]Zr-mAb to target all tumor lesions. Therefore, for each mAb, information should be obtained to assess whether a dose-dependent correlation between imaging dose and tumor uptake exists. Preferably a pilot study with different dose levels, within the same patient, is used to define the optimal [89]Zr-mAb dose for imaging, i.e. the dose that reflects the therapeutic dose best. With respect to this, in case of co-administration of [89]Zr-labeled and cold mAb, it should also be confirmed whether simultaneous administration is needed, or whether sequential administration immediate after each other is allowed.

Another requirement is that tumor uptake of the [89]Zr-mAb reflects specific, antigen-mediated, tumor targeting. Next to specific uptake, also non-antigen mediated tumor uptake can occur, possibly caused by enhanced permeability and retention in tumor tissue. Even when tracer uptake is visualized in the tumor, no biological effect can be expected if tumor uptake is not primarily antigen-mediated (a "false positive" [89]Zr-immuno-PET). Although no definitive proof has been reported that [89]Zr-immuno-PET reflects specific, antigen-mediated binding, two clinical studies have reported a correlation between tumor uptake on PET and target expression in biopsies (*26, 42*). These results support the assumption that tumor uptake on [89]Zr-immuno-PET is primarily driven by antigen-mediated targeting. This would allow the use of [89]Zr-immuno-PET as an imaging biomarker to assess target expression, as well as tumor targeting. However, for every mAb-antigen combination this has to be confirmed. In order to evaluate to which extent tumor uptake is driven by nonspecific and/or specific binding, studies correlating tumor uptake to target expression in biopsies, as well as exploration of kinetic modelling, may provide further insight.

Assuming these two crucial requirements are met, [89]Zr-immuno-PET can be expected to predict toxicity and response to treatment.

For RIT, it was shown that biodistribution of [89]Zr-rituximab can be used to predict biodistribution and the dose-limiting organ for subsequent treatment with ^{90}Y-ibritumomab tiuxetan (*44*). This allows for future application of [89]Zr-immuno-PET for individualized doze optimization of RIT with the aim to reduce the risk

for toxicity. However, so far no clinical studies reported that [89]Zr-immuno-PET predicted toxicity of mAb or mAb conjugate treatment, or guided drug development in early stages.

Prediction of response to treatment for mAbs, is based on the assumption that the drug can only be effective if the target antigen is reached. Although this is no guarantee for efficacy, as therapy failure may occur due to inadequate dosing of the mAb or intrinsic resistance mechanisms. To improve prediction of efficacy of treatment, confirmation of tumor targeting of the drug can be combined with early response assessment. This combined approach may be able to predict whether adequate tumor targeting is followed by sufficient cytotoxicity. Clinical application of molecular imaging to guide individualized treatment may ideally consist of the following 3-step approach:

1.  Tumor detection and staging of the disease with conventional imaging (e.g. FDG-PET/diagnostic CT)
2.  Assessment of tumor targeting of the drug with molecular imaging (e.g. [89]Zr-immuno-PET)
3.  Early response assessment on treatment with conventional imaging (e.g. FDG-PET/diagnostic CT)

So far, the ZEPHIR study is the only study utilizing this 3-step approach, using an optimized [89]Zr-mAb dose for imaging, and a visual classification for tumor uptake (*25*). This study reported that molecular imaging combined with early response assessment is able to predict response to treatment with T-DM1 in patients with HER2-positive breast cancer, opening avenues to cost-effectiveness studies and individualized treatment protocols. Still, this promising result can possibly benefit from improving criteria of positive uptake by quantitative analysis.

Currently, no standardized scale for visual scoring of [89]Zr-immuno-PET is available, as opposed to scoring FDG-PET/CT scans by the Deauville criteria (*47*). Imaging procedures, including data analysis and measurements of tumor uptake should be standardized and validated in order to use [89]Zr-immuno-PET in clinical practice. As an example, problems with partial volume effects should be solved. Ideally, by linking imaging data with corresponding clinical outcome of a large set of patients, a criterion for positive tumor uptake can be defined.

Overall, these initial clinical trials have provided indications of the potential of [89]Zr-immuno-PET as an imaging biomarker to assess target expression, as well as tumor targeting. The first results supporting application of molecular imaging

for prediction of toxicity for RIT and response prediction for treatment with an ADC, form an important first step towards individualized treatment.

## ACKNOWLEDGMENTS

# REFERENCES

1.  Feugier P, Van Hoof A, Sebban C, et al. Long-term results of the R-CHOP study in the treatment of elderly patients with diffuse large B-cell lymphoma: a study by the Groupe d'Etude des Lymphomes de l'Adulte. *J Clin Oncol*. 2005;23:4117-4126.

2.  Peeters M, Karthaus M, Rivera F, Terwey J-H, Douillard J-Y. Panitumumab in Metastatic Colorectal Cancer: The Importance of Tumour RAS Status. *Drugs*. 2015;75:731-748.

3.  Sliwkowski MX, Mellman I. Antibody therapeutics in cancer. *Science*. 2013;341:1192-1198.

4.  Evans JB, Syed BA. From the analyst's couch: Next-generation antibodies. *Nat Rev Drug Discov*. 2014;13:413-414.

5.  Reichert JM. Antibodies to watch in 2016. *MAbs*. 2016;8:197-204.

6.  Van Dongen GA, Huisman MC, Boellaard R, et al. 89Zr-immuno-PET for imaging of long circulating drugs and disease targets: why, how and when to be applied? *Q J Nucl Med Mol Imaging*. 2015;59:18-38.

7.  Verel I, Visser GWM, Boellaard R, Walsum MS, Snow GB, Dongen GAMS van. 89Zr Immuno-PET: Comprehensive Procedures for the Production of 89Zr-Labeled Monoclonal Antibodies. *J Nucl Med*. 2003;44:1271-1281.

8.  Vosjan MJWD, Perk LR, Visser GWM, et al. Conjugation and radiolabeling of monoclonal antibodies with zirconium-89 for PET imaging using the bifunctional chelate p-isothiocyanatobenzyl-desferrioxamine. *Nat Protoc*. 2010;5:739-743.

9.  Perk LR, Vosjan MJWD, Visser GWM, et al. p-Isothiocyanatobenzyl-desferrioxamine: a new bifunctional chelate for facile radiolabeling of monoclonal antibodies with zirconium-89 for immuno-PET imaging. *Eur J Nucl Med Mol Imaging*. 2010;37:250-259.

10. Makris NE, Boellaard R, Visser EP, et al. Multicenter harmonization of 89Zr PET/CT performance. *J Nucl Med*. 2014;55:264-267.

11. Börjesson PKE, Jauw YWS, Boellaard R, et al. Performance of immuno-positron emission tomography with zirconium-89-labeled chimeric monoclonal antibody U36 in the detection of lymph node metastases in head and neck cancer patients. *Clin Cancer Res*. 2006;12:2133-2140.

12. Börjesson PKE, Jauw YWS, de Bree R, et al. Radiation dosimetry of 89Zr-labeled chimeric monoclonal antibody U36 as used for immuno-PET in head and neck cancer patients. *J Nucl Med*. 2009;50:1828-1836.

13. Tijink BM, Buter J, de Bree R, et al. A phase I dose escalation study with anti-CD44v6 bivatuzumab mertansine in patients with incurable squamous cell carcinoma of the head and neck or esophagus. *Clin Cancer Res*. 2006;12:6064-6072.

14. Bree R de, Roos JC, Quak JJ, Hollander W den, Snow GB, Dongen GA van. Radioimmunoscintigraphy and biodistribution of technetium-99m-labeled monoclonal antibody U36 in patients with head and neck cancer. *Clin Cancer Res*. 1995;1:591-598.

15. Colnot DR, Quak JJ, Roos JC, et al. Phase I Therapy Study of 186Re-Labeled Chimeric Monoclonal Antibody U36 in Patients with Squamous Cell Carcinoma of the Head and Neck. *J Nucl Med*. 2000;41:1999-2010.

16. Stroomer JW, Roos JC, Sproll M, et al. Safety and biodistribution of 99mTechnetium-labeled anti-CD44v6 monoclonal antibody BIWA 1 in head and neck cancer patients. *Clin Cancer Res*. 2000;6:3046-3055.

17. Moja L, Tagliabue L, Balduzzi S, et al. Trastuzumab containing regimens for early breast cancer. *Cochrane Database Syst Rev*. 2012:CD006243.

18. Gong J, Liu T, Fan Q, et al. Optimal regimen of trastuzumab in combination with oxaliplatin/capecitabine in first-line treatment of HER2-positive advanced gastric cancer (CGOG1001): a multicenter, phase II trial. *BMC Cancer*. 2016;16:68.

19. Leone F, Perissinotto E, Cavalloni G, et al. Expression of the c-ErbB-2/HER2 proto-oncogene in normal hematopoietic cells. *J Leukoc Biol*. 2003;74:593-601.

20. Tsé C, Gauchez A-S, Jacot W, Lamy P-J. HER2 shedding and serum HER2 extracellular domain: biology and clinical utility in breast cancer. *Cancer Treat Rev*. 2012;38:133-142.

21.  Lindström LS, Karlsson E, Wilking UM, et al. Clinically used breast cancer markers such as estrogen receptor, progesterone receptor, and human epidermal growth factor receptor 2 are unstable throughout tumor progression. *J Clin Oncol*. 2012;30:2601-2608.

22.  Dijkers EC, Oude Munnink TH, Kosterink JG, et al. Biodistribution of 89Zr-trastuzumab and PET imaging of HER2-positive lesions in patients with metastatic breast cancer. *Clin Pharmacol Ther*. 2010;87:586-592.

23.  Oude Munnink TH, Dijkers EC, Netters SJ, et al. Trastuzumab pharmacokinetics influenced by extent human epidermal growth factor receptor 2-positive tumor load. *J Clin Oncol*. 2010;28:e355-356; author reply e357.

24.  Gaykema SBM, Schröder CP, Vitfell-Rasmussen J, et al. 89Zr-trastuzumab and 89Zr-bevacizumab PET to evaluate the effect of the HSP90 inhibitor NVP-AUY922 in metastatic breast cancer patients. *Clin Cancer Res*. 2014;20:3945-3954.

25.  Gebhart G, Lamberts LE, Wimana Z, et al. Molecular imaging as a tool to investigate heterogeneity of advanced HER2-positive breast cancer and to predict patient outcome under trastuzumab emtansine (T-DM1): the ZEPHIR trial. *Ann Oncol*. 2016;27:619-624.

26.  Gaykema SBM, Brouwers AH, Lub-de Hooge MN, et al. 89Zr-bevacizumab PET imaging in primary breast cancer. *J Nucl Med*. 2013;54:1014-1018.

27.  Nagengast WB, Hooge MNL, van Straten EME, et al. VEGF-SPECT with ^{111}In-bevacizumab in stage III/IV melanoma patients. *Eur J Cancer*. 2011;47:1595-1602.

28.  Bahce I, Huisman MC, Verwer EE, et al. Pilot study of (89)Zr-bevacizumab positron emission tomography in patients with advanced non-small cell lung cancer. *EJNMMI Res*. 2014;4:35.

29.  Oosting SF, Brouwers AH, van Es SC, et al. 89Zr-bevacizumab PET visualizes heterogeneous tracer accumulation in tumor lesions of renal cell carcinoma patients and differential effects of antiangiogenic treatment. *J Nucl Med*. 2015;56:63-69.

30.  van Asselt SJ, Oosting SF, Brouwers AH, et al. Everolimus Reduces (89)Zr-Bevacizumab Tumor Uptake in Patients with Neuroendocrine Tumors. *J Nucl Med*. 2014;55:1087-1092.

31.  van Zanten SV, Jansen M, van Vuurden D, et al. Innovative molecular imaging in children with diffuse intrinsic pontine glioma. *Neuro-Oncology*. 2013:15:132. Suppl 3.

32.  den Hollander MW, Bensch F, Glaudemans AWJM, et al. TGF-β Antibody Uptake in Recurrent High-Grade Glioma Imaged with 89Zr-Fresolimumab PET. *J Nucl Med*. 2015;56:1310-1314.

33.  Van Cutsem E, Köhne C-H, Láng I, et al. Cetuximab plus irinotecan, fluorouracil, and leucovorin as first-line treatment for metastatic colorectal cancer: updated analysis of overall survival according to tumor KRAS and BRAF mutation status. *J Clin Oncol*. 2011;29:2011-2019.

34.  Menke-van der Houven van Oordt CW, Gootjes EC, Huisman MC, et al. 89Zr-cetuximab PET imaging in patients with advanced colorectal cancer. *Oncotarget*. 2015;6:30384-30393.

35.  Divgi CR, Welt S, Kris M, et al. Phase I and imaging trial of indium 111-labeled anti-epidermal growth factor receptor monoclonal antibody 225 in patients with squamous cell lung carcinoma. *J Natl Cancer Inst*. 1991;83:97-104.

36.  Chang SS. Overview of prostate-specific membrane antigen. *Rev Urol*. 2004;6 Suppl 10:S13-18.

37.  Pandit-Taskar N, O'Donoghue JA, Durack JC, et al. A Phase I/II Study for Analytic Validation of 89Zr-J591 ImmunoPET as a Molecular Imaging Agent for Metastatic Prostate Cancer. *Clin Cancer Res*. 2015;21:5277-5285.

38.  Pandit-Taskar N, O'Donoghue JA, Beylergil V, et al. [89]Zr-huJ591 immuno-PET imaging in patients with advanced metastatic prostate cancer. *Eur J Nucl Med Mol Imaging*. 2014;41:2093-2105.

39.  Viola-Villegas NT, Sevak KK, Carlin SD, et al. Noninvasive Imaging of PSMA in prostate tumors with (89)Zr-Labeled huJ591 engineered antibody fragments: the faster alternatives. *Mol Pharm*. 2014;11:3965-3973.

40.  Morris MJ, Divgi CR, Pandit-Taskar N, et al. Pilot trial of unlabeled and indium-111-labeled anti-prostate-specific membrane antigen antibody J591 for castrate metastatic prostate cancer. *Clin Cancer Res*. 2005;11:7454-7461.

41.  ter Weele EJ, Terwisscha van Scheltinga AGT, Kosterink JGW, et al. Imaging the distribution of an antibody-drug conjugate constituent targeting mesothelin with [89]Zr and IRDye 800CW in mice bearing human pancreatic tumor xenografts. *Oncotarget*. 2015;6:42081-42090.

42. Lamberts LE, Menke-van der Houven van Oordt CW, ter Weele EJ, et al. ImmunoPET with Anti-Mesothelin Antibody in Patients with Pancreatic and Ovarian Cancer before Anti-Mesothelin Antibody-Drug Conjugate Treatment. *Clin Cancer Res*. 2016;22:1642-1652.

43. Mondello P, Cuzzocrea S, Navarra M, Mian M. 90 Y-ibritumomab tiuxetan: a nearly forgotten opportunityr. *Oncotarget*. 2016;7:7597-7609.

44. Rizvi SNF, Visser OJ, Vosjan MJWD, et al. Biodistribution, radiation dosimetry and scouting of 90Y-ibritumomab tiuxetan therapy in patients with relapsed B-cell non-Hodgkin's lymphoma using 89Zr-ibritumomab tiuxetan and PET. *Eur J Nucl Med Mol Imaging*. 2012;39:512-520.

45. Muylle K, Flamen P, Vugts DJ, et al. Tumour targeting and radiation dose of radioimmunotherapy with (90)Y-rituximab in CD20+ B-cell lymphoma as predicted by (89)Zr-rituximab immuno-PET: impact of preloading with unlabelled rituximab. *Eur J Nucl Med Mol Imaging*. 2015;42:1304-1314.

46. Meignan M, Gallamini A, Haioun C, Polliack A. Report on the Second International Workshop on interim positron emission tomography in lymphoma held in Menton, France, 8-9 April 2010. *Leuk Lymphoma*. 2010;51:2171-2180.

# PART II

# Validation of $^{89}$Zr-immuno-PET
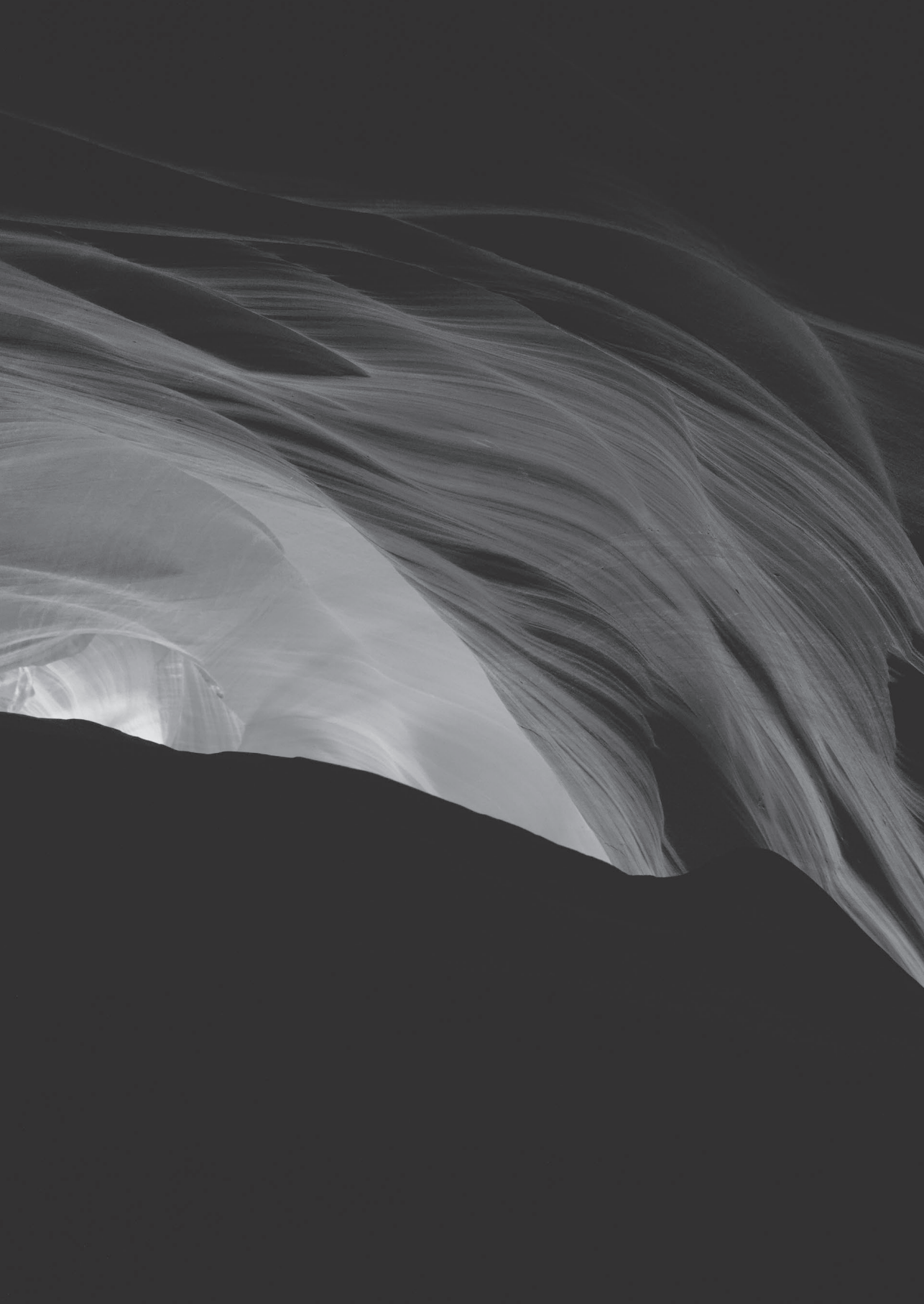
CHAPTER 5

# Noise induced variability of immuno-PET with Zirconium-89-labeled antibodies:

# an analysis based on count-reduced clinical images

Yvonne W.S. Jauw
Dennis F. Heijtel
Josée M. Zijlstra
Otto S. Hoekstra
Henrica C.W. de Vet
Danielle J. Vugts
Henk M. Verheul
Ronald Boellaard
Sonja Zweegman
Guus A.M.S. van Dongen
C. Willemien Menke-van der Houven van Oordt
Adriaan A. Lammertsma
Marc C. Huisman

# ABSTRACT

**Purpose:** Positron emission tomography (PET) with $^{89}$Zirconium (Zr-89)-labeled antibodies can be used for *in vivo* quantification of antibody uptake. Knowledge about measurement variability is required to ensure correct interpretation. However, no clinical studies have been reported on measurement variability of Zr-89-immuno-PET. As variability due to low signal-to-noise is part of the total measurement variability, the aim of this study was to assess noise induced variability of Zr-89-immuno-PET using count-reduced clinical images.

**Procedures:** Data were acquired from three previously reported clinical studies with $^{89}$Zr-antiCD20 (74 MBq, n=7), $^{89}$Zr-antiEGFR (37 MBq, n=7) and $^{89}$Zr-antiCD44 (37 MBq, n=13), with imaging obtained 1 to 6 days post injection (D0-D6). Volumes of interest (VOIs) were manually delineated for liver, spleen, kidney, lung, brain and tumor. For blood pool and bone marrow fixed-size VOIs were used. Original PET list mode data were split and reconstructed, resulting in two count-reduced images at 50% of the original injected dose (e.g. 37MBq$_{74inj}$). Repeatability coefficients (RC) were obtained from Bland-Altman analysis on standardized uptake values (SUV) derived from VOIs applied to these images.

**Results:** The RC for the combined manually delineated organs for $^{89}$Zr-antiCD20 (37MBq$_{74inj}$) increased from D0 to D6 and was less than 6% at all time points. Blood pool and bone marrow had higher RC, up to 43% for 37 MBq$_{74inj}$ at D6. For tumor, the RC was up to 42% for $^{89}$Zr-antiCD20 (37 MBq$_{74inj}$). For $^{89}$Zr-antiCD20, (18 MBq$_{74inj}$), $^{89}$Zr-antiEGFR (18 MBq$_{37inj}$) and $^{89}$Zr-antiCD44 (18 MBq$_{37inj}$) measurement variability was independent of the investigated antibody.

**Conclusions:** Based on this study, noise induced variability results in a RC for Zr-89-immuno-PET (37MBq) around 6% for manually delineated organs combined, increasing up to 43% at D6 for blood pool and bone marrow, assuming similar biodistribution of antibodies. The signal-to-noise ratio leads to tumor RC up to 42%.

# INTRODUCTION

Antibody imaging is of interest to improve efficacy and limit toxicity of antibody treatment by providing a predictive imaging biomarker for antibody uptake. Zr-89-immuno-PET can be used for *in vivo* quantification of antibody biodistribution and tumor uptake (*1,2*). Knowledge about measurement variability is required for clinical application. Usually, a test-retest study is performed for novel tracers to assess repeatability. However, for Zr-89-immuno-PET, repeatability is unknown. A classical test-retest study design with two tracer injections is challenging in case of Zr-89-immuno-PET because of the long half-life of Zr-89 (78.4 hours). This requires more than 10 days between two injections to have less than 10% of the radioactivity due to the first injection remaining in the body. In addition, radiation exposure is significant (0.5 mSv/MBq) (*3*). To date, most clinical PET studies using Zr-89-labeled mAbs are performed with an injected dose of 37 MBq, resulting in an effective dose of 18.5 mSv. We hypothesize that the relatively low signal to noise ratio for Zr-89-immuno-PET acquisition (due to the low injected dose and low positron abundance of Zr-89) results in a considerable source of measurement variability.

The primary objective of this study was therefore to assess noise induced variability of quantitative uptake measures derived from Zr-89-immuno-PET for an injected dose of 37 MBq using count-reduced images.

For this purpose, previously acquired clinical datasets can be used to assess noise induced variability at 50% of the original injected dose. Raw PET data (list mode data) can be split in two equal parts (Figure 1). The split list mode data can be reconstructed into two count-reduced images (*4*). Each of the two count-reduced images is considered to be a count statistically independent estimate of an image that would have been obtained with 50% of the original injected dose for the same scan time. For example, an original image acquired with an injected dose of 74 MBq results in two count-reduced images representing an injected dose of 37 MBq (denoted as 37MBq$_{74inj}$). The count reduced images are not independent with respect to other factors such as procedural variations or scanner drift.

In addition, we hypothesize that noise induced variability is independent of the investigated mAb, therefore the secondary objective was to investigate clinical datasets with three different Zr-89-labeled mAbs. Finally, the tertiary objective was to assess noise induced variability of Zr-89-immuno-PET for an injected dose of 18 MBq. This is the lowest injected dose used in clinical Zr-89-immuno-PET

studies for non-oncological indications, e.g. rheumatoid arthritis and multiple sclerosis (*5,6*), as further limiting radiation exposure (to <10 mSv) is necessary for these patient categories.

Knowledge of measurement variability is of interest as a small measurement error is required for the detection of even small changes over time (e.g. response evaluation, within patients). In the current study, we assessed noise induced variability as source of measurement error (expressed as repeatability coefficient (RC) in %). For clinical relevance, assessment of reliability is important as this indicates the ability to divide patients in groups of interest despite measurement errors (e.g. response prediction, between patients). Therefore an explorative reliability analysis was performed (expressed as intraclass correlation coefficients (ICC)) reflecting the contribution of this source of measurement variability to the observed differences (total variance) in biodistribution and tumor uptake in these datasets.

Potential clinical applications of Zr-89-immuno-PET include use as a quantitative imaging biomarker to assess antibody uptake in normal tissue and tumor to guide individualized treatment and/or drug development (*3*).

## MATERIALS AND METHODS

### Data sources

Original list mode data were taken from three clinical [89]Zr-immuno-PET studies: [89]Zr-antiCD20 mAb in non-Hodgkin lymphoma (*7*), [89]Zr-anti-epidermal growth factor receptor (EGFR) mAb in colorectal cancer (*8*), and [89]Zr-antiCD44 mAb in solid tumors (*9*). The original injected dose was 74 MBq for [89]Zr-antiCD20 mAb, 37 MBq for [89]Zr-antiEGFR mAb and 37 MBq for [89]Zr-antiCD44 mAb. Scans were scheduled at the following time points: 1, 72 and 144 h p.i. (D0, D3, D6) for [89]Zr-antiCD20 mAb and [89]Zr-antiEGFR mAb, and 1, 24 and 96 h p.i. (D0, D1, D4) for [89]Zr-antiCD44 mAb. Study procedures, including image acquisition protocols, have been reported previously (*7-9*). All data were acquired on a Philips Gemini 64 or Ingenuity 128 PET/CT scanner (Philips Healthcare). The number of bed positions (for a scan trajectory of mid-thigh to vertex of the skull) was 10-12, with a 50% bed overlap. Data were acquired for 5 minutes per bed. Data were normalized, corrected for decay, randoms, dead time, scatter and attenuation and reconstructed using 3D BLOB-OS-TF (3 iterations, 33 subsets). A 7mm Gaussian post

reconstruction filter was applied, in line with the recommendation for multicenter Zr-89-immuno-PET studies (*10*).

### Image generation and analysis

Using the original scans, VOIs were defined manually for liver, spleen, kidney, brain and lung (brain and lung on the low dose CT, liver, spleen, kidney on the PET image). In addition, fixed size VOIs of 8.6 and 2.9 mL were placed in the lumbar vertebrae to estimate bone marrow activity concentration (AC), and in the aortic arch to estimate blood pool AC, respectively. Tumor uptake was defined as focal uptake exceeding local background reported by the nuclear medicine physician. Tumors were manually delineated on the immuno-PET scan, using the low dose CT for anatomical reference, using in-house developed software (ACCURATE tool, developed by RB).

Original list mode data were split (all counts, including delayed): even counts were placed in one data set (e.g. H1), while the odd counts were placed in the second data set (e.g. H2), creating interleaved datasets that are count statistically independent of each other, while preserving identical scan conditions (e.g. patient movement) (Figure 1). Next, these two split data sets were reconstructed (including scatter and attenuation correction).

To assess the noise induced variability of Zr-89-immuno-PET at an injected dose of 37 $MBq_{74inj}$, the original $^{89}$Zr-antiCD20 dataset (74 MBq) was split in two equal parts (H1 and H2), which were reconstructed in count-reduced images of 37 $MBq_{74inj}$. To assess whether noise induced variability is independent of the investigated mAb, the original $^{89}$Zr-antiEGFR mAb dataset (37 MBq) and $^{89}$Zr-antiCD44 mAb dataset (37 MBq) were used to produce count-reduced images of 18 $MBq_{37inj}$ (H1 and H2). In addition, the $^{89}$Zr-antiCD20 mAb dataset (74 MBq) was split again (H1) resulting in count-reduced images at 25% of the injected dose (18 $MBq_{74inj}$) (Q1 and Q2). To keep the statistical analysis similar for all three datasets, we did not split and analyze the second dataset (H2) (effectively creating Q3, Q4) as the $^{89}$Zr-antiEGFR mAb and $^{89}$Zr-antiCD44 mAb datasets only had the availability of two splits (H1, H2).

All tissue and tumor VOIs were applied to the count-reduced images, resulting in $AC_1$ from the first count-reduced image (H1) and $AC_2$ from the second count-reduced image (H2). For the $^{89}$Zr-antiCD20 mAb dataset all VOI were also applied to the count-reduced images at 25% of the injected dose (Q1 and Q2).

For normal tissue $AC_{mean}$ was derived, for tumors $AC_{max}$, $AC_{peak}$ and $AC_{mean}$ were derived (*11*). All ACs were converted into standardized uptake values (SUV), correcting for injected dose and body weight.
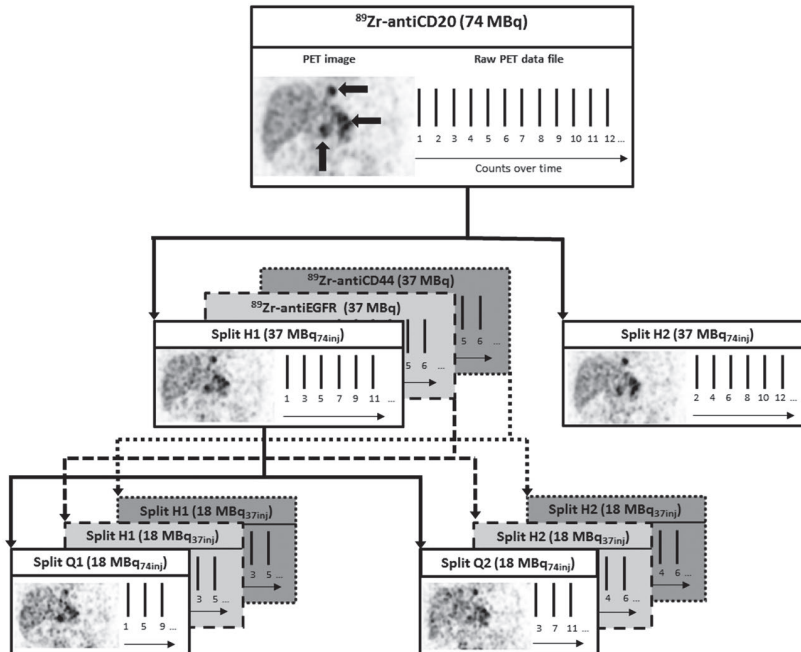


Figure 1. Noise induced variability analysis based on count-reduced images. The counts in the raw PET data file are split in two equal parts (H1 and H2), each representing 50% of the original injected dose (solid line for 37 MBq$_{74inj}$ for $^{89}$Zr-antiCD20, dashed lines for 18 MBq$_{37inj}$ for $^{89}$Zr-antiEGFR and $^{89}$Zr-antiCD44). For $^{89}$Zr-antiCD20 list mode data was split again in two equal parts (Q1 and Q2), each representing 25% of the original injected dose (18 MBq$_{74inj}$). After reconstruction of the split list mode data, two count reduced images were obtained and used for the analysis. PET images are attenuation corrected coronal slices, three large black arrows on the original PET image indicate tumor lesions.

## Noise induced variability analysis

Noise induced variability was assessed as described by Bland and Altman (*12, 13*). The measured uptake from each of the two count-reduced images was considered as repeat measures of the same quantity.

Per group of n VOIs, the mean percentage difference and standard deviation (SD) over the percent differences were calculated. The mean percentage difference is expected to be negligible, as the noise between images is assumed to be normally distributed around zero.

Repeatability coefficients (RC) in percent were calculated according to equation 1:

$$RC\ (\%) = 1.96 \cdot SD_{\left(100\% \frac{\Delta}{MV}\right)} = 1.96 \cdot CV_w(\%),$$  [1]

where $\Delta$ is ($AC_1$-$AC_2$) per VOI, MV is the mean value 0.5*($AC_1$+$AC_2$) per VOI, 100% is multiplication by 100, SD the standard deviation over all percentage differences for n VOI in the group, and $CV_w$ the coefficient of variation within scan.

RC were expressed as a percentage instead of absolute value, as the difference between $AC_1$ and $AC_2$ scaled linearly with the mean value of $AC_1$ and $AC_2$. Furthermore, the mean percentage difference was calculated as well by taking the average $\Delta$ over all VOIs in the group. The mean percentage difference and the RC combined define the limits of agreement (LoA). As a result the LoA were directly related to the coefficient of variation. Use of a relative unit allows for comparison with other studies, irrespective of the measurement unit used (e.g. type of normalization used to calculate SUV).

### Reliability analysis

To estimate the contribution of noise induced variability to the observed differences between patients or tumor lesions, the ICC was calculated in addition to the RC. The ICC was calculated as the proportion of the total variance that is due to the true variance. True variance reflects biological differences, for example between patients or between tumor lesions, while the total variance comprises both true variance as well as the measurement variance (equation 2).

$$ICC = \frac{\sigma_{voi}^2}{(\sigma_{voi}^2 + \sigma_\Delta^2)},$$  [2]

where $\sigma_{voi}^2$ is the variance between the n VOI per group, $\sigma_\Delta^2$ is the variance over the differences between $AC_1$ and $AC_2$. For a reliable measure, a high ICC is expected, as an ICC of 1 reflects that all measured variance can be attributed to biological differences (the contribution of measurement variability is negligible). An ICC of 0 signifies that all measured variance can be attributed to measurement variability (no detection of biological differences beyond measurement variability). In general, an ICC of > 0.7 is considered acceptable (*14*). The 95% confidence interval of the ICC was obtained to estimate the precision of the ICC. ICCs and 95%

confidence intervals (two-way random model, single measure, absolute agreement) were calculated using SPSS software (SPSS).

# RESULTS

Raw list mode data was retrieved for [89]Zr-antiCD20 mAb (7 patients, 20 scans), [89]Zr-antiEGFR mAb (7 patients, 21 scans) and [89]Zr-antiCD44 mAb (13 patients, 39 scans). List mode data was available for all scans at all time points, except for 1 patient in the [89]Zr-antiCD20 mAb cohort who was originally only scanned at D0 and D6, and for which no D3 scan was available.

All original datasets were split and reconstructed (Figure 1). However, not all splits could be reconstructed due to technical limitations, leading to the exclusion of 7 out of 80 scans. Technical limitations consisted of reconstruction failure (2 scans) and missing dicom information in the original data (5 scans). Acquisition time in h p.i. (average ± SD (range min-max)) for the included data was 1.3 ± 0.5 (0.9-2.4), 72.5 ± 3.6 (65.7-77.5), 147.6 ± 8.0 (138.9-165.7) for [89]Zr-antiCD20 mAb, 1.3 ± 0.5 (1.0-2.4), 68.4 ± 3.0 (64.6-72.8), 143.2 ± 2.9 (138.1-145.9) for [89]Zr-antiEGFR and 1.5 ± 0.3 (1.1- 2.1), 22.1 ± 1.5 (19.9-25.0), 97.7 ± 5.3 (91.2-114.3) for [89]Zr-antiCD44. The number of VOIs used for each analysis is denoted in Table 1, delineated organ and tumor volumes are presented in Supplemental Table 1.

## Noise induced variability analysis

*Normal tissue uptake.* For [89]Zr-antiCD20 mAb, examples of the Bland Altman plots for normal tissue are shown in Figure 2. The corresponding RC for all datasets are presented in Table 1, corresponding SUV are presented in Supplemental Table 2. Liver and lung show the best RC of all normal tissue VOI, <2% at all time points for [89]Zr-antiCD20 (37 $MBq_{74inj}$). Bone marrow, a fixed-size VOI, shows a relative large RC, ranging from 12 to 21% over time for [89]Zr-antiCD20 (mAb 37 $MBq_{74inj}$). This pattern, showing smaller RC for the manually delineated organs, and larger RC for blood pool and bone marrow, was observed for [89]Zr-antiCD20 (37 $MBq_{74inj}$ and 18 $MBq_{74inj}$) (Table 1 and Figure 2). The accompanying mean percentages differences were all near zero and are presented in Supplemental Table 3. The RC for [89]Zr-antiCD20 mAb (37 $MBq_{74inj}$) for all manually delineated organs combined (liver, spleen, kidney, lung, brain) increased from D0 to D6, but remained within 6% for all measured time points (Figure 3A).

Table 1 Repeatability coefficients (%) of Zr-89-mAbs

| VOI type | [89]Zr-antiCD20 | | | | | | [89]Zr-antiEGFR | | | [89]Zr-antiCD44 | | |
|---|---|---|---|---|---|---|---|---|---|---|---|---|
| | 37 MBq$_{74inj}$ | | | 18 MBq$_{74inj}$ | | | 18 MBq$_{37inj}$ | | | 18 MBq$_{37inj}$ | | |
| | D0 [a] n=7 | D3 [b] n=6 | D6 [c] n=6 | D0 [b] n=7 | D3 [a] n=6 | D6 [c] n=6 | D0 [d] n=6 | D3 n=6 | D6 n=6 | D0 n=12 | D1 n=12 | D4 n=12 |
| Brain | 3.5 | 6.0 | 5.2 | 2.4 | 6.5 | 7.6 | 3.0 | 7.6 | 13.8 | 3.7 | 2.9 | 7.3 |
| Kidney | 1.2 | 4.8 | 5.2 | 2.6 | 6.5 | 6.8 | 3.5 | 7.1 | 12.5 | 3.7 | 3.5 | 9.1 |
| Lung | 1.1 | 0.6 | 0.8 | 1.5 | 1.6 | 2.7 | 1.6 | 1.8 | 3.4 | 1.0 | 1.6 | 6.7 |
| Spleen | 1.9 | 4.7 | 8.2 | 3.4 | 8.8 | 17.2 | 5.2 | 8.4 | 13.9 | 4.4 | 3.7 | 7.8 |
| Liver | 1.5 | 1.6 | 1.4 | 1.6 | 0.8 | 3.9 | 1.4 | 1.6 | 1.6 | 1.2 | 2.4 | 1.7 |
| Combined | 2.3 | 4.7 | 5.5 | 2.5 | 6.3 | 11.1 | 4.2 | 6.4 | 10.7 | 3.4 | 3.0 | 7.1 |
| Blood pool | 8.3 | 17.1 | 42.7 | 10.6 | 29.9 | 38.5 | 13.4 | 28.8 | 47.4 | 10.4 | 18.3 | 32.3 |
| Bone marrow | 15.1 | 12.4 | 20.6 | 23.9 | 21.0 | 38.4 | 20.7 | 19.6 | 26.6 | 13.0 | 17.8 | 20.7 |
| Tumor | - | D3 n=26 | D6 n=32 | - | D3 n=26 | D6 n=32 | - | D3 n=7 | D6 n=7 | - | D1 n=19 | D4 n=19 |
| SUV$_{max}$ | - | 41.6 | 41.5 | - | 39.1 | 45.5 | - | 34.9 | 54.1 | - | 29.5 | 33.5 |
| SUV$_{peak}$ | - | 35.2 | 31.6 | - | 35.7 | 37.1 | - | 28.8 | 48.2 | - | 20.7 | 28.0 |
| SUV$_{mean}$ | - | 26.7 | 24.5 | - | 26.8 | 26.6 | - | 35.4 | 32.7 | - | 20.1 | 24.2 |

n = number of VOIs per group.

Combined = all VOIs of brain, kidney, lung, spleen and liver, analyzed together as one group.

[a] No brain VOI obtained in patient 2 (outside field of view) and 6 (tumor localization in the nasopharynx).

[b] No brain VOI obtained in patient 6 (tumor localization in the nasopharynx).

[c] No kidney, lung, spleen, liver, blood pool, bone marrow in patient 2 (outside field of view). No brain VOI obtained in patient 6 (tumor localization in the nasopharynx). No brain VOI obtained in patient 1 (mismatch between low dose CT and PET image due to patient movement).

[d] No brain VOI obtained in patient 8 (outside field of view).

Data marked in grey is presented as Bland-Altman plots in Figure 2 (normal tissue) and 4 (tumor).

For 18 MBq$_{74inj}$, the RC for the manually delineated large organs remained within 12% for all time points (Figure 3A). For the image derived blood pool (Figure 3B), RC increased from 8 to 43% from D0 to D6. We observed similar RC for [89]Zr-antiCD20 (18 MBq$_{74inj}$), [89]Zr-antiEGFR (18 MBq$_{37inj}$) and [89]Zr-antiCD44 (18 MBq$_{37inj}$) for the manually delineated organs (Fig. 3C) and for the image derived blood pool (Figure 3D). For the individual normal tissue VOI (brain, kidney, lung, spleen, liver, bone marrow), we found no apparent differences in RC for the various antibodies, except for kidney D6.

A decrease in RC was observed for increasing SUV and volume (Supplemental Figure 1). For example, for the fixed size blood pool VOI (2.9 mL) for [89]Zr-antiCD20 mAb (37MBq$_{74inj}$), a decrease in RC from 42%, 17% to 8% was observed, with a corresponding increase in SUV from 3.9, 5.8 to 11.7. For VOI with similar SUV (3.1-3.3) for [89]Zr-antiCD44 mAb (18MBq$_{37inj}$), a decrease in RC

from 32%, 18% to 4% was observed, with a corresponding increase in volume from 2.9 mL (blood pool), 8.6 mL (bone marrow) to 309 mL (kidney).
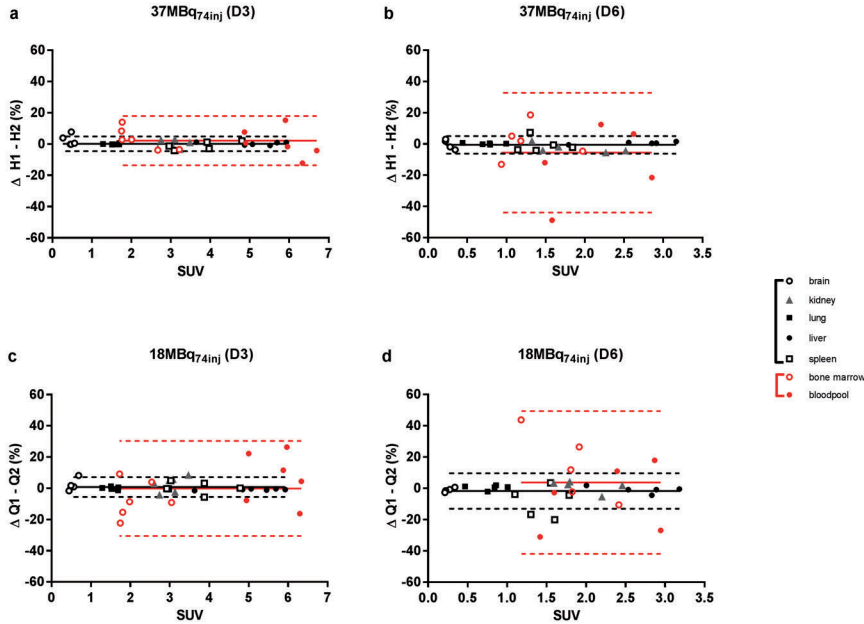


Figure 2. Noise induced variability analysis of normal tissue uptake of $^{89}$Zr-antiCD20 mAb. Manually delineated VOIs (brain, kidney, lung, liver and spleen) are represented in black. Fixed-size VOIs (bone marrow and blood pool) are represented in red. Mean percentage differences (solid lines) and corresponding limits of agreement (dashed lines) are presented for the combined group of manually delineated VOIs (black) and the combined group of fixed-size VOIs (red). a) $^{89}$Zr-antiCD20 (37 MBq$_{74inj}$) at D3, b) $^{89}$Zr-antiCD20 (37 MBq$_{74inj}$) at D6, c) $^{89}$Zr-antiCD20 (18 MBq$_{74inj}$) at D3, d) $^{89}$Zr-antiCD20 (18 MBq$_{74inj}$) at D6.

*Tumor uptake.* Bland Altman plots of tumor uptake of $^{89}$Zr-antiCD20 mAb (37MBq$_{74inj}$) are shown in Figure 4. Tumor RC are presented in Table 1, corresponding SUV in Supplemental Table 2, for mean percentages differences see Supplemental Table 3. In contrast to the RC for organs, RC for tumor uptake did not increase consistently over time for $^{89}$Zr-anti-CD20 mAb. For tumor uptake of $^{89}$Zr-anti-CD20 mAb (37 MBq$_{74inj}$), the best RC at D6 was obtained for SUV$_{mean}$ (26%), followed by SUV$_{peak}$ (34%) and SUV$_{max}$ (41%) (Table 1). The same rank order (increasing RC for SUV$_{mean}$, SUV$_{peak}$ and SUV$_{max}$) was observed for $^{89}$Zr-
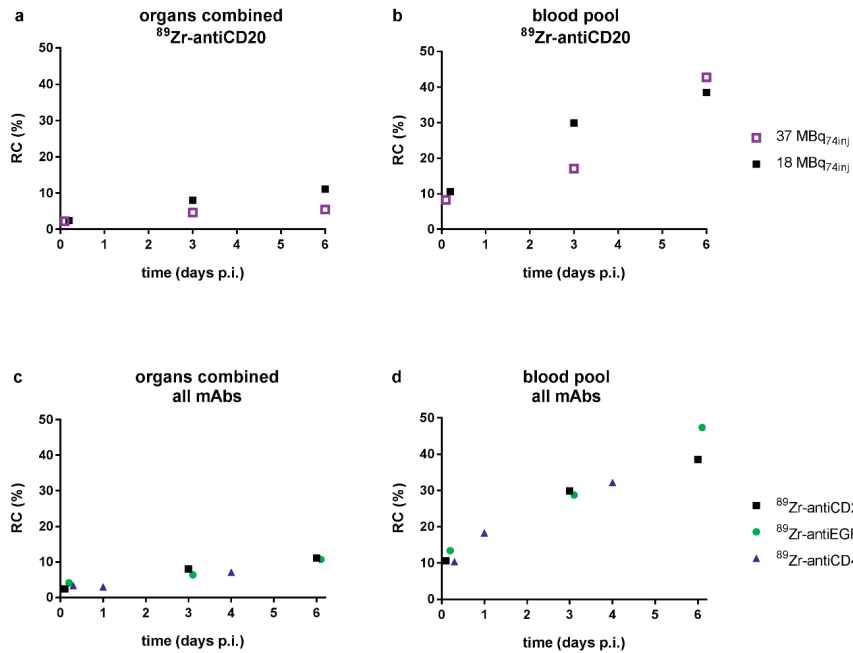
Figure 3. Repeatability coefficients (%) and their 95% CIs of normal tissue uptake of Zr-89-mAbs. a) the combined group of manually delineated organs for [89]Zr-antiCD20, b) blood pool for [89]Zr-antiCD20, c) the combined group of manually delineated organs for [89]Zr-antiCD20 (18 MBq$_{74inj}$), [89]Zr-antiEGFR (18 MBq$_{37inj}$) and [89]Zr-antiCD44 (18 MBq$_{37inj}$), d) blood pool for [89]Zr-antiCD20 (18 MBq$_{74inj}$), [89]Zr-antiEGFR (18 MBq$_{37inj}$) and [89]Zr-antiCD44 (18 MBq$_{37inj}$).

antiCD44 mAb at D4 (18 MBq$_{37inj}$) and for [89]Zr-antiEGFR mAb at D6 (18 MBq$_{37inj}$). For [89]Zr-anti-CD44 mAb the RC for SUV$_{peak}$ increased from 21 to 28% RC (D1 to D4). These values were lower than for [89]Zr-anti-CD20 mAb (Table 1). However, data for [89]Zr-antiCD44 mAb were acquired at different time points after injection (D1 and D4) compared to [89]Zr-antiCD20 mAb and [89]Zr-antiEGFR mAb (D3 and D6). No differences were observed in RC for SUV$_{peak}$ between all three mAbs at D3-D4, and between [89]Zr-antiCD20 mAb and [89]Zr-antiEGFR mAb at D6. The differences between SUV$_{mean}$ and SUV$_{max}$ were significant for the three Zr-89-mAbs combined (D3-D4), as well as on D6 for [89]Zr-antiCD20 and [89]Zr-antiEGFR combined.
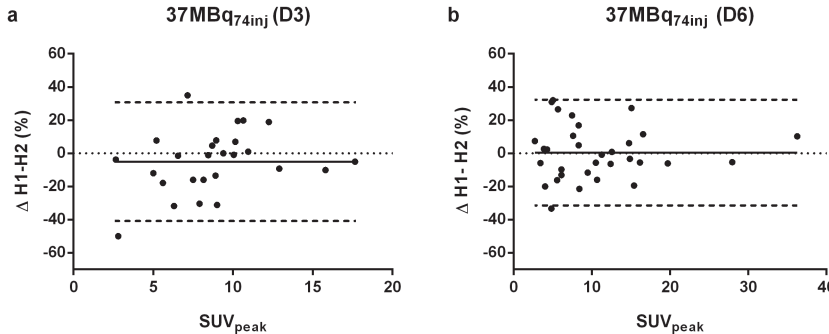
Figure 4. Tumor uptake of $^{89}$Zr-antiCD20 (37 MBq$_{74inj}$). Bland-Altman plots for two count reduced images (H1 and H2) for SUV$_{peak}$ at D3 (a) and D6 (b). Solid lines represent mean percentage difference, dashed lines represent upper and lower LoA.

## Reliability analysis

The ICCs for normal tissue and tumor uptake of Zr-89-mAbs are shown in Table 2 and Supplemental Table 4. For the manually delineated organs, ICCs > 0.9 were obtained at all time points for $^{89}$Zr-antiCD20 mAb (37 MBq$_{74inj}$ and 18 MBq$_{74inj}$). For $^{89}$Zr-antiCD20 mAb (37 MBq$_{74inj}$), blood pool and bone marrow ICCs were lower, with values as low as 0.74 and with wider 95% confidence intervals than for the manually delineated organs.

For tumor uptake of $^{89}$Zr-mAbs, ICCs of > 0.9 were obtained in all datasets, despite RC of 40%. Similar tumor ICCs of 0.9 were obtained for $^{89}$Zr-antiCD20 mAb (18 MBq$_{74inj}$), $^{89}$Zr-$^{89}$Zr-antiEGFR mAb (18 MBq37$_{MBq}$), $^{89}$Zr-antiCD44 mAb (18MBq$_{37MBq}$). Increase in the range of tumor uptake between tumor lesions over time for $^{89}$Zr-antiCD20 (37 MBq$_{74inj}$) (Fig. 5), resulted in a higher ICC at D6. This trend was not observed for $^{89}$Zr-antiEGFR (18 MBq$_{37inj}$).

Table 2 ICC for blood pool, bone marrow and tumor uptake of Zr-89-mAbs

| ICC (lower-upper 95% CI) | $^{89}$Zr-antiCD20 (37 MBq$_{74inj}$) | | |
|---|---|---|---|
| | D0 | D3 | D6 |
| Blood pool | 0.91 (0.56-0.98) | 0.78 (-0.22-0.97) | 0.74 (-0.27-0.97) |
| Bone marrow | 0.81 (0.26-0.96) | 0.98 (0.86-1.00) | 0.97 (0.59-0.99) |
| Tumor (peak) | NA | 0.92 (0.83-0.96) | 0.98 (0.96-0.99) |
| | $^{89}$Zr-antiCD20 (18 MBq$_{74inj}$) | | |
| | D0 | D3 | D6 |
| Blood pool | 0.92 (0.59-0.99) | 0.25 (-0.60-0.84) | 0.79 (-0.19-0.98) |
| Bone marrow | 0.72 (0.11-0.94) | 0.90 (0.50-0.99) | 0.72 (-0.05-0.97) |
| Tumor (peak) | NA | 0.89 (0.78-0.95) | 0.97 (0.93-0.98) |
| | $^{89}$Zr-antiEGFR (18 MBq$_{37inj}$) | | |
| | D0 | D3 | D6 |
| Blood pool | 0.98 (0.87-1.00) | 0.96 (0.75-0.99) | 0.89 (0.43-0.98) |
| Bone marrow | 0.93 (0.59-0.99) | 0.98 (0.88-1.00) | 0.91 (0.55-0.99) |
| Tumor (peak) | NA | 0.94 (0.47-0.99) | 0.88 (0.47-0.99) |
| | $^{89}$Zr-antiCD44 (18 MBq$_{37inj}$) | | |
| | D0 | D1 | D4 |
| Blood pool | 0.99 (0.95-1.00) | 0.97 (0.89-0.99) | 0.95 (0.83-0.99) |
| Bone marrow | 0.96 (0.86-0.99) | 0.96 (0.86-0.99) | 0.87 (0.60-0.96) |
| Tumor (peak) | NA | 0.97(0.91-0.99) | 0.96 (0.90-0.99) |
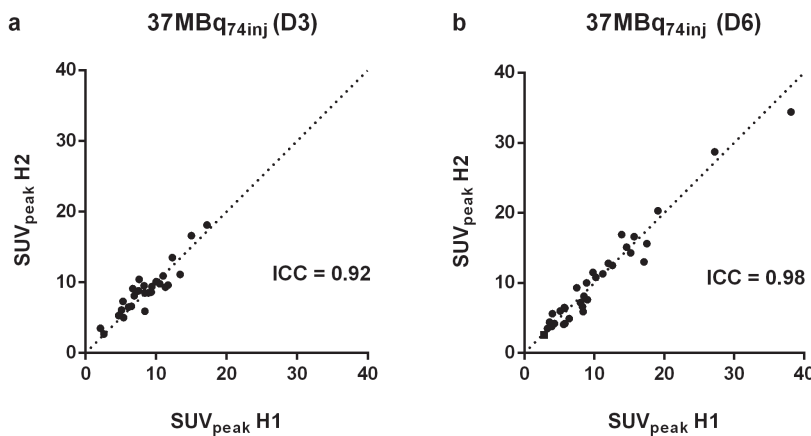


Figure 5. Tumor uptake of $^{89}$Zr-antiCD20 (37 MBq$_{74inj}$). Scatterplots of SUV$_{peak}$ in split H1 versus split H2 at D3 (a) and D6 (b). Dashed lines represent the line of identity.

# DISCUSSION

In this study noise induced variability of quantitative uptake measures was assessed for Zr-89-immuno-PET for an injected activity of 37 MBq based on count-reduced images. As expected, a variable increase in RC was observed from D0 to D6 for the manually delineated organs (Table 1). In general, the RC for the manually delineated large organs combined (liver, spleen, kidney, lung and brain) was within 6% at all time points (D0, D3, D6) for $^{89}$Zr-anti-CD20 mAb (37MBq$_{74inj}$). Larger measurement variability was observed for the bone marrow and blood pool VOIs with RC up to 40% at D6 for $^{89}$Zr-anti-CD20 (37 MBq$_{74inj}$). These results are in line with an increase in RC for a lower total activity in the VOI.

For tumor uptake of $^{89}$Zr-antiCD20 mAb (37 MBq$_{74inj}$), the lowest variability was obtained for SUV$_{mean}$ (27%), followed by SUV$_{peak}$ (35%), while SUV$_{max}$ (42%) resulted in the highest measurement variability (Table 2). This is as expected, since for a given VOI the mean value takes all voxels into account, in contrast to the peak value (based on a limited number of voxels) and max value (based on a single voxel).

RC for the three Zr-89-mAbs were similar. Therefore, the observed measurement variability is independent of the differences in biodistribution between these three Zr-89-mAbs. These results suggest that similar noise induced variability can be expected for other Zr-89-mAbs, assuming harmonized image quality and a biodistribution within the same range as the Zr-89-mAbs investigated in this study.

With the count-reduced images, noise induced variability for an injected dose of 18 MBq was assessed for all three mAbs. RC for combined organs were up to 12% at all time points (range D0-D6). Tumor RC varied between 20 to 54%, depending on time point and VOI delineation method.

Despite relatively large RC for tumor, blood pool and bone marrow, overall reliability for the three clinical Zr-89-immuno-PET studies previously reported (*7-9*) was excellent (ICCs approximately 0.9). ICC values are given to show, for these Zr-89-mAbs in their respective patient cohorts, that the measured differences in tumor uptake do exceed the variability induced by noise. ICC values, however, cannot be extrapolated to other Zr-89-mAbs or even different patient cohorts imaged with the same Zr-89-mAb.

As our study provides an assessment of measurement variability due to the signal-to-noise ratio, other sources of measurement error are not represented in

this reliability assessment (equation 2). Factors affecting [$^{18}$F]-FDG-PET quantification have been described previously (*15*). Repeatability assessed by a classical test-retest study contains intra-patient variability between the test and the retest scan as well. For a test-retest study with Zr-89-immuno-PET, the following factors are expected to play a role 1) biological factors: e.g. uptake period (higher uptake levels at increasing time interval between injection and start of PET study), estimated at 1% for ± 1h (*16,17*); 2) physical factors: VOI definition, estimated at <1% for max and peak AC to 8% for mean (*18*). Based on the results of our study, we expect that noise induced variability will be a major contribution to measurement variability in a Zr-89-immuno-PET test-retest study (3% for large organs, 20% for tumor, values presented as SD instead of RC for comparison).

In previously reported test-retest studies of repeatability of $^{18}$F-FDG-PET, RC of <10% have been reported for tumor uptake on $^{18}$F-FDG-PET, resulting in thresholds of 10-15% needed to detect therapy-induced changes in patients with non-small cell lung cancer [19-21]. For Zr-89-immuno-PET (37 MBq$_{74inj}$), we obtained similar RC of less than 10% for mean activity concentrations of manually delineated organs. However, for tumor uptake on Zr-89-immuno-PET, RC up to 42% for SUV$_{max}$ reflect the much lower signal to noise ratio in Zr-89-immuno-PET scans in comparison to [$^{18}$F]-FDG-PET scans. When immuno-PET with Zr-89-labeled mAbs is used to assess response to treatment (e.g. by alteration of antigen expression (*22*)), knowledge on measurement variability should be applied to set corresponding thresholds, following the example of the use of thresholds for response assessment with [$^{18}$F]-FDG-PET. For data already obtained, RC from our study are relevant to allow correct interpretation, as differences smaller than the measurement variability cannot be attributed to biological effects. Measurement variability (given as RC) is independent of the study population. In addition, RC of tumor and blood pool are of interest when selecting an appropriate uptake measure and/or VOI delineation method.

Tumor-to-blood ratios, which are commonly used, will result in even worse RC due to propagation of the individual RC as both numerator and denominator contain measurement variability. Future work may include an investigation to optimize delineation methods for image-derived blood pool (e.g. delineation of a larger region in the left ventricular cavity compared to a smaller fixed-size VOI in the aortic arch) to reduce noise induced variability. We designed this study based on patient data to provide a clinically relevant assessment of measurement error.

This study provides the first description of noise induced variability for Zr-89-immuno-PET. In literature more sophisticated applications of the technique of count reduced images have been described (*23,24*). By using bootstrapping the difference between the two image estimates can be obtained more precisely, which would allow for an examination of the change of noise induced variability with patient specific factors such as tumor size, uptake, patient size and location of the tumor in the patient. In addition, through application of this technique, the effect of lowering the injected dose on quantitative accuracy can be assessed.

Our results suggest that, as expected, measurement error may be dependent on volume and uptake (Supplemental Figure 1). In future work, phantoms could be used to study dependencies of noise induced variability on e.g. VOI volume and activity concentration. Such phantom experiments could be combined with tumor characteristics as derived from clinical Zr-89-immuno-PET studies (tumor volume, SUV, tumor to background ratio and localization) to obtain a detection limit for tumor identification. The trade-off between noise and contrast will determine the optimal time point for tumor imaging. In addition, tumor contrast on clinical images should be defined and characterized, allowing for a recommendation on the optimal time points for future clinical studies.

For potential application of immuno-PET with Zr-89-labeled antibodies as a quantitative imaging biomarker to predict which patients are likely to respond to antibody treatment, the ability to distinguish biological differences in antibody uptake between patients is required. We observed excellent ICCs (lesion based analysis), suggesting that an injected dose of 18-37MBq was sufficient for the datasets included. In general, justification of the injected dose should be based on the expected effect size in the population of interest.

Another clinical application of Zr-89-immuno-PET is *in-vivo* quantification of antibody biodistribution and tumor uptake to assess novel antibodies during early phases of drug development. For this purpose, noise induced variability as source of measurement error as reported in our study (expressed as RC) can be applied to estimate the minimal measurement variability (e.g. for sample size calculations for novel studies).

## CONCLUSION

Based on this study, noise induced variability results in a RC for Zr-89-immuno-PET (37MBq) of less than 6% for manually delineated organs combined, increasing up to 43% at D6 for blood pool and bone marrow, assuming similar biodistribution of mAbs. The signal to noise ratio in Zr-89-immuno-PET scans leads to tumor RC up to 42%.

## ACKNOWLEDGEMENTS

# REFERENCES

1.  Lamberts LE, Williams SP, Terwisscha van Scheltinga AGT, et al. Antibody positron emission tomography imaging in anticancer drug development. *J Clin Oncol*. 2015;33:1491-1504.

2.  Pandit-Taskar N, O'Donoghue JA, Beylergil V, et al. $^{89}$Zr-huJ591 immuno-PET imaging in patients with advanced metastatic prostate cancer. *Eur J Nucl Med Mol Imaging*. 2014;41:2093-2105.

3.  Jauw YWS, Menke-van der Houven van Oordt CW, Hoekstra OS, et al. Immuno-Positron Emission Tomography with Zirconium-89-Labeled Monoclonal Antibodies in Oncology: What Can We Learn from Initial Clinical Trials? *Front Pharmacol*. 2016;7:131.

4.  Armstrong IS, James JM, Williams HA, Kelly MD, Matthews JC. The assessment of time-of-flight on image quality and quantification with reduced administered activity and scan times in 18F-FDG PET. *Nucl Med Commun*. 2015;36:728-737.

5.  Bruijnen S, Tsang-A-Sjoe M, Raterman H, et al. B-cell imaging with zirconium-89 labelled rituximab PET-CT at baseline is associated with therapeutic response 24 weeks after initiation of rituximab treatment in rheumatoid arthritis patients. *Arthritis Res Ther*. 2016;18:266.

6.  Hagens MH, Killestein J, Yaqub MM, et al. Cerebral rituximab uptake in multiple sclerosis: A 89Zr-immunoPET pilot study. *Mult Scler*. 2018;24:543-545.

7.  Jauw YWS, Zijlstra JM, de Jong D, et al. Performance of 89Zr-Labeled-Rituximab-PET as an Imaging Biomarker to Assess CD20 Targeting: A Pilot Study in Patients with Relapsed/Refractory Diffuse Large B Cell Lymphoma. *PLoS ONE*. 2017;12:e0169828.

8.  Menke-van der Houven van Oordt CW, Gootjes EC, Huisman MC, et al. 89Zr-cetuximab PET imaging in patients with advanced colorectal cancer. *Oncotarget*. 2015;6:30384-30393.

9.  Menke-van der Houven van Oordt CW, Gomez-Roca C, van Herpen C, et al. First-in-human phase I clinical trial of RG7356, an anti-CD44 humanized antibody, in patients with advanced, CD44-expressing solid tumors. *Oncotarget*. 2016;7:80046-80058.

10. Makris NE, Boellaard R, Visser EP, et al. Multicenter harmonization of 89Zr PET/CT performance. *J Nucl Med*. 2014;55:264-267.

11. Boellaard R, Delgado-Bolton R, Oyen WJG, et al. FDG PET/CT: EANM procedure guidelines for tumour imaging: version 2.0. *Eur J Nucl Med Mol Imaging*. 2015;42:328-354.

12. Bland JM, Altman DG. Statistical methods for assessing agreement between two methods of clinical measurement. *Lancet*. 1986;1:307-310.

13. Giavarina D. Understanding Bland Altman analysis. *Biochem Med (Zagreb)*. 2015;25:141-151.

14. Nunnally JC. Psychometric theory. McGraw-Hill; 1994.

15. Boellaard R. Standards for PET image acquisition and quantitative data analysis. *J Nucl Med*. 2009;50 Suppl 1:11S-20S.

16. Shah DK, Betts AM. Towards a platform PBPK model to characterize the plasma and tissue disposition of monoclonal antibodies in preclinical species and human. *J Pharmacokinet Pharmacodyn*. 2012;39:67-86.

17. Kletting P, Maaß C, Reske S, Beer AJ, Glatting G. Physiologically Based Pharmacokinetic Modeling Is Essential in 90Y-Labeled Anti-CD66 Radioimmunotherapy. *PLoS ONE*. 2015;10:e0127934.

18. Jauw Y, Hoekstra O, Mulder E, et al. Inter-observer agreement for tumor uptake quantification of 89Zr-labeled anti-CD20 antibodies with PET. *J Nucl Med*. 2016;57:1412-1412.

19. Lodge MA. Repeatability of SUV in Oncologic 18F-FDG PET. *J Nucl Med*. 2017;58:523-532.

20. Kramer GM, Frings V, Hoetjes N, et al. Repeatability of Quantitative Whole-Body 18F-FDG PET/CT Uptake Measures as Function of Uptake Interval and Lesion Selection in Non-Small Cell Lung Cancer Patients. *J Nucl Med*. 2016;57:1343-1349.

21. Hoekstra CJ, Hoekstra OS, Stroobants SG, et al. Methods to monitor response to chemotherapy in non-small cell lung cancer with 18F-FDG PET. *J Nucl Med*. 2002;43:1304-1309.

22. Gaykema SBM, Schröder CP, Vitfell-Rasmussen J, et al. 89Zr-trastuzumab and 89Zr-bevacizumab PET to evaluate the effect of the HSP90 inhibitor NVP-AUY922 in metastatic breast cancer patients. *Clin Cancer Res*. 2014;20:3945-3954.

23. Lartizien C, Aubin J-B, Buvat I. Comparison of bootstrap resampling methods for 3-D PET imaging. *IEEE Trans Med Imaging*. 2010;29:1442-1454.

24. Markiewicz PJ, Reader AJ, Matthews JC. Assessment of bootstrap resampling performance for PET data. *Phys Med Biol*. 2015;60:279-299.

# SUPPLEMENTARY DATA
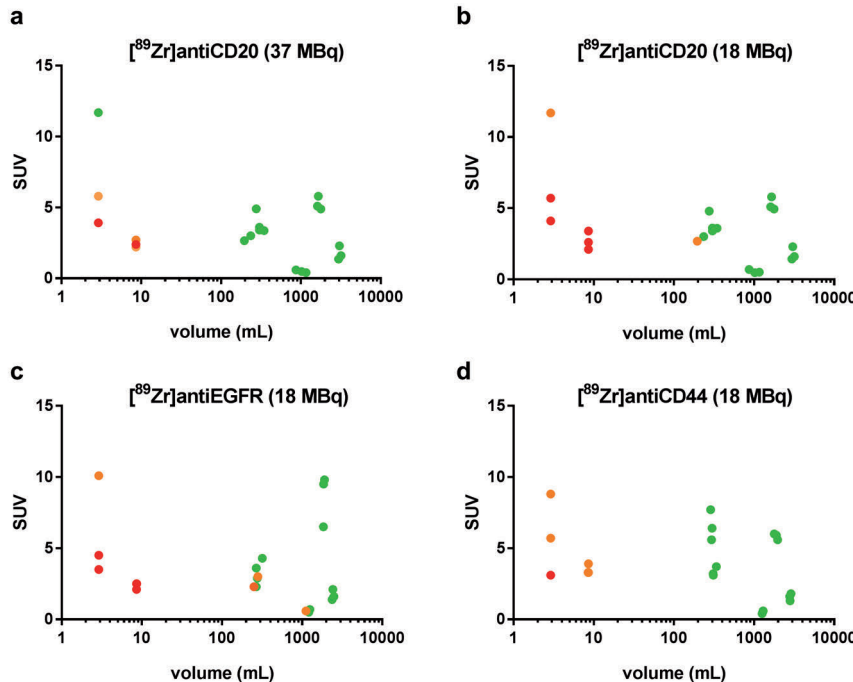


**Supplemental Figure 1** Noise induced variability (RC in color, green 0-10%, orange 10 to 20%, red >20%) as a function of SUV and volume for all normal tissue VOI for (a) $^{89}$Zr-antiCD20; 37MBq$_{74inj}$ (b) $^{89}$Zr-antiCD20; 18MBq$_{74inj}$ (c) $^{89}$Zr-antiEGFR; 18 MBq$_{37inj}$ and (d) $^{89}$Zr-antiCD44; 18 MBq$_{37inj.}$

**Supplemental Table 1** Delineated organ and tumor volumes

|  | Volume (mL) |
| --- | --- |
| Brain | 1190 ± 204 |
| Kidney | 304 ± 79 |
| Lung | 2788 ± 754 |
| Spleen | 275 ± 163 |
| Liver | 1817 ± 362 |
| Tumor |  |
| $^{89}$Zr-antiCD20 | 5.9 (1.5-261.4) |
| $^{89}$Zr-antiEGFR | 3.2 (1.6-480.3) |
| $^{89}$Zr-antiCD44 | 8.0 (1.80-467.4) |

Organ volumes (average ± SD), all mAbs, all timepoints
Tumor volumes (median, range), last time point

Supplemental Table 2 Normal tissue and tumor uptake of Zr-89-mAbs

| VOI type | 89Zr-antiCD20 37 MBq 74inj | | | 89Zr-antiCD20 18 MBq 74inj | | | 89Zr-antiEGFR 18 MBq 37inj | | | 89Zr-antiCD44 18 MBq 37inj | | |
|---|---|---|---|---|---|---|---|---|---|---|---|---|
| | D0[a] n=7 | D3[b] n=6 | D6[c] n=6 | D0[b] n=7 | D3[a] n=6 | D6[c] n=6 | D0[d] n=6 | D3 n=6 | D6 n=6 | D0 n=12 | D1 n=12 | D4 n=12 |
| Brain | 0.6 (0.5-0.7) | 0.5 (0.4-0.6) | 0.5 (0.4-0.6) | 0.7 (0.7-0.9) | 0.5 (0.4-0.6) | 0.5 (0.4-0.5) | 0.7 (0.6-1.0) | 0.5 (0.3-0.6) | 0.5 (0.4-0.7) | 0.7 (0.6-0.7) | 0.6 (0.4-0.7) | 0.4 (0.4-0.5) |
| Kidney | 3.2 (3.0-3.9) | 3.5 (3.1-4.2) | 3.2 (1.4-2.4) | 3.2 (3.0-3.8) | 3.5 (3.0-4.1) | 3.4 (3.2-4.1) | 3.6 (3.1-4.1) | 3.2 (1.9-3.8) | 3.0 (2.5-3.4) | 3.4 (2.9-3.6) | 3.8 (3.1-4.4) | 3.1 (2.4-3.4) |
| Lung | 2.3 (1.9-2.4) | 1.6 (1.4-1.7) | 1.5 (1.1-1.6) | 2.3 (2.2-2.4) | 1.6 (1.5-1.7) | 1.5 (1.2-1.6) | 1.9 (1.7-2.8) | 1.5 (0.8-2.1) | 1.8 (1.1-1.9) | 1.8 (1.4-2.0) | 1.5 (1.3-1.9) | 1.3 (1.1-1.4) |
| Spleen | 4.7 (4.2-5.7) | 3.1 (2.7-3.3) | 2.7 (2.3-3.0) | 4.7 (4.2-5.7) | 3.0 (2.7-3.2) | 2.9 (2.3-3.0) | 4.4 (3.4-5.1) | 2.4 (1.4-3.2) | 2.3 (1.8-2.8) | 6.5 (5.6-8.6) | 5.2 (4.4-7.7) | 4.7 (3.4-6.9) |
| Liver | 5.9 (5.6-6.5) | 5.3 (4.6-5.7) | 4.9 (4.0-5.8) | 5.9 (5.6-6.4) | 5.3 (4.5-5.7) | 4.8 (4.2-5.8) | 6.3 (5.7-7.6) | 9.7 (7.9-10.6) | 10.3 (7.2-11.8) | 5.6 (5.2-6.0) | 5.8 (4.8-6.2) | 5.5 (5.1-6.3) |
| Combined | 3.6 (2.2-5.4) | 3.0 (1.5-5.7) | 2.6 (1.4-3.9) | 3.4 (2.2-5.4) | 2.9 (1.5-3.9) | 2.9 (1.5-3.9) | 3.2 (1.8-4.9) | 2.2 (0.8-3.8) | 2.1 (1.2-4.0) | 3.2 (1.3-5.7) | 3.7 (1.3-5.0) | 3.0 (1.1-5.0) |
| Blood pool | 11.5 (10.5-12.6) | 5.9 (4.9-6.4) | 4.2 (2.9-4.7) | 11.2 (10.8-12.7) | 5.9 (5.0-6.3) | 3.9 (2.9-5.5) | 9.5 (7.8-13.1) | 4.7 (2.3-6.3) | 4.0 (1.9-4.7) | 9.1 (7.4-11.2) | 5.8 (4.3-7.0) | 3.0 (1.9-3.9) |
| Bone marrow | 2.8 (2.4-2.9) | 1.9 (1.8-2.8) | 2.2 (1.8-3.1) | 2.7 (2.2-2.9) | 1.9 (1.7-2.7) | 3.5 (2.6-4.1) | 2.6 (2.1-3.0) | 2.3 (1.5-2.8) | 2.5 (1.8-3.0) | 3.9 (3.1-4.5) | 3.0 (2.4-4.2) | 3.2 (2.8-4.9) |
| Tumor | - | D3 n=26 | D6 n=32 | - | D3 n=26 | D6 n=32 | - | D3 n=7 | D6 n=7 | - | D1 n=19 | D4 n=19 |
| SUV$_{max}$ | - | 10.7 (8.2-13.1) | 11.5 (6.8-17.8) | - | 11.1 (7.9-14.3) | 12.7 (8.2-19.8) | - | 5.5 (4.6-7.0) | 7.7 (4.9-10.6) | - | 4.0 (2.6-5.1) | 5.1 (3.0-9.0) |
| SUV$_{peak}$ | - | 8.8 (6.5-10.4) | 8.4 (4.0-14.8) | - | 9.0 (6.3-11.2) | 9.2 (6.8-15.5) | - | 4.8 (4.0-5.7) | 6.3 (3.9-8.6) | - | 3.5 (2.1-4.7) | 4.2 (2.5-7.4) |
| SUV$_{mean}$ | - | 6.9 (5.7-7.8) | 7.2 (4.0-10.7) | - | 6.3 (4.7-8.1) | 7.5 (4.7-10.8) | - | 3.3 (2.5-4.4) | 3.9 (2.4-5.6) | - | 2.2 (1.7-2.9) | 3.3 (2.0-4.9) |

Data is presented as median SUV (interquartile range). SUV calculated as the average of split 1 and split 2.

n = number of VOIs per group.

Combined = all VOIs of brain, kidney, lung, spleen and liver, analyzed together as one group.

[a] No brain VOI obtained in patient 2 (outside field of view) and 6 (tumor localization in the nasopharynx).
[b] No brain VOI obtained in patient 6 (tumor localization in the nasopharynx).
[c] No kidney, lung, spleen, liver, blood pool, bone marrow in patient 2 (outside field of view). No brain VOI obtained in patient 6 (tumor localization in the nasopharynx). No brain VOI obtained in patient 1 (mismatch between low dose CT and PET image due to patient movement).
[d] No brain VOI obtained in patient 8 (outside field of view).

Supplemental Table 3 Mean differences (%) for normal tissue and tumor uptake of Zr-89-mAbs

| | $^{89}$Zr-antiCD20 | | | | | | $^{89}$Zr-antiEGFR | | | $^{89}$Zr-antiCD44 | | |
|---|---|---|---|---|---|---|---|---|---|---|---|---|
| | 37 MBq$_{74inj}$ | | | 18 MBq$_{74inj}$ | | | 18 MBq$_{37inj}$ | | | 18 MBq$_{37inj}$ | | |
| | D0 n=7 | D3 n=6 | D6 n=6 | D0 n=7 | D3 n=6 | D6 n=6 | D0 n=6 | D3 n=6 | D6 n=6 | D0 n=12 | D1 n=12 | D4 n=12 |
| Brain | -1.5 | 2.4 | 0.3 | 0.3 | 2.0 | -2.9 | 0.8 | -0.6 | 0.9 | -1.3 | 0.6 | 0.5 |
| Kidney | 0.1 | -1.5 | -2.7 | -0.1 | 0.4 | 1.3 | -1.8 | 1.5 | -0.8 | 0.2 | 0.4 | -0.6 |
| Lung | 0.2 | -0.1 | 0.2 | 0.2 | 0.0 | 0.5 | -0.2 | 0.3 | -0.5 | 0.1 | -0.1 | 1.4 |
| Spleen | 0.2 | 0.0 | -0.6 | 0.0 | 2.7 | -8.3 | 2.1 | 2.3 | -2.4 | 0.0 | -0.4 | 0.8 |
| Liver | -0.1 | 0.2 | 0.6 | -0.1 | -0.8 | -0.9 | 0.7 | 0.2 | -0.4 | 0.7 | 0.0 | 0.0 |
| Combined | -0.2 | 0.1 | -0.6 | 0.0 | 0.9 | -1.7 | 0.3 | 0.7 | -0.7 | -0.1 | 0.1 | 0.4 |
| | | | | | | | | | | | | |
| Blood pool | 0.4 | 0.9 | -12.7 | 0.4 | 6.8 | -6.3 | 4.3 | -3.1 | -2.1 | -2.9 | 2.3 | 0.5 |
| Bone marrow | -5.7 | 3.4 | 1.6 | -8.5 | -7.0 | 13.9 | -2.3 | -0.1 | 6.3 | 0.3 | -0.9 | -5.5 |
| | | | | | | | | | | | | |
| Tumor | - | D3 n=26 | D6 n=32 | - | D3 n=26 | D6 n=32 | - | D3 n=7 | D6 n=7 | - | D1 n=19 | D4 n=19 |
| SUV$_{max}$ | - | -4.1 | 0.3 | - | -5.0 | 1.7 | - | 9.5 | 1.3 | - | -3.0 | -4.8 |
| SUV$_{peak}$ | - | -4.9 | 0.4 | - | -4.7 | 2.0 | - | 9.4 | 4.5 | - | -2.6 | -3.5 |
| SUV$_{mean}$ | - | -6.5 | 0.3 | - | -1.0 | 2.7 | - | 5.6 | 2.1 | - | -1.3 | -2.3 |

Supplemental Table 4 ICC for normal tissue uptake of Zr-89-mAbs

| ICC (lower-upper 95% CI) | $^{89}$Zr-antiCD20 (37 MBq$_{74inj}$) | | |
|---|---|---|---|
| | D0 | D3 | D6 |
| Brain | 0.92 (0.16-0.99) | 0.99 (0.90-1.00) | 0.99 (0.89-1.00) |
| Kidney | 1.00 (0.99-1.00) | 0.99 (0.94-1.00) | 0.99 (0.85-1.00) |
| Lung | 1.00 (0.99-1.00) | 1.00 (1.00-1.00) | 1.00 (1.00-1.00) |
| Spleen | 1.00 (0.99-1.00) | 0.97 (0.81-1.00) | 0.98 (0.81-1.00) |
| Liver | 1.00 (0.99-1.00) | 1.00 (0.99-1.00) | 1.00 (0.99-1.00) |
| | $^{89}$Zr-antiCD20 (18 MBq$_{74inj}$) | | |
| | D0 | D3 | D6 |
| Brain | 1.00 (0.97-1.00) | 0.96 (0.73-1.00) | 1.00 (0.96-1.00) |
| Kidney | 0.99 (0.97-1.00) | 0.98 (0.91-1.00) | 0.98 (0.83-1.00) |
| Lung | 1.00 (0.98-1.00) | 1.00 (0.99-1.00) | 1.00 (0.99-1.00) |
| Spleen | 0.99 (0.96-1.00) | 0.86 (0.39-0.98) | 0.81 (0.10-0.98) |
| Liver | 1.00 (0.99-1.00) | 1.00 (0.78-1.00) | 0.99 (0.94-1.00) |
| | $^{89}$Zr-antiEGFR (18 MBq$_{37inj}$) | | |
| | D0 | D3 | D6 |
| Brain | 1.00 (0.97-1.00) | 0.99 (0.94-1.00) | 0.99 (0.97-1.00) |
| Kidney | 0.97 (0.85-1.00) | 0.99 (0.96-1.00) | 0.97 (0.78-1.00) |
| Lung | 1.00 (1.00-1.00) | 1.00 (1.00-1.00) | 1.00 (0.99-1.00) |
| Spleen | 0.99 (0.92-1.00) | 1.00 (0.97-1.00) | 0.98 (0.89-1.00) |
| Liver | 1.00 (0.99-1.00) | 1.00 (0.99-1.00) | 1.00 (1.00-1.00) |
| | $^{89}$Zr-antiCD44 (18 MBq$_{37inj}$) | | |
| | D0 | D1 | D4 |
| Brain | 1.00 (0.99-1.00) | 1.00 (1.00-1.00) | 0.99 (0.97-1.00) |
| Kidney | 1.00 (0.99-1.00) | 1.00 (0.99-1.00) | 0.98 (0.93-0.99) |
| Lung | 1.00 (1.00-1.00) | 1.00 (1.00-1.00) | 0.99 (0.97-1.00) |
| Spleen | 1.00 (1.00-1.00) | 1.00 (1.00-1.00) | 1.00 (0.99-1.00) |
| Liver | 1.00 (1.00-1.00) | 1.00 (1.00-1.00) | 1.00 (1.00-1.00) |
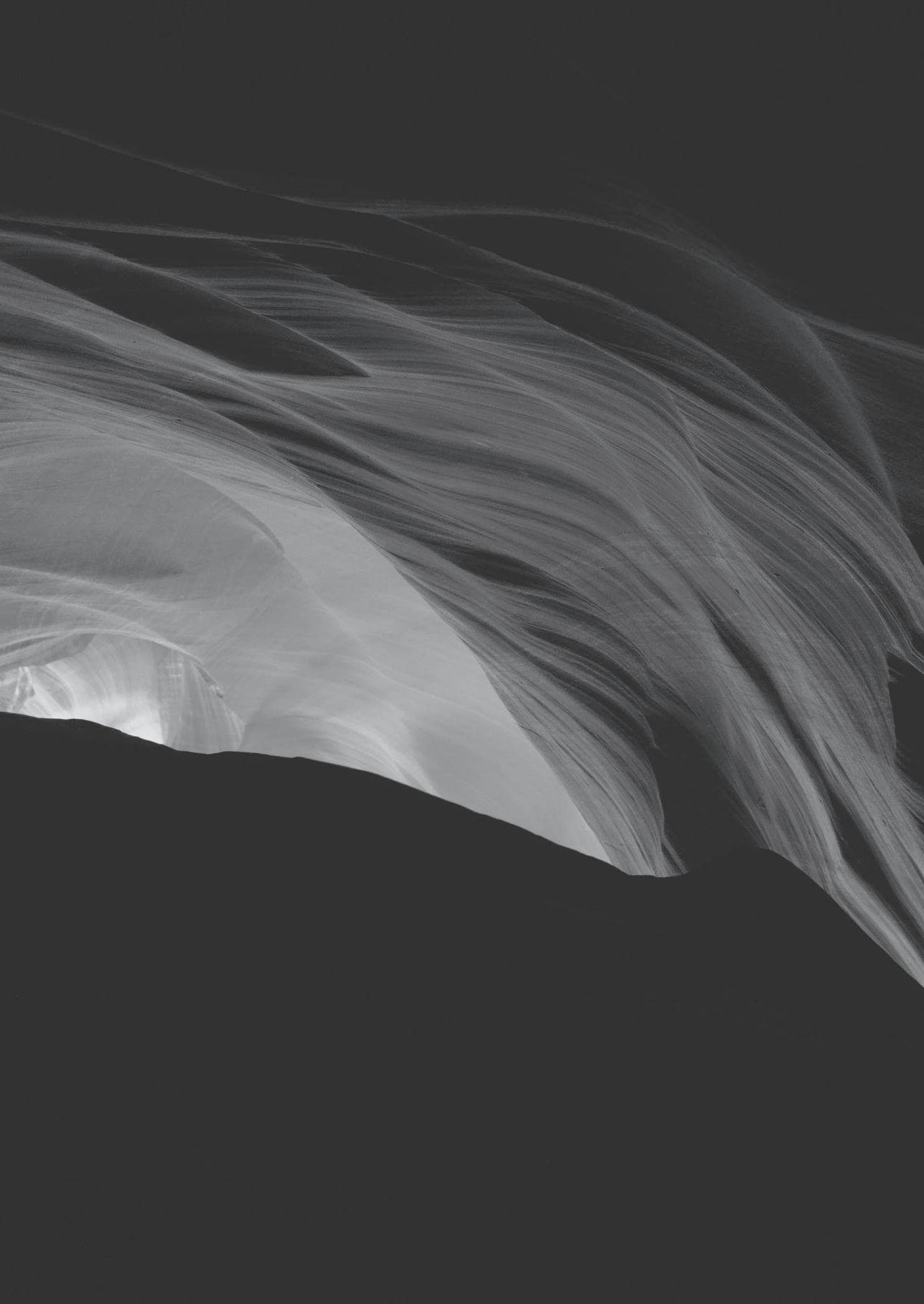
# Interobserver reproducibility of tumor uptake quantification with $^{89}$Zr-immuno-PET: a multicenter analysis

Yvonne W.S. Jauw

Frederike Bensch

Adrienne H. Brouwers

Otto S. Hoekstra

Josée M. Zijlstra

Simone Pieplenbosch

Carolien P. Schröder

Sonja Zweegman

Guus A.M.S. van Dongen

C. Willemien Menke-van der Houven van Oordt

Elisabeth G.E. de Vries

Henrica C.W. de Vet

Ronald Boellaard

Marc C. Huisman

# ABSTRACT

**Purpose:** In-vivo quantification of tumor uptake of 89-zirconium ($^{89}$Zr)-labeled monoclonal antibodies (mAbs) with PET provides a potential tool in strategies to optimize tumor targeting and therapeutic efficacy. A specific challenge for $^{89}$Zr-immuno-PET is low tumor contrast. This is expected to result in interobserver variation in tumor delineation. Therefore, the aim of this study was to determine interobserver reproducibility of tumor uptake measures by tumor delineation on $^{89}$Zr-immuno-PET scans.

**Methods:** Data were obtained from previously published clinical studies performed with $^{89}$Zr-rituximab, $^{89}$Zr-cetuximab and $^{89}$Zr-trastuzumab. Tumor lesions on $^{89}$Zr-immuno-PET were identified as focal uptake exceeding local background by a nuclear medicine physician. Three observers independently manually delineated volumes of interest (VOI). Maximum, peak and mean standardized uptake values (SUV$_{max}$, SUV$_{peak}$ and SUV$_{mean}$) were used to quantify tumor uptake. Interobserver variability was expressed as the coefficient of variation (CoV). The performance of semi-automatic VOI delineation using 50% of background-corrected AC$_{peak}$ was described.

**Results:** In total, 103 VOI were delineated (3-6 days post injection (D3-D6)). Tumor uptake (median, interquartile range) was 9.2 (5.2-12.6), 6.9 (4.0-9.6) and 5.5 (3.3-7.8) for SUV$_{max}$, SUV$_{peak}$ and SUV$_{mean}$. Interobserver variability was 0% (0-12), 0% (0-2) and 7% (5-14), respectively (n=103). The success rate of the semi-automatic method was 45%. Inclusion of background was the main reason for failure of semi-automatic VOI.

**Conclusions:** This study shows that interobserver reproducibility of tumor uptake quantification on $^{89}$Zr-immuno-PET was excellent for SUV$_{max}$ and SUV$_{peak}$ using a standardized manual procedure for tumor segmentation. Semi-automatic delineation was not robust due to limited tumor contrast.

# INTRODUCTION

Therapy with monoclonal antibodies (mAbs) has greatly improved the outcome of cancer patients (*1*). However, treatment failure due to the biology of the disease is a substantial problem. In addition to disease-related factors, therapy-related factors have been found to be responsible (*2*). There is mainly information on pharmacokinetics in blood, whereas tumor targeting is crucial for mAb efficacy. Therefore, in-vivo quantification of antibody uptake in tumors is of interest in strategies to improve the efficacy of antibody treatment (e.g. using optimized pharmacokinetic models in early drug development to improve dosing schedules). PET imaging with zirconium-89 ($^{89}$Zr)-labeled mAbs provides a non-invasive tool to visualize and quantify mAb tumor uptake (*3*), providing that biodistribution of the radiolabeled mAb represents that of the total mAb dose (radiolabeled and unlabeled). The number of clinical studies on $^{89}$Zr-labeled mAbs, also referred to as 89Zr-immuno-PET, increased in recent years (*4*). Sources of measurement errors (including factors as interobserver reproducibility of tumor uptake quantification and noise induced variability) should be known to define true biological differences. A standardized method of data acquisition and tumor uptake quantification forms the basis for obtaining experimental data that will allow such an understanding.

For quantification of tumor uptake, a volume of interest (VOI) is delineated. Subsequently, a tumor uptake measure is selected to characterize tumor uptake. Maximum (max) or peak standard uptake values ($SUV_{max}$ and $SUV_{peak}$, respectively) provide information on a limited part of the tumor. Mean standardized uptake values ($SUV_{mean}$) and total lesion uptake (TLU) serve to capture the entire lesion. In clinical studies, tumor uptake is quantified at a single (late) timepoint, or at multiple timepoints. Additionally, quantification of tumor uptake at an early timepoint (D0) can be considered, for example to estimate the blood volume fraction of the tumor.

For imaging of mAbs, $^{89}$Zr is considered a suitable radioactive isotope due to its long half-life (t1/2=78.4h), which matches the slow kinetics of large-sized proteins. Consequences of imaging with $^{89}$Zr are low positron abundance and relatively high radiation exposure, resulting in lower injected doses compared to $^{18}$F. Therefore, lower signal to noise ratios due to lower count rates may result in interobserver variability of tumor uptake quantification in $^{89}$Zr-immuno-PET. Other specific challenges for $^{89}$Zr-immuno-PET tumor delineation and

quantification are relatively low, sometimes heterogeneous, tumor uptake (Figure 1) and low (or even negative) contrast depending on tumor localization and background activity (5). Therefore, the aim of this study was to determine interobserver reproducibility of tumor uptake values by manual delineation on 89Zr-immuno-PET.
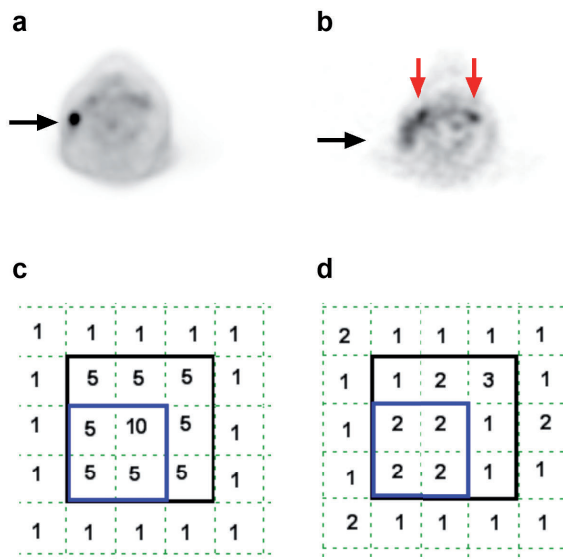


**Figure 1.** Challenges for 89Zr-immuno-PET tumor delineation and quantification

Example of 18F-FDG-PET (a) for a patient with a non-Hodgkin lymphoma showing intense tumor uptake (black arrow) and excellent contrast, while 89Zr-immuno-PET (b) with 89Zr-labeled-rituximab shows limited contrast for this tumor. Red arrows indicate uptake in blood vessels. Example of tumor delineation by two observers (observer 1 = blue line, observer 2 = black line) for 18F-FDG-PET (c) and 89Zr-immuno-PET (d). This example illustrates that excellent interobserver reproducibility ($SUV_{max}$ = 10 for both observers) can be expected for 18F-FDG-PET, despite variability in tumor delineation. The limited tumor contrast for 89Zr-immuno-PET may result in substantial interobserver variability, even for $SUV_{max}$ (a value of 2 and 3 for observer 1 and 2, respectively).

## MATERIALS AND METHODS

### Data inclusion

For this retrospective study, 89Zr-immuno-PET scans with corresponding 18F-FDG-PET scans were collected. Data were selected from previously published clinical studies with therapeutic mAbs: 89Zr-rituximab in patients with B cell

lymphoma ((6); Dutch Trial Register NTR 3392), $^{89}$Zr-cetuximab in patients with colorectal cancer ((5); NCT01691391) and $^{89}$Zr-trastuzumab in patients with breast cancer ((7); NCT01691391). These studies had been approved by the ethics committees (Medisch Ethische Toetsingscommissie VUmc and Medisch Ethische Toetsingscommissie UMC Groningen) and all subjects signed an informed consent. Data acquisition and visual assessment of tumor uptake was done locally: from the first two studies performed at the VUmc all subjects with visible tumor uptake were included, from the last study performed at the UMCG seven subjects were selected randomly. Scan data at 1 hour (D0), 72 hours (D3) and 144 hours (D6) post injection (p.i.) for $^{89}$Zr labeled rituximab and cetuximab and at 96 hours (D4) p.i. for $^{89}$Zr-trastuzumab were included. See Table 1 for patient characteristics and $^{89}$Zr-immuno-PET scan details. $^{89}$Zr-rituximab and $^{89}$Zr-cetuximab PET scans were performed on a Philips Gemini TF-64 or Ingenuity TF-128 PET-CT scanner (Philips Healthcare, the Netherlands). A Siemens Biograph mCT64 PET-CT scanner (Siemens Healthcare, the Netherlands) was used for the $^{89}$Zr-trastuzumab-PET scans.

## VOI delineation

All immuno-PET scans were acquired and reconstructed to conform to recommendations for multicenter harmonization of $^{89}$Zr-immuno-PET (8). Visual assessment of immuno-PET scans was performed by an experienced nuclear medicine physician (OSH for $^{89}$Zr-rituximab and $^{89}$Zr-cetuximab, AHB for $^{89}$Zr-trastuzumab). Tumor uptake was defined as focal uptake exceeding local background. For visually positive tumor lesions, a screenshot indicating tumor localization on immuno-PET was obtained for tumor uptake quantification. Quantitative assessment of tumor uptake for all lesions was independently performed by 3 observers (1 data analyst (SP), 2 physician-researchers (FB, YJ)). Tumor delineation for all VOI was performed using the ACCURATE software tool (developed in IDL version 8.4 (Harris Geospatial Solutions, Bloomfield, USA)) [9].

The observers recorded the analysis time per tumor lesion and VOI delineation method.

*Manual tumor delineation on immuno-PET*. The observers manually delineated tumor VOI on the immuno-PET scans (attenuation corrected image), using the low dose CT for anatomical reference (Figure 2a). Adjustment of the following

settings was allowed: zoom, contrast and orientation (coronal/axial/sagittal). Use of a threshold (upper or lower limit) or fixed size VOI was not allowed. For [89]Zr-rituximab and [89]Zr-cetuximab, tumors were manually delineated on both the D3 and D6 scans, starting with the latest time point. On D0, no tumor uptake was visible, therefore the VOI delineated on D6 were imported to the D0 scan. Observers could manually adjust localization of the VOI to optimize matching of the anatomical position of the tumor lesion on the D0 scan.

For all VOI, max, peak and mean activity concentrations (AC in Bq/mL) were derived and converted to standardized uptake values (SUV), by correcting for body weight and injected dose (ID). In addition, delineated volume (mL) and TLU (defined as $AC_{mean}$ * volume, in %ID) were obtained.

*Manual tumor delineation on immuno-PET after viewing the ^{18}F-FDG-PET.* In order to support delineation of the tumor, the observers had access to the corresponding ^{18}F-FDG-PET and could adapt the original manually delineated VOI if necessary (for example by creating a smaller or larger VOI, or changing the position of the VOI) (Figure 2b). This procedure was performed on scans with visible tumor uptake (D3, D4, D6). The number of VOI that were adapted after viewing the ^{18}F-FDG-PET was obtained.

*Semi-automatic VOI delineation.* Finally, we investigated the feasibility of a mask-restricted semi-automatic VOI delineation method. Each observer, for every tumor lesion, manually delineated a mask, which is a VOI including the tumor, excluding non-tumor structures (e.g. nearby blood vessels) on the immuno-PET scan. Subsequently, the semi-automatic VOI was generated including all voxels with a value ≥50% of background-corrected $AC_{peak}$ within the mask (Figure 2c). The semi-automatic isocontour was defined as 0.5 * (peak value + average background value). The background region was determined with a region growing algorithm of the tumour border, expanding three voxels away from the border of the tumour in all three dimensions (*10*). The observers rated the semi-automatic VOI and accepted the VOI if it contained the tumor and no other structures or background. The number of tumor lesions for which the semi-automatic VOI was accepted by all observers was obtained.
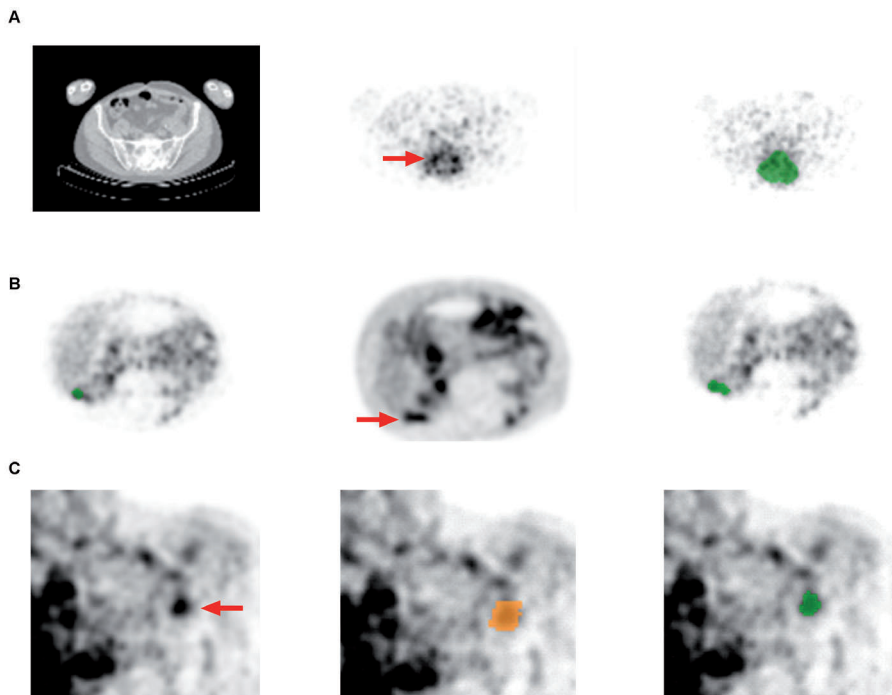
Figure 2 VOI delineation methods for $^{89}$Zr-immuno-PET

Manual tumor delineation on immuno-PET (a) using the low dose CT (left panel), attenuation corrected $^{89}$Zr-cetuximab-PET on D6 (middle panel) with tumor lesion indicated by the red arrow and example VOI on $^{89}$Zr-cetuximab-PET shown in green (right panel).

Manual tumor delineation on immuno-PET after reviewing the corresponding $^{18}$F-FDG-PET (b) the original manually delineated VOI shown in green on the $^{89}$Zr-trastuzumab-PET on D4 (left panel), reviewing the $^{18}$F-FDG-PET scan with tumor lesion indicated by the red arrow (middle panel) and adapting the original VOI after reviewing the $^{18}$F-FDG-PET scan, the FDG adapted tumor VOI shown on $^{89}$Zr-trastuzumab-PET is in green (right panel). Semi-automatic delineation (c) with the attenuation corrected $^{89}$Zr-rituximab-PET on D6 (left panel), the mask delineated on the $^{89}$Zr-rituximab-PET shown in orange (middle panel) and the semi-automatic VOI (50% of $AC_{peak}$, mask restricted) on the $^{89}$Zr-rituximab-PET shown in green (right panel). This semi-automatic VOI was accepted by the observer, as it contains tumor and no other structures or background.

## Eligibility criteria for VOI delineation

Quantification of lesions with low tumor uptake and/or high background uptake (e.g. lesions with low contrast and/or nearby presence of blood vessels or elevated healthy tissue uptake) is difficult, due to the intrinsically low signal to noise ratios in $^{89}$Zr-immuno-PET. To ensure that quantification is only reported when delineation is feasible, a method to determine eligibility for VOI delineation was explored. Criteria were selected based on the potential for incorporation in a standardized workflow for tumor identification by a nuclear medicine physician, followed by tumor delineation by a data-analist.

When measurement variability for SUV$_{max}$ was > 0, VOI were assessed for apparent insufficient tumor contrast for manual tumor delineation.
Based on this assessment VOI were deemed ineligible for quantification, according to the following criteria:

1. A different structure was delineated by at least 1 observer.
2. The voxel with maximum intensity was located at the border of the VOI, of at least 1 observer.

Interobserver variability and reliability were analyzed for the entire group of VOI, as well as for the subset of VOI eligible for quantification.

## Interobserver reproducibility

Interobserver reproducibility for manual tumor delineation on immuno-PET was assessed by an agreement parameter (standard error of measurement (SEM)) as well as a reliability parameter (ICC; (*11*)). As we expected that the interobserver variability between lesions within a single patient was equal or higher than between patients, we performed a VOI-based analysis.

*Interobserver variability.* The agreement parameter reflects the measurement error due to interobserver variability (*11*). For every tumor lesion, three values (value$_1$, value$_2$ and value$_3$) were obtained from observer 1, 2 and 3, respectively. Absolute interobserver variability was calculated as:

$$SEM = SD\ (value1, value2, value3), \tag{1}$$

where SD is the standard deviation.
SEM was calculated for each individual tumor lesion and has the same unit as the uptake measure (SUV$_{max}$, SUV$_{peak}$ and SUV$_{mean}$, dimensionless; volume in mL; TLU in %ID).
Relative interobserver variability was calculated as:

$$CoV = SEM\ /\ average\ (value\ 1,\ value\ 2,\ value\ 3)\ *\ 100, \tag{2}$$

where CoV (%) is the coefficient of variation.

When all observers measure the exact same tumor uptake, SEM and CoV equal 0. Correlation of absolute and relative variability with tumor uptake was assessed.

For a group of $n$ VOI, the interobserver variability is given as the median (interquartile range).

*Reliability.* A reliability parameter was used to assess whether differences in tumor uptake between lesions can be distinguished, despite measurement error due to interobserver variability. A two-way random model with absolute agreement (single measure) was used to obtain the ICC and 95% confidence interval. This means that the 3 observers in our study were considered as a random sample of all possible observers, and the systematic differences between the observers were included in the measurement error as we were interested in absolute agreement between the observers.

Reliability, expressed as ICC, was calculated as:

$$ICC = \sigma^2_{lesion} / (\sigma^2_{lesion} + \sigma^2_{obs} + \sigma^2_{error}), \qquad [3]$$

where $\sigma^2_{obs}$ is the systematic part, and $\sigma^2_{error}$ is the random part of the measurement error, while $\sigma^2_{lesion}$ is the true variance between tumor lesions. ICC calculations were performed in SPSS, version 22.

## Statistical analysis

For comparison of interobserver variability between two groups, Wilcoxon matched-pairs signed rank test was used for paired data (e.g. SUV$_{mean}$ on D3 and D6 for the same tumor lesions). For comparison of median CoV between multiple groups, a one-way ANOVA (non-parametric) was performed, using Friedman test with Dunn's multiple correction to compare median CoV for paired data (SUV$_{mean}$, SUV$_{max}$ and SUV$_{peak}$ for the same tumor lesions). For all statistical tests, a p-value $<0.05$ was considered statistically significant. Statistical tests were performed in GraphPad Prism, version 6.02.

# RESULTS

## VOI delineation

In total, 103 VOI were manually delineated by each observer. The number of VOI was not evenly distributed over the patients (Table 1). The range in interobserver variability (SEM for SUV$_{peak}$) for all VOI combined was 0 to 2.3 (median 0.4,

n=103). The range in interobserver variability between VOI within a single patient was 0 to 2.3 (median 0.6, n=22) for patient 2 ($^{89}$Zr-rituximab at D6). Interobserver variability (SEM) at D6 for the remaining five $^{89}$Zr-rituximab patients ranged from 0.1 to 1.4 (median 0.3, n=8). Thus, as interobserver variability was higher within a single patient than between patients, a VOI-based analysis was performed.

Table 1 Patient characteristics and $^{89}$Zr-immuno-PET scan details

| Patient | mAb | Gender | Injected dose (MBq) | $^{89}$Zr-immuno-PET (n= number of VOI) | | | |
|---|---|---|---|---|---|---|---|
| | | | | D0 | D3 | D4 | D6 |
| 1 | rituximab | F | 69.8 | 1 | 1 | - | 1 |
| 2 | rituximab | M | 75.3 | 22 | 22 | - | 22 |
| 3 | rituximab | M | 79.2 | 2 | 2 | - | 2 |
| 4 | rituximab | M | 75.0 | 0* | 1 | - | 1 |
| 5 | rituximab | F | 75.6 | 6 | 0 | - | 6 |
| 6 | cetuximab | F | 36.7 | 2 | 2 | - | 2 |
| 7 | cetuximab | M | 35.6 | 2 | 2 | - | 2 |
| 8 | cetuximab | F | 36.2 | 2 | 2 | - | 2 |
| 9 | cetuximab | F | 36.5 | 1 | 1 | - | 1 |
| 10 | cetuximab | F | 35.5 | 2 | 0 | - | 2 |
| 11 | cetuximab | M | 38.1 | 0† | 0 | - | 1 |
| 12 | trastuzumab | F | 35.0 | - | - | 5 | - |
| 13 | trastuzumab | F | 38.2 | - | - | 4 | - |
| 14 | trastuzumab | F | 35.8 | - | - | 5 | - |
| 15 | trastuzumab | F | 37.3 | - | - | 4 | - |
| 16 | trastuzumab | F | 38.3 | - | - | 5 | - |
| 17 | trastuzumab | F | 35.3 | - | - | 2 | - |
| 18 | trastuzumab | F | 37.0 | - | - | 3 | - |
| Total | | | | 40 | | 103 | |

*Technical error: 1 VOI missing for patient 4.
†No D0 scan available: 1 VOI missing for patient 11.
D0 VOI were delineated on D6 and imported to the D0 scan (data marked in grey).

Manual delineation on $^{89}$Zr-immuno-PET required a median time of 2 minutes (range 1 to 5 minutes). Viewing of the $^{18}$F-FDG-PET /adaption of the original VOI required an additional time of 1 minute (range 1 to 30 minutes). The semi-automatic procedure required 1 minute (range 1 to 5 minutes).

All observers reported difficulties to distinguish the borders of some tumor lesions on immuno-PET, especially if the tumor was in proximity to other structures with high uptake, e.g. a blood vessel. Viewing the corresponding $^{18}$F-FDG-PET did not resolve this issue, as the localization and borders of the

tumor lesions on immuno-PET were still not fully clear when viewing both the immuno-PET and the ^{18}F-FDG-PET. After viewing the corresponding ^{18}F-FDG-PET, 25% of the VOI were adapted by at least 1 observer (Table 2).

Semi-automatically generated VOI were accepted by all three observers in 45% of all VOI (Table 2). Inclusion of background was the main reason for failure of semi-automatic VOI.

Table 2 Effect of viewing the ^{18}F-FDG-PET on manual tumor delineation on immuno-PET and success rate of semi-automatic delineation

| | [89]Zr-rituximab | | [89]Zr-cetuximab | | [89]Zr-trastuzumab | All |
|---|---|---|---|---|---|---|
| | D3 | D6 | D3 | D6 | D4 | |
| % of VOI changed by ≥ 1 observer after viewing the ^{18}F-FDG-PET | 19% | 34% | 0% | 10% | 31%[*] | 25% |
| % of VOI accepted after semi-automatic delineation | 58% | 66% | 14% | 30% | 21% | 45% |

[*]No ^{18}F-FDG-PET available for patient 17

### Eligibility criteria for VOI delineation

Measurement variability for $SUV_{max}$ was > 0 in 25% (26/103) of the manually delineated VOI.

In 4% of the cases (4/103) a different structure (e.g. another tumor lesion) was delineated by at least 1 observer (2/32 (D6) for [89]Zr-rituximab; 1/10 (D6) for [89]Zr-cetuximab and 1/28 (D4) for [89]Zr-trastuzumab). In 15% of the cases (15/103), the voxel with the maximum intensity was located at the border of the VOI (3/26 (D3) and 2/30 (D6) for [89]Zr-rituximab; 5/7 (D3) and 1/9 (D6) for [89]Zr-cetuximab and 4/27 (D4) for [89]Zr-trastuzumab).

Application of eligibility criteria resulted in exclusion of 19 VOI, as tumor contrast was apparently insufficient for correct VOI delineation.

### Interobserver reproducibility
*Interobserver variability.*

Relative interobserver variability (CoV) was not correlated with tumor uptake ($SUV_{mean}$) (Figure 3). Therefore, interobserver variability is reported as a relative value per individual VOI and per datagroup (e.g. timepoint, mAb) (Table 3). For all VOI combined (n=103), interobserver variability was 0% (0-2) for $SUV_{max}$, 0% (0-12) for $SUV_{peak}$ and 7% (5-14) for $SUV_{mean}$. Manual delineation resulted in an interobserver variability of 35% (21-49) for delineated volume and 30% (17-44) for TLU.

There was no difference in interobserver variability for VOI delineated at D3 or D6 for $^{89}$Zr-rituximab (6 vs 8%, p =0.38, n=26). To obtain tumor uptake at D0 (without visible tumor contrast), a different technique was applied (importing VOI delineated at D6 to the D0 scan). Using this method, interobserver variability for SUV$_{mean}$ at D0 was 13% (8-28) for $^{89}$Zr-rituximab and 10% (5-27) for $^{89}$Zr-cetuximab (Supplemental Table 1). Interobserver variability did not change after viewing the corresponding $^{18}$F-FDG-PET (p=0.62, n = 25 VOI adapted by at least 1 observer).

VOI eligible for quantification (n=84) showed higher tumor uptake (median SUV$_{peak}$ of 7.6 vs 3.8, p<0.001) and lower interobserver variability (SUV$_{peak}$, 0 vs 17%, p<0.001) compared to ineligible VOI (n=19).



**a**
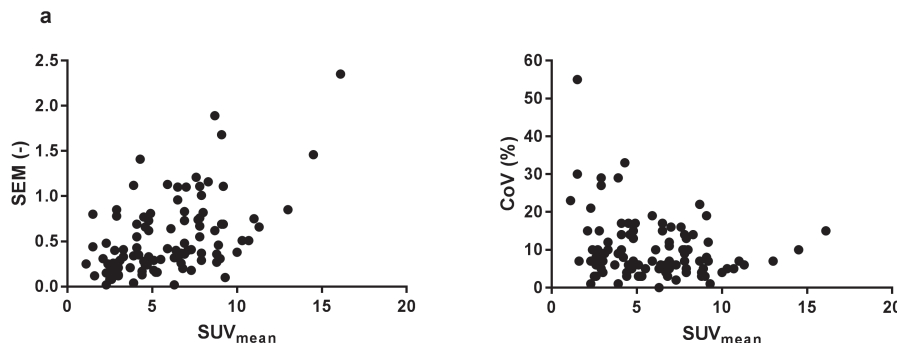
Figure 3 Absolute and relative interobserver variability as a function of tumor uptake

a) Absolute variability (SEM) per individual VOI as a function of tumor uptake (SUV$_{mean}$), Spearman correlation coefficient is 0.47 and p <0.0001 (n=103).

b) Relative variability (CoV) per individual VOI as a function of tumor uptake (SUV$_{mean}$).

Spearman correlation coefficient is -0.16 and p= 0.10 (n=103).

SUV$_{mean}$ is presented as the average value for observer 1, 2 and 3.

Table 3 Interobserver variability for $^{89}$Zr-immuno-PET

| | | $^{89}$Zr-rituximab | | $^{89}$Zr-cetuximab | | $^{89}$Zr-trastuzumab | | all VOI combined |
| --- | --- | --- | --- | --- | --- | --- | --- | --- |
| | | D3 | D6 | D3 | D6 | D4 | D6 | |
| SUV$_{max}$ | all | 0 (0-5); n=26<br>8.0 (5.3-11.5) | 0 (0-1); n=32<br>11.8 (5.3-17.3) | 0 (0-0); n=7<br>10.2 (9.3-13.0) | 0 (0-5); n=10<br>5.4 (3.7-8.8) | 0 (0-7); n=28<br>8.6 (5.6-12.1) | 0 (0-5); n=10<br>5.4 (3.7-8.8) | 0 (0-2); n=103<br>9.2 (5.2-12.6) |
| | eligible | 0 (0-5); n=23<br>8.4 (5.3-11.4) | 0 (0-0); n=28<br>12.4 (6.1-18.0) | 0 (0-0); n=2<br>14.2 (13.0-15.4) | 0 (0-0); n=8<br>4.1 (3.6-8.3) | 0 (0-0); n=23<br>9.9 (5.9-12.6) | 0 (0-0); n=8<br>4.1 (3.6-8.3) | 0 (0-0); n=84<br>9.8 (5.5-13.5) |
| SUV$_{peak}$ | all | 0 (0-0); n=26<br>8.7 (5.9-10.0) | 0 (0-3); n=32<br>8.5 (4.3-14.1) | 0 (12-17); n=7<br>4.2 (1.8-5.8) | 0 (0-6); n=10<br>4.4 (3.0-7.3) | 18 (0-32); n=28<br>5.6 (3.7-8.2) | 0 (0-6); n=10<br>4.4 (3.0-7.3) | 0 (0-12); n=103<br>6.9 (4.0-9.6) |
| | eligible | 0 (0-0); n=23<br>8.9 (7.3-10.1) | 0 (0-0); n=28<br>9.7 (4.7-14.5) | 0 (0-0); n=2<br>5.7 (5.3-6.1) | 0 (0-0); n=8<br>3.2 (2.9-6.8) | 0 (0-30); n=23<br>6.3 (4.0-8.8) | 0 (0-0); n=8<br>3.2 (2.9-6.8) | 0 (0-0); n=84<br>7.6 (4.7-10.4) |
| SUV$_{mean}$ | all | 6 (5-12); n=26<br>6.8 (5.0-7.7) | 7 (4-14); n=32<br>7.0 (3.9-9.1) | 12 (7-15); n=7<br>3.3 (1.6-4.8) | 10 (5-15); n=10<br>3.8 (2.7-4.8) | 7 (5-15); n=28<br>5.0 (3.1-7.9) | 10 (5-15); n=10<br>3.8 (2.7-4.8) | 7 (5-14); n=103<br>5.5 (3.3-7.8) |
| | eligible | 6 (5-12); n=23<br>6.9 (6.1-7.3) | 7 (4-12); n=28<br>7.8 (4.2-9.2) | 6 (3-8); n=2<br>4.7 (4.2-5.1) | 8 (4-10); n=8<br>3.1 (2.6-4.6) | 7 (5-13); n=23<br>5.1 (3.9-8.0) | 8 (4-10); n=8<br>3.1 (2.6-4.6) | 7 (5-11); n=84<br>6.5 (4.1-8.0) |
| Volume (mL) | all | 26 (19-47); n=26<br>7.8 (4.2-25.0) | 41 (18-59); n=32<br>7.7 (3.9-17.6) | 35 (29-47); n=7<br>3.6 (2.3-7.4) | 39 (29-66); n=10<br>4.1 (2.2-44.8) | 36 (25-77); n=28<br>4.9 (2.1-8.7) | 39 (29-66); n=10<br>4.1 (2.2-44.8) | 35 (21-49); n=103<br>6.1 (3.6-14.8) |
| | eligible | 23 (19-35); n=23<br>8.8 (3.8-25.6) | 36 (17-49); n=28<br>7.7 (3.8-16.5) | 42 (35-48); n=2<br>85.1 (2.3-167.9) | 35 (22-46); n=8<br>3.2 (2.1-106) | 35 (24-48); n=23<br>5.1 (2.4-10.8) | 35 (22-46); n=8<br>3.2 (2.1-106) | 33 (19-46); n=84<br>6.5 (3.5-16.5) |
| TLU (%ID) | all | 21 (15-34); n=26<br>0.06 (0.03-0.13) | 32 (13-45); n=32<br>0.05 (0.02-0.17) | 38 (34-46); n=7<br>0.02 (0.01-0.03) | 32 (21-56); n=10<br>0.01 (0.01-0.26) | 27 (18-70); n=28<br>0.05 (0.01-0.08) | 32 (21-56); n=10<br>0.01 (0.01-0.26) | 30 (17-44); n=103<br>0.05 (0.02-0.12) |
| | eligible | 18 (14-31); n=23<br>0.07 (0.03-0.18) | 27 (12-42); n=28<br>0.05 (0.02-0.15) | 36 (34-38); n=2<br>0.43 (0.01-0.85) | 30 (18-39); n=8<br>0.01 (0.01-0.55) | 26 (18-35); n=23<br>0.06 (0.02-0.12) | 30 (18-39); n=8<br>0.01 (0.01-0.55) | 25 (16-37); n=84<br>0.06 (0.02-0.13) |

Data is presented as interobserver variability (CoV in %) on the first line and VOI metric on the second line (median value (interquartile range)

*Reliability.* ICC data are presented in Table 4. For eligible VOI, ICC values for $SUV_{max}$, $SUV_{peak}$ and $SUV_{mean}$ were $\geq 0.90$ for [89]Zr-rituximab (D3, D6) and for [89]Zr-cetuximab (D6). For [89]Zr-trastuzumab, ICC values $\geq 0.82$ were obtained. For volume and TLU ICC values were $> 0.66$ for all mAbs. In addition, ICC values for all combinations of 2 observers were calculated (Supplemental Table 2).

Table 4 Reliability of tumor uptake quantification for [89]Zr-immuno-PET

| | | [89]Zr-rituximab | | [89]Zr-cetuximab | | [89]Zr-trastuzumab |
|---|---|---|---|---|---|---|
| | | D3 | D6 | D3 | D6 | D4 |
| $SUV_{max}$ | all | 1.00; n=26 (1.00-1.00) | 1.00; n=32 (1.00-1.00) | 0.93; n=7 (0.77-0.99) | 0.72; n=10 (0.41-0.91) | 0.97; n=28 (0.95-0.99) |
| | eligible | 1.00; n=23 (1.00-1.00) | 1.00; n=28 (1.00-1.00) | NA* | 1.00; n=8 (NA-NA) | 0.97; n= 23 (0.95-0.99) |
| $SUV_{peak}$ | all | 1.00; n=26 (1.00-1.00) | 1.00; n=32 (1.00-1.00) | 0.94; n=7 (0.82-0.99) | 0.75; n=10 (0.46-0.92) | 0.83; n=28 (0.69-0.92) |
| | eligible | 1.00; n=23 (1.00-1.00) | 1.00; n=28 (1.00-1.00) | NA* | 1.00; n=8 (1.00-1.00) | 0.82; n= 23 (0.64-0.91) |
| $SUV_{mean}$ | all | 0.92; n=26 (0.84-0.96) | 0.95; n=32 (0.91-0.97) | 0.93; n=7 (0.79-0.99) | 0.79; n=10 (0.56-0.96) | 0.94; n=28 (0.89-0.97) |
| | eligible | 0.90; n=23 (0.80-0.96) | 0.94; n=28 (0.90-0.97) | NA* | 0.92; n=8 (0.73-0.98) | 0.93; n= 23 (0.86-0.97) |
| Volume (mL) | all | 0.85; n=26 (0.74-0.92) | 0.12; n=32 (-0.07-0.36) | 0.80; n=7 (0.46-0.96) | 0.83; n=10 (0.60-0.95) | 0.67; n=28 (0.48-0.82) |
| | eligible | 0.87; n=23 (0.77-0.94) | 0.72; n=28 (0.55-0.85) | NA* | 0.83; n=8 (0.56-0.96) | 0.66; n= 23 (0.45-0.82) |
| TLU (%ID) | all | 0.90; n=26 (0.83-0.95) | 0.65; n=32 (0.47-0.79) | 0.86; n=7 (0.61-0.97) | 0.89; n=10 (0.72-0.97) | 0.71; n=28 (0.54-0.84) |
| | eligible | 0.90; n=23 (0.82-0.96) | 0.83; n=28 (0.72-0.91) | NA* | 0.89; n=8 (0.70-0.98) | 0.70; n= 23 (0.51-0.85) |

Data presented as ICC (95% confidence interval).
* NA = ICC not available, 2 eligible VOI

## DISCUSSION

Interobserver reproducibility for tumor uptake measures was investigated, as knowledge of measurement error is required for future clinical application of [89]Zr-immuno-PET. Interobserver reproducibility was excellent for $SUV_{max}$ and $SUV_{peak}$ (variability of 0%) and very reasonable for $SUV_{mean}$ (variability of 7%), especially

considering the lower signal to noise ratios for $^{89}$Zr-immuno-PET compared to $^{18}$F-FDG-PET. For example, interobserver variability of 14% for SUV$_{mean}$ has been reported for manual tumor delineation of pulmonary lesions on $^{18}$F-FDG-PET (*12*).

For $^{89}$Zr-immuno-PET, this is the first study to report interobserver reproducibility of tumor uptake measures. Several factors should be considered to determine to which extent these results are generalizable. Interobserver reproducibility was determined for three different $^{89}$Zr-labeled mAbs (rituximab, cetuximab and trastuzumab), at different time points (D3, D4, D6) and different injected doses (74MBq for $^{89}$Zr-rituximab vs 37MBq for $^{89}$Zr-trastuzumab and $^{89}$Zr-cetuximab). This study was not designed to assess how these factors individually impact interobserver variability. Instead, the results obtained reflect a broad range of uptake characteristics, which can be used as a general estimate of the measurement error due to interobserver variability in VOI delineation. Future, larger studies can focus on factors that influence tumor contrast (e.g. tumor localization, differences in uptake characteristics between mAbs).

Although ICC are reported, reliability is dependent on the range in tumor uptake and therefore not directly generalizable to other studies. In addition, tumor uptake and interobserver variability are influenced by the disproportionate high number of lesions in patient 2. Therefore, ICC values for this lesion-based analysis cannot be applied to determine whether we can reliably detect differences between patients. Improved tumor contrast, in combination with a broad range in tumor uptake, is expected to result in improved interobserver reproducibility for all tumor uptake measures.

Another aspect to consider is that all observers used the same quantification software and a standardized operating procedure (no use of thresholds or fixed size VOI). Use of different software platforms without a standardized procedure may result in lower interobserver reproducibility. In addition, generalizability could be hampered if the three observers would have read the images in a systematically different way. In this study, there was no indication for such a systematic difference between the three observers.

These results suggest that interobserver agreement for SUV$_{mean}$ is sufficient to consider this uptake measure to quantify tumor uptake in a larger tumor area (opposed to only the maximum voxel or very small sample of the tumor as defined by SUV$_{peak}$). However, manual tumor delineation is a laborious task. As the concept of total lesion mAb uptake is of interest, the feasibility of semi-automatic VOI

delineation was explored. For ^{18}F-FDG-PET with perfect interobserver agreement for $SUV_{max}$ (*13*) and higher tumor contrast, semi-automatic procedures are used to obtain $SUV_{mean}$ based on a semi-automatic method (e.g. with a threshold of 0.6 of $SUV_{max}$), total lesion glycolysis (TLG) and total metabolic tumor volume (TMVT) (*14, 15*). For our datasets, the area included by the semi-automatic VOI was often too large, indicating low tumor to local background ratios, resulting in inclusion of background voxels in the semi-automatic VOI.

For mAbs showing higher tumor contrast, as well as imaging with higher count statistics (due to e.g. higher injected doses or the availability of scanners with improved detection sensitivity or time of flight resolution), semi-automatic delineation may be feasible. Reduction of noise (e.g. by introduction of total body PET scanners) is the first step towards further improvement of tumor delineation procedures. Future studies into accuracy of tumor delineation should include 'supervised' delineation methods (semi-automatic procedures with a manual check) in which the optimal threshold is experimentally determined. If the success rate can thus be increased, this may lead to further development towards a robust automatic method, which is desired for clinical application. As semi-automatic delineation was not feasible in our datasets, we explored eligibility criteria to improve standardization for manual tumor delineation, especially in case of limited tumor contrast.

In our study, 81% of the VOI (84 out of 103) were considered suitable for quantification. Based on these results, we recommend a two-step procedure to exclude lesions with insufficient tumor contrast for manual delineation: 1) Verification of VOI delineation by a nuclear medicine physician to identify delineation of an incorrect structure due to limited tumor contrast, 2) Exclusion of VOI with the voxel with the highest uptake located at the border of the VOI, indicating low tumor uptake and/or high background uptake. These measures support optimal scan interpretation and standardization, which is an essential step towards potential clinical implementation of [89]Zr-immuno-PET.

For this study, we performed a multicenter interobserver analysis for data that was originally obtained in single center studies. With this experience, the next step towards standardization of quantification for [89]Zr-immuno-PET studies can be done in the context of a multicenter study (e.g. the IMPACT trials, (NCT02228954, NCT02117466 and NCT01957332)).

Reliable delineation of tumor uptake on [89]Zr-immuno-PET allows future use as a non-invasive clinical tool to determine mAb concentrations in the tumor.

Knowledge on *in-vivo* drug delivery of mAb-based therapy (including antibody-drug conjugates, bispecific mAbs and immune checkpoint inhibitors) is crucial to understand and predict efficacy of treatment.

## CONCLUSION

This study shows that interobserver reproducibility of tumor uptake quantification on $^{89}$Zr-immuno-PET was excellent for $SUV_{max}$ and $SUV_{peak}$ using a standardized manual procedure for tumor segmentation. Semi-automatic delineation was not robust due to limited tumor contrast.

## ACKNOWLEDGEMENTS

6

# REFERENCES

1. Oldham RK, Dillman RO. Monoclonal antibodies in cancer therapy: 25 years of progress. J Clin Oncol. 2008; 26: 1774-1777.

2. Tout M, Casasnovas O, Meignan M, et al. Rituximab exposure is influenced by baseline metabolic tumor volume and predicts outcome of DLBCL patients: a Lymphoma Study Association report. Blood. 2017; 129 (19): 2616-2623.

3. Lamberts LE, Williams SP, Terwisscha van Scheltinga AG, et al. Antibody positron emission tomography imaging in anticancer drug development. J Clin Oncol. 2015; 33: 1491-504.

4. Jauw, YWS, Menke-van der Houven van Oordt CW, Hoekstra OS, et al. Immuno-positron emission tomography with zirconium-89-labeled monoclonal antibodies in oncology: what can we learn from initial clinical trials? Front. Pharmacol. 2016; 7: 131.

5. Menke-van der Houven van Oordt, CW, Gootjes EC, Huisman MC, et al. [89]Zr-cetuximab PET imaging in patients with advanced colorectal cancer. Oncotarget. 2015; 30: 30384-93.

6. Jauw, YWS, Zijlstra JM, de Jong D, et al. Performance of [89]Zr-labeled-rituximab-PET as an imaging biomarker to assess CD20 targeting: a pilot study in patients with relapsed/refractory diffuse large B cell lymphoma. PLoS One. 2017; 12: e0169828.

7. Bensch F, Brouwers AH, Lub-de Hooge MN, et al. [89]Zr-trastuzumab PET supports clinical decision making in breast cancer patients, when HER2 status cannot be determined by standard work up. Eur J Nucl Med Mol Imaging. 2018;45(13): 2300-2306. doi: 10.1007/s00259-018-4099-8. Epub 2018 Jul 30.

8. Makris NE, Boellaard R, Visser EP, et al. Multicenter harmonization of [89]Zr PET/CT performance. J Nucl Med. 2014; 55: 264-7.

9. Boellaard R. QuAntitative onCology moleCUlaR Analysis suiTE: ACCURATE. J Nucl Med. 2018; 59: 1753.

10. Frings V, de Langen AJ, Yaqub M, et al. Methodological considerations in quantification of 3'-deoxy-3'-[18F]fluorothymidine uptake measured with positron emission tomography in patients with non-small cell lung cancer. Mol Imaging Biol. 2014; 16:136-145.

11. de Vet HC, Terwee CB, Knol DL, et al. When to use agreement versus reliability measures. J Clin Epidemiol. 2006; 59: 1033-1039.

12. Huang YE, Chen CF, Huang YJ, et al. Interobserver variability among measurements of the maximum and mean standardized uptake values on (18)F-FDG PET/CT and measurements of tumor size on diagnostic CT in patients with pulmonary tumors. Acta Radiol. 2010; 51: 782-788.

13. Lee JR, Madsen MT, Bushnel D, et al. A threshold method to improve standardized uptake reproducibility. Nucl Med Commun. 2000; 21: 685-690.

14. Kanoun S, Tal I, Berriolo-Riedinger A, et al. Influence of software tool and methodological aspects of total metabolic tumor volume calculation on baseline [18F]FDG PET to predict survival in Hodgkin lymphoma. PLoS One. 2015; 10: e0140830.

15. Boellaard R, Delgado-Bolton R, Oyen WJ, et el. FDG PET/CT: EANM procedure guidelines for tumour imaging: version 2.0. Eur J Nucl Med Mol Imaging. 2015; 42: 328-354.

# SUPPLEMENTARY DATA

Supplemental Table 1. Interobserver variability for $^{89}$Zr-immuno-PET at D0

| | | $^{89}$Zr-rituximab | $^{89}$Zr-cetuximab |
|---|---|---|---|
| | | D0 | D0 |
| SUV$_{max}$ | all | 19 (8-31);n=32<br>3.7 (2.4-5.3) | 6 (6-19);n=9<br>2.7 (2.2-5.3) |
| | eligible | 17 (4-29);n=28<br>3.4 (2.2-5.3) | 8 (6-21);n=8<br>3.2 (2.5-5.4) |
| SUV$_{peak}$ | all | 18 (9-30);n=32<br>3.2 (2.0-4.8) | 5 (4-18);n=9<br>2.5 (1.8-4.9) |
| | eligible | 17 (8-24);n=28<br>3.0 (1.8-4.8) | 7 (4-21);n=8<br>3.0 (2.3-5.1) |
| SUV$_{mean}$ | all | 13 (8-28);n=32<br>1.6 (1.3-2.3) | 10 (5-27);n=9<br>1.8 (1.2-3.1) |
| | eligible | 12 (8-19);n=28<br>1.6 (1.3-2.3) | 17 (5-27);n=8<br>1.8 (1.7-3.2) |
| Volume (mL) | all | 31(17-53);n=32<br>7.7 (4.4-19.1) | 33 (27-55);n=9<br>3.6 (2.2-9.9) |
| | eligible | 26(16-45);n=28<br>7.7 (3.7-18.0) | 32 (26-49);n=8<br>3.2 (2.1-6.1) |
| TLU (%ID) | all | 38(23-56);n=32<br>0.02(0.01-0.04) | 38 (33-63);n=9<br>0.01(0.01-0.02) |
| | eligible | 34(20-46);n=28<br>0.01(0.01-0.04) | 38 (33-49);n=8<br>0.01(0.01-0.02) |

Data is presented as interobserver variability (CoV in %) on the first line and VOI metric on the second line (median value (interquartile range)).

Supplemental Table 2 ICC calculations for all possible combinations of 2 observers

| SUV$_{mean}$ | $^{89}$Zr-rituximab | | | $^{89}$Zr-cetuximab | | | $^{89}$Zr-trastuzumab |
|---|---|---|---|---|---|---|---|
| | D0 | D3 | D6 | D0 | D3 | D6 | D4 |
| O1, O2, O3 | 0.77 (0.62-0.87) | 0.90 (0.80-0.96) | 0.94 (0.90-0.97) | 0.77 (0.41-0.95) | NA | 0.92 (0.73-0.98) | 0.93 (0.86-0.97) |
| O1, O2 | 0.79 (0.60-0.90) | 0.86 (0.60-0.95) | 0.96 (0.91-0.98) | 0.94 (0.73-0.99) | NA | 0.96 (0.75-0.99) | 0.94 (0.87-0.98) |
| O1, O3 | 0.83 (0.65-0.92) | 0.94 (0.75-0.98) | 0.94 (0.88-0.97) | 0.61 (-0.05-0.92) | NA | 0.88 (0.28-0.98) | 0.93 (0.83-0.97) |
| O2, O3 | 0.69 (0.44-0.85) | 0.91 (0.80-0.96) | 0.93 (0.86-0.97) | 0.70 (0.07-0.94) | NA | 0.93 (0.71-0.99) | 0.93 (0.83-0.97) |

Data presented as ICC (95% confidence interval).

All ICC calculations were performed on VOI eligible for quantification (n=84).

D0 VOI were delineated on D6 and imported to the D0 scan (data marked in grey).
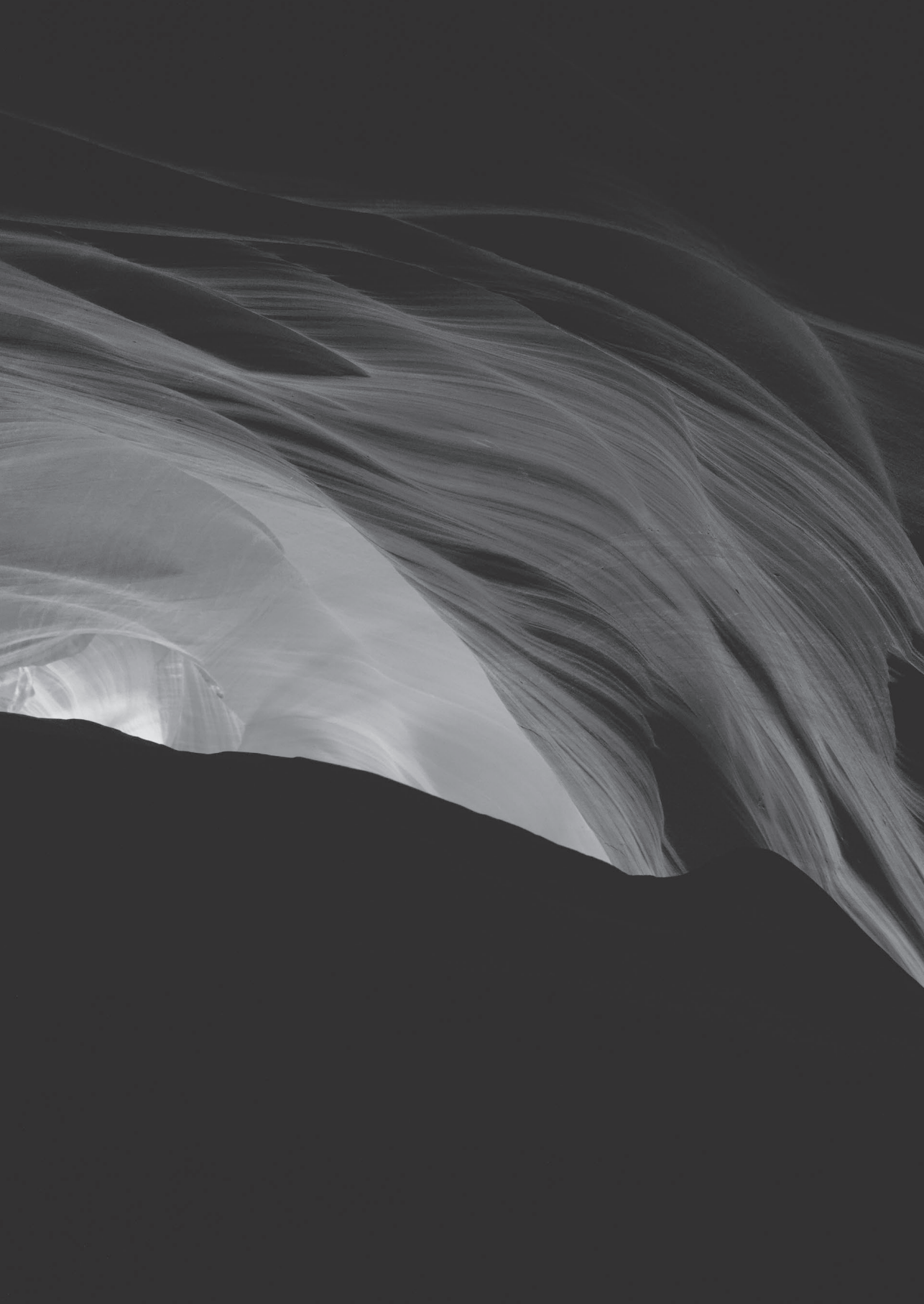
# Performance of $^{89}$Zr-labeled-rituximab PET as an imaging biomarker to assess CD20 targeting:

# a pilot study in patients with relapsed/refractory diffuse large B cell lymphoma

Yvonne W.S. Jauw
Josée M. Zijlstra
Daphne de Jong
Danielle J. Vugts
Sonja Zweegman
Otto S. Hoekstra
Guus A.M.S. van Dongen
Marc C. Huisman

# ABSTRACT

**Purpose:** Treatment of patients with diffuse large B cell lymphoma (DLBCL) includes rituximab, an anti-CD20 monoclonal antibody (mAb). Insufficient tumor targeting might cause therapy failure. Tumor uptake of $^{89}$Zirconium ($^{89}$Zr)-mAb is a potential imaging biomarker for tumor targeting, since it depends on target antigen expression and accessibility. The aim of this pilot study was to describe the performance of $^{89}$Zr-labeled-rituximab PET to assess CD20 targeting in patients with relapsed/refractory DLBCL.

**Methods:** Six patients with biopsy-proven DLBCLwere included. CD20 expression was assessed using immunohistochemistry (IHC). 74 MBq $^{89}$Zr-rituximab (10 mg) was administered after the therapeutic dose of rituximab. Immuno-PET scans on day 0, 3 and 6 post injection (D0, D3 and D6 respectively) were visually assessed and quantified for tumor uptake. Spearman's rank correlation coefficient was used to assess the correlation between tumor uptake of $^{89}$Zr-rituximab and ranking of CD20 expression in biopsies.

**Results:** Tumor uptake of $^{89}$Zr-rituximab and CD20 expression were concordant in 5 patients: for one patient, both were negative, for the other four patients visible tumor uptake was concordant with CD20-positive biopsies. Intense tumor uptake of $^{89}$Zr-rituximab on PET ($SUV_{peak}$=12.8) corresponded with uniformly positive CD20 expression on IHC with in one patient. Moderate tumor uptake of $^{89}$Zr-rituximab (range $SUV_{peak}$=3.2-5.4) corresponded with positive CD20 expression on IHC in three patients. In one patient tumor uptake of $^{89}$Zr-rituximab was observed ($SUV_{peak}$ = 3.8), while the biopsy was CD20-negative. Overall, a positive correlation was observed between tumor uptake of $^{89}$Zr-rituximab and CD20 expression in the biopsied tumor lesions ($r_s$=0.83, p=0.04, n=6).

**Conclusions:** This study provides evidence for the use of $^{89}$Zr-rituximab-PET as an imaging biomarker to assess CD20 targeting, given the observed correlation between tumor uptake of $^{89}$Zr-rituximab and CD20 expression in biopsies. Therefore, $^{89}$Zr-rituximab-PET allows for further studies relating tumor targeting to clinical benefit of rituximab treatment in individual patients.

# INTRODUCTION

DLBCL is an aggressive, potentially fatal, but curable form of lymphoma. It is the most common lymphoma subtype, representing 30% of all lymphoma. This malignancy develops from the B-cells in the lymphatic system and is characterized by expression of CD20, a transmembrane protein. The function of CD20 is still unknown, but as it is only expressed on B cells and not on other tissues, it is a usefull target for treatment. Rituximab, an anti-CD20 mAb, is currently incorporated in all first line and subsequent treatment regimens. The introduction of rituximab in first line treatment has improved the prognosis of a three-year event-free survival (EFS) from 59% to 79% for patients of 18 to 60 years old. However, patients with relapsed/refractory DLBCL have a three-year overall survival (OS) of only 49% (*1*). Early relapse (<12 months) and prior rituximab treatment are associated with a worse outcome, with a three-year EFS of 21% versus 47%, suggesting rituximab resistance. Although it is standard practice to include rituximab in second line treatment, it is unclear whether individual patients benefit from repeated rituximab treatment. To obtain clinical benefit from mAb treatment tumor targeting is required. It comprises target antigen expression, as well as a drug that reaches and binds to the target.

Target expression of CD20 is assessed by IHC on a single tumor biopsy as part of the routine work up to confirm the diagnosis of DLBCL, or to confirm relapsed/refractory disease (*2*). [Fluorine-18]-2-fluoro-2-deoxy-D-glucose ($^{18}$F-FDG)-PET is incorporated in staging and response evaluation of DLBCL (*3*), but provides no information on expression of CD20.

Molecular imaging with $^{89}$Zirconium ($^{89}$Zr)-labeled mAbs, also known as immuno-PET, allows for visualization and quantification of tumor uptake and whole body biodistribution of $^{89}$Zr-mAbs. Since tumor uptake depends on target expression and accessibility, it is a potential imaging biomarker for tumor targeting.

Two clinical trials on immuno-PET with $^{89}$Zr-labeled mAbs have reported whether tumor uptake on immuno-PET and target expression in biopsies are correlated. These studies were on $^{89}$Zr-bevacizumab, an anti-endothelial growth factor (VEGF)-A mAb, in patients with breast cancer (*5*) and $^{89}$Zr-labeled anti-membrane-bound surface glycoprotein mesothelin (MSLN) mAb in patients with pancreatic and ovarian cancer (*6*). Correlations between a measure of tumor uptake and a measure of target status were reported, to provide evidence that immuno-PET may be used as an imaging biomarker to assess tumor targeting.

The aim of this pilot study was to describe the performance of [89]Zr-labeled-rituximab PET as an imaging biomarker to assess CD20 targeting in patients with relapsed/refractory diffuse large B cell lymphoma, by correlating tumor uptake of [89]Zr-rituximab with CD20 expression in biopsied tumor lesions.

## MATERIALS AND METHODS

Data used in this pilot study was obtained as part of an ongoing main trial (registered in the Dutch Trial Register http://www.trialregister.nl, NTR 3392) with formal ethical approval from the Medical Ethics Committee of the VU University Medical Center, Amsterdam, The Netherlands (approval date July 2012, reference 2012/165). The study was performed in compliance with the principles of the Declaration of Helsinki. All patients signed an informed consent form.

Patients with a primary diagnosis of CD20-positive DLBCL, relapsed after or refractory to first line treatment with rituximab combined with anthracycline-based chemotherapy (R-CHOP), were eligible for inclusion. A ^{18}F-FDG-PET scan was performed as routine clinical staging before start of second line treatment (7).

Patients were included before start of second line treatment with rituximab combined with cisplatin-based chemotherapy. Inclusion criteria consisted of age ≥18 years, WHO performance score 0-2 and eligibility for high dose chemotherapy and autologous stem cell transplant. Patients with known central nervous system (CNS) involvement were not eligible.

Tumor biopsies were obtained to confirm refractory/relapsed disease before start of second line treatment. IHC was performed, including at least staining for CD20, CD79a, CD3 and MIB1 to support the diagnosis. As part of the routine work-up CD20 expression was reported as either present (+) or absent (-). In addition, CD20 expression was assessed semi-quantitatively as:

A. Uniformly positive in all tumor cells.
B. Heterogeneously positive, ranging from positive in the majority of cells to positivity limited to sparse groups of cells.
C. Absent, ranging from extremely sparse groups of CD20-positive cells to completely absent in all tumor cells, with a positive internal control sample and CD79a-positive.

A qualitative assessment was made for membranous or granular staining patterns. Tumor biopsies were assessed by a pathologist blinded for immuno-PET results.

89Zr (T½ =78.4 hrs) (BV Cyclotron VU, Amsterdam, the Netherlands) was coupled to rituximab via the bifunctional chelator N-succinyl-desferal. Methods used for radiolabeling have been described previously (*8-10*). The radiochemical purity was assessed by instant thin layer chromatography (iTLC) and high-performance liquid chromatography (HPLC). The immunoreactive fraction was assessed by Lindmo binding assay using either Ramos (patient 1, 2, 3) or Su-DHL4 (patient 4, 5, 6) cells. The endotoxin content was determined according to pharmacopeia using an endosafe PTS reader. Sterility of each 89Zr-rituximab batch was assured by performing a media fill immediately after final filter sterilization of each batch. The radiochemical purity, immunoreactivity and endotoxin content of every batch were assessed prior to administration to a patient. Manufacturing and radiolabeling were performed according to Good Manufacturing Practice (GMP) standards.

Patients received a therapeutic dose of rituximab (range 700-1000 mg) on day 1 of cycle 1 of second line treatment, within 2 hours followed by 89Zr-rituximab (10 mg, 74 MB +/- 10%) as an intravenous bolus injection. Venous blood samples were scheduled at t=120 min (D0), 72 hrs (D3) and 144 hrs (D6) post injection (p.i.). Whole blood and plasma radioactivity concentrations were measured with a gamma well counter (Wallac 1480 Wizard, Turku, Finland). Radioactivity measurements obtained with venous blood samples were correlated with image-derived blood pool measurements. Percentage injected dose (%ID) in blood pool on D6 was calculated using image derived radioactivity concentrations and total blood volume (*11*). Tracer availability is commonly defined as the concentration of the tracer in the plasma fraction, therefore the total activity in plasma needs to be calculated and compared to the total activity in whole blood.

Total activity in plasma on D6 was calculated from the venous blood samples, using standard hematocrit values (0.45 for males and 0,4 for females) and total blood volume. Total activity in whole blood was calculated from the venous blood samples and total blood volume. A two-tailed paired t-test was used to test for a difference between both measures of total activity.

Immuno-PET scans (Gemini TF-64/Ingenuity TF-128; Philips Healthcare, Best, the Netherlands), were acquired at D0, D3 and D6 p.i., and reconstructed as described previously (*12*). Each whole body immuno-PET scan was preceded by a 35 mAs low-dose computed tomography (ldCT) scan for attenuation and scatter correction. Immuno-PET scans were evaluated by a nuclear medicine physician, blinded for the 18F-FDG-PET and biopsy results. Lesions were considered positive

in case of focal uptake exceeding local background. Immuno-PET scans were classified as positive (moderate or intense, at the D6 scan) or negative for tumor uptake of $^{89}$Zr-rituximab in the biopsied tumor lesion. Thereafter, the immuno-PET scans were compared with the $^{18}$F-FDG-PET scans to confirm tumor localization. Tumor volumes of interest (VOIs) were manually delineated on immuno-PET scans at D3 and D6, using a semi-automatic in-house software tool. Peak (i.e. average value of a 12mm sphere positioned within the VOI so as to obtain the highest value) and mean activity concentrations ($AC_{peak}$ and $AC_{mean}$, respectively) were derived per tumor VOI. For $AC_{mean}$ standard deviations (SD) were derived per VOI. Blood pool VOIs were delineated using a fixed size VOI of the aortic arch (volume of 1.6 mL), on the ldCT and imported to the PET images. $AC_{mean}$ was derived per blood pool VOI. Standardized uptake values ($SUV_{peak}$ and $SUV_{mean}$ ± SD, respectively) were calculated for tumor lesions, and decay corrected to the time of injection. Tumor to blood ratio's (T/B) for tumor lesions were calculated as tumor AC on D6 divided by image derived blood pool AC on D6. To assess tumor uptake over time, $SUV_{peak}$ D6/D3 ratios were calculated.

Patients were ranked based on the level of CD20 expression in order to correlate biopsy results to tumor uptake of $^{89}$Zr-rituximab, defined on PET images. Spearman's rank correlation coefficient ($r_s$) as well as the two-tailed p-value were calculated to explore the relation between tumor uptake of $^{89}$Zr-rituximab, measured as $SUV_{peak}$, and the level of CD20 expression in the biopsied lesions. Statistical tests were performed using SPSS Statistics Version 22 (IBM software).

## RESULTS

Six patients with a primary diagnosis of CD20-positive DLBCL, with refractory or relapsed disease after first line treatment with R-CHOP, were included. Patient characteristics are summarized in Table 1.

Patient 2 and 6 had primary refractory disease, with a partial remission (PR) after R-CHOP. The other patients had relapsed disease, of whom two patients (1 and 3) had an early relapse within 1 year after R-CHOP. In all patients $^{18}$F-FDG-PET scans were obtained for staging, before start of second line treatment. All patients were subsequently treated in second line with rituximab combined with high dose cytarabine, cisplatin and dexamethasone (R-DHAP).

Table 1 Patient characteristics

| Patient | Gender | Age | Response to first line | Ann Arbor stage at relapse | Disease localization at relapse on 18F-FDG-PET |
|---|---|---|---|---|---|
| 1 | M | 23 | complete remission | IV A | liver |
| 2 | F | 55 | partial remission | III B | cervical, para-iliac, spleen |
| 3 | M | 46 | complete remission | III B | supraclavicular, mediastinal, hilar, mesenteric, retro-peritoneal, para-iliac, inguinal |
| 4 | M | 46 | complete remission | II A | retro-peritoneal |
| 5 | M | 47 | complete remission | I E | nasopharynx |
| 6 | F | 69 | partial remission | III A | submandibular, retro-clavicular, axillar, inguinal |

Administration of 89Zr-rituximab was well tolerated by all patients. Four patients underwent all scans according to protocol. Due to chemotherapy induced nausea, only a scan of the head and neck area could be obtained in patient 2, and blood sampling at D3 and 6 was not feasible. Patient 6 cancelled the D3 scan due to diarrhea and nausea, most likely caused by an infectious entero-colitis. For patient 3 no venous blood sample was obtained at D3.

89Zr-rituximab in blood pool, liver, spleen and kidneys was evident at D0, decreasing over time in all patients (Figure 1).
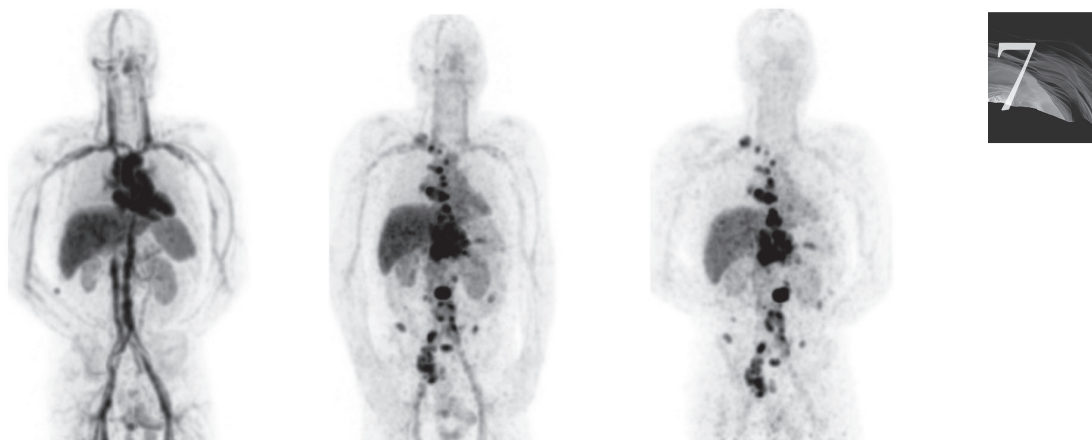


Figure 1 Example of whole body distribution of 89Zr-rituximab over time
Maximum intensity projections at D0, D3 and D6 p.i. for patient 3.

All sites of positive tumor uptake identified at D6 were also observed at D3, whereas no tumor uptake was identified on D0. At D6 on average 27.6% ± 5.7% ID of $^{89}$Zr-rituximab was still circulating in blood pool. The total activity at D6 as derived from plasma samples was not significantly different from the whole blood samples (n=5). Image derived and venous sampled whole blood activity concentrations were correlated with an $R^2$ of 0.98 and slope of 0.85.

All biopsied tumor sites showed uptake of $^{18}$F-FDG and DLBCL localization was confirmed by pathology. IHC was negative for CD20 expression in patient 1 and 6 (Figure 2), and positive in the other patients (Figure 3). Patients were ranked based on the intensity level and pattern of CD20 expression.

Tumor uptake of $^{89}$Zr-rituximab and CD20 expression on IHC were concordant in five patients: for patient 1, both were negative (Figure 4 and 2A), for the other four patients visible tumor uptake was concordant with CD20-positive biopsies. Intense visual tumor uptake of $^{89}$Zr-rituximab on PET was observed in patient 3, corresponding with uniformly positive CD20 expression on IHC (Figure 5 and 3D). $SUV_{peak}$ for this tumor lesion on D6 was 12.8. CD20 expression on IHC was also observed in patient 2 (Figure 3A), 4 (Figure 3B) and 5 (Figure 3c), concordant with tumor uptake of $^{89}$Zr-rituximab. $SUV_{peak}$ for these tumor lesions on D6 was 3.2, 5.4, 3.4, respectively. In patient 6 tumor uptake of $^{89}$Zr-rituximab was observed ($SUV_{peak}$ on D6 = 3.8) (Figure 6) while a core needle biopsy was CD20 negative (Figure 2B). Tumor uptake over time ($SUV_{peak}$ D6/D3 ratio) was calculated and ranged between 0.6 and 1.4. See Table 2 for additional PET uptake measures.

Overall, a positive correlation was observed between tumor uptake of $^{89}$Zr-rituximab, measured as $SUV_{peak}$, and the CD20 expression ranking ($r_s$ = 0.83, p=0.04, n = 6).
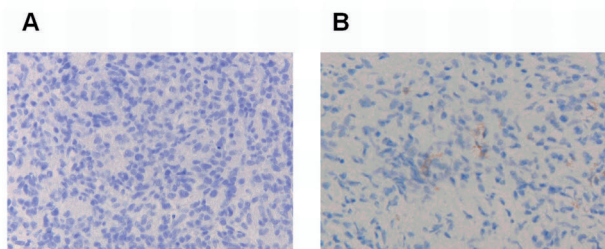


Figure 2 Biopsies: absence of CD20 expression

A) Core-needle biopsy of DLBCL (liver) in patient 1 shows completely absent CD20 expression (rank 1).
B) Core-needle biopsy of DLBCL (axillar lymph node) in patient 6 showing almost completely absent CD20 expression: extremely sparse groups of CD20-positive tumor cells with granular staining pattern (rank2).
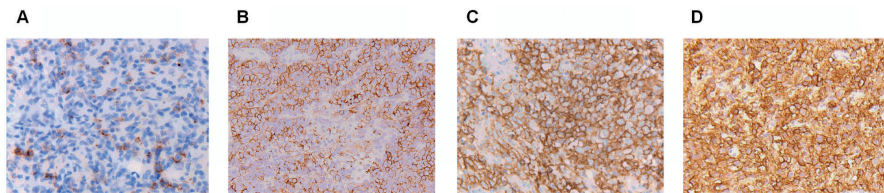
Figure 3 Biopsies: presence of CD20 expression

A) Excision biopsy of DLBCL (cervical lymph node) in patient 2 shows heterogeneously positive CD20 expression in sparse groups of cells, granular staining pattern (rank 3).

B) Excision biopsy of DLBCL (nasopharynx) in patient 5 showing heterogeneously positive CD20 expression in the majority of cells, membranous staining pattern (rank 4).

C) Excision biopsy of DLBCL (retroperitoneal lymph node) in patient 4 showing uniformly positive CD20 expression, membranous staining pattern (rank 5).

D) Excision biopsy of DLBCL (inguinal lymph node) in patient 3 showing uniformly positive CD20 expression, membranous staining pattern (rank 6).

Table 2 Additional quantitative tumor uptake measures of $^{89}$Zr-rituximab in the biopsied tumor lesions

| Patient | $SUV_{mean}$ ±SD D6 | Tumor to blood ratio D6 | $SUV_{peak}$ ratio D6/D3 | VOI (mL) |
|---|---|---|---|---|
| 1 | - | - | - | - |
| 2 | 2.3 ± 0.4 | NA* | 0.6 | 5.3 |
| 3 | 9.1 ± 2.6 | 4.7 | 1.4 | 32 |
| 4 | 4.3 ± 0.9 | 1.6 | 1.1 | 7.6 |
| 5 | 2.5 ± 0.4 | 1.1 | 1.0 | 25 |
| 6 | 3.5 ± 0.5 | 0.8 | NA* | 3.5 |

*NA = not available
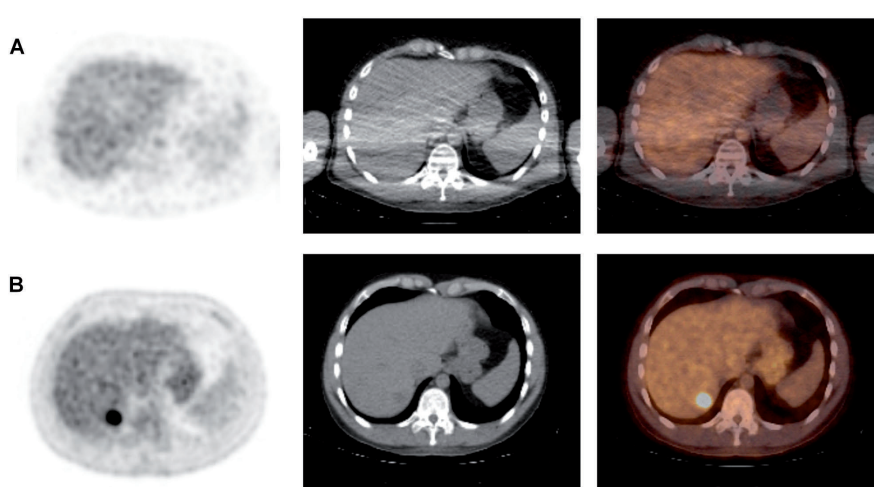


Figure 4 No tumor uptake on $^{89}$Zr-rituximab-PET, concordant with CD20 expression in biopsy. Axial images: from left to right attenuation corrected PET, low dose CT and fused PET/CT image of patient1.

A) $^{89}$Zr-rituximab-PET shows no tumor uptake concordant with a CD20-negative liver biopsy.

B) Corresponding tumor location on $^{18}$F-FDG-PET.
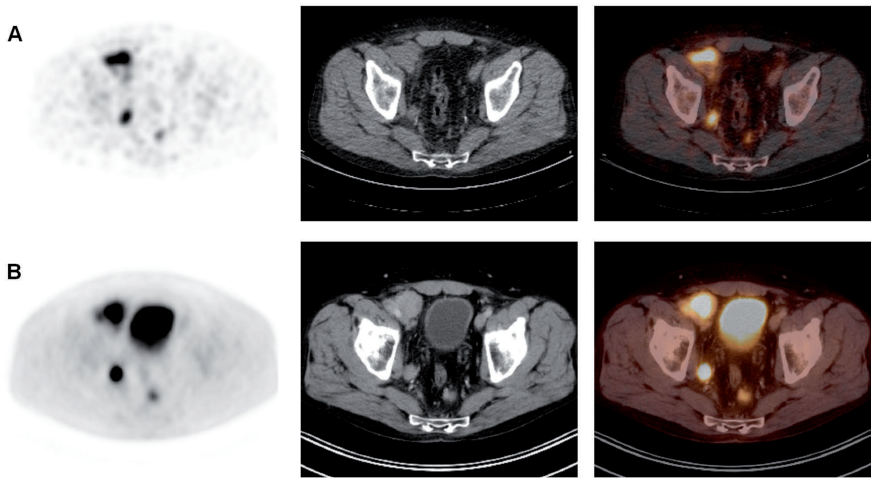
Figure 5 Example of tumor uptake on $^{89}$Zr-rituximab-PET, concordant with CD20 expression in biopsy. Axial images: from left to right attenuation corrected PET, low dose CT and fused PET/CT image of patient 3.

A) $^{89}$Zr-rituximab-PET shows intense tumor uptake concordant with a CD20-positive biopsy (inguinal lymph node).
B) Corresponding tumor location on $^{18}$F-FDG-PET.
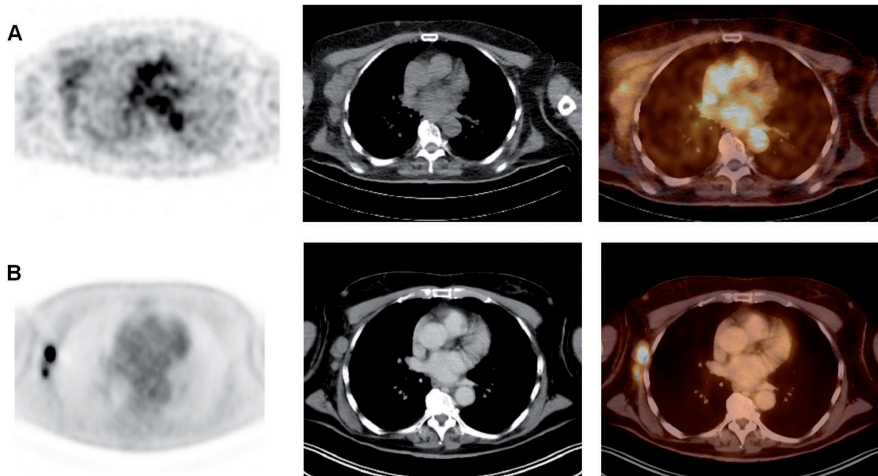


Figure 6 Tumor uptake on $^{89}$Zr-rituximab-PET, discordant with CD20 expression in biopsy. Axial images: from left to right attenuation corrected PET, low dose CT and fused PET/CT image of patient 6.

A) $^{89}$Zr-rituximab-PET shows tumor uptake discordant with a CD20-negative biopsy (axillar lymph node).
B) Corresponding tumor location on $^{18}$F-FDG-PET.

## DISCUSSION

Therapy failure in patients with relapsed/refractory DLBCL may be caused by insufficient CD20-mediated tumor targeting of rituximab. To elucidate the role of tumor targeting, development of an imaging biomarker to assess tumor targeting of rituximab is needed.

To our knowledge, this is the first study to report the performance of [89]Zr-rituximab-PET as an imaging biomarker for CD20 targeting by correlating tumor uptake of [89]Zr-rituximab as defined with PET and CD20 expression in biopsied tumor lesions. Tumor biopsies were obtained as routine work-up and tumor uptake on immuno-PET was evaluated at the biopsy sites. Overall, a positive correlation between tumor uptake of [89]Zr-rituximab and CD20 expression in biopsies was observed.

In one patient, tumor uptake of [89]Zr-rituximab was discordant with a CD20-negative biopsy. A possible explanation for the discrepancy is that the tumor site was biopsied in a ^{18}F-FDG-PET positive, [89]Zr-rituximab-PET negative part. IHC is the current gold standard for determination of CD20 expression, however heterogeneity in target expression within and between tumor lesions may not be detected by a single biopsy. Practical limitations of tumor biopsies are the invasiveness of the procedure and the fact that the tumor is not always safely accessible.

Tumor uptake was quantified in regions with focal uptake exceeding local background. $SUV_{peak}$ is commonly used as a measure of tumor uptake, but reflects only the highest uptake in a small part of the tumor. Manual delineation aims to capture total tumor uptake of [89]Zr-rituximab, and allows for the derivation of $SUV_{mean}$, its standard deviation and VOI volume. In this study the ranking of PET uptake was identical for $SUV_{peak}$ and $SUV_{mean}$. For ^{18}F-FDG-PET in lymphoma, the Deauville criteria are used to define tumor uptake using liver and mediastinal blood pool as reference region (15). The observed tumor to blood ratios in this study (range 0.8-4.7) indicate a difference in an uptake criterion based on local contrast versus bloodpool as reference region. To develop a clinically relevant criterion for positive tumor uptake of [89]Zr-rituximab further studies are required, linking tumor uptake to clinical outcome to rituximab treatment.

A limitation of our study is that the amount of circulating CD20+ B cells, which could influence tracer availability for tumor targeting, was not measured. However, tracer availability in the blood pool could be derived accurately from the

image data and was found to be more than 25% ID at D6. By using the blood samples this activity was found to be present in the plasma fraction. Therefore, the presence of a significant CD20 antigen sink hampering tracer availability for tumor targeting can be ruled out in this study.

So far, two other clinical studies have been published on the use of [89]Zr-labeled anti-CD20 with focus on prediction of toxicity for radio-immunotherapy treatment planning in patients with B cell lymphoma (13, 14).

The current study provides evidence for the use of [89]Zr-rituximab-PET as an imaging biomarker to assess CD20 targeting. These results allow for further studies to assess whether [89]Zr-rituximab-PET is able to predict which patients will or will not respond to repeated rituximab treatment, and select which patients will benefit from a change of treatment (dose optimization, switch to a different targeted therapy or ADC). Novel treatment options emerge, including new anti-CD20 mAbs as obinutuzumab and ofatumumab with enhanced capacity for cytotoxicity as well as mAbs for other targets, for instance the anti-CD38 mAb daratumumab, and antibody-drug conjugates (ADC's) as brentuximab vedotin, an anti-CD30 mAb linked to the antimitotic agent monomethyl auristatin E (MMAE). Molecular imaging with immuno-PET is a promising strategy to guide individualized treatment to improve efficacy, reduce toxicity and costs of mAb treatment.

## CONCLUSION

This study provides evidence for the use of [89]Zr-rituximab-PET as an imaging biomarker to assess CD20 targeting, given the observed correlation between tumor uptake of [89]Zr-rituximab and CD20 expression in biopsies. Therefore, [89]Zr-rituximab-PET allows for further studies relating tumor targeting to clinical benefit of rituximab treatment in individual patients.

# REFERENCES

1. Gisselbrecht C, Glass B, Mounier N, et al. Salvage regimens with autologous transplantation for relapsed large B-cell lymphoma in the rituximab era. *J Clin Oncol*. 2010;28:4184-4190.

2. de Jong D, Rosenwald A, Chhanabhai M, et al. Immunohistochemical prognostic markers in diffuse large B-cell lymphoma: validation of tissue microarray as a prerequisite for broad clinical applications--a study from the Lunenburg Lymphoma Biomarker Consortium. *J Clin Oncol*. 2007;25:805-812.

3. Cheson BD, Fisher RI, Barrington SF, et al. Recommendations for initial evaluation, staging, and response assessment of Hodgkin and non-Hodgkin lymphoma: the Lugano classification. *J Clin Oncol*. 2014;32:3059-3068.

4. Lamberts LE, Williams SP, Terwisscha van Scheltinga AGT, et al. Antibody positron emission tomography imaging in anticancer drug development. *J Clin Oncol*. 2015;33:1491-1504.

5. Gaykema SBM, Brouwers AH, Lub-de Hooge MN, et al. 89Zr-bevacizumab PET imaging in primary breast cancer. *J Nucl Med*. 2013;54:1014-1018.

6. Lamberts LE, Menke-van der Houven van Oordt CW, ter Weele EJ, et al. ImmunoPET with Anti-Mesothelin Antibody in Patients with Pancreatic and Ovarian Cancer before Anti-Mesothelin Antibody-Drug Conjugate Treatment. *Clin Cancer Res*. 2016;22:1642-1652.

7. Cheson BD, Pfistner B, Juweid ME, et al. Revised response criteria for malignant lymphoma. *J Clin Oncol*. 2007;25:579-586.

8. Verel I, Visser GWM, Boellaard R, Walsum MS, Snow GB, Dongen GAMS van. 89Zr Immuno-PET: Comprehensive Procedures for the Production of 89Zr-Labeled Monoclonal Antibodies. *J Nucl Med*. 2003;44:1271-1281.

9. Perk LR, Vosjan MJWD, Visser GWM, et al. p-Isothiocyanatobenzyl-desferrioxamine: a new bifunctional chelate for facile radiolabeling of monoclonal antibodies with zirconium-89 for immuno-PET imaging. *Eur J Nucl Med Mol Imaging*. 2010;37:250-259.

10. Vosjan MJWD, Perk LR, Visser GWM, et al. Conjugation and radiolabeling of monoclonal antibodies with zirconium-89 for PET imaging using the bifunctional chelate p-isothiocyanatobenzyl-desferrioxamine. *Nat Protoc*. 2010;5:739-743.

11. Nadler SB, Hidalgo JH, Bloch T. Prediction of blood volume in normal human adults. *Surgery*. 1962;51:224-232.

12. Makris NE, Boellaard R, Visser EP, et al. Multicenter harmonization of 89Zr PET/CT performance. *J Nucl Med*. 2014;55:264-267.

13. Rizvi SNF, Visser OJ, Vosjan MJWD, et al. Biodistribution, radiation dosimetry and scouting of 90Y-ibritumomab tiuxetan therapy in patients with relapsed B-cell non-Hodgkin's lymphoma using 89Zr-ibritumomab tiuxetan and PET. *Eur J Nucl Med Mol Imaging*. 2012;39:512-520.

14. Muylle K, Flamen P, Vugts DJ, et al. Tumour targeting and radiation dose of radioimmunotherapy with (90)Y-rituximab in CD20+ B-cell lymphoma as predicted by (89)Zr-rituximab immuno-PET: impact of preloading with unlabelled rituximab. *Eur J Nucl Med Mol Imaging*. 2015;42:1304-1314.

15. Barrington SF, Mikhaeel NG, Kostakoglu L, et al. Role of imaging in the staging and response assessment of lymphoma: consensus of the International Conference on Malignant Lymphomas Imaging Working Group. *J Clin Oncol*. 2014;32:3048-3058.

7

# SUPPLEMENTARY DATA
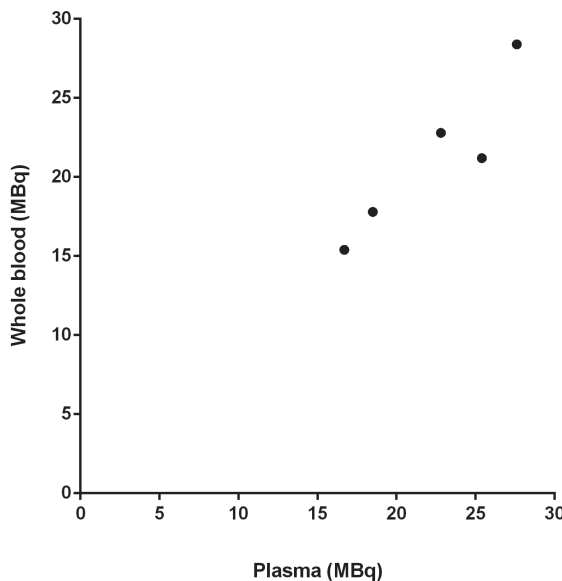


**Supplemental Figure 1** Total activity (in MBq) in whole blood and plasma on D6.
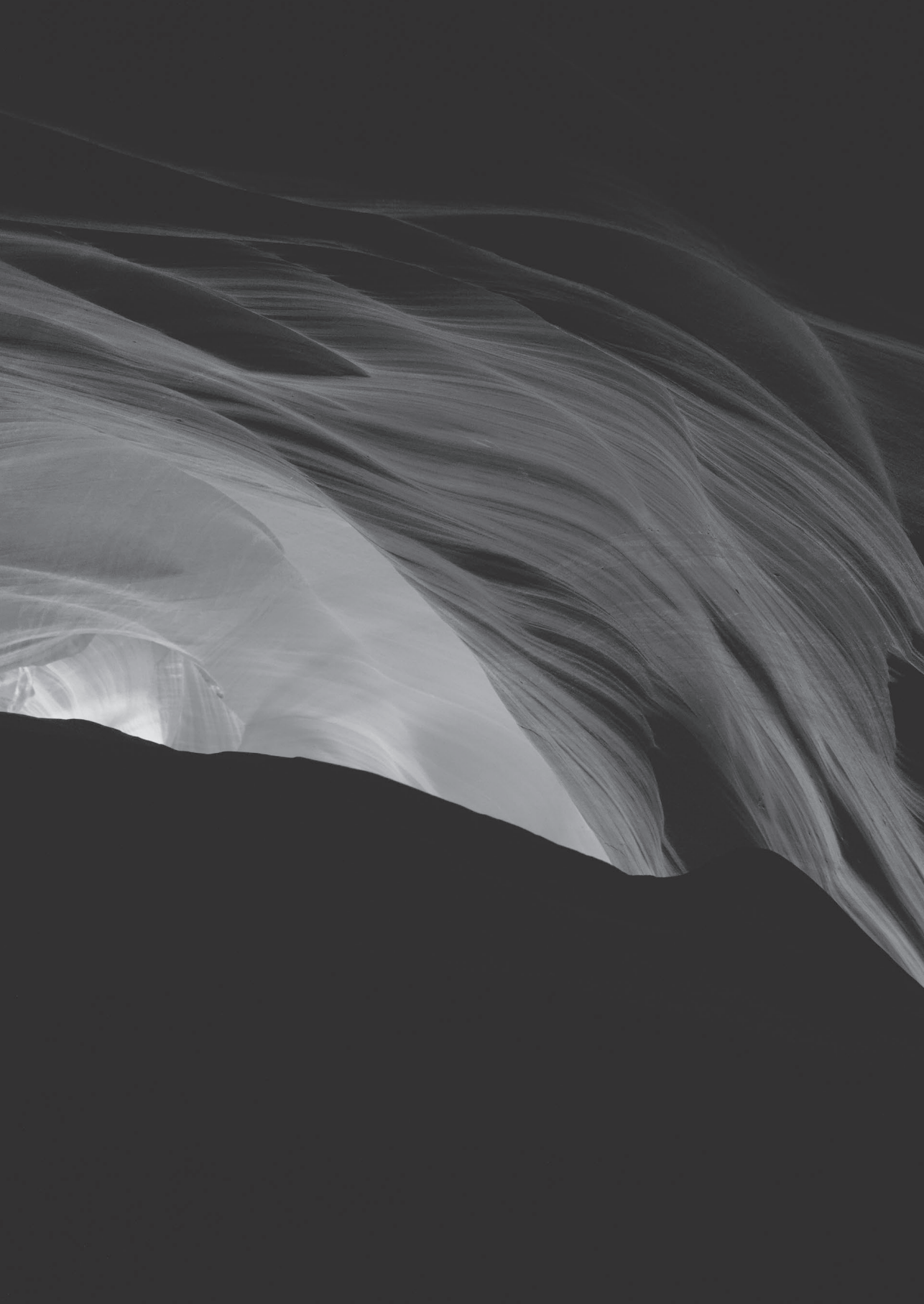
# Assessment of target-mediated uptake with immuno-PET:

# analysis of a phase I clinical trial with an anti-CD44 antibody

Yvonne W.S. Jauw
Marc C. Huisman
Tapan K. Nayak
Danielle J. Vugts
Randolph Christen
Valerie Meresse Naegelen
Dominik Ruettinger
Florian Heil
Adriaan A. Lammertsma
Henk M.W. Verheul
Otto S. Hoekstra
Guus A.M.S. van Dongen
C. Willemien Menke-van der Houven van Oordt

# ABSTRACT

**Purpose:** Ideally, monoclonal antibodies provide selective treatment by targeting the tumor, without affecting normal tissues. Therefore antibody imaging is of interest, preferably in early stages of drug development. However, the imaging signal consists of specific, as well as non-specific uptake. The aim of this study was to assess specific, e.g. target-mediated uptake in normal tissues, with immuno-PET in a phase I dose escalation study, using the anti-CD44 antibody RG7356 as example.

**Methods:** Thirteen patients with advanced CD44-expressing solid tumors were included in this imaging sub-study of a phase I dose escalation clinical trial. 37 MBq of $^{89}$Zirconium-labeled RG7356 (1 mg) was administered after a variable dose of unlabeled RG7356 (0 to 675 mg). Tracer uptake in normal tissues (liver, spleen, kidney, lung, bone marrow, brain and blood pool) was used to calculate the area under the time antibody concentration curve (AUC) and expressed as tissue-to-blood AUC ratio's.

**Results:** Within the dose range of 1 to 450 mg, tissue-to-blood AUC ratios decreased from 10.6 to $0.75 \pm 0.16$ for the spleen, 7.5 to $0.86 \pm 0.18$ for the liver, 3.6 to $0.48 \pm 0.13$ for bone marrow, 0.69 to $0.26 \pm 0.1$ for lung and 1.29 to $0.56 \pm 0.14$ for the kidney, indicating dose-dependent uptake. In all patients receiving $\geq 450$ mg (n=7), tumor uptake of the antibody was observed.

**Conclusion:** This study demonstrates how immuno-PET in a dose-escalation study provides a non-invasive technique to quantify dose-dependent uptake in normal tissues, indicating specific, target-mediated uptake.

# INTRODUCTION

Treatment of cancer has improved as a result of immunotherapy with monoclonal antibodies (mAbs). Ideally, mAbs selectively target tumor cells, resulting in limited toxicity compared to classical chemotherapy.

However, lack of mAb selectivity may result in significant toxicity and/or suboptimal tumor targeting, leading to therapy failure. Therefore, it is important to confirm tumor selectivity of a novel candidate mAb to minimize toxicity and maximize efficacy, preferably in early stages of drug development. Currently, toxicity is assessed by dose escalation in traditional phase I trials, using dose limiting toxicity and a maximum tolerated dose to establish the therapeutic dose for the next stages of drug development (phase II and III trials). For the ideal mAb, selective tumor targeting is expected, with limited target antigen-mediated specific uptake in normal tissues.

Recently, there is increasing interest in the use of imaging techniques to measure the mAb biodistribution *in vivo* without requiring blood or tissue samples (*1*). After inert and stable radiolabeling, the radioactive mAb can be used to study the biodistribution of the non-radioactive mAb. According to this principle, positron emission tomography (PET) with 89Zr-labeled mAbs provides a non-invasive tool for *in vivo* visualization and quantification of mAbs (*2-4*).

Quantification of antibody accumulation in normal tissues and tumor using PET imaging can be an important non-invasive tool to evaluate the therapeutic potential of antibodies and antibody conjugates. For this purpose, target-mediated specific uptake is of interest. However, the measured PET signal comprises non-specific uptake (dependent on the tissue blood volume fraction, as well as other tissue characteristics, for example size of endothelial fenestrae by which the antibody passes through the capillary wall) and potentially target antigen-mediated specific uptake. Differentiation between these specific and non-specific contributions to the PET signal is possible, if we assume that they are dose-dependent and dose-independent, respectively (Figure 1). In this paper, we present an experimental approach to assess specific uptake with immuno-PET in a dose-escalation study, using RG7356 as an example.

Investigational RG7356 is an anti-CD44 recombinant humanized mAb, which targets the constant region of the extracellular domain of CD44 and provides antibody-dependent cellular phagocytosis of the malignant cells by macrophages (*5*). CD44 is a human cell-surface glycoprotein, which is expressed by several solid

tumors as well as cancer stem cells and has a role in cell proliferation, migration and angiogenesis. This target antigen has been considered attractive for immunotherapy (*6*), as blocking inhibits tumor growth and metastatic potential (*7,8*). A preclinical dose-escalation study with [89]Zr-labeled RG7356 confirmed tumor targeting of CD44+ tumors in xenografts bearing mice. Since RG7356 is not cross-reactive with murine CD44, studies in mice do not provide any information regarding accessible binding sites in physiologically normal organs. Assessment of biodistribution in cynomolgus monkeys showed uptake in normal CD44+ tissues, for example spleen and bone marrow (*9*). Subsequently, a first-in-human phase I dose-escalation trial was performed in patients with advanced, CD44-expressing solid tumors, showing that RG7356 was well tolerated with modest clinical efficacy (*10*). PET imaging with [89]Zr-labeled RG7356 was performed to assess biodistribution and tumor uptake of RG7356 in a subgroup (13 of 65 patients) of this phase I trial. The previous publication on the main trial (*10*) included the background of the antigen and antibody as well as a brief summary of visual assessment of the imaging subgroup. [89]Zr-RG7356 was localized to spleen, bone marrow and liver, while tumor accumulation of [89]Zr-RG7356 with co-administration of unlabeled antibody (≥ 199mg), suggesting that the modest efficacy was not related to poor drug delivery to the tumor perse (*10*). In the current study, we separately report on the exploratory imaging sub-study with [89]Zr-labeled RG7356 by performing quantitative analysis of the imaging data.

The aim of this study was to quantify biodistribution and tumor uptake of [89]Zr-RG7356, and to evaluate whether uptake of [89]Zr-RG7356 in normal tissues was dose-dependent as indication of target-mediated specific uptake. With this example, we aim to provide a general approach for application of immuno-PET to evaluate new drug-target-combinations in first-in-human studies.
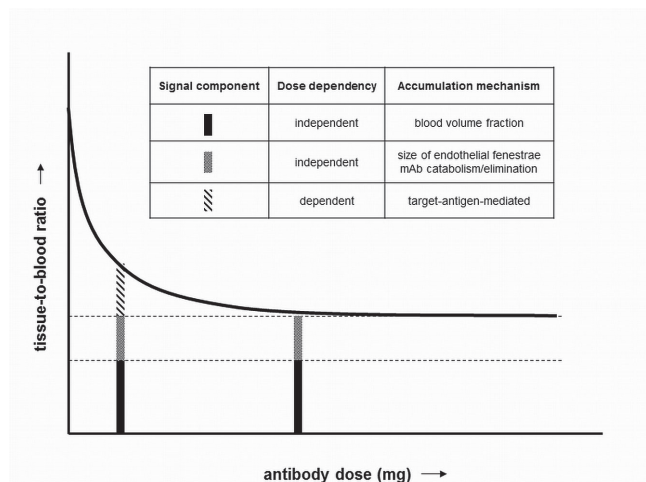
Figure 1. Immuno-PET signal components in a phase I dose escalation study. The tissue-to-blood ratio is shown as a function of administered antibody dose. For example target-antigen-mediated uptake is dose-dependent, while blood volume fraction, catabolism or elimination are dose-independent accumulation mechanisms.

# MATERIALS AND METHODS

## Patient population

Patients with advanced CD44-expressing solid tumors were included in a multicentre phase I clinical study with RG7356 (ClinicalTrials.gov Identifier NCT01358903) (10). As part of the screening procedure, tumor biopsies were obtained and analysed centrally by Ventana Medical Systems Inc. (VSMI, Tucson, AZ, USA), using clone SP37 as anti-CD44 primary antibody to assess tissue quality, tumor content and CD44 expression by immunohistochemistry (IHC). Patients with a IHC score of ≥1+ for CD44-positivity on the pretreatment biopsy were included. For specific scoring criteria for CD44 expression in patient samples, see Supplemental Table 1. Study design as well as inclusion and exclusion criteria have been reported previously (5). This study was approved by the Medical Ethics Review Committee of the VU University Medical Center, Amsterdam, and performed in accordance with the Declaration of Helsinki. All study-related procedures were performed after patients gave their written informed consent. Patients enrolled in this phase I study at the VU University Medical Center were asked to participate in the exploratory imaging sub-study.

## PET imaging study design

For PET imaging, RG7356 (Roche, Basel, Switzerland) was labeled with [89]Zr (BV Cyclotron VU, Amsterdam, the Netherlands) according to Good Manufacturing Practice (GMP) standards, as previously described (*11-13*). Information on the quality control of the radiolabeled tracer can be found in the Supplementary Data. Patients received ~37 MBq [89]Zr-labeled RG7356 (1 mg) within two hours after administration of a variable dose (range 0-675 mg) of unlabeled RG7356. Pre-loading with unlabeled mAb was preferred from a logistical perspective (infusion of the unlabeled mAb in a phase I Oncology unit), assuming no difference in uptake between pre-loading and co-infusion.

Whole body PET and low dose CT (ldCT) scans were acquired on a Gemini TF-64 PET/CT scanner (Philips Healthcare, Best, the Netherlands) and scheduled at 1, 24 and 96 h p.i.. Images were reconstructed as described previously (*14*). After completing the imaging procedure, patients continued in the main study and received RG7356 in the highest dose cohort that was cleared for safety.

## [89]Zr-RG7356 PET analysis

Visual assessment of biodistribution and tumor uptake was performed by a nuclear medicine physician. Tumor uptake of [89]Zr-RG7356 was defined as focal uptake exceeding local background. PET scans were considered positive if at least 1 tumor lesion showed [89]Zr uptake at 96 h p.i..

Volumes of interest (VOIs) of liver, spleen, kidney, lung, bone marrow, blood pool and brain were delineated to derive mean activity concentrations ($AC_{mean}$ in $Bq \cdot mL^{-1}$). For lung and brain, VOIs were semi-automatically defined on the ldCT and projected on the PET images. The thresholds for lung VOI's were based on Houndsfield units (lower limit -1000, upper limit -400), therefore excluding tissue with higher Houndsfield units (e.g. tumor localisations in the lung). VOIs of the liver, spleen and kidney were manually delineated on the PET images themselves, using the ldCT as reference. Fixed sized VOIs with volumes of 8.6 and 2.9 mL were placed on lumbar vertebrae and aortic arch (on ldCT) to estimate $AC_{mean}$ in bone marrow and blood pool, respectively. Tumor lesions were manually delineated and peak activity concentrations ($AC_{peak}$) were derived per tumor VOI (*15*). Assuming that tumor uptake is only due to non-specific uptake (blood volume fraction), the tumor blood volume fraction can be estimated by dividing the AC in the tumor by the AC in the blood pool.

For all VOIs, SUV's were calculated by dividing AC (decay corrected to time of injection) by injected dose (ID in Bq) corrected for body weight. Additionally,

all radioactivity concentrations were converted to antibody concentrations by the following formula: $C_{mAb} = (AC / ID) * D_{mAb}$, where $C_{mAb}$ is the mAb concentration in mg/mL and $D_{mAb}$ is the total (=labeled + unlabeled) antibody dose administered in mg.

All measured time points were combined to derive a time antibody concentration curve. Subsequently, using trapezoidal integration, the AUC in mg·h·mL$^{-1}$ was calculated. For each tissue, the tissue-to-blood AUC ratio was obtained by dividing the tissue AUC by the blood pool AUC. Data, averaged over the number of patients per dose cohort, are presented as mean ± SD.

## RESULTS

### Patient characteristics

Thirteen patients with advanced CD44-expressing solid tumors were included. Five cohorts with different doses of antibody were evaluated: 1 mg (n=1), 100 mg (n=3), 200 mg (n=2), 450 mg (n=5) and 675 mg (n=2). These dose cohorts were determined based on safety as assessed in the main phase I trial. Subsequently, the imaging dose was increased when imaging and tumor characteristics were not satisfactory (e.g. no visible tumor uptake due to uptake in normal tissues/high background). Patient details are provided in Table 1. In each case CD44 expression was confirmed by central reviewing of tumor biopsies (Figure 1S in Supplementary Data).

Table 1 Patient details

| Patient | Gender | Tumor type | CD44 expression (IHC) | | |
| --- | --- | --- | --- | --- | --- |
| | | | Membrane Score | H-Score | Biopsy location |
| 1 | F | squamous cell carcinoma cervix | 3 | 285 | lung |
| 2 | M | adenocarcinoma oesophagus | 2 (focal) | 30 | oesophagus |
| 3 | M | colorectal carcinoma | 2 (focal) | 25 | liver |
| 4 | M | melanoma | 3 | 250 | liver |
| 5 | M | colorectal carcinoma | 2 | 130 | peritoneal |
| 6 | F | squamous cell carcinoma cervix | 2 (focal) | 65 | cervix |
| 7 | M | basaloid carcinoma tonsil | 3 | 135 | lung |
| 8 | M | squamous cell carcinoma oesophagus | 3 | 210 | neck left |
| 9 | M | colorectal carcinoma | 2 | 85 | liver |
| 10 | M | cholangiocarcinoma | 3 | 200 | liver |
| 11 | F | squamous cell carcinoma earcanal | 3 | 260 | neck left |
| 12 | M | colorectal carcinoma | 2 (focal) | 35 | liver |
| 13 | M | colorectal carcinoma | 3 | 218 | liver |

### [89]Zr-RG7356 PET: biodistribution

Overall, visual assessment of PET images showed mainly blood pool activity of [89]Zr-labeled-RG7356 at 1 hour post injection (p.i.), decreasing over time (Figure 2A). Differences in biodistribution of [89]Zr-labeled-RG7356 were observed for patients in the different dose cohorts. Intense tracer uptake in the spleen, liver and bone marrow was visualized for the lowest dose cohorts (1 and 100 mg), decreasing with increasing antibody doses (Figure 2B).

The blood pool activity concentration of [89]Zr-labeled-RG7356, expressed as standardized uptake value (SUV) over time is shown in Figure 3A. This graph displays only the measured activity of the radioactive tracer. In Figure 3B, derived absolute antibody concentrations in blood pool, which represent the total amount of antibody (labeled + unlabeled dose) are shown. The area under the curve (AUC) of this time antibody concentration curve is shown as a function of the administered antibody dose in Figure 3C. Dose independent uptake would result in a linear relationship of AUC with antibody dose. Figure 3C does, overall, show this linear relationship. The 100 mg datapoint, however, has a measured AUC lower than expected based on this linear trend.

Tissue-to-blood AUC ratios are presented as a function of administered antibody dose in Figure 4. For the brain, the tissue-to-blood AUC ratio was constant ($0.07 \pm 0.01$) and independent of administered antibody dose. All other tissue-to-blood AUC ratios (spleen, liver, bone marrow, kidney and lung) were dependent of the antibody dose administered.

For the lowest dose cohorts (1 and 100 mg), relative high tissue-to-blood AUC ratios were observed. The spleen showed the highest tissue-to-blood AUC ratio for the 1 mg dose cohort (10.6), followed by liver (7.5), bone marrow (3.6), kidney (1.3), lung (0.7) and brain (0.08). For liver, spleen and kidney, a constant tissue-to blood AUC ratio was reached for doses ≥ 450 mg, for the lung at doses ≥ 200 mg. For the 675 mg dose cohort, the liver showed the highest tissue-to-blood AUC ratio of $0.85 \pm 0.08$, followed by spleen ($0.72 \pm 0.09$), kidney ($0.59 \pm 0.08$), bone marrow ($0.40 \pm 0.04$), lung ($0.27 \pm 0.03$) and brain ($0.07 \pm 0.02$).
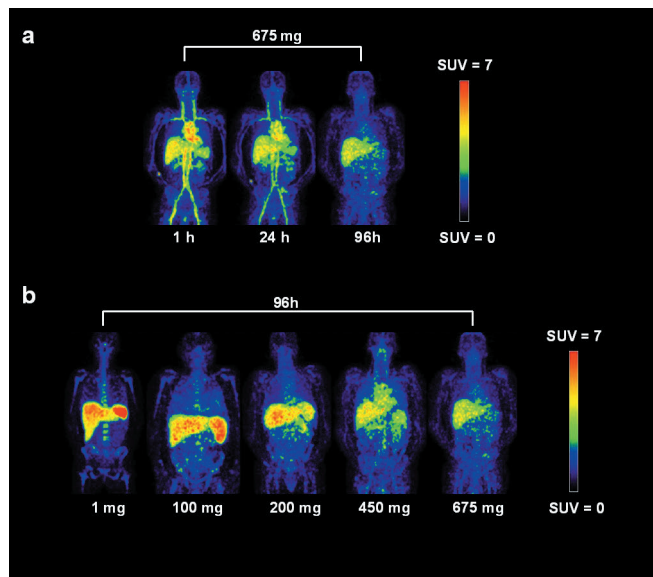
**Figure 2.** Biodistribution of 89Zr-labeled-RG7356. (a) as function of time: maximum intensity projections at 1, 24 and 96 h p.i. for patient 12 (675mg dose cohort) (b) as function of total administered antibody dose: maximum intensity projections at 96 h p.i. for various dose cohorts (1, 100, 200, 450 and 675 mg).
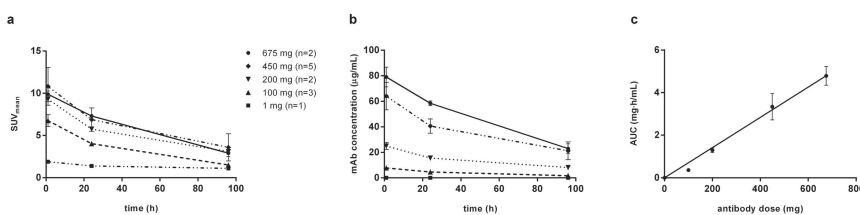


**Figure 3.** Blood pool concentrations of 89Zr-RG7356 and RG7356. (a) Radioactivity concentrations of 89Zr-RG7356 in blood pool as function of time. (b) Antibody concentrations of RG7356 in blood pool as function of time. (c) AUC of the time antibody concentration curve of RG7356 in blood pool as function of antibody dose.

Data is presented as mean, error bars represent SD.
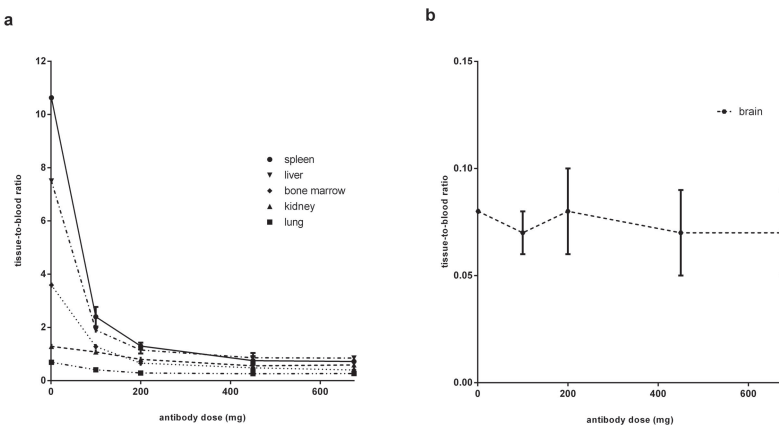
Figure 4 Tissue-to-blood AUC ratio of RG7356 as a function of antibody dose.

Data is presented as mean, error bars represent SD.

## [89]Zr-RG7356 PET: tumor uptake

Assessment of tumor uptake of [89]Zr-RG7356 at 96 hours p.i. per tumor lesion is shown in Table 2. In all patients receiving ≥ 450 mg RG7356 (n=7) tumor uptake was observed. An example image of visible tumor uptake is shown in Figure 5. For this patient, the time activity curves for blood pool, normal tissues and tumor are provided as an example (Figure 2S in Supplementary Data). In 1 out of 6 patients receiving ≤ 200 mg RG7356, diffuse uptake of [89]Zr-labeled-RG7356 was observed in the lung, indicating diffuse tumor localisation. Quantification was not feasible due to the diffuse localization. Quantification of mAb uptake in focal tumor lesions resulted in an average $SUV_{peak}$ of 3.7 ± 1.7 for the 450 mg cohort and 6.5 ± 1.3 for the 675 mg cohort. Average tumor AUC was 1.5 ± 0.5 mg·h/mL in the 450 mg cohort and 3.2 ± 0.5 mg·h/mL for the 675 mg cohort. Average tumor to blood AUC ratio was 0.46 ± 0.15 in the 450 mg cohort and 0.65 ± 0.07 for the 675 mg cohort. For the 675mg cohort, the average tumor blood volume fraction was 67%.
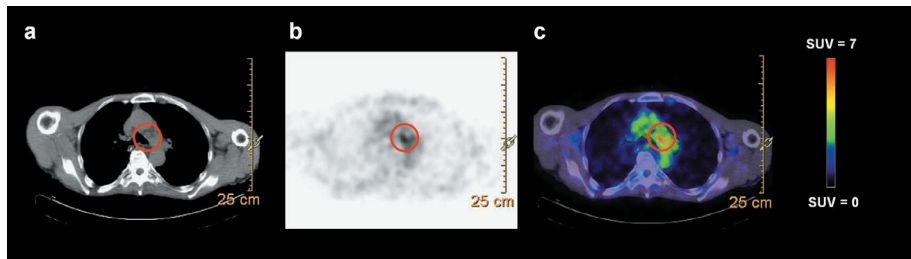


Figure 5. Example of tumor uptake of [89]Zr-RG7356 at 96 h p.i.. Tumor lesion mediastinal/in the aorta-pulmonary window (patient 8, 450 mg cohort). (a) low dose CT (b) attenuation corrected PET (c) fused image.

Table 2 Tumor uptake of $^{89}$Zr-RG7356 and RG7356 at 96 h p.i..

| Patient | Dose cohort (mg) | Visual assessment | Localisation | SUV$_{peak}$ | AUC (mg·h/mL) | Tumor to blood AUC ratio |
|---|---|---|---|---|---|---|
| 1 | 1 | - | - | - | - | - |
| 2 | 100 | - | - | - | - | - |
| 3 | 100 | + | Lung (diffuse) | NA* | NA* | - |
| 4 | 100 | - | - | - | - | - |
| 5 | 200 | - | - | - | - | - |
| 6 | 200 | - | - | - | - | - |
| 7 | 450 | + | Brain L | 1.8 | 0.35 | 0.09 |
|   |     |   | Lung R | 8.4 | 2.06 | 0.55 |
| 8 | 450 | + | Skull L | 3.3 | 1.41 | 0.43 |
|   |     |   | Upper neck L | 3.5 | 1.62 | 0.49 |
|   |     |   | Lower neck L | 2.8 | 1.43 | 0.43 |
|   |     |   | Supraclavicular R | 3.1 | 1.67 | 0.50 |
|   |     |   | Mediastinal | 4.8 | 2.37 | 0.72 |
|   |     |   | Lung L | 2.2 | 1.29 | 0.39 |
|   |     |   | Lung R1 | 2.1 | 1.06 | 0.32 |
|   |     |   | Lung R2 | 4.3 | 1.75 | 0.53 |
| 9 | 450 | + | Lung L | 1.8 | 0.89 | 0.32 |
|   |     |   | Lung R | 2.2 | 0.99 | 0.36 |
|   |     |   | Rectum | 5.6 | 1.75 | 0.64 |
| 10 | 450 | + | Lung L | 4.6 | 1.47 | 0.56 |
|    |     |   | Lung R | 3.9 | 1.41 | 0.53 |
| 11 | 450 | + | Mastoid L | 4.5 | 1.81 | 0.42 |
| 12 | 675 | + | Sigmoid L | 4.9 | 2.55 | 0.59 |
| 13 | 675 | + | Pelvic R | 6.5 | 3.83 | 0.73 |
|    |     |   | Sacrum | 8.1 | 3.29 | 0.63 |

- = no visible tumor uptake
*NA=not available (diffuse localization)

# DISCUSSION

In this study, we assessed dose-dependent and dose-independent uptake of the $^{89}$Zr-labeled anti-CD44 antibody RG7356 in normal tissues to identify specific, e.g. target-mediated uptake on immuno-PET in a dose-escalation phase 1 study.

Both dose-dependent and dose-independent uptake was observed, reflecting specific as well as non-specific uptake of RG7356. For tissues without antigen expression, a linear increase in antibody concentrations can be expected for increasing antibody doses, driven by perfusion and blood volume of the tissue. However, our results suggest a mechanism that extracts antibody from the blood pool to tissues, in addition to the non-specific uptake mechanisms (Figure 3C).

Therefore, tissue-to-blood AUC ratios were used to evaluate dose-dependent uptake of RG7356 for the following tissues: liver, spleen, bone marrow,

kidney, lung and brain. For the brain, a constant low tissue-to-blood AUC ratio was observed for all dose cohorts. Assuming that RG7356 does not cross the blood-brain-barrier, this value is determined by the blood volume fraction of the brain. For the spleen, liver, bone marrow, kidney and lung, dose-dependent uptake of [89]Zr-RG7356 was observed, indicating target-antigen mediated specific uptake in these tissues. A very similar pattern of dose-dependent uptake in the spleen, liver and bone marrow has been reported previously in the preclinical study with [89]Zr-RG7356 in cynomolgus monkeys, indicating that such preclinical immuno-PET studies can be predictive with respect to normal tissue uptake in human (*9*).

Target antigen expression in these tissues is a plausible explanation for dose-dependent uptake, as protein expression of CD44 has been reported for normal bone marrow, spleen, lung, kidney and liver (bile ducts) (*16,17*). Although dose-dependent uptake in tissues was observed, a constant tissue-to-blood AUC ratio was reached at 450 mg for all tissues, indicating target antigen saturation.

In addition, dose-independent uptake of the tracer in liver, spleen, bone marrow, kidney and lung was observed, indicating non-specific uptake. For the liver, based on a 30% blood volume fraction (*18*), a liver to blood AUC ratio of 0.3 would be expected. However, we observed a liver to blood AUC ratio of 0.85± 0.08 for the 675 mg dose cohort. The difference between the tissue-to-blood AUC ratio and blood volume fraction represents an additional accumulation mechanism in the liver, for example the large endothelial fenestrae or antibody catabolism. Stability of [89]Zr-labeled antibodies, with minimal release of [89]Zr, has been demonstrated in many in vitro and in vivo preclinical as well as clinical studies (*11,19,20*). There are no experimental data supporting accumulation of free [89]Zr in normal tissues, except for the observation that free [89]Zr, arising after internalisation and intracellular catabolism of the conjugate, may accumulate in bone tissue (not bone marrow) (*19*). However, in our study, we did not observe [89]Zr accumulation in bone (Figure 2).

Although dose-dependent as well as dose-independent uptake in normal tissues was found in this imaging study, there were no safety concerns in the corresponding phase I dose escalation study, with treatment doses up to 1500 mg biweekly/2250 mg weekly. The overall safety profile of RG7356 was acceptable. Dose limiting toxicities included febrile neutropenia and aseptic meningitis (*10*). However, this phase I study was terminated at an early stage due to the lack of evidence of a clinical and/or pharmacodynamic (PD) dose-response relationship with RG7356.

We observed tumor uptake in all patients receiving ≥ 450 mg, with an extremely high tumor blood volume fraction estimated for the 675 mg cohort. Although this might suggest target-mediated specific tumor uptake, another study design would have been more informative on this point (*21*). This requires measurement of the same tumor lesion after administration of different antibody doses to exclude differences in tumor characteristics, for example blood volume fraction. Learning from the present study, we recently demonstrated target-mediated specific tumor uptake in a PET imaging study with an anti-HER3 mAb in which the $^{89}$Zr-labeled antibody was administered twice (with a variable dose of unlabeled antibody) to a single patient (*21*). Although biopsies taken after the immuno-PET could have provided additional confirmation with immunohistochemistry, this was not included in the study design due to the fragile patient population.

No focal tumor uptake was visualized in the lowest dose cohorts (1-200 mg). This observation cannot be explained by the level of CD44 expression or the percentage of CD44-positive tumor cells (Table 1). A probable explanation why tumor visualization is hampered for the lowest dose cohorts, is that dose-dependent uptake in normal tissues leads to lower visual tumor contrast, assuming similar binding constants and accessibilities of the target antigen in both normal tissues and tumor. However, in the higher dose cohorts, differences between binding constant became apparent where the dose-dependent tracer uptake in normal tissues does not significantly contribute to the imaging signal anymore (Figure 1), target antigen mediated tracer uptake will result in sufficient visual contrast to allow identification and quantification of tumor targeting.

In this study, PET imaging with the novel anti-CD44 monoclonal antibody RG7356 confirmed tumor uptake for patients receiving ≥ 450 mg. However, dose dependent uptake of RG7356 in normal tissues indicates target antigen expression, limiting the use of RG7356 for targeting toxic payloads to the tumor like in antibody-drug conjugate (ADC) approaches.

This exploratory imaging study demonstrates how immuno-PET with a $^{89}$Zr-labeled mAb can be used as a general method during phase I dose escalation studies to evaluate the therapeutic potential of an antibody. Evaluation of dose-dependent and dose-independent normal tissue uptake with immuno-PET reflects specific and non-specific uptake. Antibody quantification obtained by molecular imaging provides an additional, non-invasive method to study in vivo mAb biodistribution, besides traditional PK obtained by blood sampling. Especially for a candidate mAb with a potential future as ADC, the resulting information

(prevention of potential toxicity/additional development costs) may justify the patient burden and cost for additional scans in a limited number of patients in a phase I setting.

For a mAb which continues in further stages of drug development, in vivo-measurements of antibody concentrations in tissue and tumor can be of value for PK/PD modelling/dose optimization and response prediction to guide individualized treatment.

## CONCLUSION

This study demonstrates how immuno-PET in early clinical drug development provides a non-invasive technique to quantify dose-dependent uptake in normal tissues, indicative of specific, target-mediated uptake.

## ACKNOWLEDGEMENTS

# REFERENCES

1. Glassman PM, Balthasar JP. Physiologically-based pharmacokinetic modeling to predict the clinical pharmacokinetics of monoclonal antibodies. *J Pharmacokinet Pharmacodyn*. 2016;43:427-446.

2. Dijkers EC, Oude Munnink TH, Kosterink JG, et al. Biodistribution of 89Zr-trastuzumab and PET imaging of HER2-positive lesions in patients with metastatic breast cancer. *Clin Pharmacol Ther*. 2010;87:586-592.

3. Lamberts LE, Williams SP, Terwisscha van Scheltinga AGT, et al. Antibody positron emission tomography imaging in anticancer drug development. *J Clin Oncol*. 2015;33:1491-1504.

4. Jauw YWS, Menke-van der Houven van Oordt CW, Hoekstra OS, et al. Immuno-Positron Emission Tomography with Zirconium-89-Labeled Monoclonal Antibodies in Oncology: What Can We Learn from Initial Clinical Trials? *Front Pharmacol*. 2016;7:131.

5. Maisel D, Birzele F, Voss E, et al. Targeting Tumor Cells with Anti-CD44 Antibody Triggers Macrophage-Mediated Immune Modulatory Effects in a Cancer Xenograft Model. *PLoS ONE*. 2016;11:e0159716.

6. Orian-Rousseau V, Ponta H. Perspectives of CD44 targeting therapies. *Arch Toxicol*. 2015;89:3-14.

7. Ponta H, Sherman L, Herrlich PA. CD44: from adhesion molecules to signalling regulators. *Nat Rev Mol Cell Biol*. 2003;4:33-45.

8. Toole BP. Hyaluronan-CD44 Interactions in Cancer: Paradoxes and Possibilities. *Clin Cancer Res*. 2009;15:7462-7468.

9. Vugts DJ, Heuveling DA, Stigter-van Walsum M, et al. Preclinical evaluation of 89Zr-labeled anti-CD44 monoclonal antibody RG7356 in mice and cynomolgus monkeys: Prelude to Phase 1 clinical studies. *MAbs*. 2014;6:567-575.

10. Menke-van der Houven van Oordt CW, Gomez-Roca C, van Herpen C, et al. First-in-human phase I clinical trial of RG7356, an anti-CD44 humanized antibody, in patients with advanced, CD44-expressing solid tumors. *Oncotarget*. 2016;7:80046-80058.

11. Verel I, Visser GWM, Boellaard R, Walsum MS, Snow GB, Dongen GAMS van. 89Zr Immuno-PET: Comprehensive Procedures for the Production of 89Zr-Labeled Monoclonal Antibodies. *J Nucl Med*. 2003;44:1271-1281.

12. Perk LR, Vosjan MJWD, Visser GWM, et al. p-Isothiocyanatobenzyl-desferrioxamine: a new bifunctional chelate for facile radiolabeling of monoclonal antibodies with zirconium-89 for immuno-PET imaging. *Eur J Nucl Med Mol Imaging*. 2010;37:250-259.

13. Vosjan MJWD, Perk LR, Visser GWM, et al. Conjugation and radiolabeling of monoclonal antibodies with zirconium-89 for PET imaging using the bifunctional chelate p-isothiocyanatobenzyl-desferrioxamine. *Nat Protoc*. 2010;5:739-743.

14. Makris NE, Boellaard R, Visser EP, et al. Multicenter harmonization of 89Zr PET/CT performance. *J Nucl Med*. 2014;55:264-267.

15. Lodge MA, Chaudhry MA, Wahl RL. Noise considerations for PET quantification using maximum and peak standardized uptake value. *J Nucl Med*. 2012;53:1041-1047.

16. Uhlen M, Oksvold P, Fagerberg L, et al. Towards a knowledge-based Human Protein Atlas. *Nat Biotechnol*. 2010;28:1248-1250.

17. Mackay CR, Terpe HJ, Stauder R, Marston WL, Stark H, Günthert U. Expression and modulation of CD44 variant isoforms in humans. *J Cell Biol*. 1994;124:71-82.

18. Basic anatomical and physiological data for use in radiological protection: reference values. A report of age- and gender-related differences in the anatomical and physiological characteristics of reference individuals. ICRP Publication 89. *Ann ICRP*. 2002;32:5-265.

19. Perk LR, Visser GWM, Vosjan MJWD, et al. 89Zr as a PET Surrogate Radioisotope for Scouting Biodistribution of the Therapeutic Radiometals 90Y and 177Lu in Tumor-Bearing Nude Mice After Coupling to the Internalizing Antibody Cetuximab. *J Nucl Med*. 2005;46:1898-1906.

20. Börjesson PKE, Jauw YWS, Boellaard R, et al. Performance of immuno-positron emission tomography with zirconium-89-labeled chimeric monoclonal antibody U36 in the detection of lymph node metastases in head and neck cancer patients. *Clin Cancer Res*. 2006;12:2133-2140.

21. Menke-van der Houven van Oordt CW, McGeoch A, Bergstrom M, et al. ImmunoPET imaging to assess target engagement: Experience from 89Zr-anti-HER3 mAb (GSK2849330) in patients with solid tumors. *J Nucl Med*. February 2019.

8

# SUPPLEMENTARY DATA
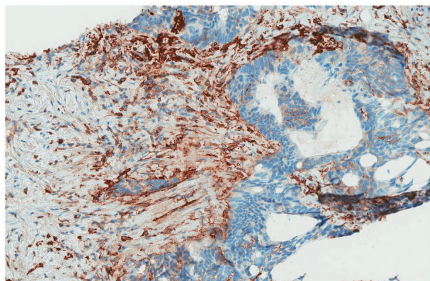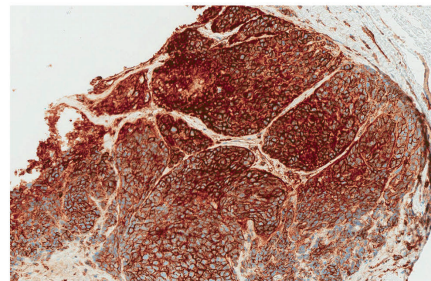


**Supplemental Figure** 1. Example of immunohistochemistry staining for CD44 for (a) patient 9, rectum carcinoma, biopsy of a liver metastasis CD44 Score: 2+ (b) patient 8, squamous cell carcinoma of the head and neck, biopsy of a neck metastasis, CD44 Score: 3+
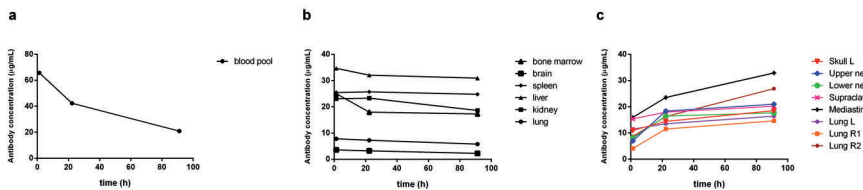


**Supplemental Figure** 2. Example graph of blood pool (a), normal tissue (b) and tumor (c) for patient 8. The mediastinal tumor (patient 8) corresponds with Fig. 5. The tumor in the skull L (patient 8) corresponds with Supplemental Fig 3.
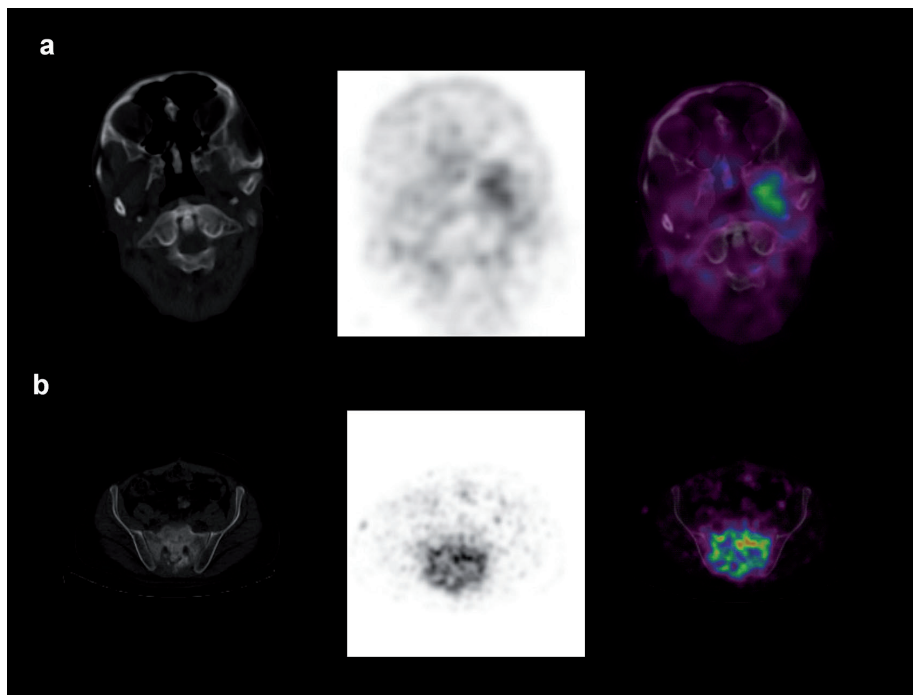
**Supplemental Figure** 3. Additional examples of focal tumor uptake of 89Zr-RG7356 at 96 h p.i.. From left to right: low dose CT, attenuation corrected PET and fused image. (a) Tumor lesion: left side of the skull (patient 8, 450mg cohort). (b) Tumor lesion: sacrum (patient 13, 675mg cohort).

**Supplemental Table 1** Specific scoring criteria for CD44 expression in patient samples

| Staining Intensity in tumor cells | CD44 Scoring Assignment | Eligible for inclusion in trial |
|---|---|---|
| 3+ in >30% of tumour cells | 3 | Yes |
| 2+ in >30% of tumor cells | 2 | Yes |
| 2+ or 3+ in <30% of tumor cells | 2 (focal) | Yes |
| (1+) or 1+ in >30% of tumor cells | 1 | Yes |
| (1+) or 1+ in <30% of tumor cells | 1 (focal) | No |
| No staining present in tumor cells | 0 | No |
| Indeterminate | Determination of reactivity not possible. Includes necrosis, no tumor present, no tissue present, or artifacts. | No |
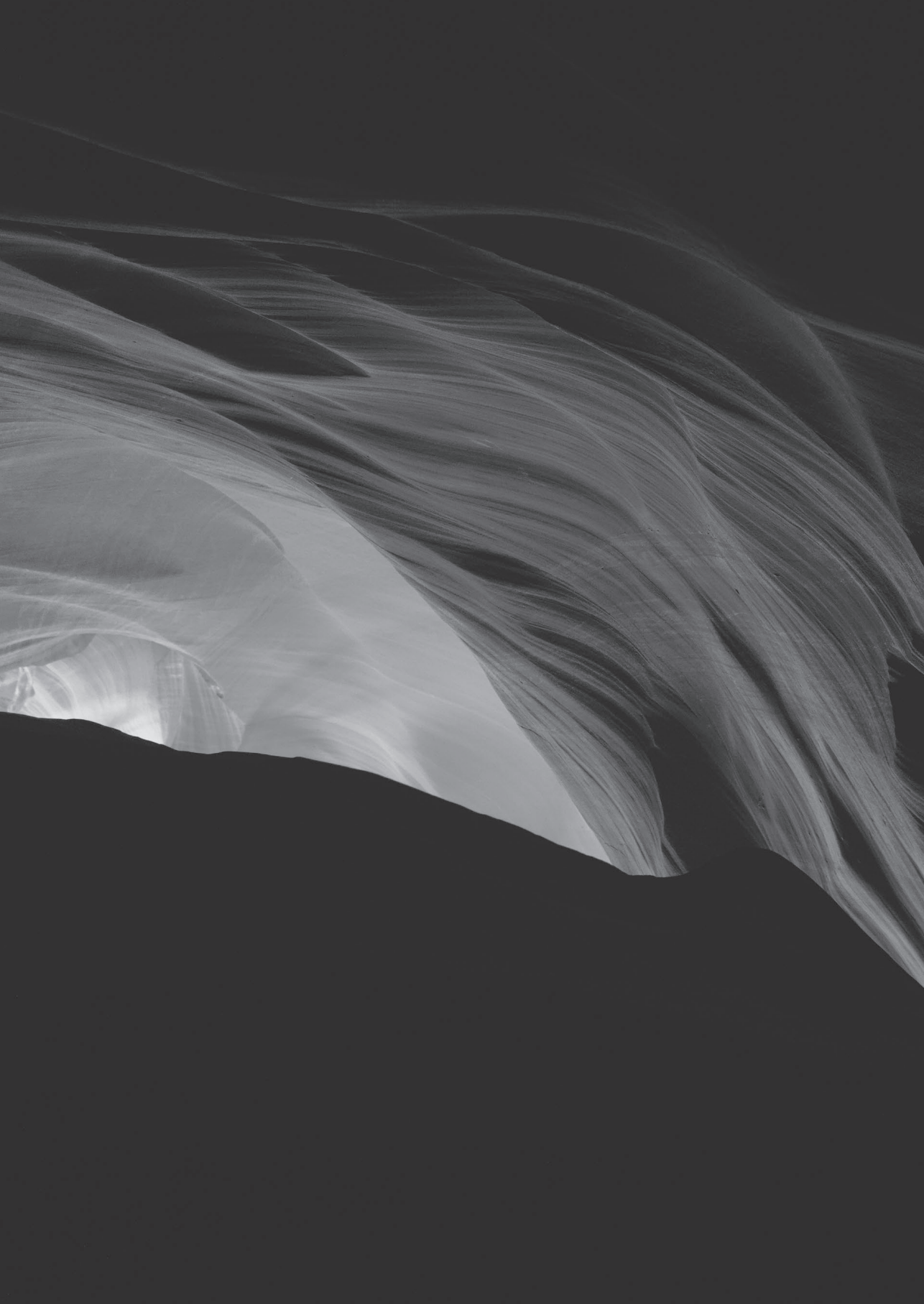
# <sup>89</sup>Zr-immuno-PET:

# Towards a non-invasive clinical tool to measure target engagement of therapeutic antibodies in-vivo

Yvonne W.S. Jauw
Joseph A. O'Donoghue
Josée M. Zijlstra
Otto S. Hoekstra
Willemien Menke-van der Houven van Oordt
Franck Morschhauser
Jorge Carrasquillo
Sonja Zweegman
Neeta Pandit-Taskar
Adriaan A. Lammertsma
Guus. A.M.S. van Dongen
Ronald Boellaard
Wolfgang A Weber
Marc C. Huisman

# ABSTRACT

**Rationale:** Zirconium-89-immuno-positron emission tomography ([89]Zr-immuno-PET) is a promising non-invasive clinical tool to measure target engagement of monoclonal antibodies (mAbs); in normal tissues to predict toxicity and in tumors to predict efficacy. Quantification of [89]Zr-immuno-PET will need to move beyond standardized uptake values (SUV), since total uptake may contain a significant non-target-specific contribution. Non-specific uptake is reversible (e.g. blood volume) or irreversible (due to [89]Zr-residualization after mAb degradation). The aim of this study was to assess non-specific uptake in normal tissues as a first critical step towards quantification of target engagement in normal tissues and tumors using [89]Zr-immuno-PET.

**Methods:** Data from clinical studies with 4 [89]Zr-labeled intact IgG1 antibodies were collected, resulting in a total of 128 PET scans (1 to 7 days p.i. from 36 patients: [89]Zr-antiCD20 (n=9), [89]Zr-antiEGFR (n=7), [89]Zr-antiPSMA (n=10) and [89]Zr-HER2 (n=10). Non-specific uptake was defined as uptake measured in tissues without known target expression. Patlak graphical evaluation of transfer constants was used to estimate the reversible ($V_t$) and irreversible ($K_i$) contributions to the total measured uptake for the kidney, liver, lung and spleen. Baseline values were calculated per tissue combining all mAbs without target expression (kidney: [89]Zr-antiCD20, [89]Zr-antiEGFR, [89]Zr-antiHER2; liver: [89]Zr-antiCD20; lung: [89]Zr-antiCD20, [89]Zr-antiEGFR, [89]Zr-antiPSMA; spleen: [89]Zr-antiEGFR, [89]Zr-antiHER2).

**Results:** Baseline $V_t$ for the kidney, liver, lung and spleen was 0.20, 0.24, 0.09 and 0.24 mL×cm$^{-3}$, respectively. Baseline $K_i$ was 0.7, 1.1, 0.2 and 0.5 μL×g$^{-1}$×h$^{-1}$ for the kidney, liver, lung and spleen. For [89]Zr-antiPSMA, a four-fold higher $K_i$ was observed for the kidney, indicating target engagement. In this case, non-specific uptake accounted for 66, 34 and 22% of the total signal in the kidney at 1, 3, 7 days p.i. respectively.

**Conclusion:** This study shows that non-specific uptake of mAbs for tissues without target expression can be quantified using [89]Zr-immuno-PET at multiple time points. These results form a crucial base for measurement of target-engagement by therapeutic antibodies *in-vivo* with [89]Zr-immuno-PET. For future studies, a pilot phase including at least 3 scans ≥ 1 day p.i., is required to assess non-specific uptake as a function of time, to optimize study design for detection of target engagement.

# INTRODUCTION

In-vivo assessment of target engagement is of interest to understand efficacy (tumor selectivity) and toxicity (due to target expression in normal tissues) of treatment with monoclonal antibodies (mAbs) or mAb conjugates. Currently, only plasma concentrations of mAbs can be easily measured in-vivo by obtaining blood samples. Direct measurement in tissues is difficult, as this requires invasive tissue sampling, limiting clinical application.

89Zr-immuno-PET is a non-invasive, whole body technique with the potential to measure target engagement of therapeutic antibodies (or mAb conjugates) *in-vivo* (*1*). Future applications of this clinical tool are selection of mAbs during drug development and selection of patients who are likely to benefit from treatment (*2*).

Currently, it is common practice to report a single uptake value, expressed as standardized uptake value (SUV) or percentage injected activity per mL (%IA/mL) for 89Zr-immuno-PET. However, the measured uptake in tissue is the sum of specific uptake (target engagement by the therapeutic antibody) and non-specific uptake (i.e. activity in the blood vessels or in the interstitial space that does not interact with the target and therefore has no pharmacologic effects). The ratio between specific uptake and non-specific uptake is expected to be time dependent. Measured uptake at early time points mainly consists of the blood volume fraction, while specific uptake increases over time. If specific uptake dominates, a single uptake value is an appropriate estimate to assess target engagement (*3*). This measurement is then expected to correlate with target expression in biopsies (determined by immunohistochemistry) and treatment outcome. However, also biopsy sampling has several limitations, e.g. sampling error and heterogeneity in target expression. Although biopsies may not provide a true gold standard for target engagement, it is the commonly available comparator. So far, clinical 89Zr-immuno-PET studies have reported equivocal results; sometimes suggesting a correlation and sometimes not (*4-7*). These results indicate that a single uptake value could be insufficient due to the contribution of non-specific uptake. Therefore, knowledge of non-specific uptake is required to optimize study design.

The aim of this study was to assess non-specific uptake for tissues without target expression, as a first step towards quantification of target engagement using 89Zr-immuno-PET.

Non-specific uptake is due to the blood volume fraction of the tissue, as well as antibody distribution (entering the tissue interstitium through paracellular pores, and through endothelial cells mediated by the neonatal Fc-receptor, leaving the tissue by convective transport through lymph flow) (Figure 1A)(*8*). At equilibrium, this physiological component is linear with the plasma concentration (*9*) and is characterized as reversible uptake. In addition, non-specific catabolism of antibodies occurs by pinocytosis (e.g. in endothelial cells) and subsequent lysosomal proteolytic degradation (*10,11*). After the antibody is degraded, [89]Zr residualizes, leading to another component of non-specific uptake (Figure 1B) (*11,12,13*). This component is proportional to the area under the plasma time activity curve from the time of injection up to the scan time point, and is characterized as irreversible uptake. For tissues without target expression, this uptake is solely due to residualization of [89]Zr after non-target-mediated degradation of the mAb.

These two components of non-specific uptake can be quantified using graphical evaluation of transfer constants, commonly known as the 'Patlak linearization' approach as used for ^{18}F-FDG-PET (*14*). For tissues without target expression, we expect transfer constants in agreement with known literature for non-binding mAbs. For tissues with target expression, transfer constants would potentially differ due to target engagement (Figure 1C)(*15*).

## MATERIALS AND METHODS

### Data collection

[89]Zr-immuno PET scans and blood sample data were obtained for [89]Zr-obinutuzumab (*16*), [89]Zr-cetuximab (*17*), [89]Zr-huJ591 (*18*) and [89]Zr-trastuzumab (*19*)(Table 1). In the remainder of this report, the [89]Zr-labeled-mAbs used in these studies will be denoted as [89]Zr-antiCD20, [89]Zr-antiEGFR, [89]Zr-antiPSMA and [89]Zr-antiHER2, respectively. Data were selected based on the availability of scans at multiple time points (at least 3) for each patient, including plasma or serum activity concentrations from venous blood sampled at each scan time point.

Data was collected from 1) Amsterdam UMC, the Netherlands, 2) CHU Lille, France and 3) Memorial Sloan Kettering Cancer Center (MSKCC), USA. All studies were approved by an institutional review board and ethics committee. At CHU Lille and MSKCC, PET scans were acquired on a GE Discovery PET/CT
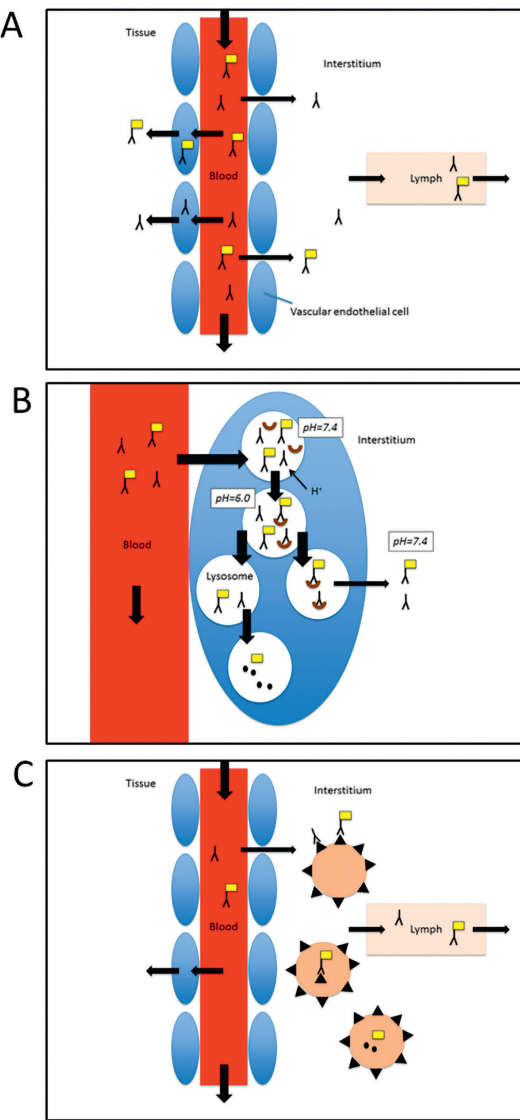
**Figure 1** Biodistribution of a $^{89}$Zr-labeled mAb: physiological components

Reversible non-specific uptake (A) due to antibody in the vascular tissue compartment and antibody entering the tissue interstitium through paracellular pores, and through endothelial cells mediated by the neonatal Fc-receptor, leaving the tissue by convective transport through lymph flow. Irreversible non-specific uptake (B) due to mAb degradation in the lysosome, followed by residualization of $^{89}$Zr. Specific uptake (C) due to target engagement (target binding and internalization of mAb-target antigen).

*Adapted from Lobo 2004 (8) and Chen 2012 (10).*

Table 1 Data characteristics

| | 89Zr-antiCD20 | 89Zr-antiEGFR | 89Zr-antiPSMA | 89Zr-antiHER2 |
|---|---|---|---|---|
| **General information** | | | | |
| mAb | Obinutuzumab | Cetuximab | Hu-J591 | Trastuzumab |
| Type | Humanized | Chimeric | Humanized | Humanized |
| IgG subclass | IgG1 | IgG1 | IgG1 | IgG1 |
| Target expression(20) | | | | |
| • - Kidney | Absent | Absent | Present | Absent |
| • - Liver | Absent | Present | Present | Present |
| • - Lung | Absent | Absent | Absent | Present |
| • - Spleen | Present | Absent | Absent* | Absent |
| | | | | |
| **Study design** | | | | |
| Center | Amsterdam UMC(n=4) CHU Lille(n=5) | Amsterdam UMC | MSKCC | MSKCC |
| Patient category | Non-Hodgkin lymphoma | Colo-rectal carcinoma | Prostate cancer | Gastric cancer |
| Number of patients | 9 | 7 | 10 | 10 |
| Injected activity/mAb dose | 37MBq/10 mg 1000mg unlabeled mAb | 37MBq/10mg 500mg/m² unlabeled mAb | 185MBq/1.7mg total mass of 25mg mAb | 185MBq/3mg total mass of 50mg mAb |
| Administration** | predose | predose | co-injection | co-injection |
| PET scan time points | 1 hr;72h,144h p.i. | 1hr;72h,144h p.i. | 2-4h,24h,48-120h,144-168h p.i. | 4h,24h,48-96h,120-192h p.i. |
| Blood sample*** | plasma | plasma | serum | serum |
| Blood sampling timepoints | 5,30,60,120min,24h****, 72h,144h p.i. | 1-2h,24h,48h,72h,144h | 5,30,60,120-240min,24h,48-120h, 144-168h p.i. | 5,15,30,60min,2h,24h,48-96h, 120-192h p.i. |
| Reference | Jauw, et al.(16) | Menke, et al.(17) | Pandit-Taskar, et al.(18) | O'Donoghue,et al.(19) |

*Expression of PSMA in the spleen has been reported(24)

**Administration: predose = 89Zr-mAb within 2 hours after administration of unlabeled mAb.

co-injection = unlabeled mAb infused intravenously over 5min followed immediately by a 1min infusion of the radiolabeled mAb.

***Blood samples consisted of plasma or serum samples; assuming no practical difference between these assays for our purposes, since mAb binding does not occur to coagulation factors (the difference between plasma and serum).

****Blood samples obtained at 24h p.i. at CHU Lille(n=5), no 24h sample obtained at Amsterdam UMC

scanner (GE Healthcare, Waukesha, WI, USA). At Amsterdam UMC, PET scans were acquired on a Philips Gemini TF-64 or Ingenuity TF-128 PET/CT scanner (Philips Healthcare, Best, the Netherlands). For all procedures, a low dose computed tomography scan was used for attenuation and scatter correction. Volumes of interest (VOI) of the kidney, liver, lung and spleen were manually delineated on each scan and characterized by the mean radioactivity concentration in Bq×cm$^{-3}$. All radioactivity concentrations were decay corrected to the time of injection.

For each antibody, the Human Protein Atlas (*20*) was used as reference for lack of target antigen expression in tissues of interest.

### Patlak Linearization

Patlak linearization applied to multiple-time tissue activity concentration measurements allows an estimate of the reversible and the irreversible contributions to the measured activity. The method was initially applied to blood-to-brain transfer and considered the fate of a test solute to obtain transfer constants (*14,21*). For $^{89}$Zr-immuno-PET, we utilized this method to determine reversible and irreversible non-specific uptake of therapeutic antibodies. This analysis was performed per patient, for each tissue (liver, spleen, lung, kidney).

Input data consisted of the activity concentration in plasma ($AC_p$ in Bq×mL$^{-1}$) and in tissue ($AC_t$ in Bq×cm$^{-3}$) as a function of time post injection. The data were plotted as

$$\frac{AC_t}{AC_p} = K_i \frac{\int_0^t AC_p(\tau)d\tau}{AC_p} + V_T,$$

with $AC_t/AC_p$ along the y-axis and $\int AC_p(\tau)d\tau \, / \, AC_p$ along the x-axis (commonly known as a 'Patlak plot').

The $\int AC_p(\tau)d\tau$ term represents the area under the plasma curve from the time of injection up to the time of the measurement, and will be referred to as $AUC_p^{0-t}$. The offset of the Patlak plot represents the distribution volume $V_T$ (in mL×cm$^{-3}$) and the slope of the Patlak plot, $Ki$ (in mL×g$^{-1}$×min$^{-1}$), the net rate of irreversible uptake.

Late time points (defined as ≥ 1day p.i) were included in the linear fit, as equilibrium state was assumed for these time points (*1*). Early time points (scans at 1h p.i.) were therefore not included.

The quality of the linear fit was assessed if at least 3 late time points were available. An r-value>0.9 was considered acceptable. Linear fits with an r-value <0.9 were excluded from the analysis.

The reversible and irreversible contributions to the uptake of [89]Zr-mAb (AC[f]) at each time point were calculated as

$$AC_t^r = V_T \cdot AC_p, and\ AC_t^i = K_i \cdot AUC_p^{0-t},$$

with superscript *r* for the reversible and *i* for the irreversible component. In addition, the percentage difference between fitted (AC[f] = AC[r] + AC[i]) and measured tissue activity concentrations per time point was calculated as (AC[f]-AC[t])/AC[t] x 100 (%).

## Predicted Values for Transfer Constants

The transfer constants obtained were interpreted in terms of physiological components of antibody biodistribution. A literature search was performed to obtain predicted values for these physiological components for a non-binding intact IgG1 mAb.

To predict the value for the reversible component for a non-binding mAb, we used the proportionality constant between the tissue and plasma concentration, referred to as the antibody biodistribution coefficient (ABC). ABC for various tissues were obtained by a physiologically-based pharmacokinetic (PBPK) model of mAbs and validated with experimental data (*9*). The reported ABC for brain was 0.004 (*9*), indicating that the plasma volume fraction of 0.02 (*22*) was not included. Therefore, we defined the predicted value for $V_T$ as the ABC plus the plasma volume fraction (within a 2-fold error margin, as reported for all ABC). The volume fraction was calculated as the plasma volume of the tissue (in mL) divided by the total volume of the tissue (in mL). Plasma and total tissue volumes were obtained from previously published physiological model parameters for human (*22*). For example, for the kidney, the reported ABC was 0.137 and the plasma volume fraction 0.055 (*22*), leading to a predicted $V_T$ of 0.19. The predicted values for $V_T$ for liver and spleen were 0.21 and 0.25 (*9,22*). The ABC for lung requires special consideration, since lung has a density of ~0.3g/mL. Volumes of distribution are in mL×cm[-3], and therefore the ABC for lung was divided by three in order to compare with $V_T$ values derived from [89]Zr-immuno-PET. For lung, the predicted value for $V_T$ was 0.10 (*9,22*).

For tissues without target expression, the entire irreversible component is due to non-target mediated mAb degradation (and subsequent residualizing of [89]Zr). Endosomal mAb degradation is a non-specific catabolic mechanism for all intact IgG molecules. Per day, 6.3% of the intravascular IgG pool is catabolized (*23*). Therefore, the whole body catabolic rate was estimated at 7.8 mL·h$^{-1}$, using a reference total plasma volume (*22*). The contribution of individual tissues (experimentally determined in mice) was 6%, 30%, 1.3% and 2.8% for kidney, liver, lung and spleen, respectively (*11*). These values were used to predict the irreversible component for tissues without target expression.

To compare the [89]Zr-immuno-PET derived value for the net rate of irreversible uptake in $\mu L \times g^{-1} \times h^{-1}$ to the catabolic rate in $mL \times h^{-1}$, $K_i$ was multiplied by tissue volume (*22*).

Predicted values for $V_T$ and $K_i$, including literature values used, are presented in Supplemental Table 1.

**Statistical Analysis**

Values for $V_T$ and $K_i$ are presented per tissue, and per [89]Zr-mAb. Median values and interquartile ranges were reported due to the small sample size per group.

In addition, a baseline value was obtained by combining the *n* values for tissues without target expression. For example, no target expression in the kidney was reported for CD20, EGFR and HER2 (Table 1) (*20*). Therefore, [89]Zr-antiCD20, [89]Zr-antiEGFR and [89]Zr-antiHER data were combined to determine the baseline value for $V_T$ and $K_i$, for kidney tissue without target expression. Baseline values for liver consisted of [89]Zr-antiCD20. For lung, data on [89]Zr-antiCD20, [89]Zr-antiEGFR and [89]Zr-antiPSMA were combined to obtain the baseline value. For spleen, the baseline value consisted of [89]Zr-antiEGFR and [89]Zr-antiHER2.

The Wilcoxon signed rank test was used to determine whether the *n* values for $V_T$ for tissues without target expression (baseline values) differed from the predicted value. A p-value <0.05 was considered statistically significant. Statistical tests were performed in GraphPad Prism, version 6.02.

9

# RESULTS

## Patlak Linearization
Per patient, Patlak linearization was conducted for each tissue (kidney, liver, lung, spleen) (Fig.2). An r-value of >0.9 was obtained for 71/80 linear fits for [89]Zr-antiPSMA and [89]Zr-antiHER2 (3 late time points available). Therefore, we assumed that data for [89]Zr-antiCD20 and [89]Zr-EGFR were consistent with the assumptions under the Patlak method. For these datasets, the r-value for the linear fit could not be obtained (only 2 late time points available). For [89]Zr-antiHER2 an *r*-value <0.9 was obtained for 1/10 fits for kidney uptake, 2/10 for liver, 4/10 for lung and 2/10 for spleen. The mean percentage difference between fitted and measured tissue activity concentrations per time point for all fits through 3 time points with r >0.9 was ±4%, except for [89]Zr-antiPSMA in the kidney (Supplemental Table 2).
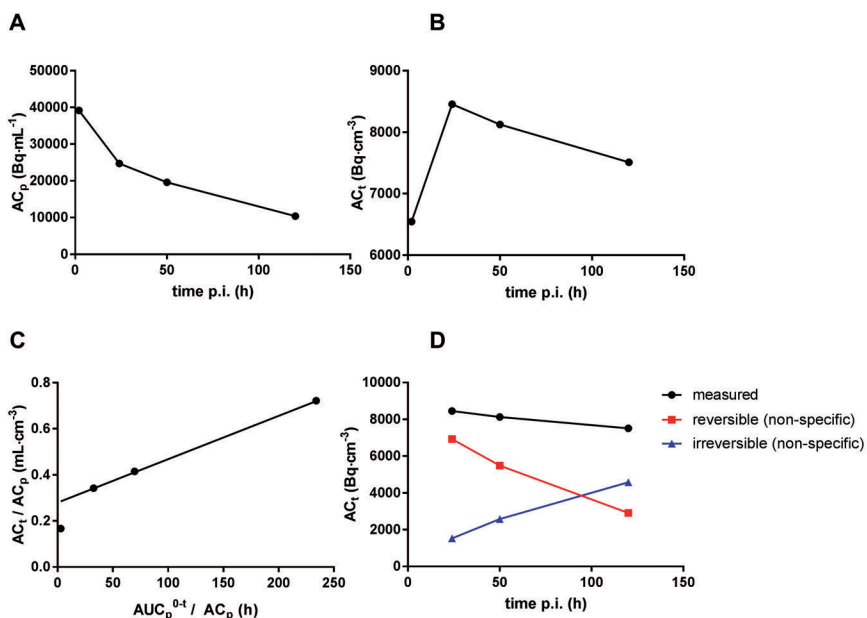


Figure 2 Transfer constants for [89]Zr-antiHER2 in the kidney

Example for one patient in the [89]Zr-antiHER2 study, with (A) measured activity concentrations in serum and (B) measured activity concentrations in the kidney. Patlak linearization (C) to determine the offset ($V_T$) and slope ($K_i$) of the linear fit to the last three time points (same data). (D) Reversible (red line) and irreversible (blue line) contributions to the total measured signal (black line). No target expression has been reported for HER2 in the normal kidney. Therefore, we hypothesize that the total signal consists of non-specific uptake. After 100h p.i., total uptake predominantly consists of irreversible non-specific uptake due to [89]Zr-residualization after mAb degradation.

## Volume of Distribution ($V_T$)

Values for $V_T$ per mAb are presented in Table 2. Non-specific, reversible uptake is reflected by baseline values for $V_T$ for tissues without target expression. For the kidney, liver, lung and spleen respectively, measured baseline values for $V_T$ were 0.20 (0.16-0.25), 0.24 (0.21-0.28), 0.09 (0.07-0.10) and 0.24 (0.20-0.27) mL×cm$^{-3}$. For these tissues, the predicted values for $V_T$ (ABC + plasma volume fraction) were 0.19, 0.21, 0.10 and 0.25, respectively. No differences were observed between the measured baseline value for $V_T$ and the predicted value for kidney (p=0.24; $n$=25), liver (p= 0.07; $n$=9) and spleen (p=0.12; $n$=15). For lung, the measured baseline value for $V_T$ (0.09, 0.07-0.10) was statistically different (p< 0.02; $n$=25) from the predicted value of 0.10, but within the two-fold error range (0.05-0.20) of the predicted value.

Table 2 Volume of distribution $V_t$

|  | [89]Zr-antiCD20 | [89]Zr-antiEGFR | [89]Zr-antiPSMA | [89]Zr-antiHER2 | Baseline |
|---|---|---|---|---|---|
| Kidney | 0.18(0.15-020) | 0.25(0.23-0.29) | 0.28(0.21-0.32) | 0.19(0.15-0.25) | 0.20(0.16-0.25) |
| Liver | 0.24(0.21-0.28) | 0.64(0.54-0.91) | 0.29(0.23-0.43) | 0.24(0.22-0.29) | 0.24(0.21-0.28) |
| Lung | 0.08(0.08-0.10) | 0.11(0.09-0.13) | 0.07(0.06-0.09) | 0.08(0.05-0.11) | 0.09(0.07-0.10) |
| Spleen | 0.20(0.18-0.21) | 0.23(0.20-0.27) | 0.22(0.20-0.28) | 0.24(0.18-0.27) | 0.24(0.20-0.27) |

$V_t$ (mL×cm$^{-3}$) presented as median (interquartile range)

## Net Rate of Irreversible uptake ($K_i$)

Values for $K_i$ per mAb are presented in Table 3. Non-specific, irreversible uptake is reflected by baseline values for $K_i$ for tissues without target expression. For kidney, liver, lung and spleen respectively, measured baseline values for $K_i$ were 0.7 (0.4-1.3), 1.1 (0.8-2.1), 0.2 (0.1-0.3) and 0.5 (0.3-0.7) μL×g$^{-1}$×h$^{-1}$. For kidney, the baseline catabolic rate was 0.23 mL×h$^{-1}$, equal to 3% of the whole body catabolic rate (predicted value 6%). Fractional catabolic rate of liver, lung and spleen were 30%, 3% and 1%, respectively (predicted values were 30%, 1.3% and 2.8%).

## Detection of Target Engagement

In case of target engagement (Figure 1C), we expect to observe an increased rate of irreversible uptake compared to the baseline value. Expression of PSMA was reported for the kidney (*18*) and therefore target engagement of [89]Zr-antiPSMA is expected in this tissue. Patlak linearization for [89]Zr-antiPSMA was performed (Figure 3). In this case, a four-fold higher $K_i$ (2.8 vs 0.7) was obtained compared to the baseline value for the kidney, indicating target engagement by irreversible

uptake. For liver, an increased $K_i$ was observed for [89]Zr-antiEGFR, [89]Zr-antiPSMA and [89]Zr-antiHER2 (3.8, 5.7 and 1.7 respectively compared to 1.1), corresponding with known target expression (20). No increased $K_i$ was observed for lung and spleen (Table 3).

Table 3 Net rate of irreversible uptake $K_i$

|  | [89]Zr-antiCD20 | [89]Zr-antiEGFR | [89]Zr-antiPSMA | [89]Zr-antiHER2 | Baseline |
|---|---|---|---|---|---|
| Kidney | 0.4(0.2-0.6) | 0.7(0.4-1.2) | 2.8(2.4-3.1) | 1.5(0.9-1.8) | 0.7(0.4-1.3) |
| Liver | 1.1(0.8-2.1) | 3.8(1.9-5.8) | 5.7(4.9-8.4) | 1.7(1.4-2.0) | 1.1(0.8-2.1) |
| Lung | 0.2(0.1-0.3) | 0.4(0.2-0.6) | 0.1(0.0-0.2) | 0.2(0.0-0.5) | 0.2(0.1-0.3) |
| Spleen | 0.6(0.5-0.8) | 0.5(0.3-0.5) | 1.5(1.2-1.7) | 0.7(0.4-0.8) | 0.5(0.3-0.7) |

$K_i$ ($\mu L \times g^{-1} \times h^{-1}$) presented as median (interquartile range)
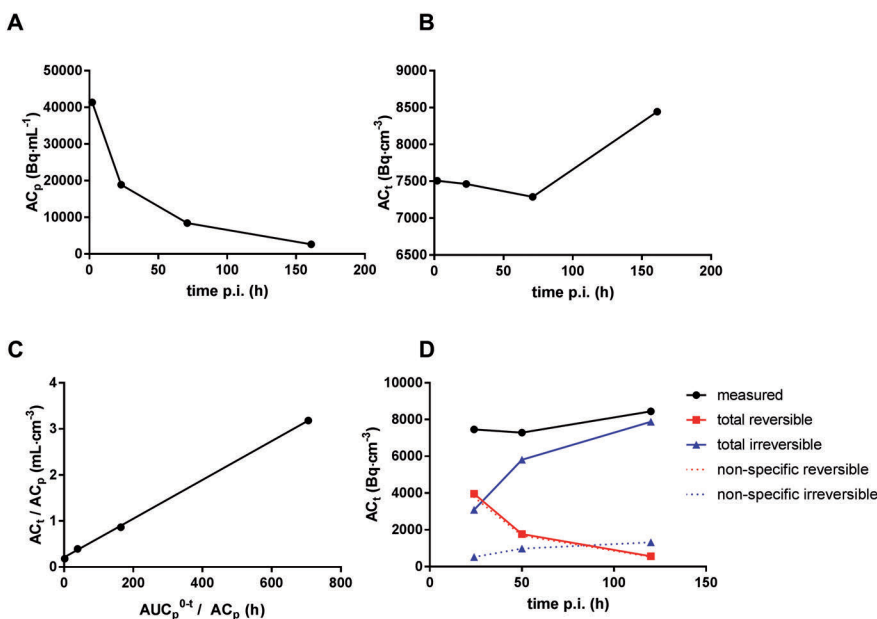


Figure 3 Transfer constants for [89]Zr-antiPSMA in the kidney

Example for one patient in the [89]Zr-antiPSMA study, with (A) measured activity concentrations in serum (A) and (B) measured activity concentrations in the kidney. Patlak linearization (C) to determine the offset ($V_T$) and slope ($K_i$) of the linear fit to the last three time points (same data). (D) Total reversible (red line) and total irreversible (blue line) contributions to the measured signal (black line).

Dashed lines represent estimated values for non-specific reversible uptake (calculated as baseline $V_T \cdot AC_p$) and non-specific irreversible uptake (calculated as baseline $K_i \cdot AUC_p^{0-t}$).

# DISCUSSION

[89]Zr-immuno-PET is a promising, non-invasive clinical tool to measure antibody target engagement *in-vivo*. As a first step towards quantification of target engagement, non-specific uptake for tissues without target expression was assessed for four [89]Zr-labeled mAbs. This study showed that non-specific, reversible uptake ($V_T$) was similar to the predicted value for a non-binding mAb. Non-specific, irreversible uptake ($K_i$) corresponded with the predicted value for the fractional catabolic rate of IgG. Patlak linearization is applied to data obtained from a single subject. The range of values observed for the baseline transfer constants reflects inter-patient variability. This method allows, for a single subject, to assess whether target-mediated binding does occur in a certain normal tissue for the antibody under investigation. Similar as for PKPD type analysis, Patlak linearization can be applied with sparse temporal sampling, but does not require assumptions that underlying parameters are the same among patients. Moreover, it uses the individually measured input functions, i.e. bioavailability of the tracer in blood over time and it can therefore account for inter-individual variability of the tracer bioavailability in the central compartment (i.e. blood). For these reasons this method was applied in our present study. An increase in $K_i$ indicates target engagement, as was observed for e.g. [89]Zr-antiPSMA in the kidney. In this study, baseline values for $K_i$ and $V_T$ were tissue dependent. Especially for the liver, relatively high non-specific, irreversible uptake was observed compared to other tissues, indicating that this organ is strongly involved in mAb catabolism. Therefore, detection of target engagement with a single uptake value is expected to be more difficult in the liver.

Study design can have a significant impact of the ability to detect target engagement. For example, for [89]Zr-antiCD20, no increase of irreversible uptake ($K_i$) was observed in the spleen, although expression of CD20 in the spleen is known to be high (*20*). A plausible explanation for this observation is saturation of the CD20 receptors due to high dose of unlabeled antiCD20 (1000mg), which was administered before the radiolabeled antibody. So, antibody dose is a parameter to be taken into account in assessment of target engagement. Another important consideration for design of [89]Zr-immuno-PET studies, is that scans obtained at multiple late time points are required for the Patlak linearization to determine reversible and irreversible uptake. At least 3 late time points are required to assess whether the data can be fitted to a straight line.

9

In some cases (9/80), the data could not be described by a linear fit. Especially for the lung (4/9), this could be explained by an unfavorable signal to noise ratio (low signal and relative low tissue density). The observed overestimation of fitted uptake data at 24h p.i. accompanied with an underestimation of the uptake at 48-120h p.i. for [89]Zr-antiPSMA in the kidney only may indicate that the reversible uptake processes were not yet in the equilibrium state at 24h p.i.. From a methodological perspective, collection of more data points would be preferred. This method could be further validated in future preclinical [89]Zr-immuno-PET studies, where scans at more time points can be acquired, including invasive tissue sampling to assess target expression by immunohistochemistry.

Usually, [89]Zr-immuno-PET scans are analyzed at a single time point, representing the sum of all physiological components of antibody distribution, being either target specific or non-specific. This study showed how the various physiological components of antibody distribution contribute to the measured SUV (Figure 2 and 3). For the kidney as an example, a SUV of around 2.5 was measured for [89]Zr-antiPSMA at 1 to 7days p.i.. Non-specific uptake was estimated to account for a SUV of 1.6 (66%) at 1day p.i.. The contribution of non-specific uptake decreased to a SUV of 0.6 (22%) at 7days p.i..

Detection of target engagement in normal tissues is of interest to assess which mAb has potential for further development into an antibody-drug conjugate (ADC). For an ADC, absence of target engagement in normal tissues is considered important to limit potential toxicity.

To understand and predict efficacy of mAb-based treatments, measurement of target engagement in tumors is essential. However, the method described in this paper cannot be directly applied to tumors, as these are expected to be more complex than normal tissues. Non-specific, reversible uptake in tumors (blood volume fraction and non-target mediated antibody distribution to tumor tissue ("tight or leaky tissue")) may be more variable between tumors and between patients. In addition, non-specific, irreversible uptake may be increased by the rate of protein catabolism in the tumor and uptake in tumor immune filtrates (e.g. macrophages). In future work, we aim to explore which method can be applied to measure target engagement for tumors. Especially target-negative tumors are of interest to study factors that influence non-specific uptake.

In the present study, [89]Zr-immuno-PET was used as a non-invasive clinical tool to assess physiological components of antibody distribution *in-vivo* and target engagement of therapeutic antibodies was observed. For future studies to assess

target engagement for other $^{89}$Zr-labeled mAbs, a multiple time point pilot study (with at least 3 late time points) is advised to determine the contribution of non-specific uptake as a function of time and mAb dose. This knowledge can be used to optimize study design and assess whether single time point scanning to detect target engagement is feasible and at which time point. This concept is widely applicable as mAbs and mAb conjugates against many target antigens are developed for a broad range of clinical indications.

## CONCLUSION

This study shows that non-specific uptake of mAbs for tissues without target expression can be quantified using $^{89}$Zr-immuno-PET at multiple time points. These results form a crucial base for measurement of target-engagement by therapeutic antibodies *in-vivo* with $^{89}$Zr-immuno-PET. For future studies, a pilot phase including at least 3 scans at ≥ 1 day p.i., is required to assess non-specific uptake as a function of time, to optimize study design for detection of target engagement.

## ACKNOWLEDGEMENTS

9

# REFERENCES

1.  Bergstrom M. The Use of Microdosing in the Development of Small Organic and Protein Therapeutics. *J Nucl Med*. 2017;58:1188-1195.

2.  Jauw YWS, Menke-van der Houven van Oordt CW, Hoekstra OS, et al. Immuno-Positron Emission Tomography with Zirconium-89-Labeled Monoclonal Antibodies in Oncology: What Can We Learn from Initial Clinical Trials? *Front Pharmacol*. 2016;7:131.

3.  Lammertsma AA. Forward to the Past: The Case for Quantitative PET Imaging. *J Nucl Med*. 2017;58:1019-1024.

4.  Gaykema SBM, Brouwers AH, Lub-de Hooge MN, et al. 89Zr-bevacizumab PET imaging in primary breast cancer. *J Nucl Med*. 2013;54:1014-1018.

5.  Lamberts LE, Menke-van der Houven van Oordt CW, ter Weele EJ, et al. ImmunoPET with Anti-Mesothelin Antibody in Patients with Pancreatic and Ovarian Cancer before Anti-Mesothelin Antibody-Drug Conjugate Treatment. *Clin Cancer Res*. 2016;22:1642-1652.

6.  Jauw YWS, Zijlstra JM, de Jong D, et al. Performance of 89Zr-Labeled-Rituximab-PET as an Imaging Biomarker to Assess CD20 Targeting: A Pilot Study in Patients with Relapsed/Refractory Diffuse Large B Cell Lymphoma. *PLoS ONE*. 2017;12:e0169828.

7.  McKnight BN, Viola-Villegas NT. 89 Zr-ImmunoPET companion diagnostics and their impact in clinical drug development. *J Labelled Comp Radiopharm*. 2018;61:727-738.

8.  Lobo ED, Hansen RJ, Balthasar JP. Antibody pharmacokinetics and pharmacodynamics. *J Pharm Sci*. 2004;93:2645-2668.

9.  Shah DK, Betts AM. Antibody biodistribution coefficients: inferring tissue concentrations of monoclonal antibodies based on the plasma concentrations in several preclinical species and human. *MAbs*. 2013;5:297-305.

10.  Chen Y, Balthasar JP. Evaluation of a catenary PBPK model for predicting the in vivo disposition of mAbs engineered for high-affinity binding to FcRn. *AAPS J*. 2012;14:850-859.

11.  Eigenmann MJ, Fronton L, Grimm HP, Otteneder MB, Krippendorff B-F. Quantification of IgG monoclonal antibody clearance in tissues. *MAbs*. 2017;9:1007-1015.

12.  Cheal SM, Punzalan B, Doran MG, et al. Pairwise comparison of 89Zr- and 124I-labeled cG250 based on positron emission tomography imaging and nonlinear immunokinetic modeling: in vivo carbonic anhydrase IX receptor binding and internalization in mouse xenografts of clear-cell renal cell carcinoma. *Eur J Nucl Med Mol Imaging*. 2014;41:985-994.

13.  Ferl GZ, Kenanova V, Wu AM, DiStefano JJ. A two-tiered physiologically based model for dually labeled single-chain Fv-Fc antibody fragments. *Mol Cancer Ther*. 2006;5:1550-1558.

14.  Patlak CS, Blasberg RG, Fenstermacher JD. Graphical evaluation of blood-to-brain transfer constants from multiple-time uptake data. *J Cereb Blood Flow Metab*. 1983;3:1-7.

15.  Li Z, Krippendorff B-F, Sharma S, Walz AC, Lavé T, Shah DK. Influence of molecular size on tissue distribution of antibody fragments. *MAbs*. 2016;8:113-119.

16.  Jauw Y, Zijlstra J, Hoekstra O, et al. First-in-human in-vivo biodistribution of a glyco-engineered antibody: 89Zirconium-labeled obinutuzumab in patients with non-Hodgkin lymphoma. *J Nucl Med*. 2017;58:387-387.

17.  Menke-van der Houven van Oordt CW, Gootjes EC, Huisman MC, et al. 89Zr-cetuximab PET imaging in patients with advanced colorectal cancer. *Oncotarget*. 2015;6:30384-30393.

18.  Pandit-Taskar N, O'Donoghue JA, Beylergil V, et al. [89]Zr-huJ591 immuno-PET imaging in patients with advanced metastatic prostate cancer. *Eur J Nucl Med Mol Imaging*. 2014;41:2093-2105.

19.  O'Donoghue JA, Lewis JS, Pandit-Taskar N, et al. Pharmacokinetics, Biodistribution, and Radiation Dosimetry for 89Zr-Trastuzumab in Patients with Esophagogastric Cancer. *J Nucl Med*. 2018;59:161-166.

20.  Uhlen M, Oksvold P, Fagerberg L, et al. Towards a knowledge-based Human Protein Atlas. *Nat Biotechnol*. 2010;28:1248-1250.

21.  Blasberg RG, Fenstermacher JD, Patlak CS. Transport of alpha-aminoisobutyric acid across brain capillary and cellular membranes. *J Cereb Blood Flow Metab*. 1983;3:8-32.

22.  Shah DK, Betts AM. Towards a platform PBPK model to characterize the plasma and tissue disposition of monoclonal antibodies in preclinical species and human. *J Pharmacokinet Pharmacodyn*. 2012;39:67-86.

23.  Waldmann TA, Strober W. Metabolism of immunoglobulins. *Prog Allergy*. 1969;13:1-110.

24.  Weineisen M, Schottelius M, Simecek J, et al. 68Ga- and 177Lu-Labeled PSMA I&T: Optimization of a PSMA-Targeted Theranostic Concept and First Proof-of-Concept Human Studies. *J Nucl Med*. 2015;56:1169-1176.

# SUPPLEMENTARY DATA

Supplemental Table 1 Predicted and observed transfer constants

| | Literature values | | | | | | Predicted transfer constants | | Observed transfer constants | |
|---|---|---|---|---|---|---|---|---|---|---|
| | ABC (2-fold error) (9) | total tissue volume (mL) (22) | tissue plasma volume (mL) (22) | plasma volume fraction * | Fraction of whole body catabolic rate per tissue (11) | No target expression for (20) | $V_t$ † | $K_i$ ‡ | Baseline $V_t$ § | Baseline $K_i$ § |
| kidney | 0.137 (0.07–0.27) | 332 | 18.2 | 0.055 | 0.06 | CD20 EGFR HER2 | 0.19 | 1.41 | 0.20 (0.16–0.25) | 0.7 (0.4–1.3) |
| liver | 0.121 (0.06–0.24) | 2143 | 183 | 0.085 | 0.30 | CD20 | 0.21 | 1.13 | 0.24 (0.21–0.28) | 1.1 (0.8–2.1) |
| lung | 0.149 ‖ (0.07–0.30) | 1000 | 55 | 0.055 | 0.013 | CD20 EGFR PSMA | 0.10 | 0.10 | 0.09 (0.07–0.10) | 0.2 (0.1–0.3) |
| spleen | 0.128 (0.06–0.26) | 221 | 26.8 | 0.121 | 0.028 | EGFR HER2 | 0.25 | 0.99 | 0.24 (0.20–0.27) | 0.5 (0.3–0.7) |

Observed values for $V_t$ ($mL \times cm^{-3}$) and $K_i$ ($\mu L \times g^{-1} \times h^{-1}$) presented as median (interquartile range)

* Plasma volume divided by total tissue volume.

† ABC plus plasma volume fraction.

‡ Fraction of whole body catabolic rate per tissue multiplied by the estimated whole body catabolic rate of 7.8 $mL \cdot h^{-1}$, divided by the tissue plasma volume, multiplied by 1000.

§ To determine baseline values per tissue, data from [89]Zr-labeled mAbs, for which no target expression was reported, were used.

‖ The ABC for lung was reported as 0.149 based on quantified tissue biodistribution per gram. To correct for the density of the lung in the calculation of predicted Vt (per ml), the ABC was multiplied by 0.3 g/mL.

9

**Supplemental Table 2** Relative difference between fitted and measured tissue activity concentrations

| | $^{89}$Zr-antiHER2 24 h p.i. | $^{89}$Zr-antiHER2 48-96 h p.i. | $^{89}$Zr-antiHER2 120-192 h p.i. | $^{89}$Zr-antiPSMA 24 h p.i. | $^{89}$Zr-antiPSMA 48-120 h p.i. | $^{89}$Zr-antiPSMA 144-168 h p.i. |
|---|---|---|---|---|---|---|
| kidney | -1.1 (11.0) n=10 | 3.3 (14.3) n=10 | -1.1 (3.6) n=10 | 18 .2 (14.5) n=9 | -8.3 (6.6) n=9 | 2.0 (1.6) n=9 |
| liver | 3.5 (5.6) n=10 | -3.3 (5.4) n=10 | 0.7 (2.1) n=10 | 0.5 (11.2) n=8 | 0.6 (6.2) n=8 | 0.1 (1.5) n=8 |
| lung | -1.7 (6.1) n=10 | 3.0 (10.9) n=10 | -0.6 (3.0) n=10 | 1.1 (5.0) n=6 | -1.0 (10.4) n=6 | 0.0 (2.0) n=6 |
| spleen | 1.4 (4.0) n=10 | -1.1 (4.9) n=10 | 0.2 (1.7) n=10 | 0.4 (8.2) n=8 | 0.2 (6.6) n=8 | 0.1  (1.4) n=8 |

Data presented as mean (SD) in %
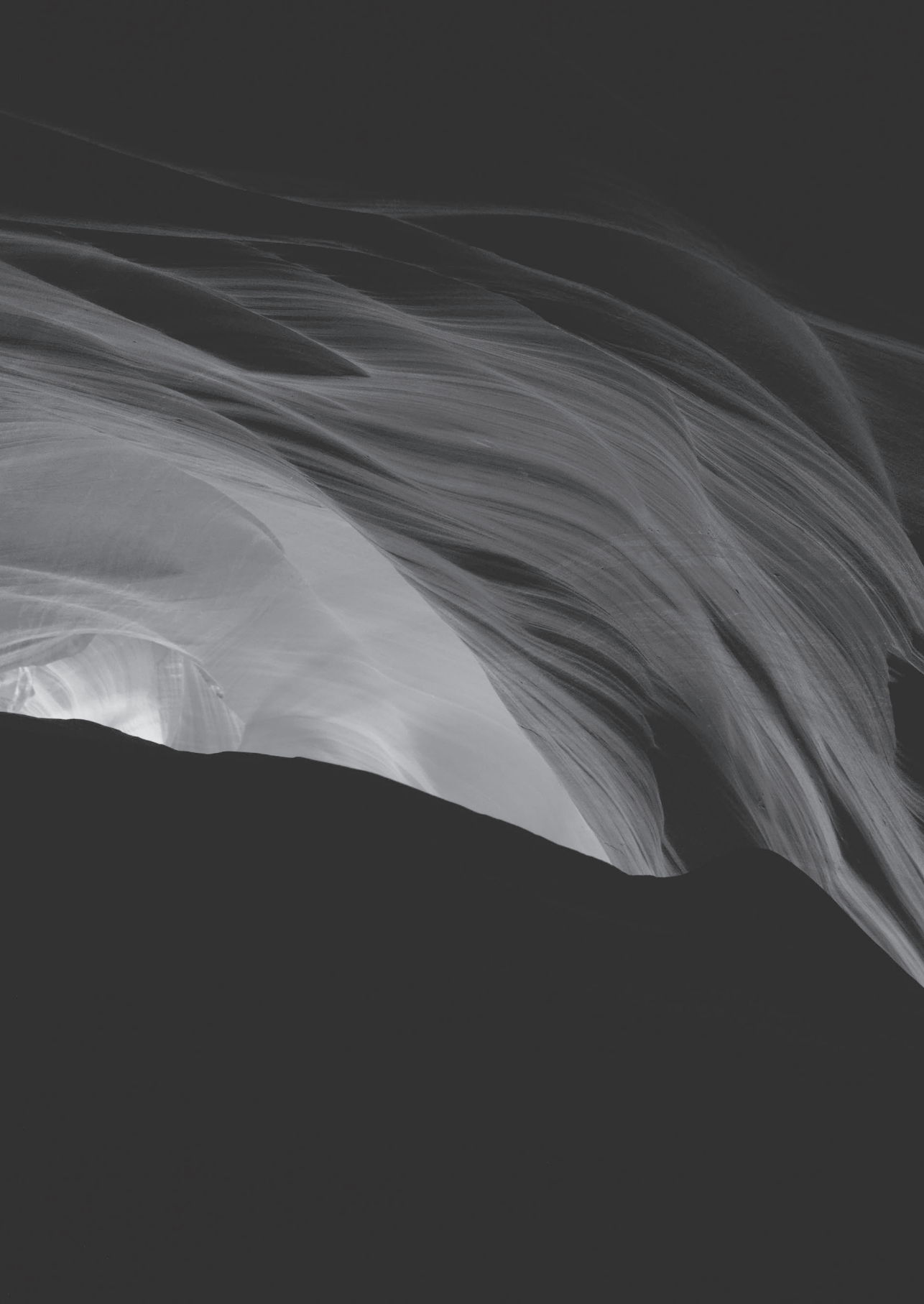
# CHAPTER 10

**Summary and discussion**

# SUMMARY AND DISCUSSION

There is an urgent need for reliable biomarkers to increase efficacy and reduce unnecessary toxicity and costs of antibody-based therapy in cancer. Antibody imaging using positron emission tomography (PET) with 89-Zirconium ([89]Zr)-labeled mAbs provides a potential imaging biomarker by assessment of target engagement of therapeutic mAbs.

The aim of this thesis was to develop [89]Zr-immuno-PET as a clinical tool to guide antibody-based therapy. Feasibility, technical and biological validation of [89]Zr-immuno-PET were investigated as essential steps towards application in drug development and routine clinical practice.

**Part I Feasibility of [89]Zr-immuno-PET**

*[89]Zr-labeled mAbs are safe to administer*

**Chapter 2** describes the first clinical [89]Zr-immuno-PET study. This study was performed in twenty patients with squamous cell carcinoma of the head and neck (HNSCC). Patients were at high risk of having neck lymph node metastases and therefore scheduled to undergo neck dissection (with or without resection of the primary tumor). All patients received 75 MBq of [89]Zr-labeled chimeric monoclonal antibody (cmAb) U36 (10 mg) and immuno-PET scans were obtained up to 6 days post injection (p.i.).

**Chapter 2** describes the safety of administration of [89]Zr-cmAb U36. The procedure was well tolerated in all patients; no serious or drug-related adverse events were reported. Two patients developed a human-anti-chimeric antigen (HACA) response, related to the protein part of the [89]Zr-labeled mAbconjugate, not to the chelate.

Administration of [89]Zr-labeled mAbs was also well tolerated in the other clinical studies described in this thesis. No adverse events related to the radiotracer were reported for [89]Zr-rituximab in patients with diffuse large B cell lymphoma (**Chapter 7**) and [89]Zr-antiCD44 in patients with CD44-expressing solid tumors (**Chapter 8**). In addition, the first 15 clinical trials with [89]Zr-immuno-PET in oncology (published between 2006 and 2016) showed no safety issues (**Chapter 4**).

10

*The radiation exposure due to [89]Zr-immuno-PET is ~0.6 mSv/MBq*

In **Chapter 2**, biodistribution and radiation dose of [89]Zr-cmAb U36 were investigated in the cohort of 20 patients with head and neck cancer. The normal organ with the highest absorbed dose was the liver (mean dose: 1.25±0.27 mSv/MBq in men and 1.35±0.21 mSv/MBq in women, due to clearance and catabolism of antibodies via the liver), thereafter followed by kidneys, thyroid, lungs and spleen. The mean absorbed red marrow dose was 0.07±0.02 mSv/MBq and 0.09±0.01 mSv/MBq in men and women, respectively. Measured excretion via the urinary tract was less than 3% during the first 3 days p.i.. The mean effective dose was 0.53±0.03 mSv/MBq in men and 0.66±0.03 mSv/MBq in women.

Similar values for the mean effective dose have been reported in the literature for [89]Zr-cetuximab (0.61 mSv/MBq) (*1*) and [89]Zr-trastuzumab (0.48 mSv/MBq) (*2*).

Based on these studies, a typical [89]Zr-immuno-PET study, performed with an injected dose of 37 MBq, results in an effective dose of 22.2 mSv (plus 3mSv for each low dose CT scan). The radiation exposure due to [89]Zr-immuno-PET is relatively high (compared to 4.8 mSv for ^{18}F-FDG-PET, ~13.3 mSv for a diagnostic CT-scan of the neck, thorax and abdomen (depending on the protocol), 0.04 mSv for a chest X-ray, 0.05 mSv for a transatlantic flight) (*3*). The average lifetime risk of dying from cancer due to radiation exposure of 1 mSv is estimated at 1 in 20.000 for a 40-year old person (*4*). However, this risk should be seen in perspective for patients who already have a form of cancer. In general, the radiation safety principle 'as low as reasonably achievable (ALARA)' should be applied (*5*).

*Tumor uptake can be visualized with [89]Zr-immuno-PET*

**Chapter 3** describes the performance of immuno-PET with [89]Zr-cmAb U36 for the same cohort of twenty patients with HNSCC as in Chapter 2. The target antigen of cmAb U36, CD44v6, is abundantly expressed in HNSCC.

Prior to surgery, all patients were evaluated by computed tomography (CT) and/or magnetic resonance imaging (MRI) and [89]Zr-immuno-PET. Imaging results were compared with histopathological findings per neck side (left or right), as well as per lymph node level (6 levels per side). All primary tumors were visualized on [89]Zr-immuno-PET (n=17). Lymph node metastases were identified in 18 of 25 positive levels (sensitivity 72%) and in 11 of 15 positive sides (sensitivity 73%). For CT/MRI, sensitivity per level and per side was 60% and 73%, respectively. [89]Zr-immuno-PET corresponded with pathology in 112 of 121 operated levels

(accuracy 93%) and in 19 of 25 sides (accuracy 76%). Two false-positive findings (two levels) were obtained with [89]Zr-immuno-PET, without explanation. Seven tumor-involved lymph node levels were missed by [89]Zr-immuno-PET. These tumor-involved lymph nodes were relatively small (<1x 1.5cm), and contained just a small proportion of tumor tissue (~50% tumor infiltration). For CT/MRI, accuracy per level and per sided were 90% (109/121) and 80% (20/25), respectively. Six out of 7 tumor-involved lymph node levels that had been missed by [89]Zr-immuno-PET, were also missed by CT and/or MRI. In conclusion, these results indicate that the diagnostic imaging performance of [89]Zr-immuno-PET was similar to CT/MRI for the detection of HNSCC lymph node metastases.

In daily clinical practice, CT and MRI are already established diagnostic imaging modalities. This study shows that visual detection of tumor uptake of [89]Zr-cmAb U36, a novel imaging technique, is feasible. Next to diagnostic implications, these achievements might open avenues for guiding the development and application of therapeutic antibodies.

*Tumor uptake and blood pool activity can be quantified with [89]Zr-immuno-PET*
In **Chapter 2,** feasibility of quantification with immuno-PET with [89]Zr-cmAb U36 is described. PET-derived quantification of radioactivity concentrations in the left ventricle of the heart showed good agreement with radioactivity concentrations measured in venous blood samples (difference equals 0.2% ± 16.7% [mean ± SD]), except for heavyweight patients (>100kg). For tumors, good agreement was found between PET-derived quantification at 6 days p.i. and measurement of radioactivity concentrations in surgical biopsies obtained at 7 days p.i., with slightly lower values for PET (mean deviation -8.4% ± 34.5%).

*Clinical [89]Zr-immuno-PET studies in oncology provide relevant and sustainable results*
In **Chapter 4**, we provide a review summarizing the results from the first 15 clinical trials with [89]Zr-immuno-PET in oncology published between 2006 and 2016. These trials have contributed towards the development of [89]Zr-immuno-PET as an imaging biomarker by showing correlation between uptake of [89]Zr-labeled mAbs on PET and target expression levels in biopsies.

The ZEPHIR study is an example how [89]Zr-immuno-PET, combined with early response assessment by ^{18}F-FDG-PET, can be used to predict response to antibody-based therapy, in this case with the antibody-drug conjugate,

10

trastuzumab-emtansine (T-DM1). In this study in patients with HER2-positive metastatic breast cancer, tumor detection and staging was performed with conventional imaging (^{18}F-FDG-PET) and in addition, tumor targeting was assessed with [89]Zr-trastuzumab-PET (*6*). After 3 cycles of treatment with trastuzumab-emtansine (T-DM1), early response was assessed with conventional imaging (^{18}F-FDG-PET). This is a promising design for future application of [89]Zr-immuno-PET as a clinical tool to guide antibody-based therapy.

*"All that is gold does not glitter"*

Based on this review of initial clinical trials with [89]Zr-immuno-PET, further development of [89]Zr-immuno-PET is required to allow assessment of target engagement. Two requirements for each [89]Zr-labeled mAb were identified to realize its full potential. One requirement is that the biodistribution of the [89]Zr-labeled mAb (imaging dose) reflects the biodistribution of the drug during treatment (therapeutic dose). Another requirement is that PET should be capable to assess the specific, antigen-mediated, tumor uptake of the [89]Zr-MAb. Currently, there are no standardized criteria to define positive uptake on [89]Zr-immuno-PET. This may be improved by quantitative analysis of tumor uptake on [89]Zr-immuno-PET. Therefore, imaging procedures, including data analysis and quantitative measurements of tumor uptake should be standardized and validated for future application of [89]Zr-immuno-PET.

**Part II Validation of [89]Zr-immuno-PET**

For each new measurement instrument, knowledge of measurement variability is required for correct interpretation of the results. For ^{18}F-FDG-PET, measurement variability for tumor uptake measured with SUV is approximately 10% (*7*). [89]Zr-immuno-PET is challenged by the low injected dose and low positron abundance of [89]Zr, leading to a relative low signal-to-noise ratio. These factors will result in increased measurement variability for [89]Zr-immuno-PET compared to ^{18}F-FDG-PET.

Therefore, we investigated two sources of measurement variability for [89]Zr-immuno-PET: noise-induced variability (**Chapter 5**) and interobserver reproducibility of tumor uptake quantification (**Chapter 6**).

*Measurement variability due to noise is significant in $^{89}$Zr-immuno-PET*

**Chapter 5** evaluates noise-induced variability of $^{89}$Zr-immuno-PET for quantification of uptake in normal tissues and tumors. Per original scan, raw PET data was split in two equal parts and reconstructed into two count-reduced images (each representing 50% of the original injected dose). Noise-induced variability (expressed as the within-subject coefficient of variation (CoV)) for $^{89}$Zr-antiCD20, $^{89}$Zr-antiEGFR and $^{89}$Zr-antiCD44 was ~3% for large organs (brain, liver, lung, kidney, spleen) and ~20% for tumors. For tumor quantification, this is a significant source of measurement variability.

*Interobserver reproducibility of tumor quantification for $^{89}$Zr-immuno-PET is excellent*

Before tumor uptake quantification with $^{89}$Zr-immuno-PET can be evaluated in large clinical trials, multicenter reproducibility has to be assessed. In **Chapter 6**, interobserver reproducibility of tumor uptake quantification for $^{89}$Zr-immuno-PET was determined, using the same software and standard operating procedure in two centers (VUMC and UMCG). Three observers manually delineated tumor volumes of interest (VOI) (n=103) for $^{89}$Zr-antiCD20, $^{89}$Zr-antiEGFR and $^{89}$Zr-antiHER2. Maximum, peak and mean standardized uptake values (SUV$_{max}$, SUV$_{peak}$ and SUV$_{mean}$) were used to quantify tumor uptake.

Interobserver reproducibility (median CoV) was excellent for SUV$_{max}$ and SUV$_{peak}$ (0% and 0%). For SUV$_{mean}$, measurement error due to interobserver variability in tumor uptake quantification was 7%. Even for SUV$_{max}$, there were cases where the three observers did not obtain exact the same value (26/103). This was due to insufficient contrast for manual delineation, resulting in delineation of a different structure (4/103) or location of the voxel with the maximum intensity at the border of the VOI (16/103). These tumor lesions cannot reliably be quantified and should therefore be excluded. Standardization by application of eligibility criteria for VOI quantification (e.g. VOI are deemed ineligible when the voxel with the maximum uptake was located at the edge of the VOI) is recommended to optimize interobserver reproducibility.

For clinical application, it is not only necessary to determine measurement variability, but also to assess reliability. Reliability is defined as 'the degree to which measurement is free from measurement error' (8). Reliability in our datasets was good (ICC > 0.8; **Chapter 5 and 6**). It is important to realize that reliability depends on the range in measurements (for example tumor uptake) and this is not directly generalizable between different datasets.

10

*Tumor uptake of [89]Zr-rituximab-PET was correlated to CD20 expression in biopsies*

As mentioned in the introduction, treatment of patients with B cell non-Hodgkin lymphoma includes rituximab, an anti-CD20 mAb. Insufficient tumor targeting might cause therapy failure in relapsed/refractory disease. In **Chapter 7**, we investigated the performance of [89]Zr-rituximab-PET for assessment of CD20 targeting. CD20 expression in tumor biopsies was assessed by immunohistochemistry (IHC) in six patients with relapsed/refractory diffuse large B-cell lymphoma (DLBCL). [89]Zr-rituximab-PET scans were acquired and tumor uptake was assessed for the corresponding tumor lesions.

Tumor uptake on [89]Zr-immuno-PET was concordant with IHC in 5 patients: in one patient no tumor uptake was observed on immuno-PET with absence of CD20 expression in the tumor biopsy, in the other four patients tumor uptake was concordant with CD20-positive biopsies. Intense tumor uptake of [89]Zr-rituximab on PET ($SUV_{peak}$=12.8) corresponded with uniformly positive CD20 expression on IHC in one patient. Moderate tumor uptake of [89]Zr-rituximab (range $SUV_{peak}$ = 3.2-5.4) corresponded with positive CD20 expression on IHC in three patients. In one patient tumor uptake of [89]Zr-rituximab was observed ($SUV_{peak}$ = 3.8), while the biopsy was CD20-negative, indicating either a false-positive immuno-PET finding or heterogeneous target expression/sampling error of the biopsy. Therefore, to understand the cause of this discordant finding further analysis of the imaging signal is required, as the total PET signal consists the sum of non-specific and target-mediated, specific uptake.

Overall, these results indicate the potential of [89]Zr-rituximab-PET as an imaging biomarker for CD20 expression. Subsequently, the value of PET imaging with [89]Zr-rituximab to predict response to therapy has to be determined.

*[89]Zr-immuno-PET can be used to assess antigen-mediated uptake in normal tissues*

Especially in early stages of drug development, it is of interest to identify which therapeutic mAb has high potential to provide selective treatment by targeting the tumor, without affecting normal tissues. A non-invasive technique to investigate and predict antigen-mediated uptake in normal tissues is expected to improve drug development strategies. Antigen-mediated, specific uptake is expected to be dose-dependent. If the target antigen is present on normal tissues, dose-dependent uptake is expected (this is also referred to as the antigen sink).

In **Chapter 8**, we investigated application of [89]Zr-immuno-PET as a clinical tool to assess antigen-mediated uptake in normal tissues in a phase I dose escalation study, using the anti-CD44 antibody RG7356 as an example. Thirteen patients with CD44-expressing solid tumors received [89]Zr-labeled RG7356 after a variable dose of unlabeled antibody (0 to 675 mg). Tracer uptake in normal tissues (liver, spleen, kidney, lung, bone marrow and brain, blood pool) was used to calculate the area under the time antibody concentration curve (AUC).

Within the dose range of 1 to 450 mg tissue-to-blood AUC ratios decreased for the spleen, liver, bone marrow, lung and kidney, indicating dose-dependent uptake. This observation indicates target antigen expression in normal tissues, limiting the use of RG7356 for targeting toxic payloads to the tumor (e.g. antibody–drug conjugate approaches). This study demonstrates how immuno-PET in a dose escalation study provides a non-invasive technique to quantify dose-dependent uptake in normal tissues, indicating specific, target-mediated uptake. No focal tumor uptake was observed in the lowest dose cohorts (1-200 mg), suggesting insufficient supply of mAb for tumor targeting. In all patients receiving ≥ 450 mg (n=7) tumor uptake of the antibody was observed, suggesting antigen-mediated uptake. However, a different study design using two administrations of the tracer per patient (with a variable dose of unlabeled antibody), would be better suited to determine dose-dependency for tumors. Recently, an example of such a study design was reported to assess antigen-mediated specific tumor uptake for a [89]Zr-labeled antiHER3 mAb (*9*).

*[89]Zr-immuno-PET can be used to assess non-specific uptake in normal tissues*
Currently, it is common practice to report the result of [89]Zr-immuno-PET studies as SUV. However, this value represents the total PET signal and may contain a significant non-antigen mediated contribution. Quantification of non-specific uptake in normal tissues is the first critical step towards quantification of target-engagement in normal tissues and tumor with [89]Zr-immuno-PET. This non-specific contribution in normal tissues is expected to be similar for a non-binding mAb and for mAbs without target expression in the respective tissue. Non-specific uptake is reversible (e.g. blood volume) or irreversible (due to [89]Zr-residualization after mAb degradation).

In **Chapter 9**, non-specific uptake in normal tissues without known target expression was assessed for four [89]Zr-labeled intact IgG1 antibodies ([89]Zr-antiCD20, [89]Zr-antiEGFR, [89]Zr-antiPSMA and [89]Zr-antiHER2). Patlak graphical

**10**

evaluation of transfer constants was used to estimate the reversible ($V_t$) and irreversible ($K_i$) contributions to the total measured uptake for the kidney, liver, lung and spleen. At least 3 scans at equilibrium state ($\geq 1$ day p.i.) are required to assess the quality of the fit. Baseline values were calculated per tissue combining all mAbs without target expression. The transfer constants obtained were interpreted in terms of the physiological components of antibody biodistribution. A literature search was performed to obtain predicted values for these physiological components for a non-binding intact IgG1 mAb.

We found that non-specific, reversible uptake was similar to the predicted value for a non-binding mAb (*10*). Non-specific, irreversible uptake corresponded with the predicted value for the fractional catabolic rate of IgG. In case of target engagement, we expect to observe an increased $K_i$ compared to the baseline value. Expression of PSMA was reported for the kidney and therefore target engagement of [89]Zr-antiPSMA is expected in this tissue. For [89]Zr-antiPSMA, a four-fold higher $K_i$ was observed for the kidney, indicating target engagement.

Usually, [89]Zr-immuno-PET scans are analyzed at a single time point, representing the sum of all physiological components of antibody distribution, being either target specific or non-specific. This study showed how the various physiological components of antibody distribution contribute to the measured SUV. For example, in the kidney a SUV of ~2.5 was measured for [89]Zr-antiPSMA at 1 to 7 days p.i.. Non-specific uptake accounted for a SUV of ~1.6 (66%) at 1 day p.i. and decreased to ~0.6 (22%) at 7 days p.i.. This observation indicates how the contribution of non-specific uptake decreases over time.

*"It is sometimes a good idea to develop a new measurement instrument"*
This study shows that non-specific uptake of mAbs for tissues without target expression can be quantified using [89]Zr-immuno-PET at multiple time points. These results form a crucial base for measurement of target-engagement by therapeutic antibodies *in-vivo* with [89]Zr-immuno-PET. For future studies, a pilot phase including at least 3  scans $\geq 1$ day p.i., is required recommended to assess non-specific uptake as a function of time, to optimize study design for detection of target engagement.

# FUTURE PERSPECTIVES

In this thesis, we found that [89]Zr-immuno-PET is safe and feasible. An important advantage of [89]Zr-immuno-PET is that whole-body information can be obtained non-invasively and quantitatively. Recently, progress has been made to facilitate improved chemical procedures (*11*) and by providing recommendations to obtain quantitative accuracy and harmonized image quality for [89]Zr-immuno-PET in a multicenter setting (*12, 13*). [89]Zr-immuno-PET studies have been collected in an online accessible warehouse of molecular imaging data with the aim to increase and exchange knowledge on whole body drug distribution (*14*). The first [89]Zr-immuno-PET studies with immune checkpoint inhibitors, antibody drug conjugates and bispecific antibodies show promising results (*15-17*).

Disadvantages of [89]Zr-immuno-PET are the radiation exposure, scan time required and the complexity of logistics. The studies on measurement variability of [89]Zr-immuno-PET for tumor quantification described in this thesis indicate that noise is a significant contribution. We studied validity of [89]Zr-immuno-PET and observed correlations between tumor uptake on [89]Zr-immuno-PET and underlying biology. However, potential false-positive findings indicate the need for quantification. Therefore, we developed methods using dose-dependency and multiple time point scans to assess target-mediated uptake for normal tissues as a crucial step.

Future studies should focus on the following aspects:

1. Improvement of precision by reduction of noise

   New technical developments to optimize sensitivity are expected to result in shorter scan time, higher resolution and increased precision. In 2018, the first total-body PET/CT scanner was introduced (*18,19*). Opposed to current PET/CT scanners that use a ring that allows only 10-15% of the body within the field of view at one time, the total-body PET/CT scanner uses detector rings that cover the entire body. This system allows almost maximal detection of radiation emitted, resulting in increased signal-to-noise ratio in the images (*18*). This can become a game changer in the application of [89]Zr-immuno-PET. Shorter scan time/reduction of administered radioactivity will allow to perform test-retest studies to assess repeatability of [89]Zr-immuno-PET. Repeatability studies are usually performed for technical validation. However, until

now this type of study design has been limited by the relative high radiation exposure of [89]Zr-immuno-PET.

In addition, reduction of radiation exposure will allow application of [89]Zr-immuno-PET for indications beyond oncology, for example in auto-immune diseases where mAb-based therapy is also used (*20*). Finally, increase in sensitivity is expected to allow molecular imaging of other slow-kinetic drugs (e.g. nanoparticles) and cell imaging.

2. Further biological and clinical validation (including cost effectiveness)
Before [89]Zr-immuno-PET can be applied in large scale clinical trials or in daily clinical practice, the link with underlying biology and clinical outcome should be confirmed. We observed a potential false-positive finding for [89]Zr-rituximab in relapsed/refractory non-Hodgkin lymphoma (Chapter 7) and two false-positive findings for [89]Zr-cmAb U36 in head and neck cancer (Chapter 3). Visual assessment of [89]Zr-immuno-PET is used to localize non-physiological accumulation of the radiotracer, indicating target-mediated uptake. Visual assessment provides a qualitative biomarker, assuming that target-mediated, specific uptake increases over time, and dominates the total PET signal at late time points (e.g. 3-6 days p.i.) when tumor uptake is visible.

 Future studies are required to develop a method for quantification of target-engagement in tumors. However, tumor characteristics are more complex and more variable (within and between patients) compared to normal tissues. Therefore, tumors with and without target expression can be studied to investigate non-specific uptake in tumors.

Although tumor biopsies are often used as reference, immunohistochemistry may not be a true gold standard for target engagement of mAbs. Biopsies have several limitations, for example sampling error due to heterogeneity in target expression. In addition, detection of target expression by IHC does not provide information on accessibility of the target in-vivo (whether the therapeutic mAb has reached the target). Future work to relate quantification of [89]Zr-labeled mAbs to PBPK modeling is expected to provide more insight in how the PET signal is linked to the underlying biology. This information is required to define which measure (visual, SUV, Ki) is suitable for assessment of target engagement. The type of measure (e.g. single time point, or multiple time point) has impact on study design for further clinical validation studies and cost-effectiveness.

Provided that all requirements are met, we envision that $^{89}$Zr-immuno-PET can be used in the near future for the following clinical applications:

- "whole-body in-vivo immunohistochemistry" for individualized treatment
- measurement of target engagement in tumor and normal tissues to guide drug development

The latest developments in mAb-based treatment of cancer include many new drugs that have now reached the clinic: antibody-drug conjugates, bispecific antibodies, immune checkpoint inhibitors and chimeric antigen receptor (CAR)-T cells (*21*). Different mechanisms have been explored to increase the efficacy of traditional mAbs (e.g. use of a toxic payload (ADC) or by triggering the immune system (e.g. activating T-cells to kill the malignant cells). These treatment approaches have in common that their effects are all target-antigen mediated. Therefore, we need to shine a light on whether these drugs reach the disease. This is essential information to better understand their efficacy and toxicity and to learn how to dose appropriately. The timing is crucial to accompany these expensive novel targeted therapies with $^{89}$Zr-immuno-PET as biomarker for target engagement, especially as society struggles to find a way towards affordable and accessible healthcare.

## CONCLUSION

This thesis describes the development of $^{89}$Zr-immuno-PET as a clinical tool to guide antibody-based treatment in cancer. Initial clinical studies of $^{89}$Zr-immuno-PET in oncology show feasibility, including safety. Technical validation indicates that multi-center interobserver reproducibility of tumor uptake quantification was excellent, although measurement variability due to noise was substantial. Biological validation studies show that $^{89}$Zr-immuno-PET is able to measure the underlying biology (correlation with target expression, dose-dependency and assessment of non-specific uptake). Future work should be aimed at reduction of measurement variability using improved PET-CT scanners, quantification of specific uptake in tumor and clinical validation (e.g. prediction of response to antibody-based treatment). If these requirements are met, $^{89}$Zr-immuno-PET can be used as a clinical tool to guide patient and drug selection for antibody-based treatment in cancer.

10

# REFERENCES

1.  Makris NE, Boellaard R, van Lingen A, et al. PET/CT-derived whole-body and bone marrow dosimetry of 89Zr-cetuximab. *J Nucl Med*. 2015;56:249-254.

2.  O'Donoghue JA, Lewis JS, Pandit-Taskar N, et al. Pharmacokinetics, Biodistribution, and Radiation Dosimetry for 89Zr-Trastuzumab in Patients with Esophagogastric Cancer. *J Nucl Med*. 2018;59:161-166.

3.  Diagnostiek | RIVM [Internet]. [cited 2019 Feb 22]. Available from: https://www.rivm.nl/medische-stralingstoepassingen/trends-en-stand-van-zaken/diagnostiek

4.  Fahey FH, Treves ST, Adelstein SJ. Minimizing and communicating radiation risk in pediatric nuclear medicine. *J Nucl Med Technol*. 2012;40:13-24.

5.  ICRP Publication 62. SAGE Publications Ltd [Internet]. [cited 2019 Feb 22]. Available from: https://uk.sagepub.com/en-gb/eur/icrp-publication-62/book243732.

6.  Gebhart G, Lamberts LE, Wimana Z, et al. Molecular imaging as a tool to investigate heterogeneity of advanced HER2-positive breast cancer and to predict patient outcome under trastuzumab emtansine (T-DM1): the ZEPHIR trial. *Ann Oncol*. 2016;27:619-624.

7.  Lodge MA. Repeatability of SUV in Oncologic 18F-FDG PET. *J Nucl Med*. 2017;58:523-532.

8.  Vet HCW de, Terwee CB, Mokkink LB, Knol DL. Measurement in Medicine: A Practical Guide. Cambridge University Press; 2011.

9.  Menke-van der Houven van Oordt CW, McGeoch A, Bergstrom M, et al. ImmunoPET imaging to assess target engagement: Experience from 89Zr-anti-HER3 mAb (GSK2849330) in patients with solid tumors. *J Nucl Med*. February 2019.

10. Glassman PM, Abuqayyas L, Balthasar JP. Assessments of antibody biodistribution. *J Clin Pharmacol*. 2015;55 Suppl 3:S29-38.

11. Vugts DJ, Klaver C, Sewing C, et al. Comparison of the octadentate bifunctional chelator DFO*-pPhe-NCS and the clinically used hexadentate bifunctional chelator DFO-pPhe-NCS for 89Zr-immuno-PET. *Eur J Nucl Med Mol Imaging*. 2017;44:286-295.

12. Makris NE, Boellaard R, Visser EP, et al. Multicenter harmonization of 89Zr PET/CT performance. *J Nucl Med*. 2014;55:264-267.

13. Kaalep A, Huisman M, Sera T, et al. Feasibility of PET/CT system performance harmonisation for quantitative multicentre 89Zr studies. *EJNMMI Phys*. 2018;5:26.

14. Bensch F, Smeenk MM, van Es SC, et al. Comparative biodistribution analysis across four different 89Zr-monoclonal antibody tracers-The first step towards an imaging warehouse. *Theranostics*. 2018;8:4295-4304.

15. Niemeijer AN, Leung D, Huisman MC, et al. Whole body PD-1 and PD-L1 positron emission tomography in patients with non-small-cell lung cancer. *Nat Commun*. 2018;9:4664.

16. Bensch F, van der Veen EL, Lub-de Hooge MN, et al. 89Zr-atezolizumab imaging as a non-invasive approach to assess clinical response to PD-L1 blockade in cancer. *Nat Med*. 2018;24:1852-1858.

17. Waaijer SJH, Warnders FJ, Stienen S, et al. Molecular Imaging of Radiolabeled Bispecific T-Cell Engager 89Zr-AMG211 Targeting CEA-Positive Tumors. *Clin Cancer Res*. 2018;24:4988-4996.

18. Cherry SR, Jones T, Karp JS, Qi J, Moses WW, Badawi RD. Total-Body PET: Maximizing Sensitivity to Create New Opportunities for Clinical Research and Patient Care. *J Nucl Med*. 2018;59:3-12.

19. Badawi RD, Shi H, Hu P, et al. FIRST HUMAN IMAGING STUDIES WITH THE EXPLORER TOTAL-BODY PET SCANNER. *J Nucl Med*. 2019: Epub ahead of print.

20. Veldhuijzen van Zanten SEM, De Witt Hamer PC, van Dongen GAMS. Brain access of monoclonal antibodies as imaged and quantified by 89Zr-antibody-PET: perspectives for treatment of brain diseases. *J Nucl Med*. February 2019.

21. Corraliza-Gorjón I, Somovilla-Crespo B, Santamaria S, Garcia-Sanz JA, Kremer L. New Strategies Using Antibody Combinations to Increase Cancer Treatment Effectiveness. *Front Immunol*. 2017;8:1804.

ADDENDUM

# NEDERLANDSE SAMENVATTING

**[89]Zr-immuno-PET: naar een klinische methode om antilichaam-therapie voor kanker te sturen**

**Hoofdstuk 1** geeft een algemene introductie over de ontwikkeling van antilichaam-therapie voor kanker. Monoclonale antilichamen zijn antistoffen gericht tegen specifieke eiwitten (antigenen) die tot expressie komen op het celoppervlak. Deze vorm van doelgerichte behandeling maakt het mogelijk om kwaadaardige cellen te doden, terwijl normale gezonde cellen gespaard blijven. Voor een effectieve behandeling is het noodzakelijk dat het antigeen voorkomt op de tumorcellen en dat het antilichaam de tumorcel bereikt. Om toxiciteit te minimaliseren wordt een antigeen gekozen dat niet of nauwelijk op normale weefsels voorkomt.

Antilichaam-therapie heeft de perspectieven op goede resultaten van behandeling verbeterd, maar niet alle patienten hebben baat bij deze behandeling en de kosten van deze dure geneesmiddelen zijn aanzienlijk.

Om de behandelmogelijkheden voor patienten met kanker te optimaliseren, is een methode nodig om te voorspellen welke patienten baat zullen hebben bij een bepaalde antilichaam-therapie. Hiermee kan het effectief gebruik verbeterd worden en toxiciteit en kosten voorkomen worden. Daarnaast kunnen subgroepen van patienten gedetecteerd worden die voordeel hebben van een bepaalde antilichaam-therapie, waardoor de noodzaak voor grote klinische studies achterwege kan blijven. Een doelgerichte studie-opzet die gebruik maakt van een dergelijke methode kan helpen om nieuwe geneesmiddelen sneller te ontwikkelen voor gebruik in de dagelijkse klinische praktijk.

Voor deze doeleinden wordt in dit proefschrift de ontwikkeling van een nieuwe methode beschreven: positron-emissie tomografie (PET) met 89-Zirconium (89Zr)-gelabelde antilichamen, oftewel [89]Zr-immuno-PET. Dit is een beeldvormende techniek waarbij gebruik gemaakt wordt van langlevend radioactief isotoop (t½ van [89]Zr is 78.4 uur). Voordelen van deze methode zijn dat deze informatie geeft over het gehele lichaam en niet-invasief is. Essentiele aspecten bij de ontwikkeling van dit nieuwe meetinstrument zijn de uitvoerbaarheid, technische en biologische validatie. In deel I van dit proefschrift wordt de uitvoerbaarheid van [89]Zr-immuno-PET onderzocht. In deel II wordt de validatie van [89]Zr-immuno-PET beschreven.

**Deel I Uitvoerbaarheid van [89]Zr-immuno-PET**

*Toediening van [89]Zr-gelabelde antilichamen is veilig*

In **Hoofdstuk 2** wordt de eerste klinische [89]Zr-immuno-PET studie beschreven. Dit onderzoek werd uitgevoerd bij twintig patienten met hoofd-halsplaveiselcelcarcinoom (HHPCC) met een hoog risico op lymfekliermetastasen, waarvoor een operatieve behandeling (halsklierdissectie met of zonder resectie van de primaire tumor) gepland was. Alle patienten kregen 75 MBq [89]Zr-gelabeld chimeer monoclonaal antilichaam (cmAb) U36 (10mg) en immuno-PET scans werden verricht tot 6 dagen na toediening.

       **Hoofdstuk 2** beschrijft de veiligheid van de toediening van [89]Zr-cmAbU36. De procedure werd goed verdragen door alle patienten; er werden geen ernstige bijwerkingen ten gevolge van de toediening gerapporteerd. Twee patienten ontwikkelden een humaan-anti-chimeer antigeen (HACA) respons, gerelateerd aan het antilichaam gedeelte (niet tegen de [89]Zr-verbinding).

       De toediening van [89]Zr-gelabelde antilichamen werd ook goed verdragen in de andere klinische studies beschreven in dit proefschrift. Er werden geen bijwerkingen van het radioactief gelabelde antilichaam gerapporteerd voor [89]Zr-rituximab bij patienten met een diffuus grootcellig B cel lymfoom (**Hoofdstuk 7**) en [89]Zr-antiCD44 bij patienten met CD44-positieve solide tumoren (**Hoofdstuk 8**). Daarnaast waren er bij de eerste 15 klinische studies met [89]Zr-immuno-PET in de oncologie (gepubliceerd tussen 2006 en 2016) geen problemen met de veiligheid (**Hoofdstuk 4**).

*De stralingsbelasting van [89]Zr-immuno-PET is ~0.6 mSv/MBq*

In **Hoofdstuk 2** wordt de biodistributie en stralingsbelasting van [89]Zr-cmAb U36 onderzocht in het cohort van twintig patienten met HHPCC. Het normale weefsel met de hoogst geabsorbeerde stralingsdosis was de lever (gemiddelde dosis: 1.25±0.27 mSv/MBq bij mannen en 1.35±0.21 mSv/MBq bij vrouwen, ten gevolge van klaring en katabolisme van antilichamen via de lever), daarna gevolgd door de nieren, schildklier, longen en milt. De gemiddelde geabsorbeerde dosis voor het beenmerg was 0.07±0.02 mSv/MBq voor mannen en 0.09±0.01 mSv/MBq voor vrouwen. De gemeten excretie via de urinewegen was minder dan 3% gedurende de eerste 3 dagen na toediening. De gemiddelde effectieve dosis was 0.53±0.03 mSv/MBq voor mannen en 0.66±0.03 mSv/MBq voor vrouwen.

Op basis van deze resultaten, is de berekende effectieve dosis 22.2 mSv (plus 3 mSv voor elke bijbehorende lage dosis CT scan) voor een [89]Zr-immuno-PET onderzoek met een geinjecteerde dosis van 37 MBq.

De stralingsbelasting ten gevolge van [89]Zr-immuno-PET is relatief hoog (ten opzichte van andere onderzoeken, zoals 4.8 mSv voor ^{18}F-FDG-PET, ~13.3 mSv voor een diagnostische CT-scan van de hals, borstkas en buik (afhankelijk van het protocol), 0.04 mSv voor een X-thorax). Echter, het risico op een secundaire maligniteit ten gevolge van de stralingsbelasting dient in perspectief gezien te worden voor een patient die reeds een vorm van kanker heeft. Over het algemeen dient het stralingsveiligheidsprincipe 'zo laag als redelijkerwijs haalbaar' toegepast te worden.

*Tumoropname kan gevisualiseerd worden met [89]Zr-immuno-PET*
**Hoofdstuk 3** beschrijft de detectie van lymfekliermetastasen met immuno-PET met [89]Zr-gelabeld cmAb U36 voor bij dezelfde groep patienten met HHPCC zoals beschreven in Hoofdstuk 2. Het target antigeen van cmAb U36, CD44v6, komt uitgebreid tot expressie bij HHPCC.

Voorafgaand aan de operatie werden alle patienten geevalueerd met [89]Zr-immuno-PET, naast het standaard onderzoek met CT en/of MRI. Alle primaire tumoren werden gevisualiseerd met [89]Zr-immuno-PET (n=17). Lymfkliermetastasen werden geidentificeerd in 18 van de 25 positieve niveaus (sensitiviteit 72%). [89]Zr-immuno-PET kwam in 112 van de 121 geopereerde niveaus overeen met de histopathologische bevindingen (accuratesse 93%). [89]Zr-immuno-PET leverde twee fout-positieve bevindingen op zonder verklaring. Zeven tumor-geinfiltreerde lymfeklierniveaus werden gemist met [89]Zr-immuno-PET. Deze klieren waren relatief klein (<1x1.5cm) en bevatten slechts gedeeltelijk tumor weefsel (~50% tumor infiltratie). Voor CT/MRI was de sensitiviteit per niveau 60% en de accuratesse 90% (109/121). Zes van de zeven lymfeklieren die gemist waren met [89]Zr immuno-PET, werden ook gemist met CT/MRI. Concluderend was [89]Zr-immuno-PET minstens even goed als de routine diagnostische onderzoeken, te weten CT/MRI, voor de detectie van lymfkliermetasten bij HHPCC. Deze studie liet zien dat visualisatie van tumoropname van [89]Zr-cmAbU36, een nieuwe beeldvormende techniek, haalbaar is. Naast diagnostische implicaties, bieden deze resultaten de gelegenheid om ontwikkeling en toepassing van therapeutische antilichamen te sturen.

*Opname in tumor en bloed kunnen gekwantificeerd worden met $^{89}$Zr-immuno-PET*

In **Hoofdstuk 2** is de haalbaarheid van kwantificatie met immuno-PET met $^{89}$Zr-cmAb U36 beschreven. Kwantificatie van de concentratie radioactiviteit in de linker ventrikel van het hart, gemeten met $^{89}$Zr-immuno-PET, kwam goed overeen met radioactiviteits concentraties gemeten in veneuze bloed samples (verschil gelijk aan 0.2% ± 16.7% [gemiddelde ± SD]), behalve voor uitzonderlijk zware patienten (>100kg). Voor tumoren werd een goede overeenkomst gevonden tussen kwantificatie met $^{89}$Zr-immuno-PET op 6 dagen na toediening van het radioactief gelabelde antilichaam en gemeten radioactiviteits concentraties in chirurgische biopten verkregen 7 dagen na toediening.

*Klinische studies met $^{89}$Zr-immuno-PET in de oncologie geven relevante en duurzame resultaten*

In **Hoofdstuk 4** wordt een overzicht gegeven van de resultaten van de eerste 15 klinische studies met $^{89}$Zr-immuno-PET in de oncologie, gepubliceerd tussen 2006 en 2016. Deze studies hebben bijgedragen aan de ontwikkeling van $^{89}$Zr-immuno-PET door een correlatie tussen opname van $^{89}$Zr-gelabelde antilichamen en target antigeen expressie in biopten te laten zien.

De ZEPHIR studie is een international studie die beschrijft hoe $^{89}$Zr-immuno-PET, gecombineerd met vroege respons monitoring met $^{18}$F-FDG-PET, gebruikt kan worden om de respons te voorspellen op antilichaam-therapie, in dit geval met het antilichaam-drug-conjugaat trastuzumab-emtansine (T-DM1). In deze studie bij patienten met HER2-positief gemetastaseerd mammacarcinoom, werd tumor detectie en stagering verricht met conventionele beeldvorming ($^{18}$F-FDG-PET). Daarnaast werd tumor targeting onderzocht met $^{89}$Zr-trastuzumab-PET. Na 3 cycli behandeling met T-DM1, werd een vroege respons beoordeling uitgevoerd met conventionele imaging ($^{18}$F-FDG-PET). Dit is een veelbelovende studie opzet voor een toekomstige toepassing van $^{89}$Zr-immuno-PET om antilichaam-therapie te sturen.

*"Het is niet alles goud wat er blinkt"*

Uit dit overzicht van de eerste klinische studies met $^{89}$Zr-immuno-PET is gebleken dat verdere ontwikkeling nodig is om antigeen-gemedieerde opname te meten. Om $^{89}$Zr-immuno-PET daadwerkelijk in de klinische praktijk in te zetten, moet aan twee voorwaarden voldaan worden. De eerste voorwaarde is dat de

biodistributie van het [89]Zr-gelabelde antilichaam (de speurdosis) de biodistributie van het geneesmiddel tijdens behandeling (de therapeutische dosis) reflecteert. De tweede voorwaarde is dat PET in staat moet zijn om specifieke, antigeen-gemedieerde, tumor opname van het [89]Zr-gelabelde antilichaam te meten. Momenteel zijn er geen gestandaardiseerde criteria om tumor opname op [89]Zr-immuno-PET te definieren. Daarom is het van belang dat de volledige procedure, inclusief data analyse en kwantificatie van tumor opname gestandaardiseerd en gevalideerd wordt voor toekomstige toepassing van [89]Zr-immuno-PET.

## Deel II Validatie van [89]Zr-immuno-PET

Voor elk nieuw meetinstrument is kennis van de meetfout noodzakelijk om de resultaten correct te kunnen interpreteren. Voor ^{18}F-FDG-PET is de variatie in de tumoropname (uitgedrukt als 'standardized uptake value' (SUV)) ten gevolge van de meetfout ongeveer 10%. [89]Zr-immuno-PET heeft twee extra uitdagingen: de lage geinjecteerde dosis en lage positron abundantie van [89]Zr. Deze factoren leiden tot een ongunstige signaal-ruis-verhouding (ruis) en daardoor een grotere meetfout voor [89]Zr-immuno-PET ten opzichte van ^{18}F-FDG-PET.

Om deze reden werd de meetfout voor [89]Zr-immuno-PET onderzocht in Hoodstuk 5 en 6.

### *De meetfout ten gevolge van ruis is significant voor [89]Zr-immuno-PET*

In **Hoofdstuk 5** wordt de variatie in kwantificatie van opname in normale weefsels en tumoren ten gevolge van ruis bij [89]Zr-immuno-PET onderzocht. De meetfout ten gevolge van ruis (weergegeven als intra-subject coefficient of variation (CoV)) voor [89]Zr-antiCD20, [89]Zr-antiEGFR en [89]Zr-antiCD44 was ~3% voor grote organen (brein, lever, long, nier, milt) en ~20% voor tumoren. Deze resultaten laten zien dat ruis een significante bron van meetfout is voor tumor kwantificatie met [89]Zr-immuno-PET.

### *De interobserver reproduceerbaarheid van tumorkwantificatie met [89]Zr-immuno-PET is uitstekend.*

Voordat tumorkwantificatie met [89]Zr-immuno-PET geevalueerd kan worden in grote klinische trials, dient eerst multicenter reproduceerbaarheid vastgesteld te worden. In **Hoofdstuk 6** is de interobserver reproduceerbaarheid van tumorkwantificatie van [89]Zr-immuno-PET onderzocht, waarbij dezelfde software en een gestandaardiseerde procedure gebruikt werd in twee centra (VUMC en

UMCG). Drie observers hebben handmatig tumoren ingetekend voor $^{89}$Zr-antiCD20, $^{89}$Zr-antiEGFR en $^{89}$Zr-antiHER2 (n=103(. De maximum, peak and mean standardized uptake values (SUV$_{max}$, SUV$_{peak}$ en SUV$_{mean}$) werden gebruikt om tumor opname te kwantificeren.

De interobserver reproduceerbaarheid (mediane CoV) was uitstekend voor SUV$_{max}$ en SUV$_{peak}$ (0% en 0%). Interobserver variatie was 7% voor SUV$_{mean}$.

Voor klinische toepassing is het van belang om ook de betrouwbaarheid (weergegeven als intraclass correlation coefficient (ICC)) van de meting vast te stellen. Dat wil zeggen in hoeverre dit meetinstrument ondanks de meetfout in staat is om klinisch relevante verschillen te onderscheiden. De betrouwbaarheid van de metingen in Hoofdstuk 5 en 6 was goed (ICC>0.8).

*Tumor opname van $^{89}$Zr-rituximab-PET is gecorreleerd met CD20 expressie in biopten*

De behandeling van patienten met B-cel non-Hodgkin lymfoom (NHL) omvat onder andere rituximab, een antiCD20 antilichaam. Onvoldoende tumor targeting kan mogelijk resulteren in therapiefalen. In **Hoofdstuk 7** is onderzocht of $^{89}$Zr-rituximab-PET gebruikt kan worden om CD20 targeting vast te stellen. Bij zes patienten met een recidief of refractair NHL werd CD20 expressie in tumor biopten vastgesteld met immunohistochemie (IHC). Vervolgens werden $^{89}$Zr-rituximab PET scans gemaakt en is opname in dezelfde tumor lesies met PET gemeten.

Tumor opname op $^{89}$Zr-rituximab-PET was concordant met IHC bij 5 patienten: in 1 patient werd geen tumoropname gezien op immuno-PET in afwezigheid van CD20 expressie in het tumor biopt, in de andere vier patienten werd tumor opname gezien concordant met CD20-positieve biopten. Intense tumor opname van $^{89}$Zr-rituximab op PET (SUV$_{peak}$ = 12.8) was gerelateerd aan uniform positieve CD20 expressie in 1 patient. Matige tumor opname van $^{89}$Zr-rituximab (range SUV$_{peak}$ = 3.2-5.4) was gerelateerd aan positieve CD20 expressie op IHC bij 3 patienten. In 1 patient werd tumoropname van $^{89}$Zr-rituximab gezien (SUV$_{peak}$ = 3.8), terwijl er geen CD20 expressie in het biopt was. Deze bevinding suggereert een fout-positieve immuno-PET of heterogene expressie van CD20 / sampling error van het biopt. Om deze discordante bevinding te begrijpen, is verdere analyse van het PET signaal noodzakelijk.

Samenvattend laat deze studie zien dat $^{89}$Zr-rituximab-PET potentieel gebruikt kan worden om CD20 targeting vast te stellen. Verder onderzoek is nodig

om te bepalen of [89]Zr-rituximab-PET de respons op behandeling met rituximab kan voorspellen.

## [89]Zr-immuno-PET kan gebruikt worden om antigeen-gemedieerde opname in normale weefsels vast te stellen

Met name in vroege fase van geneesmiddelenontwikkeling, is het van belang om vast te stellen welke therapeutische antilichamen geschikt zijn voor behandeling, waarbij celdood van tumorcellen geinduceerd wordt, echter zonder schade aan de normale weefsels. Onderzoek naar nieuwe geneesmiddelen kan mogelijk verbeterd worden door inzet van een niet-invasieve techniek om antigeen-gemedieerde opname in normale weefsels te onderzoeken. Antigeen-gemedieerde, specifieke opname, wordt geacht dosis-afhankelijk te zijn. Als het target antigeen ook aanwezig is op normale weefsels, wordt ook daar dosis-afhankelijke opname verwacht (dit wordt ook wel de "antigeen-sink" genoemd).

In **Hoofdstuk 8** is beschreven hoe [89]Zr-immuno-PET gebruikt kan worden om antigeen-gemedieerde opname in normale weefsels te meten in een fase I dosis escalatie studie, met het anti-CD44 antilichaam RG7356 als voorbeeld. Dertien patienten met een CD44-positieve solide tumor kregen [89]Zr-gelabeld RG7356 toegediend na een variabele dosis van ongelabeld antilichaam (0 tot 675mg). Er werd dosis-afhankelijk opname gevonden in normale weefsels, passend bij target antigeen expressie, waardoor dit antilichaam niet geschikt is voor de ontwikkeling van een antilichaam-drug conjugaat.

In deze studie werd geen tumor opname geobserveerd in de laagste dosis cohorten (1-200 mg). Dit suggereert onvoldoende aanbod van antilichaam voor tumor opname. Bij patienten die ≥ 450 mg kregen (n=7), werd wel tumor opname gezien. Dit suggereert antigeen-gemedieerde opname. Echter, een andere studie opzet, waarbij gebruik gemaakt wordt van twee toedieningen van [89]Zr-mAb per patient (met een variabele dosis van ongelabeld antilichaam) lijkt beter geschikt om dosis afhankelijkheid voor tumoren vast te stellen.

## [89]Zr-immuno-PET kan gebruikt worden om niet-specifieke opname in normale weefsels te meten

Het is gebruikelijk om als resultaat van een [89]Zr-immuno-PET studie het totale signaal, zoals bijvoorbeeld een SUV, te rapporteren. Echter, het totale PET signaal kan een significant aandeel niet-specifieke opname bevatten (dat wil zeggen, niet-antigeen gemedieerde opname, bijvoorbeeld de bloedvolume fractie van het

weefsel). Het is daarom een cruciale stap om eerst niet-specifieke opname te kwantificeren, met als doel om uiteindelijk kwantificatie van antigeen-gemedieerde opname in normale weefsels en tumoren met $^{89}$Zr-immuno-PET mogelijk te maken.

Daarbij bestaat niet-specifieke opname bestaat uit een reversibele component (bijvoorbeeld bloedvolume) en een irreversibele component (na afbraak van het antilichaam blijft $^{89}$Zr achter in de cel).

In **Hoofdstuk 9** wordt niet-specifieke opname in normale weefsels zonder target expressie onderzocht voor vier $^{89}$Zr-gelabelde antilichamen ($^{89}$Zr-antiCD20, $^{89}$Zr-antiEGFR, $^{89}$Zr-antiPSMA en $^{89}$Zr-antiHER2). Door middel van de zogenaamde 'Patlak analyse' werden de reversibele ($V_T$) en irreversibele component ($K_i$) van het totale signaal vastgesteld voor de nier, lever, long en milt. Voor de Patlak analyse zijn minimaal 3 scans nodig op verschillende tijdstippen na bereiken van een evenwichtssituatie tussen het antilichaam in het bloed en in de weefsels (vanaf 1 dag na toediening). Dit onderzoek toonde dat de niet-specifieke, reversibele opname gelijk was aan de voorspelde waarde. De niet-specifieke, irreversibele opname was gelijk aan de voorspelde waarde voor de afbraaksnelheid van antilichaam. Met deze gemeten waarden is een basiswaarde vastgesteld.

In de situatie waarbij er antigeen-gemedieerde opname is, verwachten we een hogere $K_i$ te meten in vergelijking met de basiswaarde. Voor $^{89}$Zr-antiPSMA wordt antigeen-gemedieerde opname in de nier verwacht, omdat in de literatuur expressie van PSMA in de nier beschreven is. Uit dit onderzoek blijkt de $K_i$ voor $^{89}$Zr-antiPSMA in de nier 4 keer zo hoog ten opzichte basiswaarde. Dit resultaat wijst op antigeen-gemedieerde binding van antiPSMA in de nier.

Deze resultaten vormen de cruciale basis voor kwantificatie van target-gemedieerde opname van therapeutische antilichamen *in-vivo* met $^{89}$Zr-immuno-PET. Voor toekomstige studies, met nieuwe $^{89}$Zr-gelabelde antilichamen, is een 'pilot fase' met minimaal 3 scans ≥ 1 dag na de toediening noodzakelijk om niet-specifieke opname over de tijd te meten, om de studie opzet voor detectie van antigeen-gemedieerde opname te optimaliseren.

**Hoofdstuk 10** geeft een overzicht van het onderzoek in dit proefschrift, waarin we de ontwikkeling beschrijven van $^{89}$Zr-immuno-PET als klinische methode om antilichaam-therapie voor kanker te sturen. Initiele klinische studies met $^{89}$Zr-immuno-PET in de conologie laten zien dat deze techniek uitvoerbaar en veilig is. Technische validatie heeft aangetoond dat de multi-center interobserver

reproduceerbaarheid van tumorkwantificatie uitstekend is, hoewel er een substantiele meetfout ten gevolge van ruis gevonden werd. Biologische validatie laat zien dat het mogelijk is om met [89]Zr-immuno-PET de onderliggende biologische processen te meten (correlatie met target antigeen expressie, dosis-afhankelijkheid en het vaststellen van niet-specifieke opname).

Toekomstig onderzoek is nodig om de nauwkeurigheid van de techniek te verbeteren. Verwacht wordt dat de klinische introductie van de total body PET/CT scanner dit in de nabije toekomst mogelijk zal maken, met name door significante reductie van ruis. De total body PET/CT scanner heeft een detector ring die het volledige lichaam omvat waardoor nauwkeuriger gemeten kan worden. Tenslotte is klinische validatie nodig, waarbij de voorspellende waarde van [89]Zr-immuno-PET vastgesteld wordt.Onder deze voorwaarden kan [89]Zr-immuno-PET gebruikt worden als klinische methode om te voorspellen welke patienten zullen baat hebben bij antilichaam-therapie en welke nieuwe geneesmiddelen geschikt zijn voor verdere ontwikkeling.

In het huidige tijdperk met vele nieuwe vormen van immuuntherapie, zoals antilichaam-drug conjugaten, bispecifieke antistoffen, immune checkpoint inhibitors en chimeric antigen receptor (CAR) T-cellen is het essentieel om te onderzoeken of het geneesmiddel de tumor daadwerkelijk bereikt en welke patienten zullen gaan responderen op de behandeling. Deze informatie is nodig om voor de individuele patient de behandeling gericht te sturen zodat effectieve therapie met minimale toxiciteit bereikt kan worden. Hiervoor is de ontwikkeling van [89]Zr-immuno-PET uiterst relevant. Gezien de kosten van dure geneesmiddelen is het van maatschappelijk belang dat [89]Zr-immuno-PET zo snel mogelijk wordt ingezet.

## ACKNOWLEDGEMENTS / DANKWOORD

Without water, sunlight and time, no plant can grow and flower. It is the same with research. This thesis would not have been here, without the inspiration, effort and time of many people.
I would like to thank all of you.

Ik wil echt iedereen bedanken die heeft bijgedragen aan dit proefschrift. Dat doe ik grotendeels zonder namen. Toch weet je het, dit gaat over jou!
Dankjewel dat jij er was!

Wie ben jij?
Jij bent degene die een immuno-PET scan liet maken met als doel de behandeling van kanker in de toekomst te verbeteren. Dit proefschrift is er dankzij en voor jou.
Jij bent degene die dit onderzoek mogelijk heeft gemaakt door geld of tijd te doneren.
Jij bent iemand met wie ik samen werk of heb gewerkt, in welke functie dan ook, jij hebt mij direct of indirect geholpen bij het maken van dit proefschrift.
Jij hebt mij geleerd om onderzoek te doen, jij gaf mij vertrouwen.
Jij zorgt dagelijks samen met mij voor patiënten, jij bent die leuke collega met wie ik heel graag samen werk, van wie ik energie krijg.
Jij bent degene aan wie ik om hulp en advies vraag.
Jij bent degene met wie ik een goede klik heb, met jou kan ik samen lachen.
Jij hebt voor mij gezorgd toen ik dat nodig had, jij vraagt hoe het met mij gaat.
Jij bent mijn vriend of vriendin, met jou doe ik leuke dingen zoals samen eten en kan ik praten over alle ups en downs tijdens dit promotietraject.
Jij bent mijn familie, die mij onvoorwaardelijk steunt. Je vroeg me ontelbare keren wanneer het proefschrift af zou zijn. Nu is het af!
Samen zijn jullie voor mij het klimaat, waarin ik werk en leef. Het prachtige leven om mij heen. De wereld waar ik van geniet. De wereld waar ik dankbaar voor ben.

Sonja Zweegman en Guus van Dongen, mijn promotoren, met uitzonderlijk oog voor zowel de grote lijnen als de details. Jullie zijn voor mij als water, in staat om een oceaan te vormen, maar ook een enkele regendruppel op een blad. Jullie gaven mij de mogelijkheid om te groeien en mij verder te ontwikkelen.
Josée Zijlstra en Marc Huisman, mijn co-promotoren, met enorm veel vertrouwen

en aandacht hebben jullie mij geholpen om dit proefschrift te maken. Ik heb jullie begeleiding ervaren als zonnestralen: warm en behulpzaam om mijn weg te vinden.

Ik wil jullie alle vier heel erg bedanken voor alles wat ik van jullie geleerd heb en nog zal leren.

Adrienne Brouwers, Marie-José Kersten, Adriaan Lammertsma en Willemien Menke-van der Houven van Oordt:
Veel dank voor de tijd en aandacht die jullie aan mijn proefschrift hebben besteed.
Franck Morschhauser and Wolfgang Weber:
Your evaluation of my thesis and presence as opponent is greatly appreciated. I enjoyed working with you and spending time in Lille and New York.
'Merci beaucoup' and 'vielen Dank'!

Otto Hoekstra en Peter Huijgens:
Jullie zijn mijn "Pokon"! Heel veel dank.

Coreline Burggraaff en Swie-Ien Sie-Lo, mijn paranimfen:
Mijn steun en toeverlaat, waarvoor heel veel dank!

mama en papa:
Bedankt voor alles dat jullie mij hebben gegeven. Lieve mama, in gedachten blijf je altijd bij me.

Olivier:
De aarde, ben jij voor mij. Dankjewel voor alles. Samen verkennen we de wereld!

## CURRICULUM VITAE

Yvonne Jauw was born in Utrecht, the Netherlands, on the 10th of January 1984. She graduated cum laude from secondary school in 2001 at the Christelijk Gymnasium in Utrecht. Yvonne studied Medicine at the Vrije Universiteit in Amsterdam, where she participated in the Honours Programme. Her scientific research focused on $^{89}$Zr-immuno-PET and was performed at the department of Otolaryngology/Head and Neck Surgery at the VU University Medical Center (prof.dr. Guus van Dongen, dr. Pontus Börjesson). In 2006, she did her internship Gynecology and Obstetrics at the Lyell McEwin Hospital in Adelaide, Australia (prof. dr. Gus Dekker).

Yvonne obtained her medical degree cum laude in 2007 and started her residency at the department of Internal Medicine at the VU University Medical Center (prof. dr. Mark Kramer), in part at the Kennemer Gasthuis in Haarlem (dr. Reinier ten Kate). In 2012, Yvonne entered a fellowship in Hematology at the VU University Medical Center (prof. dr. Sonja Zweegman, prof. dr. Peter Huijgens). In 2013, she received a grant from the Dutch Cancer Society for research on $^{89}$Zr-immuno-PET, which resulted in this thesis. She combined clinical training with her PhD-project and completed her specialization as internist-hematologist in 2015.

From 2015, she continued her career at the VU University Medical Center as a hematologist at the department of Hematology, and as physician-researcher at the department of Radiology and Nuclear Medicine.

Currently, Yvonne is a staff member at the department of Hematology and continues her scientific research at the department of Radiology and Nuclear Medicine, at the Amsterdam UMC location VUmc.

# LIST OF PUBLICATIONS

- **Jauw YWS**, Bensch F, Brouwers AH, Hoekstra OS, Zijlstra JM, Pieplenbosch S, Schröder CP, Zweegman S, van Dongen GAMS, Menke-van der Houven-van Oordt CW, de Vries EGE, de Vet HCW, Boellaard R, Huisman MC. Interobserver reproducibility of tumor uptake quantification with 89Zr-immuno-PET. *Eur J Nucl Med Mol Imaging*. 2019 Jun 17. doi: 10.1007/s00259-019-04377-6. [Epub ahead of print]

- **Jauw YWS**, O'Donoghue JA, Hoekstra OS, Menke-van der Houven van oordt CW, Morschhauser F, Carrasquillo JA, Zweegman S, Pandit-Taskar N, Lammertsma AA, van Dongen GAMS, Boellaard R, Weber WA, Huisman MC. [89]Zr-immuno-PET: towards a non-invasive clinical tool to measure target engagement of therapeutic antibodies in-vivo. *J Nucl Med.* 2019 May 30. pii: jnumed.118.224568. doi: 10.2967/jnumed.118.224568. [Epub ahead of print]

- **Jauw YWS**, Heijtel DF, Zijlstra JM, Hoekstra OS, de Vet HCW, Vugts DJ, Verheul HM, Boellaard R, Zweegman S, van Dongen GAMS, Menke-van der Houven-van Oordt CW, Lammertsma AL, Huisman MC. Noise induced variability of immuno-PET with Zirconium-89-labeled antibodies: an analysis based on count-reduced clinical images. *Mol Imaging Biol.* 2018 Dec;20(6):1025-1034. doi: 10.1007/s11307-018-1200-4.

- **Jauw YWS**, Huisman MC, Nayak TK, Vugts DJ, Christen R, Naegelen VM, Ruettinger D, Heil F, Lammertsma AA, Verheul HMW, Hoekstra OS, van Dongen GAMS, Menke-van der Houven van Oordt CW. Assessment of target-mediated uptake with immuno-PET: analysis of a phase I clinical trial with an anti-CD44 antibody. *EJNMMI Res.* 2018 Jan 22;8(1):6. doi: 10.1186/s13550-018-0358-8.

- **Jauw YWS**, Zijlstra JM, de Jong D, Vugts DJ, Zweegman S, Hoekstra OS, van Dongen GA, Huisman MC. Performance of [89]Zr-Labeled-Rituximab-PET as an Imaging Biomarker to Assess CD20 Targeting: A Pilot Study in Patients with Relapsed/Refractory Diffuse Large B Cell Lymphoma. *PLoS One*. 2017 Jan 6;12(1) e0169828. doi: 10.1371/journal.pone.0169828.

- **Jauw YWS**, Menke-van der Houven van Oordt CW, Hoekstra OS, Hendrikse NH, Vugts DJ, Zijlstra JM, Huisman MC, van Dongen GA. Immuno-Positron Emission Tomography with Zirconium-89-Labeled Monoclonal Antibodies in Oncology: What Can We Learn from Initial Clinical Trials? *Front Pharmacol.* 2016 May 24;7:131. doi: 10.3389/fphar.2016.00131.

- Keizer S, Gerritsen R, **Jauw Y**, Janssen J, Koopman B, Bresser P. Fatal tuberculosis during treatment with ruxolitinib. *Ned Tijdschr Geneeskd.* 2015;159:A8650.

- Wondergem MJ, Rizvi SN, **Jauw Y**, Hoekstra OS, Hoetjes N, van de Ven PM, Boellaard R, Chamuleau ME, Cillessen SA, Regelink JC, Zweegman S, Zijlstra JM. 18F-FDG or 3'-deoxy-3'-18F-fluorothymidine to detect transformation of follicular lymphoma. *J Nucl Med.* 2015 Feb;56(2):216-21. doi: 10.2967/jnumed.114.149625.

- de Jong A, Kwee TC, de Klerk JM, Adam JA, de Keizer B, Fijnheer R, Kersten MJ, Ludwig I, **Jauw YW**, Zijlstra JM, Pieters-Van den Bos IC, Stoker J, Hoekstra OS, Nievelstein RA. Relationship between pretreatment FDG-PET and diffusion-weighted MRI biomarkers in diffuse large B-cell lymphoma. *Am J Nucl Med Mol Imaging.* 2014 Apr 25;4(3):231-8.

- Börjesson PK, **Jauw YW**, de Bree R, Roos JC, Castelijns JA, Leemans CR, van Dongen GA, Boellaard R. Radiation dosimetry of [89]Zr-labeled chimeric monoclonal antibody U36 as used for immuno-PET in head and neck cancer patients. *J Nucl Med.* 2009 Nov;50(11):1828-36. doi:10.2967/jnumed.109.065862.

- Börjesson PK, **Jauw YW**, Boellaard R, de Bree R, Comans EF, Roos JC, Castelijns JA, Vosjan MJ, Kummer JA, Leemans CR, Lammertsma AA, van Dongen GA. Performance of immuno-positron emission tomography with zirconium-89-labeled chimeric monoclonal antibody U36 in the detection of lymph node metastases in head and neck cancer patients. *Clin Cancer Res.* 2006 Apr 1;12(7 Pt 1):2133-40.

**Abstracts/presentations**

- Marc Huisman, Ronald Boellaard, Josée Zijlstra, Daphne de Jong, Danielle Vugts, Sonja Zweegman, Otto Hoekstra, Guus van Dongen, **Yvonne Jauw**. Beyond SUV: from false-positive to true positive tumor uptake of $^{89}$Zr-antiCD20. Oral presentation. Society of Nuclear Medicine & Molecular Imaging Annual Meeting, Anaheim, USA, 2019.

- **Yvonne W.S. Jauw,** Joseph A. O'Donoghue, Josée M. Zijlstra, Otto S. Hoekstra, C. Willemien Menke-van der Houven van Oordt, Franck Morschhauser, Jorge A. Carrasquillo, Sonja Zweegman, Neeta Pandit-Taskar, Adriaan A. Lammertsma, Guus A.M.S. van Dongen, Ronald Boellaard, Wolfgang A. Weber, Marc Huisman. $^{89}$Zr-immuno-PET: towards a non-invasive clinical tool to measure target engagement of therapeutic antibodies in-vivo. Poster presentation. Society of Nuclear Medicine & Molecular Imaging Annual Meeting, Anaheim, USA, 2019. *Poster award candidate, Oncology track.*

- Keiichi Magota, **Yvonne W.S. Jauw**, Dennis F. Heijtel, Josée M. Zijlstra, Guus A.M.S. van Dongen, Adriaan A. Lammertsma, Ronald Boellaard, Marc C. Huisman. Optimizing iterative reconstruction settings for improved 89Zr-immuno-PET image quality. Poster presentation. European Association of Nuclear Medicine Annual Congress, Dusseldorf, Germany, 2018.

- **Yvonne W.S. Jauw**, Catharina W. Menke-van der Houven van Oordt, Tapan K. Nayak, Danielle J. Vugts, Randolph Christen, Valerie Meresse Naegelen, Adriaan A. Lammertsma, Henk M.W. Verheul, Guus A.M.S. van Dongen, Otto S. Hoekstra, Marc C. Huisman. In-vivo assessment of antibody selectivity: immuno-PET with anti-CD44 antibody in a phase I clinical trial. Oral presentation. Society of Nuclear Medicine & Molecular Imaging, Annual Meeting, Denver, USA, 2017. *Selected for Highlight Session, Oncology track.*

- **Yvonne Jauw**, Josée Zijlstra, Otto S. Hoekstra, Sonja Zweegman, Pascal Odou, Danielle Vugts, Damien Huglo, Franck Morschhauser, Marc Huisman. First-in-human in-vivo biodistribution of a glyco-engineered antibody: $^{89}$Zirconium-labeled obinutuzumab in patients with non-Hodgkin lymphoma. Oral presentation. Society of Nuclear Medicine & Molecular Imaging Annual Meeting, Denver, USA, 2017.

A

- **Yvonne W.S. Jauw**, Dennis F. Heijtel, Josée M. Zijlstra, Otto S. Hoekstra, Tapan K. Nayak, Guus A.M.S. van Dongen, C. Willemien Menke-van der Houven van Oordt, Adriaan A. Lammertsma, Marc C. Huisman. Repeatability of PET with [89]Zirconium-labeled monoclonal antibodies for quantification of antibody biodistribution. Oral presentation. Society of Nuclear Medicine & Molecular Imaging, Annual Meeting, Denver, USA, 2017.

- **Yvonne W.S. Jauw**, Marc C. Huisman, Danielle J. Vugts, Daphne de Jong, Sonja Zweegman, Guus A.M.S. van Dongen, Otto S. Hoekstra, Josée M. Zijlstra. A phase II study of obinutuzumab monotherapy in rituximab-refractory lymphoma: Zirconium-89-immuno-PET design and preliminary results of the ZON study. Laptop presentation. Dutch Hematology Congress, Papendal, the Netherlands, 2017.

- **Y.W.S. Jauw**, M. C. Huisman, D. de Jong, D. J. Vugts, S. Zweegman, G.A.M.S. van Dongen, O.S. Hoekstra, J.M. Zijlstra. [89]Zr-labeled-rituximab PET as an imaging biomarker to assess CD20 targeting: a pilot study in patients with relapsed/refractory diffuse large B cell lymphoma. Poster presentation. 6th International Workshop on PET in Lymphoma, Menton, France, 2016.

- **Y.W.S. Jauw**, J.M. Zijlstra, G.A.M.S. van Dongen, S. Zweegman, O.S. Hoekstra, M.C. Huisman. Strategies for tumor uptake quantification of [89]Zr-labeled-antiCD20 antibodies with PET in non-Hodgkin lymphoma patients. Oral presentation. Society of Nuclear Medicine & Molecular Imaging Annual Meeting, San Diego, USA, 2016.

- M.C. Huisman, **Y.W.S. Jauw**, J.M. Zijlstra, C.W. Menke - van der Houven van Oordt, G.A.M.S. van Dongen, A. van Lingen, A.A. Lammertsma. Accuracy of a dual day scan protocol to estimate the radiation dose of [89]Zr-labeled monoclonal antibodies. Poster presentation. Society of Nuclear Medicine & Molecular Imaging Annual Meeting, San Diego, USA, 2016.

- **Y.W.S. Jauw**, O.S. Hoekstra, E.R. Mulder, S. Pieplenbosch, N.J. Hoetjes, G.A.M.S. van Dongen, S. Zweegman, J.M. Zijlstra, M.C. Huisman. Inter-observer agreement for tumor uptake quantification of [89]Zr-labeled anti-CD20 antibodies with PET. Poster presentation. Society of Nuclear Medicine & Molecular Imaging Annual Meeting, San Diego, USA, 2016.

- **Y.W.S. Jauw**, J.M. Zijlstra, O.S. Hoekstra, S. Zweegman, G.A.M.S. van Dongen, M.C. Huisman. Impact of injected dose on accuracy and precision of tumor and organ uptake quantification of $^{89}$Zr-labeled anti-CD20 antibodies with PET. Poster presentation. Society of Nuclear Medicine & Molecular Imaging Annual Meeting, San Diego, USA, 2016.

- **Y.W.S. Jauw**, M.C. Huisman, G.A.M.S. van Dongen, J.A.J. Janssen, O.S. Hoekstra, S. Zweegman, J.M. Zijlstra. Immuno-PET in relapsed/refractory diffuse large B cell lymphoma: tumor uptake of $^{89}$Zr-rituximab. Oral presentation. Dutch Hematology Congress, Papendal, the Netherlands, 2016.

- **Y.W.S. Jauw**, M.C. Huisman, G.A.M.S. van Dongen, O.S. Hoekstra, J.M. Zijlstra. Biodistribution and uptake of $^{89}$Zr-rituximab and $^{89}$Zr-ofatumumab in patients with relapsed diffuse large B cell lymphoma. Poster presentation. 5th International Workshop on PET in Lymphoma, Menton, France, 2014.

# LIST OF ABBREVIATIONS

| | |
|---|---|
| ADC | antibody-drug conjugate |
| AUC | area under the curve |
| DLBCL | diffuse large B cell lymphoma |
| cmAb | chimeric monoclonal antibody |
| CoV | coefficient of variation |
| CT | computed tomography |
| $^{18}$F-FDG | 18-fluoro-2-deoxy-glucose |
| GMP | good manufacturing practice |
| HNSCC | head and neck squamous cell carcinoma |
| ICC | intraclass correlation coefficient |
| IHC | immunohistochemistry |
| $K_i$ | net rate of irreversible uptake |
| mAb | monoclonal antibody |
| MBq | megabecquerel |
| mSv | millisievert |
| MRI | magnetic resonance imaging |
| PET | positron emission tomography |
| SD | standard deviation |
| SUV | standardized uptake value |
| VOI | volume of interest |
| $V_t$ | volume of distribution |
| $^{89}$Zr | 89-zirconium |